Structure and Phase Behavior of Aqueous Methylcellulose

A DISSERTATION
SUBMITTED TO THE FACULTY OF THE GRADUATE SCHOOL
OF THE UNIVERSITY OF MINNESOTA
BY

John Winfield McAllister

IN PARTIAL FULFILLMENT OF THE REQUIREMENTS
FOR THE DEGREE OF
Doctor of Philosophy

Timothy P. Lodge
Frank S. Bates

September 2015

© John Winfield McAllister 2015
ALL RIGHTS RESERVED

Acknowledgements

Many people helped me to complete this dissertation, and I am grateful to have been supported by so many.

First to my advisers, have both provided me with unwavering intellectual stimulation, and applied just the right amount of pressure for my time to at Minnesota to be challenging, frustrating, exhausting, and above all, a lot of fun. Frank has contagious enthusiasm for any topic he picks up. Coupled with his expertise in the field of polymer science, and his "gut feelings" of how something should work, make for very stimulating conversations about a wide variety of topics. Tim's meticulous approach to science, about boiling every question down to fundamental scientific concepts is a skill I hope that I managed to pick up (at least a little bit) along the way. I'm also grateful for his insistence that, "methylcellulose will be a good project for you." He was right. I feel privileged to have spent five years learning from both Tim and Frank.

I'm very grateful to Joe Lott and Sara Arvidson, two postdocs I worked with very closely on this project. I enjoyed our time working together, and from whom I learned a great deal about what being a scientist means. I'm happy that after our years of working together that I call you friends, in addition to colleagues. And to Peter Schmidt and Amanda Maxwell who are continuing the project, It's been fun to to have worked with you.

This project was funded by Dow, so I'm grateful for the money to do this research.

But more importantly, there the great people at Dow that I've had the privilege to interact with, Bob Sammler, Bob Schmitt, Tirtha Chatterjee, Valeriy Ginzburg, Meinolf Brackhagen, John Reffner, and many others. You've all been very approachable and patient to answer any question I had.

The other members of the Lodge and Bates group have an amazing culture of excellence, and many people specifically have taught me a thing or two. For showing me my way around the labs: Brad Jones, Adam Moughton, Athanasios Touris, Sangwoo Lee, Ameara Mansour, and Yuanyan Gu, you all were really patient with me. For really great conversations about all things sciencey (and not): Megan Hoarfrost, Jenny Laaser, Rob Hickey, Sam Dalsin, Tim Gillard, Lucas McIntosh, Chris Thurber, Jie Lu, Soonyong So, Ziafei Wang, Ceci Hall, and Aakriti Kharel, it's been a lot of fun. If your name isn't on this list and you think it should be, I apologize but there's a lot of people. Just pencil it in below. It's okay with me.

Most importantly, To my family for the stress and heartache this process has been for you, and the unwavering support you've given me, I'm eternally grateful. Mom and Dad, you're insistence that I always strive for something better has lead me here. I couldn't have done it without you. And Heidi has been incredibly patient with putting up with me coming back to school, and supportive of me even when you think you aren't. And to Sam, you make it all worthwhile.

Dedication

for Sam

Abstract

Methylcellulose is a chemically modified polysaccharide that is partially substituted by methoxyl groups. When the average substitution per monomer is intermediate, MC is water soluble, and these materials see use in a wide variety of commercial products. Aqueous solutions of MC undergo gelation and phase separation upon heating. Using dynamic mechanical spectroscopy, frequency-independent loss tangents were used to identify the gel point (T_{gel}) in MC solutions well over the chain overlap concentration ($c \geq 10c^*$). Transmittance of 633 nm laser light through the solutions revealed that MC solutions cloud upon gelling, with a relative transmittance of 86% closely associated with the gel point. The gelation temperature of MC solutions was found to decrease with increasing MC concentration and the results for all molecular weights superposed.

The fibrillar structure of aqueous MC gels was probed using a combination of small-angle neutron scattering (SANS), ultra-small-angle neutron scattering (USANS), and cryogenic transmission electron microscopy (cryo-TEM). The effect of molecular weight (M_{w}) and concentration on the gel structure was explored. The fibrillar morphology was consistently observed at elevated temperatures ($\geq$ 70 °C), independent of concentration and M_w. Moreover, the fibril dimensions extracted from SANS by fitting to a scattering function for semiflexible cylinders with disperse radii revealed that the fibril diameter of ca. 14 ± 1 nm is constant for a concentration range of 0.01% to 3.79% and for all M_{w} investigated (150-530 kg/mol). Comparison of the measured SANS curves with predicted scattering traces revealed that at 70 °C the fibrils contain an average volume fraction of 40% polymer.

The linear and nonlinear viscoelastic response of MC gels can be described by a filament-based mechanical model. In particular, large-amplitude oscillatory shear experiments show that aqueous MC materials transition from shear thinning to shear

thickening behavior at the gelation temperature. The critical stress at which MC gels depart from the linear viscoelastic regime and begin to stiffen is well predicted from the filament model over a concentration range of 0.18â-2.0 wt%. These predictions are based on fibril densities and persistence lengths obtained experimentally from neutron scattering, combined with cross-link spacings inferred from the gel modulus via the same model.

M_w, z-average radius of gyration (R_g), and second virial coefficient A_2 have been determined between 15 and 52 °C for dilute aqueous solutions of methylcellulose (MC) with three different molecular weights and constant degree of substitution (DS) of 1.8 using static light scattering. These measurements, conducted within 1 hour of heating the homogeneous solutions from 5 °C, reveal that the theta temperature for MC in water is $T_\theta = 48 \pm 2$ °C, with $A_2 < 0$ for $T > T_\theta$, indicative of lower critical solution temperature (LCST) behavior. However, after annealing a solution for 2 days at 40 °C evidence of high molecular weight aggregates appears through massive increases in the apparent M_w and R_g, a process that continues to evolve for at least 12 days. Cryogenic transmission electron microscopy images obtained from a solution aged for three weeks at 40 °C reveal the presence of micron size fibrils w analogous to the fibrils that form upon gelation of aqueous MC solutions at higher concentrations and elevated temperatures. Growth of fibrils from a solution characterized by a positive A_2 indicates that semiflexible MC dissolved in water is metastable at $T < T_\theta$, even though the solvent quality is apparently good. The minimum temperature required for MC solutions to aggregate is estimated to be 30 °C, based on the rate independent gel-to-solution transition determined by small-amplitude oscillatory shear measurements conducted while cooling 0.5 and 5.0 wt% solutions. These results cannot be explained based solely on separation into two isotropic phases upon heating using classical Flory-Huggins solution theory. It was speculated that the underlying equilibrium phase behavior of aqueous MC solutions involves a nematic order parameter.

Table of Contents

List of Tables

List of Figures

Chapter 1

Introduction

1.1 Overview of Modified Polysaccharides

Cellulose is a polysaccharide that is utilized by plants to add rigidity to cell walls. Its annual biomass production is on the order of 10^{15} kg,[1] making it the most abundant organic compound on Earth. The cellulose content in wood is 40-50 wt%, depending on the species, and about 90 wt% in cotton linters. It consists of D-glucopyranose repeat units connected by $\beta(1\rightarrow4)$ linkages, illustrated in Figure 1.1. This bond morphology creates an alternating syndiotactic-like arrangement of anhydroglucose units; each monad has three hydroxyl groups (at carbon positions C2, C3 and C6). The spatial distribution of -OH groups allows for intrachain hydrogen bonding along

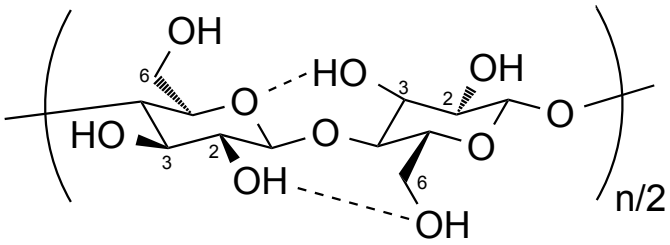

Figure 1.1: Two repeat units of a cellulose chain, showing the $\beta(1\rightarrow4)$ connection between adjacent anhydroglucose units. The dashed lines depict hydrogen bonds between the pyranosidyl oxygen and C2 hydroxyl of the unit on the left to the C3 hydroxyl and C6 hydroxyl of an adjacent unit on the right.

the polymer chain, which increases chain stiffness of cellulose compared to many other polysaccharides. The remaining hydroxyl groups form hydrogen bonds between chains, giving cellulose well-defined semicrystalline structures. The high degree of H-bonding in cellulose excludes hydrogen bonding with water, making the material water-insoluble.

The major industrial applications of cellulose, such as paper and cotton textiles, employ cellulose in a relatively unmodified form. However, the vast abundance of cellulose makes it an attractive option as a renewable feedstock for new materials. One strategy, which has been practiced for decades, is the derivatization of the hydroxyl groups to produce a class of materials known as cellulosic polymers, depicted generally in Figure 1.2. These materials include cellulose esters, in which the hydroxyl group on the cellulose chain reacts with an organic acid to create an ester linkage to the substituted group. Cellulose esters can be produced using inorganic acids, with nitrocellulose ("gun cotton") as the primary historical example. Cellulose acetates are another type, which find widespread use as air filters, photographic films, and more recently, in liquid crystal displays. Another cellulosic material is sodium carboxymethylcellulose (CMC), in which carboxymethyl group ($-CH_2COO^-$) is bonded to the pyranosidyl oxygens, find use as viscosity modifiers in many foods, detergents, and water-based paints. Cellulose ethers, the class to which methylcellulose belongs, has an ether linkage that connects the cellulose backbone to the substituted group.

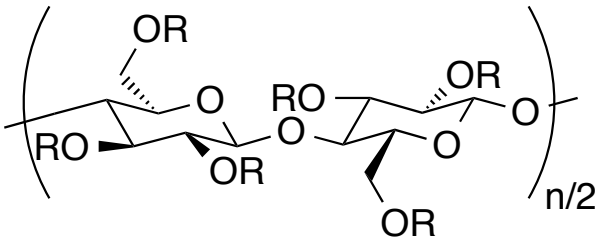

Figure 1.2: Two repeat units of a generalized modified polysaccharide chain, "R" depicts either the substituted group or a hydrogen atom at carbon positions C2, C3, and C6. The degree of substitution (DS) is a number between 0 and 3 which describes the average substitution per repeat unit.

For cellulose ethers, the reagent used to react with the hydroxyl group is usually a haloalkane or an epoxide. Cellulose ethers are often designed to be water soluble, and their uses are discussed in Section 1.2. The worldwide production for cellulose esters and ethers are each more than 8×10^8 kg for the year 2014.[2,3]

Cellulose ethers consist of a number of different materials, including methylcellulose (MC), ethylcellulose (EC), hydroxypropylcellulose (HPC), and hydroxypropylmethylcellulose (HPMC). An important parameter which greatly affects the properties of modified polysaccharides is the degree of substitution (DS) DS is a number between 0 and 3 which describes the average substitution per repeat unit. Methylcellulose is the chemically simplest cellulose derivative, and has methoxyl groups substituted onto the anhydroglucose units, and is water-soluble for intermediate substitution levels. EC is often highly substituted ($DS > 2.5$), and has thermoplastic properties.[4] Like carboxymethylcellulose, HPC and HPMC are also used as viscosity modifiers, but are non-ionic and generally do not form gels upon heating. The properties and thermodynamics of aqueous solutions of methylcellulose are addressed in this dissertation. Aqueous methylcellulose solutions turn into visually turbid hydrogels upon heating (see Figure 1.3), and this property has been studied for more than 80 years.[5] Despite a long history, there is still debate as to the structure and mechanism of the gel formation, and this work will provide new insights into the nature of this fascinating material.

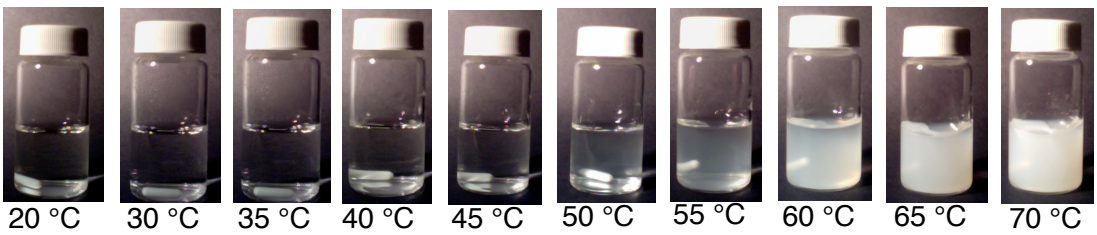

Figure 1.3: Photographs of the thermogelation of an MC solution. The solution has a concentration of 1.5 wt% MC, with 20 °C on the left slowly heated to 70 °C on the right.

1.2 Uses of Methylcellulose

MC and other cellulose ethers are classified as generally recognized as safe (GRAS) by the U. S. Food and Drug Administration,[6] so it can be included as an additive to foods, cosmetics, and pharmaceutical agents without extensive human clinical trials or other toxicity tests. Cellulose ethers are widely used in the construction industry as viscosity modifiers and aqueous lubricants and are added to many building materials. Hydroxypropylcellulose and hydroxypropylmethylcellulose are often added to gypsum-based wall plasters, tile cements, and stucco. Construction-grade cellulosics are often treated with glyoxyl, which makes the material more easily dispersed into water. Cellulose ether solutions are used as "green" lubricants for the drilling of water and oil wells.[3,7] Methylcellulose is the primary component in wallpaper paste, which is ideally suited as a weak adhesive for papers. Gelation of methylcellulose solutions on heating make it a useful additive for extruded ceramic parts, which prevents distortion in the earliest stages of kilning.

Purified cellulose ethers find use in a wide variety of manufactured foods due to their status as GRAS. From a nutritional perspective, methylcellulose is no different from dietary fiber (cellulose) in humans. The ability of MC solutions to gel is an attractive property for many foods, and MC is used as a dough binder, thickener, and as a replacement for eggs and wheat gluten.[7,8] MC is also very popular in modernist cuisine to prepare edible gels and foams.[9] Cellulose ethers are biodegradable, and can be degraded by cellulases and other enzymes that will cleave the β (1→4) linkage of the cellulose backbone. There is evidence by Wirick[10] that even sequences of trisubstituted cellulose derivatives are susceptible to cellulase degradation.

Cellulose ethers play important supporting roles for pharmaceutical products. They are used as viscosity modifiers to provide the appropriate viscoelasticity of topical creams and ointments. Cellulose ethers are also used as dietary fiber supplements, since they are indigestible and nontoxic to humans. MC, HPC, HPMC and other cellulosic materials are used as tablet binders and coatings, and importantly,

excipients for regulate the slow dissolution of drugs from tablets,[11] which is an active area of current research.[12–14]

1.3 Historical Perspective of Methylcellulose

For a material first synthesized more than 100 years ago[15] and with a sizable market for consumer products, there have been many patents and academic publications on the gelation of aqueous MC materials. Despite its long history, the nature of MC gels are still poorly understood with different hypotheses proposed for the gelation mechanism. This section touches on some of the notable reports.

1.3.1 Viscoelastic Properties of Aqueous MC Solutions

Thermogelation of aqueous MC solutions was first reported by Heymann in 1935.[5] The viscosity of a 1.56 wt% MC solution was measured by timing the flow through

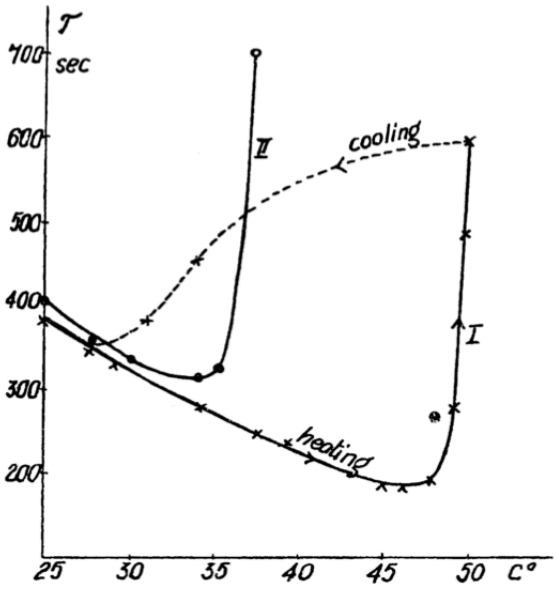

Figure 1.4: Time for a 1.56 wt% solution of MC to fall through an Ubbelohde viscometer measured by Heymann in 1935.[5] The line labeled "II" is the same concentration of MC solution in a 0.1 M solution of K_2SO_4. Reproduced with permission from The Royal Society of Chemistry.

an Ubbelohde viscometer between 25 and 60 °C on heating and cooling, as shown in Figure 1.4. On heating, there is an initial decrease in viscosity followed by a sharp increase in viscosity near 50 °C. While this report did not address the gel elasticity, the initial transition from solution to gel was visible, as was the hysteresis of MC solutions between heating and cooling: once the gel structure has developed, it persists as much as 30 °C below the sol-gel transition on heating (the dashed line in Figure 1.4). Heymann inferred that MC solutions consist of hydrated sol molecules, and upon heating MC dehydrates and coagulates to give the gel.

He proposed that the initial decrease in viscosity between 30 to 45 °C was the dehydration event, and the increase in viscosity above 45 °C is the coagulation of MC

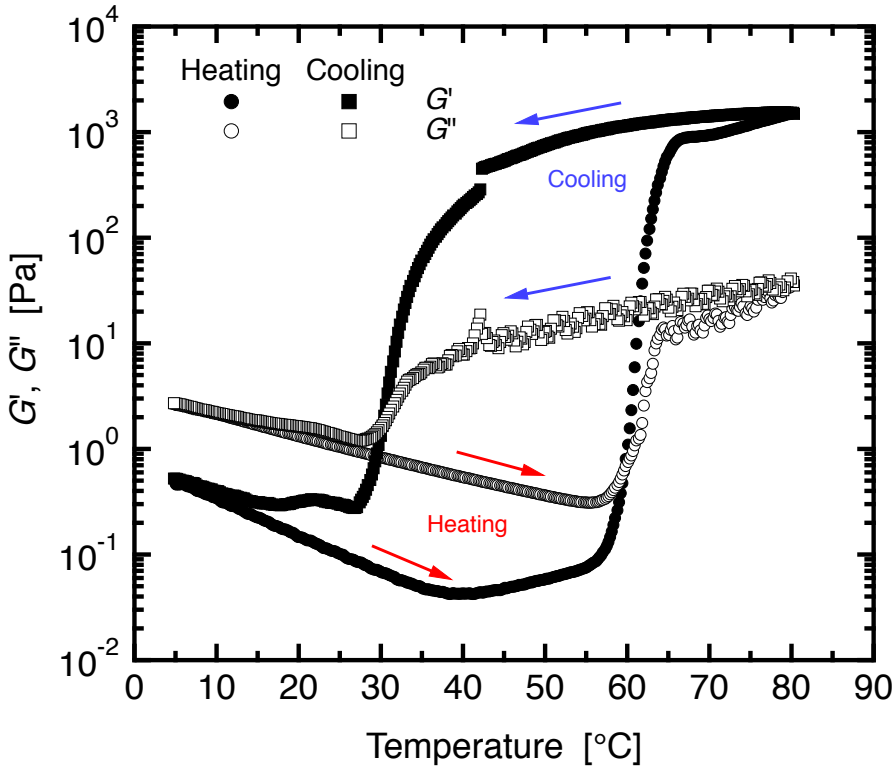

Figure 1.5: Storage and loss moduli of a 1.4 wt% ($c = 10c^*$) solution of MC300 upon heating and cooling at 1 °C min^{-1} with $\gamma_0 = 5\%$ at an oscillation frequency of $\omega = 1$ rad sec^{-1}, reported by Lott et al.[16] Two stages of MC gelation have been noted in many reports, with the first stage beginning at about 40 °C on heating, and the second beginning at about 60 °C on heating. Reproduced with permission from the American Chemical Society copyright 2013.

to make the gel. Heyman postulated that MC gels could be micellular in nature or that MC molecules form parallel-oriented crystalline structures.

More recent studies have investigated the viscoelasticity of MC solutions and gels by DMS.[17–23] All report similar properties of MC gelation, illustrated in Figure 1.5. Many[18,23–25] have noted two stages of gelation of MC on heating, one beginning at about 40 °C in Figure 1.5 where G' begins to increase gently, then a second near 60 °C where G' increases sharply with temperature. On cooling, similar hysteresis first noted by Heymann[5] can be seen, with the sample returning to the liquid state near 20 °C. There have been numerous interpretations of the two-stage gelation. It has been generally accepted in the literature that the first stage ($40 < T < 60$ °C) is attributed to some sort of chain association, while the second stage ($T > 60$ °C) is a result of gelation and/or phase separation.

For concentrations of MC above the chain overlap concentration (c^*), the onset of gelation was reported by Kobayashi et al.,[20] Desbriéres et al.,[21] and Li et al.[22,23]

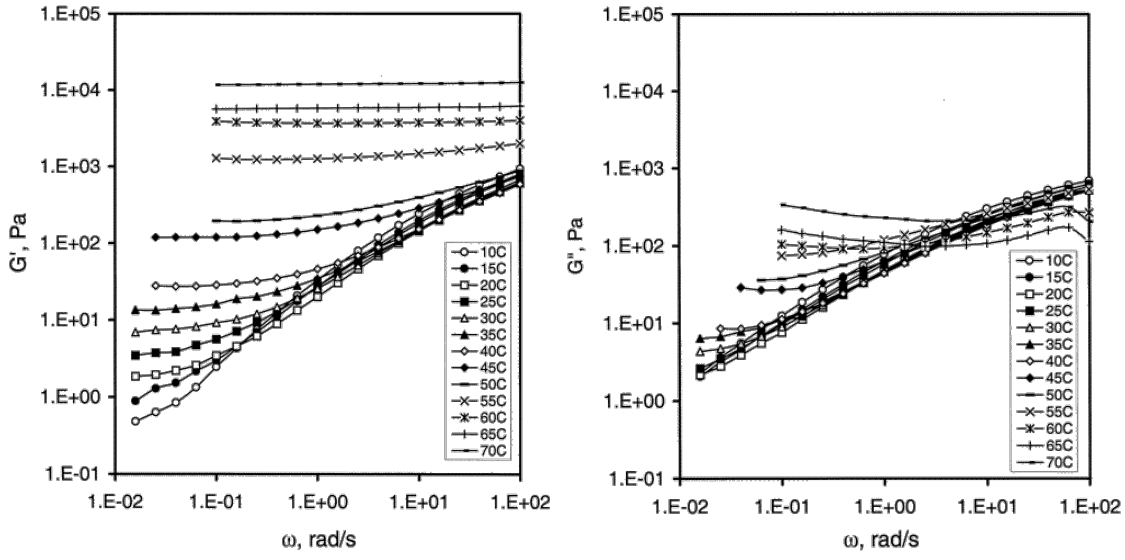

Figure 1.6: Frequency-dependent dynamic moduli for a MC solution of $M_w = 3.1 \times 10^5$ g mol^{-1} with $c = 3.9$ wt%. as reported by Li.[23] Reproduced with permission from the American Chemical Society copyright 2002.

Frequency-dependent moduli G' and G'' at temperatures between 10 and 70 °C reported by Li[23] and shown in Figure 1.6. Desbriéres et al.[21] reported terminal-regime viscoelastic flow behavior for entangled MC solutions with $T < 40$ °C utilizing a unique peizoelectric-based rheometer, which was able to measure a wide frequency range, from 0.6 to 6×10^4 rad s^{-1}. The power law slopes at the lowest frequencies were $G' \sim \omega^{1.53}$ and $G'' \sim \omega^{0.9}$. The deviation from ideal liquid-like response ($G' \sim \omega^2$ and $G'' \sim \omega^1$) is likely a result of the high dispersity of MC materials. Most rheological studies of MC indicate the slow development of a frequency-independent G' and G'' at high temperature, consistent with chemically or physical crosslinked networks. The two-stage nature of MC gelation is not apparent in Figure 1.6, because the initial rise in modulus at about 40 °C in Figure 1.5 becomes less apparent as c increases to highly entangled solutions MC solutions ($c \geq 15c^*$), which will be discussed further in Chapter 3.

The nature of the first and second stages of MC gelation hs been considered by a number of reports. Haque and Morris[18] noted that the sol-gel transition of MC depends strongly on concentration: higher concentrations undergo the gelation of MC at lower temperatures. MC gelation is also heating-rate dependent, which has been reported by Haque and Morris,[18] Sarkar,[19] and Desbriéres et al.[21] Sarkar attempted to develop an empirical rate law for the growth of G' as a function of c, T, DS, and M_w. Once the MC gel is fully developed, usually $T \geq 70$ °C, G' scales with concentration by a power-law dependence of $G' \sim c^2$ to $G' \sim c^{2.5}$, which is consistent with many swollen networks.[18,20,22] The viscoelastic properties of MC solutions all display a time-dependent increase in modulus at $T > 40$ °C concentration above and below c^*. Both the sol-gel transition temperature and the gel modulus are concentration dependent. Some have speculated on the nature of the hysteresis of MC solutions between heating and cooling[19,22,26] with various explanations. The common thread is that the hysteresis in MC solutions is a consequence of the non-equilibrium state of the gel.

1.3.2 MC Solution Structure by Scattering Techniques

There have been numerous studies to investigate the structure of MC solutions using static light scattering (SLS), and gels using small angle x-ray scattering (SAXS) and small angle neutron scattering (SANS). The wavelength of incident radiation (λ) and detection angle (θ) of the scattered radiation dictates the wavevector (q) probed by a particular experiment,

$$q = |\mathbf{q}| = \frac{4\pi n}{\lambda} \sin\left(\frac{\theta}{2}\right). \tag{1.1}$$

Use of q is often preferred over scattering angle θ because q is independent of incident wavelength, and makes for easy comparison between different experimental techniques. The measured signal requires contrast (which can be refractive index, electron density, or nuclei variation depending on the technique) between two components to resolve structures. SLS is generally suited for analyses of overall sizes of dilute polymers in solution, and requires the solution to be transparent to visible light. SAXS and SANS provide an interference pattern based upon the average shape of the scatterer, whether it be a single molecule or an aggregation of molecules.

Static light scattering (SLS) is often a preferred method to probe dilute polymer-solvent interactions. Using a Zimm analysis,[27] Equation 1.2, the weight-average molecular weight (M_w), and radius of gyration (R_g), can be determined from measurements of the scattering intensity, $I(q)$ (called the Rayleigh ratio, R_θ, for visible light), at numerous concentrations (c) and scattering wavevectors (q),

$$\frac{Kc}{R_\theta} = \frac{1}{M_\mathrm{w}} \left(1 + \frac{q^2 R_\mathrm{g}^2}{3} + \cdots\right) + 2A_2 c + \cdots \tag{1.2}$$

A collection of constants given by $K = 4\pi(\partial n/\partial c)^2 n^2/\lambda^4 N_\mathrm{A}$, where $\partial n/\partial c$ is the differential refractive index, n is the index of refraction of the solvent, λ is the incident light wavelength, and N_A is the Avogadro constant. These measurements require the Guinier scattering regime for the sample to be within the q-range of the instrument

($qR_g < 1$). The second virial coefficient A_2 can be determined by the concentration dependence of the zero-q absolute scattering intensity R_θ. Positive values of A_2 indicate a good solvent, in which solvent-polymer interactions are preferred over polymer-polymer interactions. The opposite scenario occurs when A_2 is negative: a poor solvent, in which polymer-polymer interactions are favored. $A_2 = 0$ is the *theta temperature*, which is the condition defined by the special case where polymer-water and polymer-polymer interactions compensate.

SLS of four dilute MC solutions (0.2 to 0.6 mg mL^{-1}) from a 488 nm laser were reported by Koyabashi et al.[20] A textbook-example[28] Zimm plot at 20 °C is shown in Figure 1.7. The extrapolation of Equation 1.2 to $c = 0$ gave an $R_g = 64$ nm for a MC sample with $M_w = 3.8 \times 10^5$ g mol^{-1}. Extrapolation to $q = 0$ gives a positive magnitude for A_2, indicating that water is a good solvent for MC at 20 °C. SLS is convenient

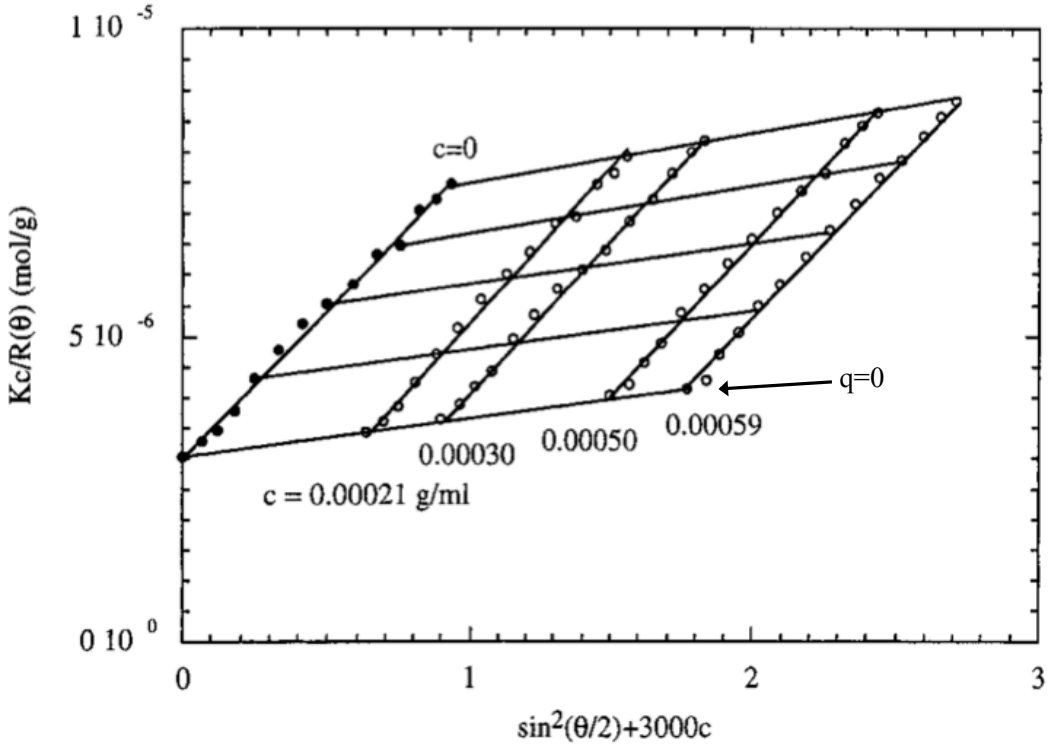

Figure 1.7: Zimm plot for a MC solution at 20 °C reported by Kobayashi et al. in 1999.[20] Reproduced with permission from the American Chemical Society.

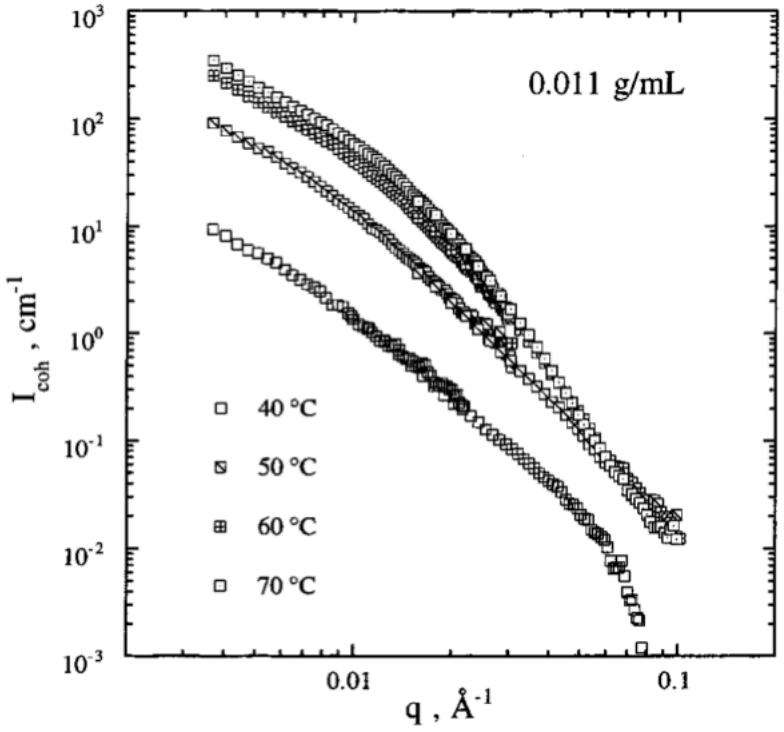

Figure 1.8: Small-angle neutron scattering curves for a 1.1 mg mL^{-1} solution (ca. 1 wt%) of MC in D_2O reported by Kobayashi in 1999.[20] Reproduced with permission from the American Chemical Society.

for measuring the size of individual molecules in solution, but is not appropriate for determining the morphology of chains after the gel has formed. Furthermore, because MC gels are often turbid, visible light scattering techniques are only appropriate for the pre-gel state at low temperatures. SANS and SAXS are a better choice to detect microstructure in MC gels, and have been also utilized by Kobayashi as well as Guillot et al.,[29] Takahashi et al.,[30] Bodvik et al.,[31] and Chatterjee et al.[32] As MC gels develop, scattered intensity monotonically increases for the longest lengthscales (lowest q), with no characteristic peaks or plateaus associated with a characteristic lengthscale, as illustrated in the SANS curves from Kobayashi et al.[20] in Figure 1.8. This suggests a heterogeneity of the gel network with no prominent features of a distinct size. There have been attempts to use phenomenological models to extract structural feature sizes from MC hydrogels,[20,30,32] though each of these utilized models which

assume form factors similar to spherical blob-like phase separated elements, for lack of morphological information for a more appropriate choice.

1.3.3 Enthalpies of Gelation for MC Solutions

There have been a number of experiments utilizing differential scanning calorimetry (DSC) to probe the sol-gel transition of MC solutions.[33–36] The transition from solution to gel (T_{gel}), is associated with an endothermic minimum between 60 and 70 °C, while the transition from a gel to solution on cooling (T_{sol}) gives an exothermic peak between 30 and 35 °C, as noted in Figure 1.9 by Hirrien et al.[33] Thus, T_{gel} and T_{sol} can be interpreted as reflecting hysteresis in a first-order phase transition. In this regard, gelation of MC is analogous to crystallization upon heating, and gel dissolution is analogous to "melting" of the gel back to semiflexible coils.

MC samples often display one peak on heating and two peaks on cooling in Figure

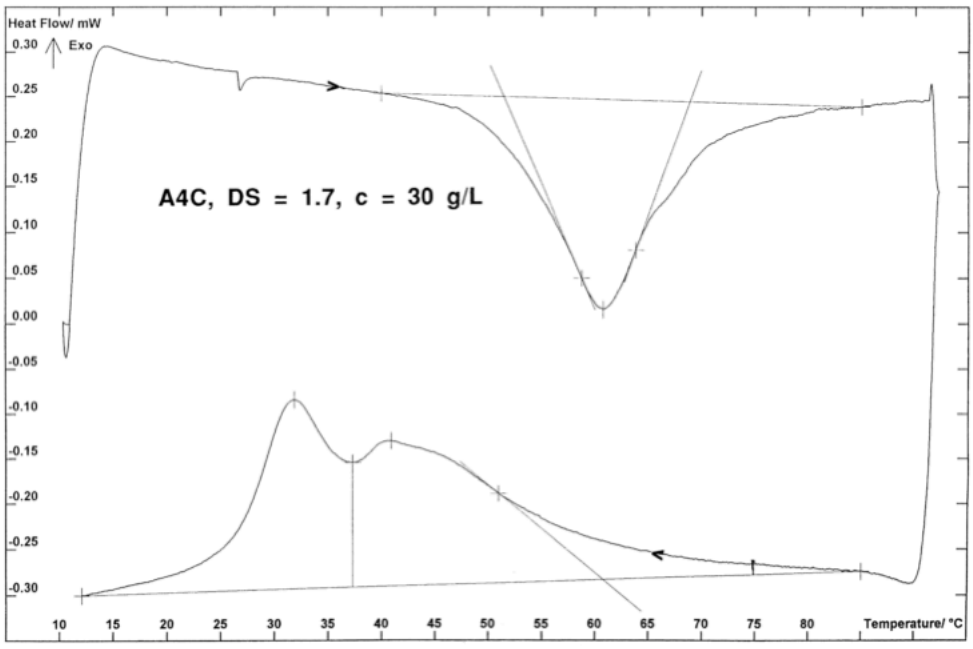

Figure 1.9: DSC curves on heating and cooling of an $M \approx 1.5 \times 10^5$ g mol^{-1} MC solution of 3.0 wt% reported by Hirrien et al.[33] Reproduced with permission from Elsevier publishing copyright 1998.

1.9, which naively could be attributed to two thermal events and the two-stage heating noted in rheological experiments.[18] DSC measurements of numerous molecular weights of MC all tend to have double peaks on cooling, while some report one or two peaks on heating at different c or M. Multiple peaks could also be attributed to the dispersity of MC samples, and since it is very difficult to produce MC of uniform M, the nature of the two peaks in the DSC curves remain unclear.

1.3.4 Effects of Salts on MC Gelation

As noted in Figure 1.4, the sol-gel transition of MC solutions changes with salts in solution, which has been reported by Heymann,[37] Neely,[38] and others.[39,40] The ability of salts to change the sol-gel transition temperature of MC solutions mirrors the lyotropic series for protein solubility.[41] As with the solubility of proteins, anions have a larger impact on the MC gelation than cations. In increasing order of anion affinity for MC solutions,

$$\mathrm{SCN^-} < \mathrm{I^-} < \mathrm{Br^-} < \mathrm{NO_3{}^-} < \mathrm{Cl^-} < \text{acetate} < \text{tartrate} < \mathrm{SO_4{}^{2-}}.$$

The first two anions above, $\mathrm{SCN^-}$ and $\mathrm{I^-}$ raise the gelation temperature of MC solutions, while $\mathrm{Br^-}$, $\mathrm{NO_3{}^-}$, $\mathrm{Cl^-}$, acetate, tartrate, and $\mathrm{SO_4{}^{2-}}$ lower the gelation temperature to an increasing degree. The hysteresis of MC gels on cooling persists and the gel-sol transition is also shifted to approximately the same hysteresis gap, so MC gelation remains thermoreversible in salt solutions. While the effect that anions play on protein solubility is not fully understood,[42] the dependence of salt concentration on MC gelation is attributed simply to competitive affinity of water between ions and hydroxyl moieties on MC molecules. Unlike proteins, pH has little effect on the gelation of MC with no change to sol-gel transition temperature or gel modulus for pH values between 2 and 12, as reported by Yu,[40] due to the nonionic character of MC. There are a number of antiquated terms associated with the lyotropic series, and are often used to describe salt in MC solutions as well. Ions which have a lower

affinity for water than the macromolecule, like SCN^- and I^-, are termed chaotropes and the effect they have on the solubility is called "salting in." Kosmotropes refer to ions on the other side of the series like Cl^- and ${SO_4}^{2-}$ have a higher affinity to water than the macromolecule, and the effect they have on the solubility is called "salting out."

Changes to the sol-gel transition using salts is an important property, since MC is often added to complex food or pharmaceutical mixtures which will have a host of other components, many of which are buffer salts or counter ions. Changes in the gelation temperature of MC solutions correlate to charge density of anions in-depth study of aqueous MC-salt solutions, with no appreciable change to low-temperature solution viscosity or high-temperature modulus. Additions of ions to MC solutions will not be considered further in this dissertation, and are not required for fundamental understandings of gel structure.

1.3.5 Proposed Structures of MC Hydrogels

There have been many hypotheses on the structure and gelation mechanism of MC hydrogels, and all agree that changes in hydrogen bonding between water and MC chains play a very important role. Some of the earliest suggested gel structures consist of a network of physically crosslinked MC chains. Sequences of MC chains which consist of fully methylated anhydroglucose units were thought to form fewer hydrogen bonds with water with increasing temperature, and act as hydrophobic "crosslinking loci," illustrated in Figure 1.10. This was first proposed by Kato et al.,[24] and was adopted and refined by numerous others.[18,21–23,30,33,43] However, water-swollen crosslinked networks of polymer chains cannot describe the turbidity of a MC gel, which will occur at characteristic lengthscales on the order of wavelengths of visible light, about 1 μm. A variation of the structure in Figure 1.10 is that the network nodes are microphase separated “blobs,” in which part of the MC molecule phase separates, and the network structure is a result of the hydrophilic sections of the

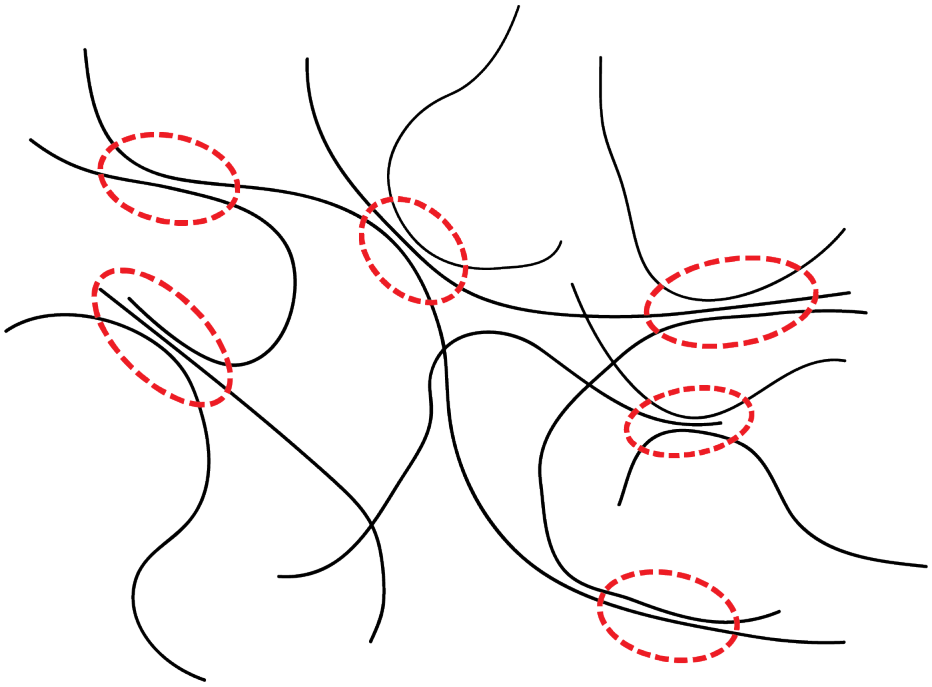

Figure 1.10: Schematic of a MC hydrogel network of crosslinking loci proposed by Kato,[24] Haque and Morris,[18] and Li[22]. The red ellipses indicate sequences of hydrophobic junctions which create the physical network.

gel spanning the space between blobs, akin to triblock polymer hydrogels.[44–46] This type of structure for MC hydrogels has been proposed more recently by Kobayashi et al,[20] and Chatterjee et al.[32]

Another hypothesis proposed for the mechanism for gelation MC solutions is viscoelastic phase separation (VPS).[19,26,32,47–51] As MC solutions are heated, hydrogen bonding between polymer and water becomes less favorable than hydrogen bonding between individual water molecules, which would cause the solution to phase separate into a polymer-rich and polymer-lean domains. The polymer-rich phase is assumed to be glassy or semicrystalline and complete phase separation is assumed be hindered by molecular mobility of the polymer-rich phase. The polymer-rich phase would be cocontinuous and span the sample, creating a microphase separated network of two domains. Presumably, the turbidity of MC gels is a consequence of the micron-sized lengthscales associated with each phase (see Figure 1.11) VPS requires

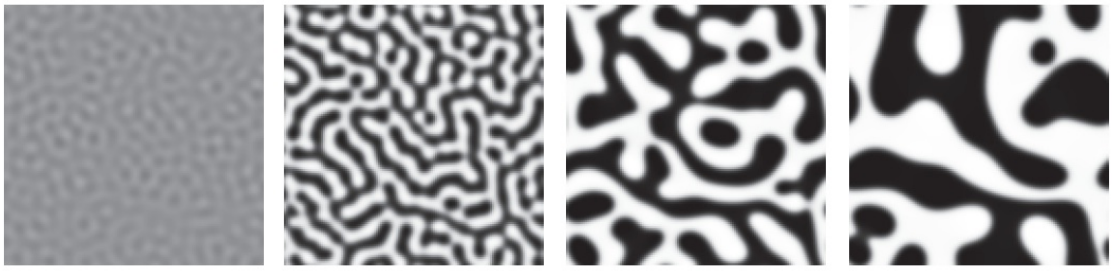

Figure 1.11: Schematic of a MC hydrogel network formed by viscoelastic phase separation, as first proposed by F. Tanaka.[48] As the two phases develop (moving from left to right), molecular mobility in the polymer-rich black region kinetically traps the gel structure in place. Figure adapted from H. Tanaka,[53] with permission from the Institute of Physics Publishing.

the polymer-rich and polymer-lean phases to develop spontaneously (called spinodal decomposition), yet the gelation of MC gels has been show to be heating rate dependent.[18,52]

1.3.6 Attempts at MC Phase Diagrams

Previous reports have correlated the onset of optical turbidity, the sol-gel transition of MC solutions, and peaks in DSC thermograms to create a phase diagrams for MC solutions. Many researchers have indicated that the sol-gel transition occurs at a lower temperature than the cloud point occurs for some or all concentrations,[21,30,43,50,54] while others have argued that cloud point occurs below the gel point for all evaluated concentration.[55] Most recently, Fairclough et al.[26] reported that the cloud point and gel point at approximately the same temperature for a single evaluated concentration. Likewise, the endothermic minimum on heating has reported to occur at a the same temperature[55] and at a higher temperature[30] as the sol-gel transition. These conflicting reports arise due to different definitions of the sol-gel transition and the cloud point, and also different heating rates between the measurements.

Takahashi et al.[30] reported a phase diagram for MC solutions, using small-angle x-ray scattering (SAXS) and DSC measurements. SAXS was fitted to a two-part

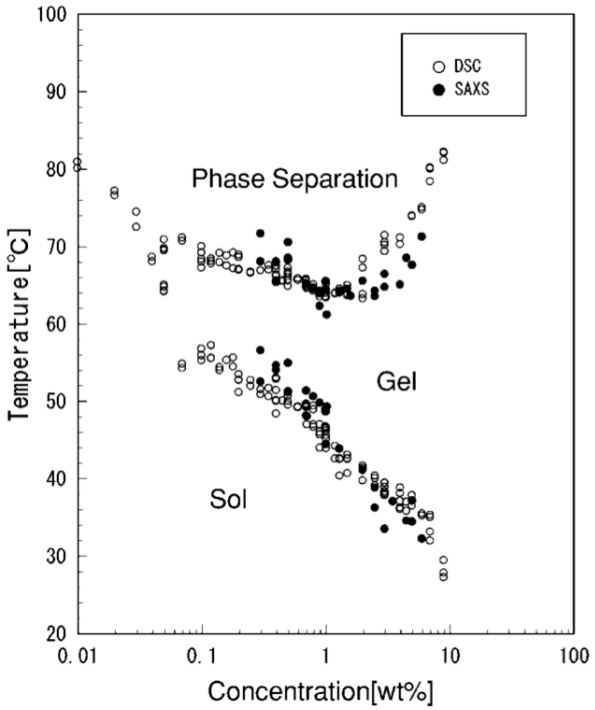

Figure 1.12: Temperatures of similar features in SAXS modeling and DSC thermograms, reported by Takahashi et al.[30] for a MC sample with $M_w = 9.36 \times 10^5$ g mol^{-1} and $DS = 1.8$, called a phase diagram by the authors. DSC and SAXS were measured on heating, at 1 °min^{-1}. Figure reproduced with permission, John Wiley and Sons copyright 2001.

model consisting of a Guinier term (for scattering by individual polymer chains) and a Lorentzian term for larger-sized structures as the gel develops. They noted that changes in the size of the Lorentzian correlation length occurred at similar temperatures to slope changes in the DSC thermogram (cooler than the endothermic minimum) on heating, and defined this as the sol-gel transition temperature. Using the same rationale, a second temperature was also noted at higher temperatures, warmer than the endothermic minimum, and this temperature was defined as the phase separation temperature. The results of the correlation between SAXS and DSC reported by Takahashi et al. can be seen in Figure 1.12. Takahashi et al. also noted that molecular weights of 1.24, 3.57, and 7.83×10^5 g mol^{-1} result in a shift of their sol-gel and phase separation boundaries to higher temperature and concentration with decreasing M. It should be noted that these definitions for sol-gel transition and phase

separation have not been used to describe the phase behavior of any other polymer solutions, and rely on assumptions that the chosen SAXS model accurately describes MC hydrogel morphology.

Chevillard et al.[43] also reported a phase diagram, shown in Figure 1.13, for MC with $M_w \approx 1.4 \times 10^5$ g mol^{-1} and $DS = 1.8$. The transition from clear to turbid was determined visually, while the solâĹŠgel transition was determined using the rheological $G''(\omega) - G'(\omega)$ crossover temperature. The "clear gel" phase in the low concentration region was not obtained using using conventional DMS approaches, where it was not evident; rather, the authors assumed that the sol-gel transition could be given by the onset of non-Newtonian flow behavior (the low-ω plateau seen in Figure 1.6). The clouding data points, at $c \approx 110$ and 140 g L^{-1} are difficult concentrations to prepare, and above the practical solubility limit of MC using the

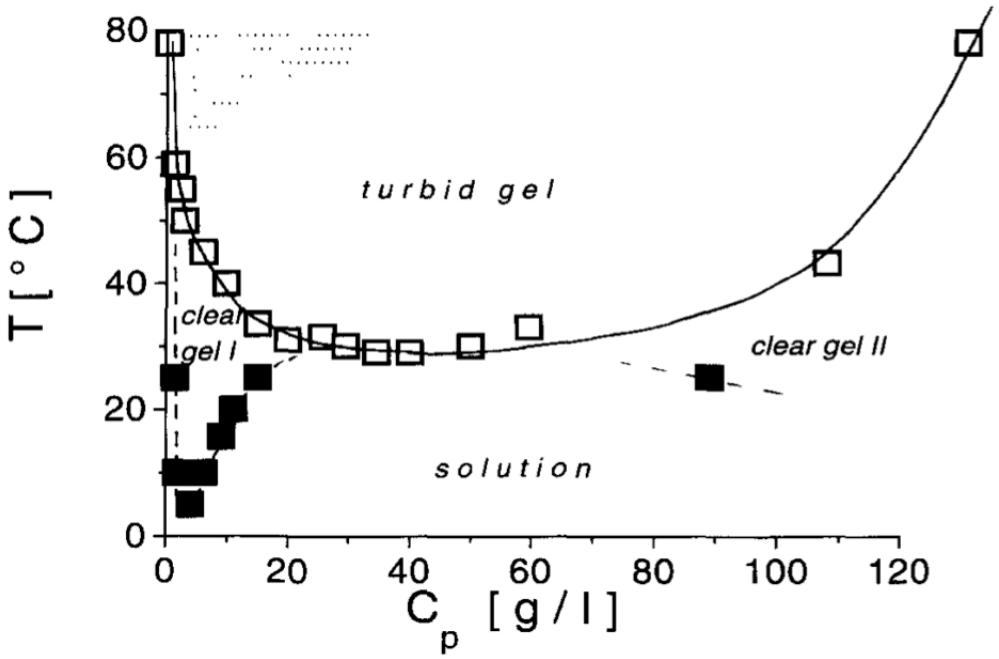

Figure 1.13: The onset of optical turbidity determined visually (open squares) and DMS measurements (closed squares) for a MC sample with $M_w \approx 1.4 \times 10^5$ g mol^{-1} from Chevillard et al.[43] Reproduced with permission from Springer-Verlag, copyright 1997.

standard preparation procedures. The heating rates between cloud points and rheological transitions in Figure 1.13 are not the same, and actual heating rate for either experiment is unclear.

The notation "phase diagram" describes thermodynamic equilibrium and/or stability of a system. Neither of the plots in Figures 1.12 nor 1.13 specify whether the phase separation boundary is a equilibrium phase boundary (binodal) or stability limit (spinodal). While these Figures can truly be called "phase diagrams" is unclear from the data presented in this section, but the plots in Figure 1.12 and 1.13 are useful nonetheless. Despite seemingly large differences in these phase diagrams, there is an overarching similarity in the sol-gel transition for an equivalent range of concentration.

1.4 Dissertation Overview

Methylcellulose has a long history, with little consensus regarding the sol-gel transition or the gel structure of the material. Figures 1.12 and 1.13 illustrate the conflicting and confusing reports of the MC literature. Often, authors' opinions and assumptions work their way into the results, which make the distinction between data and authors' conclusions. One of the objectives of the work presented in this dissertation is to characterize the MC solutions and gels and present the data separately from discussion, so that future researchers can easily distinguish the two and draw new conclusions if needed.

This dissertation will provide evidence that the properties of MC hydrogels cannot be fully described as a network of physically crosslinked chains or by VPS, contrary to many previous reports on the nature of MC hydrogels. Instead, the structure of MC hydrogels is shown to be a network of nanostructured fibrils. and proposes a mechanism for their formation. Insight into the nature of MC hydrogels has the potential to lead to a host of new materials,[56–60] and this work presents a series of

characterization techniques to probe nanoscale fibrils. The subject of this work is to characterize methylcellulose solutions, gels, and the transition between the two. A second objective proposes a mechanism for the gel formation, which is a kinetically-trapped microphase separation. The background concerning the experimental techniques used will be discussed in the introduction of each chapter, for easy reference to future readers interested in a single type of experiment.

- Chapter 1 overviews previous research efforts of aqueous methylcellulose solutions, and the understanding of methylcellulose gel structure prior to this dissertation.
- Chapter 2 describes the experimental techniques used throughout the dissertation, including dynamic mechanical spectroscopy (DMS), turbidity measurements, static light scattering (SLS), small-angle neutron scattering (SANS), and cryogenic transmission electron microscopy (cryo-TEM).
- Chapter 3 defines and describes the sol-gel transition in aqueous methylcellulose solutions, by DMS and optical turbidity.
- Chapter 4 shows a fibrillar structure of aqueous methylcellulose hydrogels using cryo-TEM, and the subsequent fibril characterization by SANS.
- Chapter 5 describes the linear and non-linear mechanical responses of MC hydrogels using DMS and steady shear rheology.
- Chapter 6 characterizes the dilute solution thermodynamics of aqueous methylcellulose solutions. This is accomplished using static light scattering (SLS). Additionally, a predictive phase diagram for aqueous methylcellulose based upon isotropic-nematic phase separation of semiflexible coils in solution is proposed.
- Chapter 7 presents a final discussion of the analyses presented in the thesis.

- The appendix includes experimental results not included in the other chapters and a description of the SANS model used to characterize MC gels.

Chapter 2

Materials and Methods

2.1 Introduction

This chapter describes the methylcellulose samples studied in this dissertation, and the experimental methods used to characterize MC solutions and hydrogels. All MC samples presented are commercially available, and the preliminary characterization provided by The Dow Chemical Company consisted of weight-average molecular weight (M_w), dispersity ($Đ$), intrinsic viscosity ($[\eta]$), and solution viscosity of 2 wt% solutions at 20 °C. Experimental methods described in this chapter include: dynamic mechanical spectroscopy (DMS), turbidity measurements, static light scattering (SLS), small-angle neutron scattering (SANS), ultrasmall-angle neutron scattering (USANS), and cyrogenic transmission electron microscopy (cryo-TEM).

2.2 Synthesis of Methylcellulose

The first reported synthesis of methylcellulose (MC) was in 1913 by Denham and Woodhouse.[15] Interestingly, this predates the work of Staudinger[61] that established the chain-like structure of polymer molecules. MC and other cellulose ethers are prepared on industrial scales by a heterogeneous-phase substitution reaction, by treating

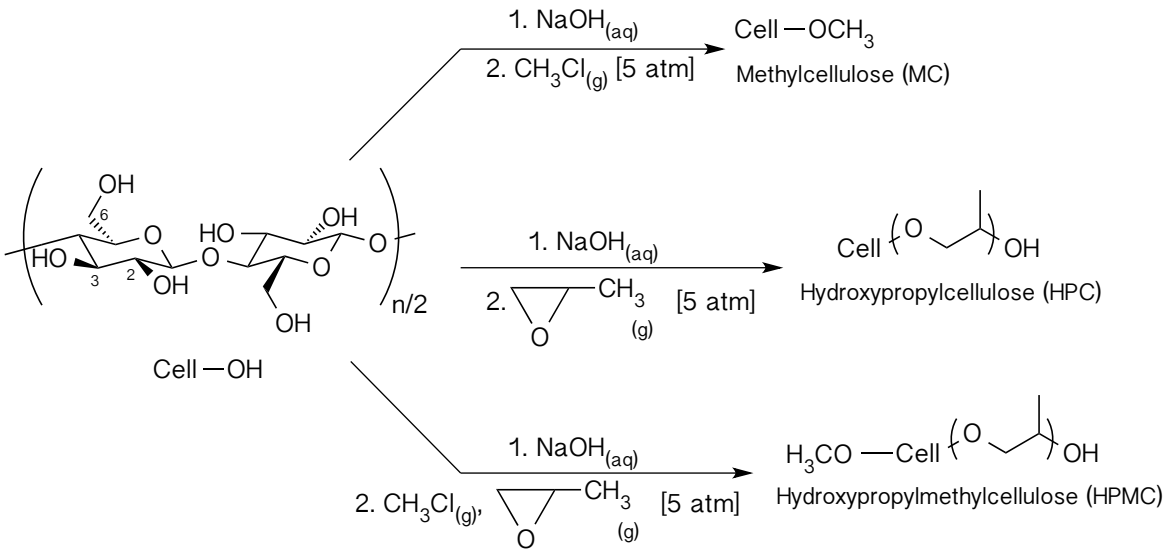

Figure 2.1: Industrial synthesis scheme for cellulose ether materials. For simplicity the cellulose backbone is abbreviated "Cell-" followed by the substituent. Cellulose ethers are water soluble for partially substituted materials.

solid cellulose with sodium hydroxide solution, followed by addition of gaseous reagent at elevated pressure (Figure 2.1).[1] After the reaction, the basic component is neutralized with hot dilute acid followed by rinsing with hot water. The resultant cellulose ether is dried and milled.

2.2.1 Composition of Commercial Methylcellulose

An important parameter for all cellulose derivatives is the degree of substitution (DS). It is a number between 0 and 3 and describes the average substitution per anhydroglucose repeat unit onto the C2, C3, and C6 hydroxyl groups. $DS = 0$ refers to unmodified cellulose, and $DS = 3$ refers to a fully substituted material. For water-soluble cellulose ethers, the substitution is intermediate, e.g. $1.1 < DS < 2.2$.[17,24] The substituted groups disrupt intra- and interchain hydrogen bonding enough so that the remaining hydroxyl groups on the cellulose backbone can form hydrogen bonds with the aqueous solvent. More highly substituted cellulosic materials ($DS > 2.5$) can be prepared that are soluble in many organic solvents.

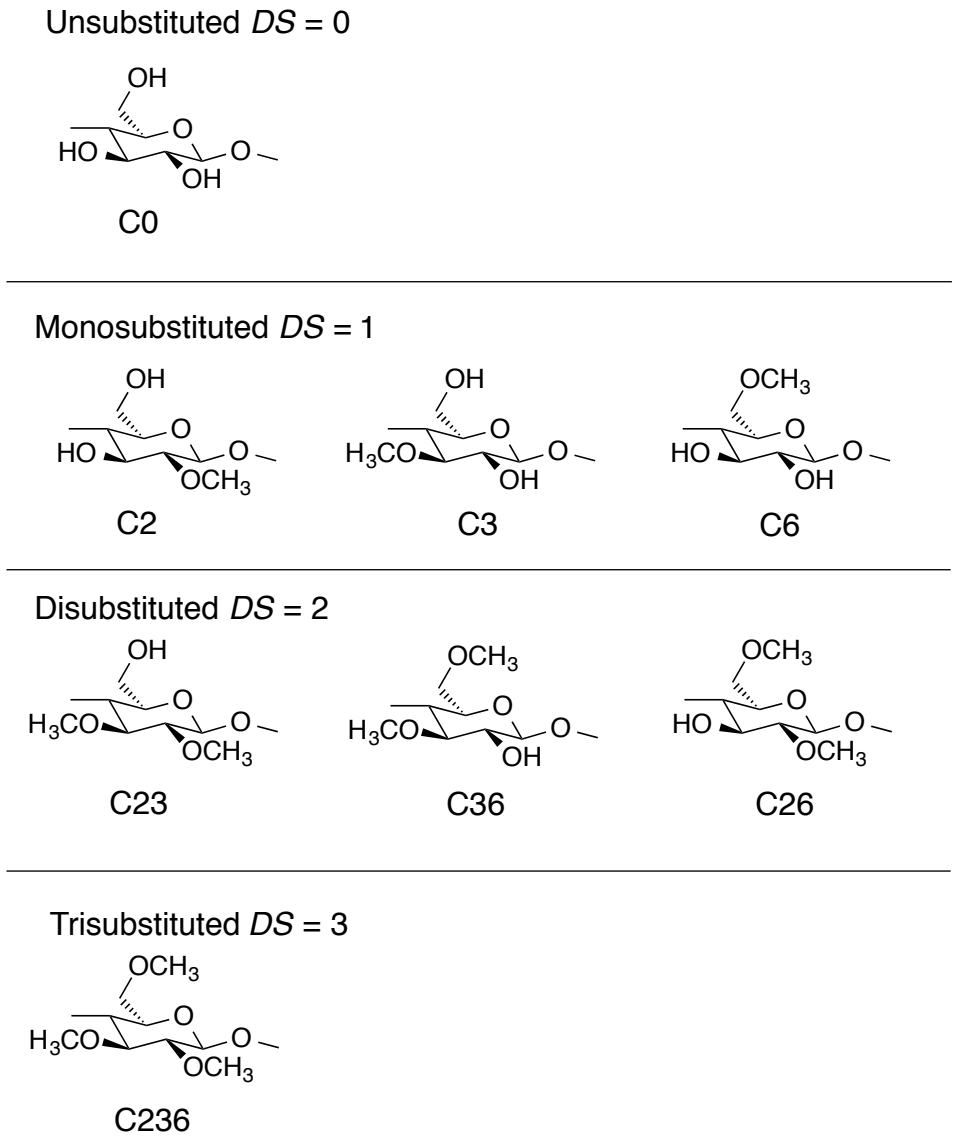

Figure 2.2: All possible substitution patterns of an anhydroglucose monad. Commercially available MC is prepared via heterogeneous substitution, and a material with a $DS = 1.8$ will likely contain all possible monads.

In the treatment of semicrystalline cellulose with base, amorphous chain domains are more susceptible to alkylation than crystalline chain domains, which results in heterogeneity in the substitution of MC. Figure 2.2 displays eight possible methoxyl substitution patterns of a single anhydroglucose unit, and commercially prepared MC can be thought of as a statistical polymer of eight repeat units. There may be some

ordering of substitution of chain segments, and heterogeneous substitution can lead to sections of higher and lower DS than the polymer as a whole, resulting in an almost block polymer-like structure. The overall DS can be determined by a number of methods, the most common of which is the Zeisel procedure,[62] which is a historical chemical test for ethers.[63] Other methods for determining the DS of MC include carbon-13 nuclear magnetic resonance spectroscopy (NMR), and mass spectroscopy (MS).[25,64] Spurlin has shown that the substitution onto the C2, C3, and C6 hydroxyl groups are of similar frequencies for commercial preparations of MC.[65] Later analyses have further quantified the reactivity ratios between substitution reactions onto C2, C3 and C6 hydroxyl groups, and have shown that substitutions onto the C3 hydroxyl are more likely to occur after the C2 hydroxyl has already been substituted. While this is an important consideration when preparing regioselectively substituted cellulose derivatives, for the commercial materials studied in this work it is less of a concern. Changes to the overall or local DS of a cellulose derivative will likely have an effect on the water solubility and thermogelation properties of MC, and should be noted when preparing new materials based upon a substituted cellulose precursor. Given the complexities of MC, this dissertation simplifies the parameter space by focusing only on MC materials with $DS = 1.8$.

2.2.2 Physical Properties of Methylcellulose

This dissertation focuses on MC provided by The Dow Chemical Company with the trade name METHOCEL $^{\text{TM}}$. MC is a white powder, with a powder density of 0.28 $\mathrm{g\,cm^{-1}}$ and a material density of 1.341 $\mathrm{g\,cm^{-1}}$.[66] The repeat unit molecular weight (M_0) depends on DS, and for materials presented in this work with $DS = 1.8$, $M_0 = 187.4\ \mathrm{g\,mol^{-1}}$. Molecular weights of MCs are based upon the cellulose feedstock, with weight-average molecular weights (M_w) usually between $1 - 5 \times 10^5\ \mathrm{g\,mol^{-1}}$. The dispersities of molecular weights ($Đ$) for MC materials are high, usually between

Table 2.1: MC Sample Characteristics

Sample	$\eta_{20\,^\circ\mathrm{C}}$ [Pa s]	$[\eta]$ (ml g^{-1})	N_w	M_w [kg mol^{-1}]	$Đ$
MC150	0.4	473 ± 3	800	150	4.1
MC300	4	736 ± 36	1600	300	5.4
MC530	40	1093 ± 18	2800	530	3.6
MC49	0.015	167 ± 2	250	46	2.5
MC160S	0.16	341 ± 4	830	156	12.4
MC400S	16	830 ± 22	2100	402	5.1

2 and 5 (with one sample as high as 12). $Đ$ of MC is mostly a consequence of the natural dispersity of cellulose, which is dependent on plant species, age, and extraction process.[67–69] Different molecular weights of MC are sold commercially by the *viscosity grade*, which is based on the viscosity of a 2 wt% solution at 20 °C. A summary of the MC materials is found in Table 2.1, reported by Yongfu Li of The Dow Chemical Company using multi-angle light scattering detection of size exclusion chromatography separations.[52] This dissertation primarily focuses on the first three polymers on Table 2.1: MC150, MC300, and MC530.

The MC sample lowest M_w in Table 2.1, MC49 is different from the other MC samples by its synthesis method. Wood pulps are not available for lower M cellulose, so the material is prepared by subjecting longer-chain MC materials to acid hydrolysis to cleave $\beta(1 \rightarrow 4)$ glucose linkages and reduce the molecular weight. The greater extent of chain degradation by acid hydrolysis, MC will turn incrementally yellow and brown in color. As a solid material MC49 is white, but aqueous solutions of MC49 with concentrations of about 1 wt% and greater have a yellow color. Colors of degraded MC indicate an unintended side reactions during acid hydrolysis. MC49 solutions still form a turbid hydrogels, but due to its coloration, this material was investigated less thoroughly than the others. The Appendix contains DMS and SANS data for MC49.

The samples designated MC160S and MC400S are prepared by a slightly altered chemical process (denoted S-type MC) from the scheme in Figure 2.1.[70] The practical difference between the samples is that S-type MC materials will undergo the transition to a turbid hydrogel at lower temperatures, with the hysteresis between heating and cooling also shifting. The degree of substitution (DS) of these altered S-type MC materials is the same as regular MC. Since the DS of these materials is unchanged, the only difference in these materials is the distribution of methoxyl groups along the polymer backbone. Numerous reports have investigated methoxyl distribution of MC by employing homogeneous reaction conditions in the solution state,[33,71–73] or the position of methoxyl groups on the individual anhydroglucose rings using regiospecific synthetic techniques.[64,74–76] These factors may influence many aspects of MC behavior including gelation and solubility.[33,64,71–76] The nature of the difference between the S-type MC and regular MC will not be discussed in this dissertation. More information regarding S-type MC materials can be found in the relevant patent by Reibert et al.[70] DMS and SANS data for these materials is also included in the Appendix.

2.2.3 Preparation of Aqueous Cellulose Ether Solutions

Thermogelation of MC solutions is one of its notable properties, and thus requires special procedures when preparing aqueous solutions.[77] Solid MC is dried in a vacuum oven (*ca.* 100 mTorr) for 12 h at 60 °C. Half the required amount of ultra pure water (less than 10 ppb organic and ion content and at least 18 MΩ cm resistivity) is heated to 70 °C, then the required amount of solid MC added. The mixture is stirred for 10 min followed by addition of the remaining ultra pure water at 25 °C and stirring in an ice bath for an additional 10 min; then it is allowed to fully hydrate at 5 °C for at least 12 h and degassed prior to use. This is the procedure used to prepare all aqueous MC solutions in this dissertation. For light, x-ray, and neutron scattering measurements the samples are filtered with a 0.45 μm syringe filter.

2.3 Rheological Measurements

Gels are materials which are mostly liquid, and have polymeric or colloidal component which provide solid-like elasticity or rigidity. Characterization of of the sol-gel transition of MC must include its viscoelastic properties, which includes the viscous liquid-like properties and the elastic solid-like properties using rheometric measurements. This section describes small-amplitude oscillatory shear (SAOS) measurements which probe the linear viscoelastic (LVE) regime, and large-amplitude oscillatory shear (LAOS) measurements which probe the nonlinear viscoelastic regime (NVLE).

2.3.1 Linear Viscoelastic Experiments

Many materials display *viscoelastisity*, which is a combination of solid-like elasticity and liquid-like viscosity. A convenient method for measuring viscoelasticity is dynamic mechanical spectroscopy (DMS), in which a SAOS strain is applied with amplitude γ_0 and frequency ω given by,

$$\gamma(t) = \gamma_0 \sin(\omega t). \tag{2.1}$$

When γ_0 is small, the oscillatory stress response of a viscoelastic material will be a sinusoidal function offset by a phase angle δ,

$$\sigma(t) = \sigma_0 \sin(\omega t + \delta). \tag{2.2}$$

If a material displays a purely elastic response, then the shear stress, $\sigma(t)$, will oscillate in phase with $\gamma(t)$ (with a phase angle $\delta = 0$), because stress is proportional to strain. Alternatively, if a material displays a liquid-like viscous response, $\sigma(t)$ will oscillate proportional to the strain rate, $\frac{d\gamma}{dt}$. Because $d(\sin(t)) = \cos(t)dt$, the oscillation of the viscous response lags out of phase with a phase angle $\delta = \pi/2$ rad. The oscillatory

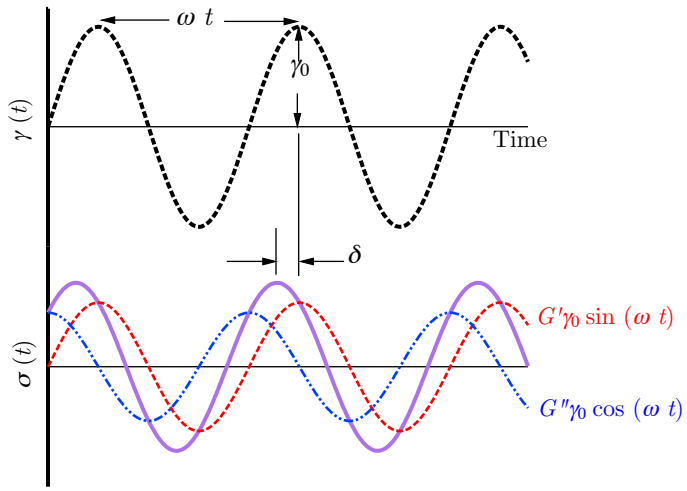

Figure 2.3: Representation of the definition of G' and G'' (red and blue, respectively), derived from the linear combination of two components of the measured shear stress (purple). The elastic component (red) is in phase with the applied shear strain (black), while the viscous component lags behind by $\pi/2$ rad. G' and G'' are determined from the amplitudes of each component.

stress response $\sigma(t)$ is defined as a linear combination of the in- and out-of-phase oscillations, given by,

$$\sigma(t) = G'\gamma_0 \sin(\omega t) + G''\gamma_0 \cos(\omega t) \tag{2.3}$$

where G' is the storage modulus and describes the elastic responses of a material, while G'' is the loss modulus and describes the viscous responses of a material (see Figure 2.3). Another useful parameter is the dynamic loss tangent,

$$\tan(\delta) = \frac{G''}{G'}. \tag{2.4}$$

Measurements of G' and G'' assume the stress response can be defined as linear combination of in- and out-of-phase components, which is called the linear viscoelastic (LVE) regime. When γ_0 is large, the strain response is more complex than a simple sinusoidal oscillation, and G' and G'' cannot be used to fully describe the oscillatory

stress response. This region is called the nonlinear viscoelastic (NVLE) regime, and will be discussed in the next subsection.

In practice, there are two types of rheometers that can collect DMS data: strain- and stess-controlled instruments. A strain-controlled rheometer applies a known displacement on the sample, and a transducer measures the stress response, as per Equations 2.1 through 2.3. The other type of rheometer is stress-controlled, which applies a sinusoidal $\sigma(t)$ and the resultant $\gamma(t)$ is determined using a displacement transducer. The equivalent equations that define the applied stress and measured strain for stress-controlled rheometers are given by,

$$\sigma(t) = \sigma_0 \sin(\omega t) \tag{2.5}$$

and

$$\gamma(t) = \frac{\sigma_0}{G'} \sin(\omega t) + \frac{\sigma_0}{G''} \cos(\omega t). \tag{2.6}$$

The choice of stress- or strain-controlled rheometer is often based upon the nature of the sample: stress-controlled rheometers often have better signal-to-noise at low stresses and are suited for lower moduli materials, whereas strain-controlled rheometers are often suited to higher moduli materials, due to better detection at the upper limit of the force transducer.[78,79] Stress-controlled rheometers can also be use in strain-controlled mode, which utilizes a software-based feedback loop to incrementally apply larger stresses until the desired strain is achieved. Using this operation mode, a stress-controlled rheometer operates effectively like a strain-controlled rheometer. The materials presented in this dissertation use a stress-controlled rheometer exclusively.

Another concern for the use of stress-controlled rheometers is the instrument's moment of inertia. The sinusoidal displacement response by a stress-controlled rheometer includes the viscoelastic data of the sample, and also the momentum of the motor and rotating shaft. The latter is accounted for by measuring the rotational inertia of the

instrument with no sample loaded (called rotational mapping) prior to use. However, for low viscosity, high frequency measurements the inertia of the oscillating motor and geometry can dominate the signal. The moment of inertia (I_{m}) is proportional to the second derivative with respect to displacement,

$$\frac{d^2\gamma}{dt^2} \sim I_{\mathrm{m}} \tag{2.7}$$

and because $d^2(\sin(t)) = -(\sin(t))dt^2$, instrument inertia will have $\delta = \pi$ rad. Whenever the raw phase angle $\delta_{raw} > \pi/2$ rad (90°) inertia has a measurable contribution to the signal, and dominates when $\delta_{\mathrm{raw}} \approx \pi$ rad (180°). Additionally, if $G' = G'' \sim \omega^2$, then the sample is completely dominated by instrument inertia.[79] The approach taken in this dissertation was to exclude all data for $\delta_{\mathrm{raw}} > 5\pi/6$ rad or 150°.

SAOS measurements of aqueous MC solutions were carried out on a TA Instruments AR-G2 stress-controlled rheometer fitted with concentric cylinders (stator i.d. 15 mm, 1 mm gap, immersed height 42 mm) and a Peltier temperature control unit. To inhibit solvent evaporation, a thin layer of silicon oil (Aldrich, density 0.963 $\mathrm{g\,mL^{-1}}$, boiling point > 140 °C) was floated over the top of the solution. G' and G'', were measured as a function of stress-amplitude at a fixed oscillation frequency (usually 1 $\mathrm{rad\,s^{-1}}$ to start) to determine the LVE regime. So long as the apparent G' and G'' do not change as σ_0 increases, the sample can be considered to be in the linear regime. For stress-controlled rheometers, determination of the LVE regime should be determined with an applied stress (i.e. not in strain-controlled mode), since the feedback loop for strain-controlled works only in the LVE. Once the linear regime is determined, $G'(T)$ and $G''(T)$ are measured at constant-ω and defined heating or cooling rates. $G'(\omega)$ and $G''(\omega)$ are also measured at a defined temperature are measured from 0.05 to 50 $\mathrm{rad\,s^{-1}}$. Each frequency sweep takes about 15 minutes, and a very slow heating rate of about 2 $\mathrm{°C\,h^{-1}}$ (0.03 $\mathrm{°C\,min^{-1}}$) can be achieved by incremental heating of 1 °C and a thermal equilibration of 15 minutes between frequency sweeps.

2.3.2 Nonlinear Viscoelastic Experiments

When γ_0 (or σ_0 for stress-controlled instruments) increases above a critical value, it will appear as if G' or G'' increase or decrease. When G' or G'' is dependent on the applied γ_0 (or σ_0 for stress-controlled instruments), this is referred to as LAOS. In the nonlinear regime, the raw sinusoidal response is more complicated than a simple sinusoidal function. A illustration of a sinusoidal signal exhibiting a nonlinear response can be seen in Figure 2.4. DMS measurements in the NVLE regime require different treatment to interpret the data, and is a topic of active research.[80–86] Linear and nonlinear properties of MC hydrogels will be discussed in Chapter 5. While G' and G'' have no formal definition in the NVLE the onset of nonlinearity can be interpreted as a critical stress, σ_c, and structural information about the sample can be interpreted from its magnitude.

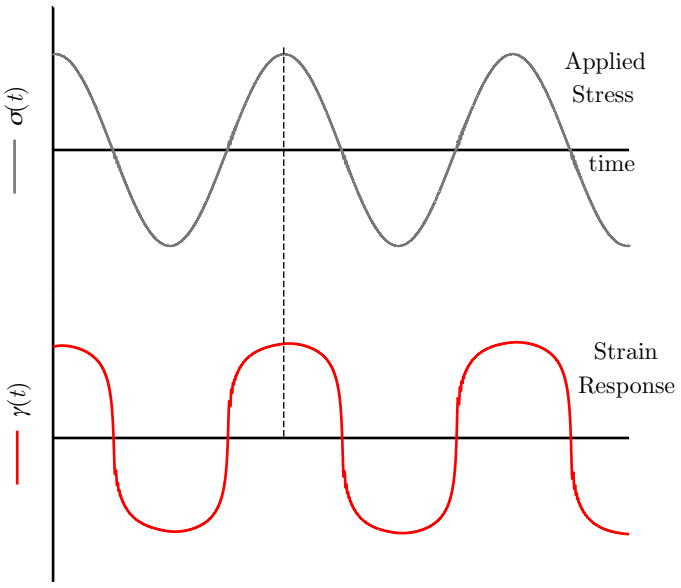

Figure 2.4: Illustration of a nonlinear DMS response from a stress-controlled rheometer. The output strain (in red) cannot be defined by the simple sinusoidal function of the applied stress (in gray). No linear combination of in-phase (G') and out-of-phase (G'') sinusoidal functions can accurately describe the strain response.

LAOS DMS measurements were performed on a stress-controlled TA Instruments AR-G2 rheometer and also a Discovery Hybrid Rheometer (DHR) using a parallel plate geometry (diameter = 40 mm, gap = $350 - 550$ μm) and also cone and plate geometry (diameter = 40 mm, cone angle 2.00°, specified gap = 50 μm) with a Peltier heating unit as the lower plate. Evaporation of the solvent was minimized by placing a low viscosity silicon oil around the sample perimeter. Stress amplitude sweeps were conducted at discrete temperatures, and stress ranges at each temperature captured the nonlinear response but were not high enough not fracture the gels. Samples were held at the desired test temperature for 15 min prior to measuring the strain response, and each isothermal stress amplitude sweep required about 10 min to complete.

2.4 Turbidity Measurements

The transition of MC solutions from clear to turbid gels on heating was quantified by measuring the of transmittance of a 30 mW 633 nm HeNe laser through the sample using a photometer (Spex Industries Laser Power Meter 1448, Metuchen, NJ). MC solutions were sealed in glass ampules with stir bars to minimize evaporation and ensure uniform heating. Samples were place in a bath of poly(dimethylsiloxane) (silicone oil for melting and boiling point apparatuses, Fisher Scientific), and heated slowly on a hot plate with slow stirring. After a period thermal equilibration, the transmittance of each solution was recorded at specific temperatures. Because the laser traveled through the silicone oil bath, it was important that the vat containing the oil bath is clean, and the silicone oil is new and of the same manufacturing lot. The transmittance of concentrated MC solutions is not 100% compared to water, so the transmittance of each sample was normalized to the transmittance for that concentration at 20 °C and is reported as relative transmittance (T_R). In the vicinity of the gel point the effective heating rate was approximately 2 °C h^{-1}. Cloud points were reported on heating of the sample.

2.5 Static Light Scattering

The first part of this experimental section outlines a method used for determining the differential refractive index increment ($\partial n/\partial c$) for dilute aqueous MC solutions using a pump and a differential refractometer, which can be applied to any polymer solution. The second part describes the SLS measurements for aqueous MC solutions. The same solutions were used for $\partial n/\partial c$ determination and SLS measurements.

Table 2.2: MC solutions for static light scattering

Sample	$[\eta]$ ($\mathrm{ml\,g^{-1}}$)	c^* ($\mathrm{mg\,mL^{-1}}$)	c range ($\mathrm{mg\,mL^{-1}}$)
MC150	473 ± 3	2.1	$0.3 - 0.9$
MC300	736 ± 36	1.4	$0.2 - 0.6$
MC530	1093 ± 18	0.93	$0.1 - 0.5$

Table 2.2 displays the MC samples and concentrations used in the SLS experiments and $\partial n/\partial c$ determination. The Zimm analysis (Equation 1.2) requires that the solutions are dilute, so all concentrations should be below the chain overlap concentration c^*. The intrinsic viscosities of MC samples, were measured by Yongfu Li of The Dow Chemical Company using size exclusion chromatography and differential solution viscometry, and reported in Arvidson et al.[52] Intrinsic viscosity ($[\eta]$) is the coefficient of which describes the change in viscosity as small amounts of polymer is added to a solvent,[87] and c^* can be estimated by $c^* \approx [\eta]^{-1}$.[88] In order to make the concentrations of solutions as accurate as possible, 500 mL of each solution were prepared using the method described in Section 2.2.3.

2.5.1 Determination of the differential refractive index

In order to determine M_w and A_2 for a dilute polymer solution, it is critical to accurately know the differential refractive index increment. $\partial n/\partial c$ for MC in water

was measured on a Wyatt OptiLab rEX differential refractometer (with an 660 nm LED light source) connected directly to a Rainin peristaltic pump for a stable flow rate of 1 mL min^{-1}. The differential refractometer was calibrated using dilute sodium chloride solutions which $\partial n/\partial c = 0.1708 \pm 0.0004$ mL g^{-1}.[89] Concentrations between 0.2 and 1.0 mg ml^{-1} were used to span the voltage output, with the results shown in Figure 2.5, which gives a calibration constant of $1.948 \pm 0.008 \times 10^{-5}$ V^{-1}.

Solutions of MC300 were prepared between 0.2 and 0.6 mg mL^{-1} which is well below the chain overlap concentration of about 1.4 mg mL^{-1}.[52] Refractometer voltage was measured at 25 and 50 °C, giving $\partial n/\partial c = 0.136 \pm 0.001$ and $\partial n/\partial c = 0.137 \pm 0.002$ mL g^{-1}, respectively (see Figure 2.6) in good agreement with previous measurements.[20] $\partial n/\partial c$ of MC in water has a negligible temperature dependence, and it is assumed that $\partial n/\partial c$ is relatively independent of molecular weight, and the same value is used in all SLS measurements.

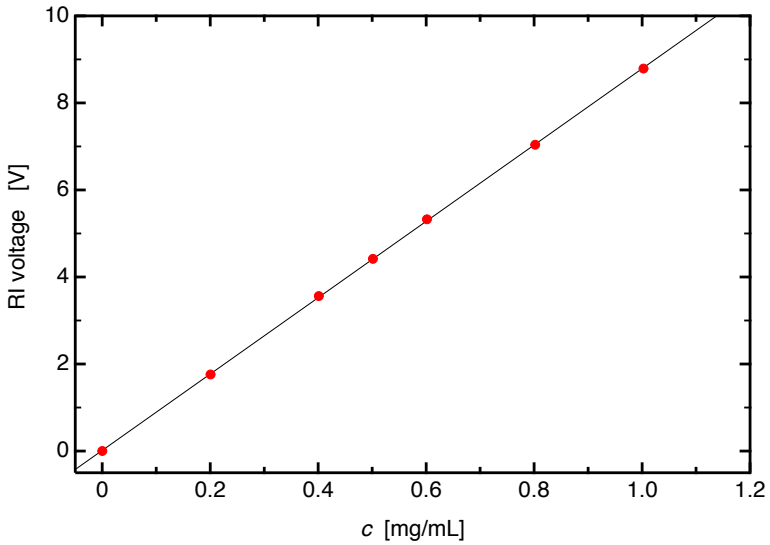

Figure 2.5: Differential refractometer voltage output for an aqueous NaCl solution at 25 °C. Given that the differential refractive index of aqueous NaCl is $\partial n/\partial c = 0.1708 \pm 0.0004$ mL g^{-1}.[89] This gives a refractometer calibration constant of $1.948 \pm 0.008 \times 10^{-5}$ V^{-1}.

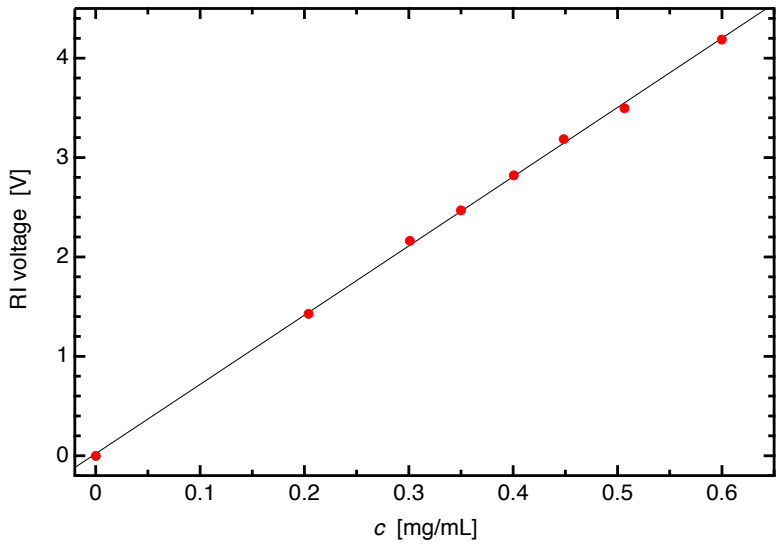

Figure 2.6: Differential refractometer voltage output for an aqueous MC solution at 25 °C, to give a differential refractive index for aqueous MC of $\partial n/\partial c = 0.136 \pm 0.001$ mL g^{-1}

2.5.2 Static light scattering measurements of aqueous MC

Dilute solutions of three molecular weights of MC were prepared with concentrations listed in Table 2.2. Light scattering measurements were performed using a Brookhaven BI-200SM light scattering instrument with a 637 nm laser operating at 10 mW and an avalanche photodiode detector with a 1 mm pinhole. It was assumed that $\partial n/\partial c$ of MC in water is the same at 637 nm (for SLS measurements) as at 660 nm (for $\partial n/\partial c$ determination). MC scattering intensity was monitored between angles of 15° and 150° corresponding to a q range of 3.5×10^{-4} to 2.5×10^{-3} Å^{-1}. The Raleigh ratio (R_θ) of the sample was calibrated using an ultra-pure ($\geq$ 99.9%) toluene standard, with $R_{(90\,^\circ)} = 8.50 \times 10^6$ cm^{-1} at 25 °C.[90] In order to maximize detector signal, MC solutions were measured in 20 mL scintillation vials (with a ID of about 25 mm. For each temperature, fresh aliquots of MC solutions were removed from the refrigerator at 5 °C and annealed at the desired test temperature for 1 hour prior to the measurement.

2.6 Neutron Scattering

Small-angle neutron scattering (SANS) experiments were utilized to probe lengthscales of MC solutions and gels from $6-600$ nm. Ultra small-angle neutron scattering (USANS) experiments were utilized to investigate lengthscales in MC hydrogels, from 300 nm to 20 μm.

2.6.1 SANS Instrumentation

SANS experiments were performed on two instruments: at the National Institute for Science and Technology (NIST) on the NG7 30 m SANS instrument[91] and also at Oak Ridge National Laboratories (ORNL) on the CG-2 SANS instrument. The sample stage consisted of demountable titanium (NIST) or copper (ORNL) cells with MC solutions between two quartz windows, heated by a circulating bath. The q range accessed in a particular experiment was a function of the neutron wavelength (4.75 Å, 12.4% $\Delta\lambda/\lambda$ and 8.08 Å, 11.5% $\Delta\lambda/\lambda$ for ORNL and NIST, respectively) in conjunction with three detector distances (1 m, 4 m, and 15 m) that allowed for data acquisition over a q range of $0.0009-0.3$ Å^{-1} on a 2D 640 mm $\times$ 640 mm ^{3}3He position-sensitive proportional counter. Data were acquired for $3-90$ min at each temperature and detector distance, depending on detector count rates.

2.6.2 USANS Instrumentation

In order to measure scattering from lengthscales longer than 600 nm in MC hydrogels, USANS measurements were carried out at NIST on the BT5 perfect double-crystal diffractometer.[92] The sample stage consisted of demountable titanium cells with MC solutions between two quartz windows, heated by a circulating bath. Using a neutron wavelength of 2.4 Å(6% $\Delta\lambda/\lambda$), a q-range of $0.00003-0.0026$ Å^{-1} was accessed using multiple reflections from perfect silicon (220) crystals before and after the sample stage. Scattering data were acquired for 7 h at each temperature.

2.6.3 Sample Preparation

MC solutions were prepared according to the method described in Section 2.2.3, except that D_2O (99.9%, Cambridge Isotope Laboratories) was used in place of water for the solvent to provide scattering contrast between polymer and solvent. The scattering length density (ρ) was calculated to be $\rho_{MC} = 1.293 \times 10^{-6}$ Å^{-2} for MC and $\rho_{D_2O} = 6.335 \times 10^{-6}$ Å^{-2} for D_2O.[93] Solutions were filtered through 0.45 μmm syringe filters into demountable sample cells with a path length of 4 and 5 mm for NIST and ORNL, respectively. The samples were kept at 5 °C overnight prior to SANS and USANS experiments and heated to each desired temperature, and allowed to thermally equilibrate for 5 minutes prior to the measurement.

2.6.4 Data Treatment and Reduction

2D SANS data were radially averaged using either NCNR or ORNL SANS reduction macros for WaveMetrics Igor Pro software to obtain $I(q)$ vs. q plots,[94] then the background D_2O scattering was subtracted. To correct for incoherent scattering in SANS, for each scattering curve the high q data ($0.15 - 0.30$ Å^{-1}) were plotted as q^4I vs. q^4, and the slopes of the resulting straight lines were subtracted from each point in the original $I(q)$ vs. q data set.[95,96] For the most part, the data above $q = 0.1$ Å^{-1} were ignored as it was outside the size range of interest, and the low intensities are prone to significant alteration during incoherent background correction. USANS data are one-dimensional in the horizontal plane, collected point-by point. Scattering from each q value were combined using the NCNR USANS reduction macro for Wavemetrics Igor Pro software,[94] and the background D_2O scattering was subtracted. So that USANS data can be easily compared to SANS data, it was desmeared. Smearing of USANS data occurs when the collimated circular neutron beam is averaged over a rectangular slit.[97]

2.7 Cryogenic Transmission Electron Microscopy

Cryogenic transmission electron microscopy (cryo-TEM) is technique that I had only cursory exposure to during my time at the University of Minnesota. As this research project was a collaboration, Prof. Joseph Lott and Peter Schmidt utilized cryo-TEM extensively. Nonetheless, the cryo-TEM images of MC hydrogels are significant enough for a brief discussion of them to be included, as well as the method of sample preparation. Real-space imaging using cryo-TEM provides a picture of the morphology of MC hydrogels, so that suitable scattering models can be applied to SANS data.

2.7.1 Sample Preparation

MC solutions with a concentration range of $0.2 - 0.4$ wt% were filtered through a 0.45 μmm syringe filter and annealed for the designated time. Small droplets (ca. $5 - 20$ μmL) of the solution were deposited onto 200 mesh carbon coated lacey Formvar TEM grids (NetMesh^{TM}, Ted Pella) inside an FEI Vitrobot device with the blotting environment set to the desired temperature and 100% relative humidity. The samples were blotted for 1 s with an offset of -1 mm and allowed to rest for 1 s then plunged into liquid ethane at its melting temperature of -183 °C. Vitrified films of MC hydrogel were $100 - 300$ nm in thickness.

2.7.2 Instrumentation

TEM grids containing vitrified MC hydrogels were stored in liquid nitrogen before being transferred to a Gatan-626 single tilt cryo-transfer holder and held at -186 °C during imaging in an FEI Technai G2 Spirit BioTWIN operating at a 120 kV accelerating voltage. TEM micrographs were recorded with a FEI Eagle CCD camera underfocused by approximately -20 μmm at a magnification range between 16 000x to 25 000x.

Chapter 3

The Sol-Gel Transition in Aqueous Methylcellulose Solutions [i,ii]

3.1 Introduction

This chapter characterizes the transition from a clear MC solution to a turbid hydrogel using dynamic mechanical spectroscopy (DMS) and turbidity measurements. Because aqueous MC solutions exist as viscous liquids at low temperatures and elastic gels at high temperatures, it is important to utilize characterization techniques which correctly report the solution-to-gel (sol-gel) transition. Previous reports have variously defined the sol-gel transition in MC solutions as the crossover of G' and G'',[21] the minimum in viscosity[17] or G',[19,23,34] and "the onset of non-Newtonian viscoelastic behavior,"[43] but none of these working definitions necessarily elucidate a true, frequency-independent gel point. Other nonrheological operating definitions of the MC gel point have included thermal events measured by differential scanning calorimetry,[30] changes in the slope of a characteristic length scale with temperature

[i] Adapted with permission from Arvidson, S. A.; Lott, J. R.; McAllister, J. W.; Zhang, J.; Bates, F. S.; Lodge, T. P.; Sammler, R. L.; Li, Y.; Brackhagen, M. *Macromolecules* **2013**, *46*, 300-309. Copyright 2013 American Chemical Society.

[ii] Adapted with permission from, McAllister, J. W. and Schmidt, P. W. and Dorfman, K. D. and Lodge, T. P. and Bates, F. S. *Macromolecules* **2015**, *submitted*.

measured by small-angle X-ray scattering,[30] and whether the sol flowed under its own weight when tilted.[98] While these methods may correlate with the gel point, they are not true measures of, and may be significantly offset from, a rheological gel point. The wide variety of sol-gel transition definitions contribute to confusion (and sometimes errors) in MC literature. The results presented in this chapter systematically compare the sol-gel transition of MC solutions on heating, and account for the two-stage gelation proposed by many previous researchers (see Section 1.3.1).

Similar to the variability in sol-gel transition, the optical cloud point has been variously defined. Some publications have reported that MC gels prior to clouding,[21,30,43,50,54] while another reported clouding before gelation.[55] More recently, Fairclough et al.[26] reported that the onset of clouding was close to the growth in G' for a single concentration and molecular weight. Sarkar[17] found no correlation between the onset of gelation and the incipient cloud points. In this chapter, the cloud point was systematically defined for MC solutions, and its relation to gelation is established.

3.2 Results

The results presented in this chapter are organized as follows: stress sweeps to determine the linear regime for small-amplitude oscillatory shear (SAOS) measurements, dynamic moduli on heating and cooling by DMS, isothermal frequency sweeps by DMS, determination of the sol-gel transition temperature (T_{gel}), and measurements of the turbidity of MC solutions and gels to establish T_{cloud}. Numerous concentrations of three molecular weights of MC were studied, in an effort to establish a complete sol-gel transition plot for MC materials with a $DS \approx 1.8$.

3.2.1 Determination of the LVE Regime

Prior to determining temperature or frequency-dependent moduli of MC solutions and gels, the linear viscoelastic regime must be evaluated. This ensures appropriate

measurements of the storage (G') and loss (G'') moduli. As described in Section 2.3.1, G' and G'' are defined by a phase shift δ between the applied sinusoidal stress and the measured sinusoidal strain. The applied sinusoidal shear must be large enough to give adequate transducer signal yet small enough to remain in the LVE regime. For a stress-controlled rheometer such as the AR-G2, evaluation of the LVE response must be done in terms an applied stress, σ_0 (not an applied strain).

Figure 3.1 displays G' and G'' as a function of σ_0 for a 1.4 wt% solution of MC300. The LVE regime is most simply defined as the range of values of σ_0 that give stress-independent G' and G". At 30 °C (in blue), G' and G'' show an apparent decrease with large σ_0. Decreases in dynamic moduli in LAOS correlates to a decrease in steady shear viscosity at high shear rates; this phenomenon is known as *shear thinning*[88] and is common for many polymer solutions. After MC transitions to a hydrogel at 60 and 70 °C (orange and red), G' and G'' show an apparent increase with large σ_0. Increases in dynamic moduli in LAOS correspond to *shear hardening*, in which the modulus increases with increased stress or strain. Shear hardening is common with biopolymer gels,[99] and has important implications for the properties of MC hydrogels. While G' and G'' are not simply defined in the NVLE, the shear thinning of MC solutions and

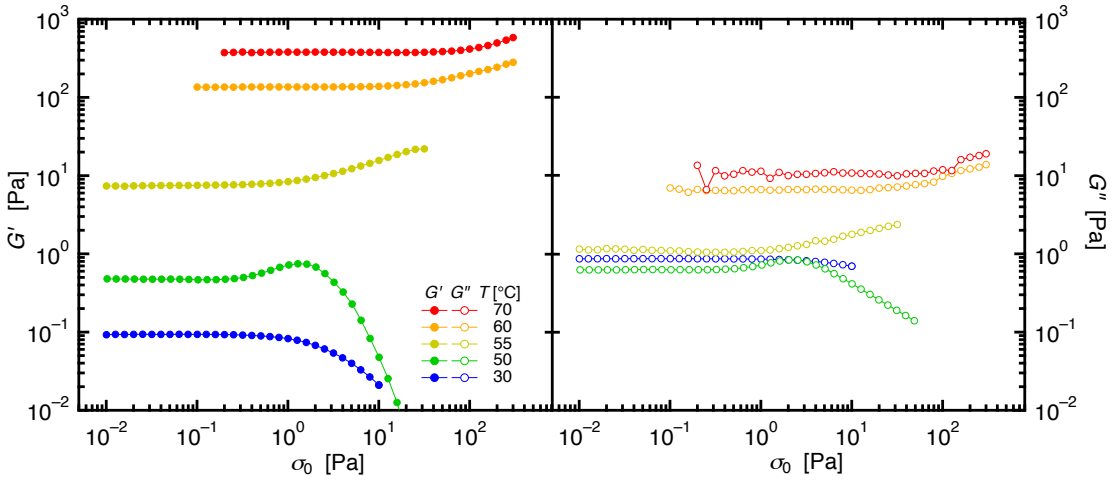

Figure 3.1: Stress-dependent moduli of a 1.4 wt% MC300 sample with an oscillation frequency of 1 rad s^{-1} and concentric cylinder geometry. At large σ_0 MC solutions undergo shear thinning (low T), and MC gels undergo shear hardening (high T).

hardening of MC gels are real, and will be discussed further in Chapter 5.

Figure 3.2 shows the same dynamic moduli as Figure 3.1, except with the strain amplitude γ_0 on the x-axis. This plot is slightly misleading since γ_0 is not the independent variable, but it makes an important point. In Figure 3.1, the value of σ_0 to give a linear response varies with temperature for MC solutions and gels. However γ_0 in Figure 3.2 a strain amplitude of $\gamma_0 = 5\%$, denoted by the dashed line will give a linear response in the temperature range from 5 to 90 °C. Operation of the AR-G2 in strain-control mode with $\gamma_0 = 5\%$ allowed for a constant operation mode that always gave a linear response for MC samples of all concentrations and temperatures. All further DMS measurements presented in this chapter were collected in strain-control mode, with $\gamma_0 = 5\%$.

3.2.2 Dynamic Moduli on Heating and Cooling

As noted in the introduction with Figure 1.5, as aqueous MC solutions are heated there is a slight increase in G' near 40 °C, followed by a steep increase in G' near 60 °C as MC transitions to a hydrogel. This has been called two-stage MC gelation

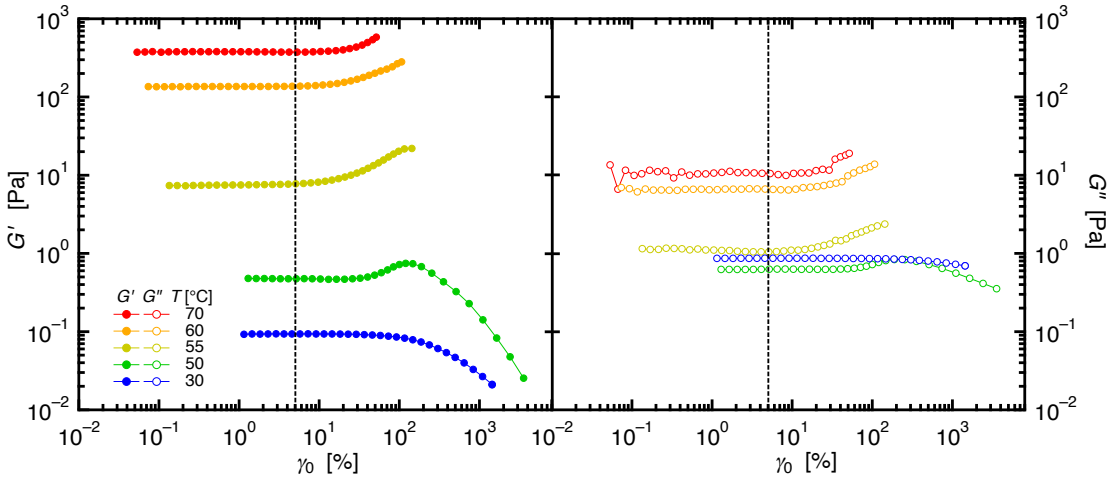

Figure 3.2: Moduli vs. strain amplitude from the stress sweeps in Figure 3.1 for a 1.4 wt% MC300 sample with an oscillation frequency of 1 rad s^{-1}. The dashed line represents a strain-amplitude of $\gamma_0 = 5\%$, which was the applied strain (in strain-control mode) for the the remaining G' and G'' measurements in this chapter.

has been widely reported.[18,20,23–25] The first increase in G' is generally agreed upon to be the result of some sort of chain association of MC molecules prior to gelation. Figure 3.3 shows G' and G'' for 5 concentrations of MC300 on heating and cooling at 1 °C min^{-1} with $\omega = 1$ rad s^{-1}. When heated from a cold solution, MC solutions display an initial decrease in dynamic moduli G' and G'' upon heating. MC solutions up to about 1.4 wt% (purple, blue, green, and yellow) display the first increase in G' beginning at about 30 °C (for low concentrations) to 40 °C (for 1.4 wt%), whereas the highest concentration (red, 2.5 wt%) does not display the first increase in G'. The gelation of MC solutions, which corresponds to the second rise in G', begins at about 65 °C for a 0.5 wt% solution (in purple). The appearance of the second rise in G'

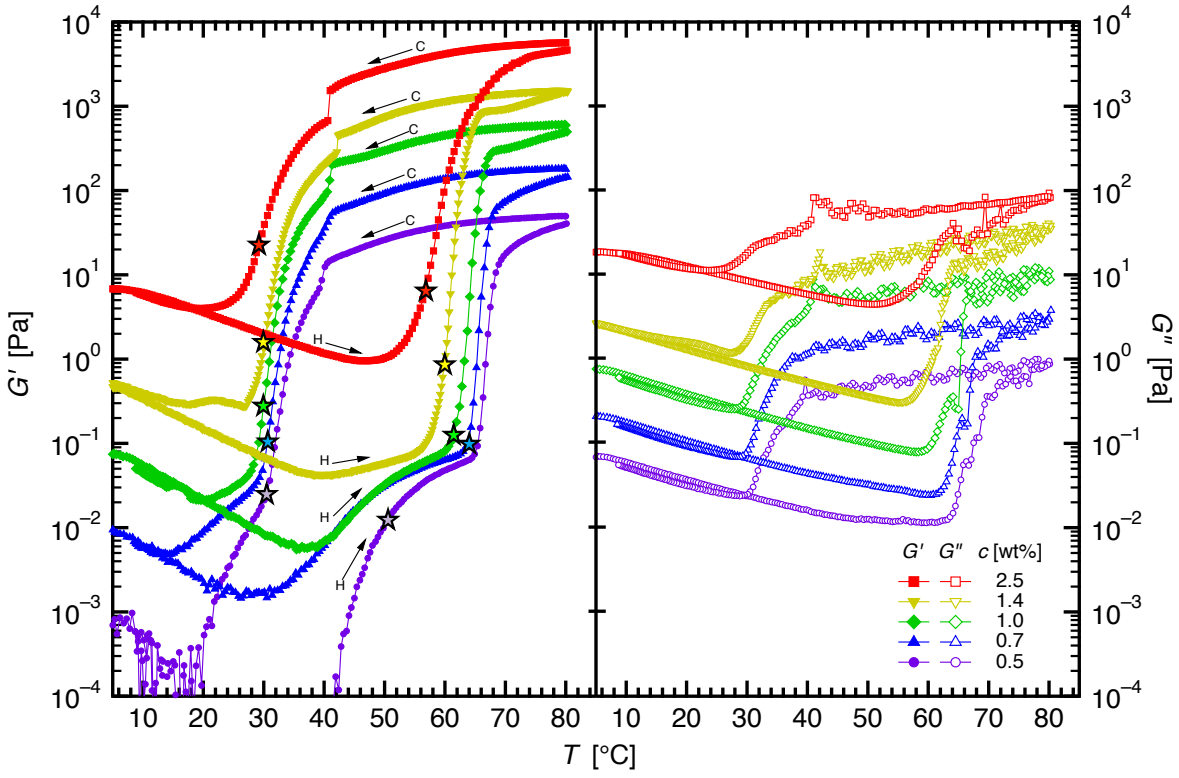

Figure 3.3: Storage (left) and loss (right) moduli of five concentrations ($c = 0.5, 0.7, 1.0, 1.4$, and 2.5, corresponding to $c/c^* = 3.6, 5, 7, 10$, and 18, respectively) of MC300 upon heating and cooling at 1 °C min^{-1} with $\gamma_0 = 5\%$ at an oscillation frequency of $\omega = 1$ rad s^{-1}. Stars indicate $T(G' = G'')$ on heating and cooling. Arrows denote heating and cooling for each curve.

decreases with temperature as concentration increases: from 65 °C at 0.5 wt% to 50 °C at 2.5 wt%. The gel modulus at 80 °C is concentration dependent.

Figure 3.4 shows G' and G'' of 1.0 wt% solutions for three molecular weights on heating and cooling at 1 °C min^{-1} with $\omega = 1$ rad s^{-1}.The two lower molecular weight samples, MC150 and MC300, show an initial increase in G' on heating, whereas the highest molecular weight, MC530 does not. Molecular weight has negligible effect on the second increase in G' starting at 60 °C, and also negligible effect on the hot gel modulus at 80 °C. Figure 3.5 shows G' and G'' for a 2.1 wt% solution of MC300 heated and cooled at different rates with $\omega = 1$ rad s^{-1}. The transition of MC solutions to

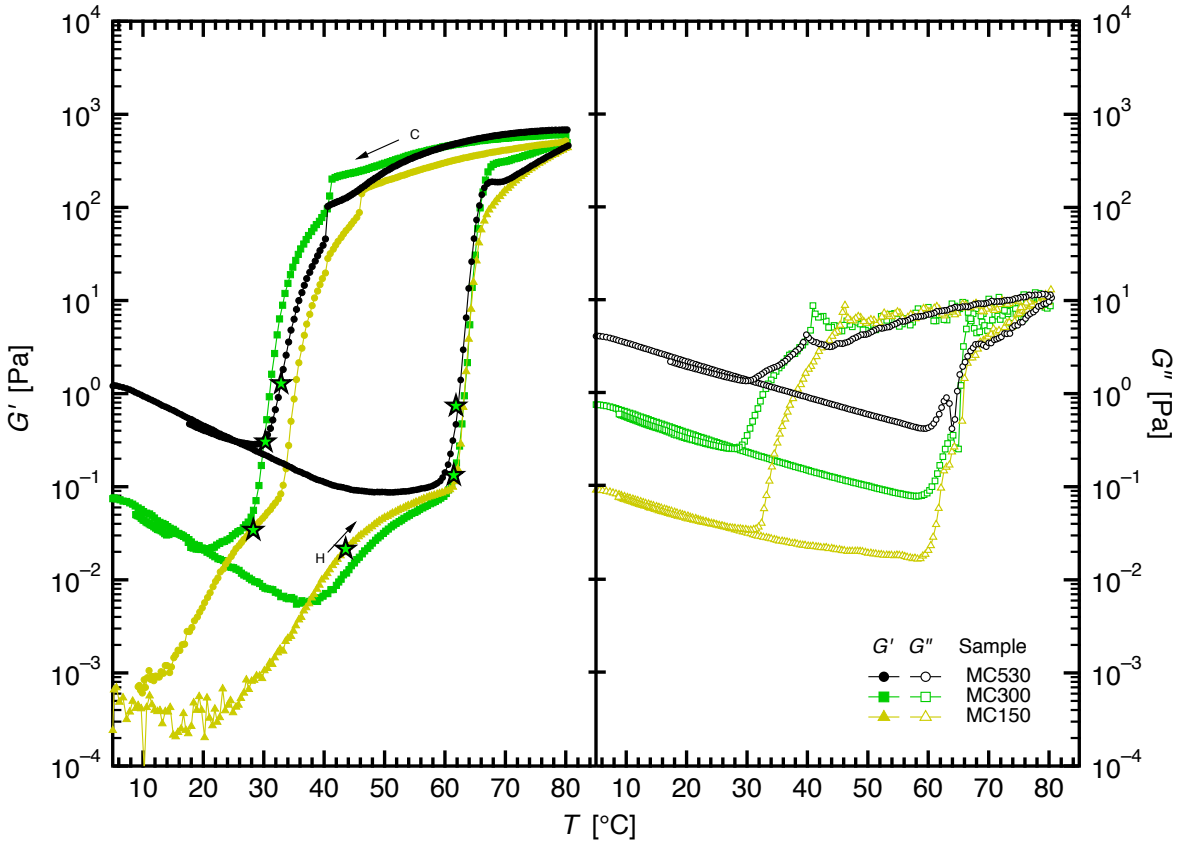

Figure 3.4: Storage (left) and loss (right) moduli of 1.0 wt% solutions of three molecular weights, upon heating and cooling at 1 °C min^{-1} with $\gamma_0 = 5\%$ at an oscillation frequency of $\omega = 1$ rad s^{-1}. 1.0 wt% corresponds to $c/c^* = 4.8, 7.1$, and 10.9 for MC150, MC300, and MC530, respectively. Stars indicate $T(G' = G'')$ on heating and cooling. Arrows denote heating and cooling for each curve.

gels is heating rate dependent, with slower heating rates accessing the gel network at lower temperatures than faster heating rates.

From Figures 3.3 and 3.4, the first increase in G' on heating approaches a constant value of $G' = 0.1$ Pa, prior to MC gelation with the second rise in G'. If an MC solution is concentrated enough so that $G' > 0.1$ Pa at all T, then the first increase in G' is not apparent. This behavior in the first increase in G' gives a clue to the structure of the initial aggregation of MC chains prior to gelation. It also explains why some publications report an initial rise in G' on heating,[18,20,23,25] whereas other publications report no initial rise.[5,21,26,31,32,37] Since the initial rise in G' is independent of concentration and molecular weight, it must be a local property inherent to the

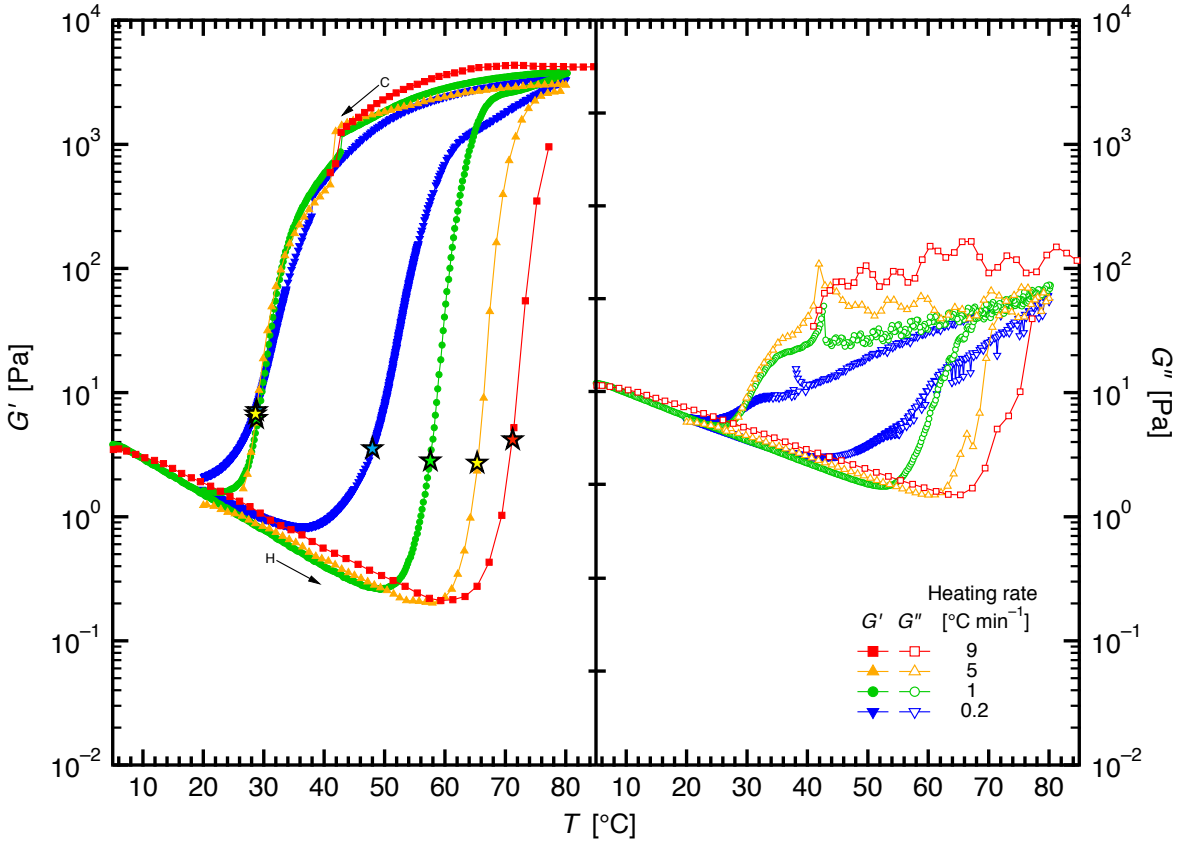

Figure 3.5: Storage (left) and loss (right) moduli of 2.1 wt% MC300 solutions ($c/c^* = 15$) heated and cooled at different rates, with 1 °C min^{-1} with $\gamma_0 = 5\%$ at an oscillation frequency of $\omega = 1$ rad s^{-1}. Stars indicate $T(G' = G")$ on heating and cooling. Arrows denote heating and cooling for each curve.

MC repeat unit structure. The initial rise is an aggregation of MC molecules, and the second rise is the result of the aggregated MC creating a percolated network. Structural aspects of the first and second rise in G' will be discussed further in Chapter 5.

When heated from a cold solution, MC solutions display an initial decrease in dynamic moduli G' and G''. The cause of the initial decrease in viscosity could partially be the temperature-dependence of the water solvent, as water has viscosities of 1.79 mPa s at 0 °C and 0.55 mPa s at 50 °C,[100] corresponding to a 3-fold decrease in viscosity. The decrease in G' and G″ in Figure 3.3 range from a 5- to 10-fold decrease in modulus, so there is likely another factor contributing to the initial decrease in moduli as MC solutions are heated. The cause for the additional decrease in G' could be a result of a contraction of radius of gyration (R_g), or changes to the hydrogen bonding between water and MC at elevated temperature. As will be shown in chapter 6, the latter is more likely the case, as R_g is relatively insensitive to T from 15 to 45°C.

While Figures 3.3 through 3.5 provide important information about the nature of MC gelation, the data in these plots were all taken at a single oscillation frequency. One of the primary objectives of this chapter is to identify the sol-gel transition temperature for MC solutions, and to illustrate the importance of oscillation frequency. The stars on the plots in Figures 3.3 through 3.5 indicate the temperature at which $G' = G''$, which many previous reports identified as the gel point.[19,21–23,43,55] Crude understandings of Equation 2.3 (and also 2.6) would may suggest that $G' = G''$ could be a sol-gel transition, yet if it were the case for MC low concentration samples (purple in Figure 3.3, and light green in 3.4), the initial rise in G' complicates interpreting the $G' - G''$ crossover temperature as the gel point.

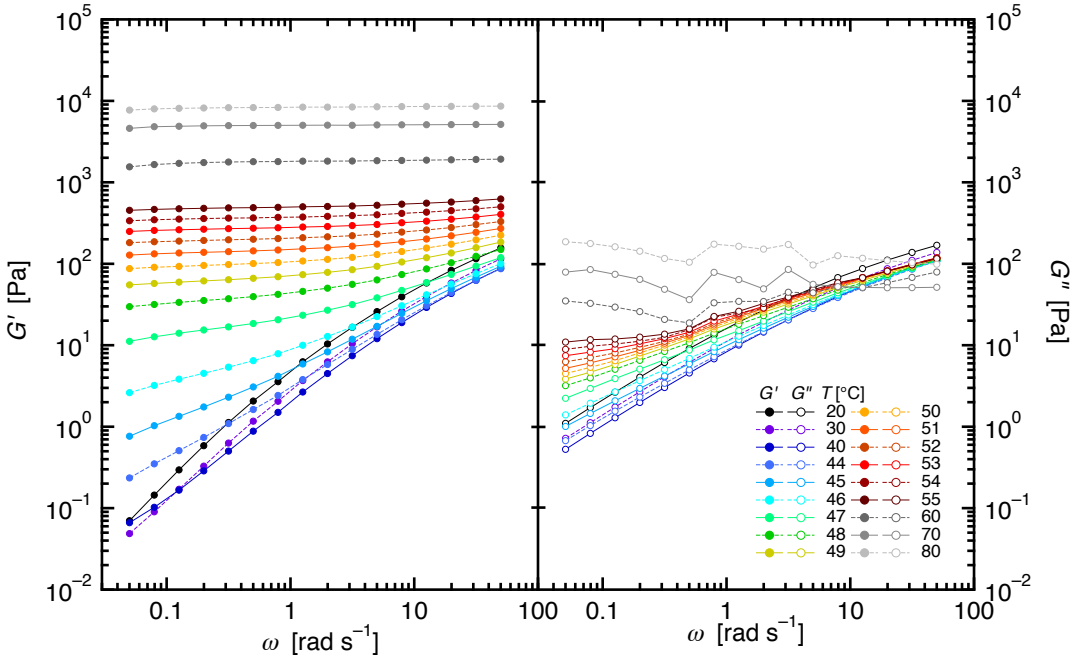

Figure 3.6: Isothermal frequency-dependent moduli of a 2.8 wt% solution of MC300, corresponding to $c/c^* = 20$. Measurements began at 20 °C, and temperature was incrementally increased to 80 °C, with 15 minutes of annealing time between measurements.

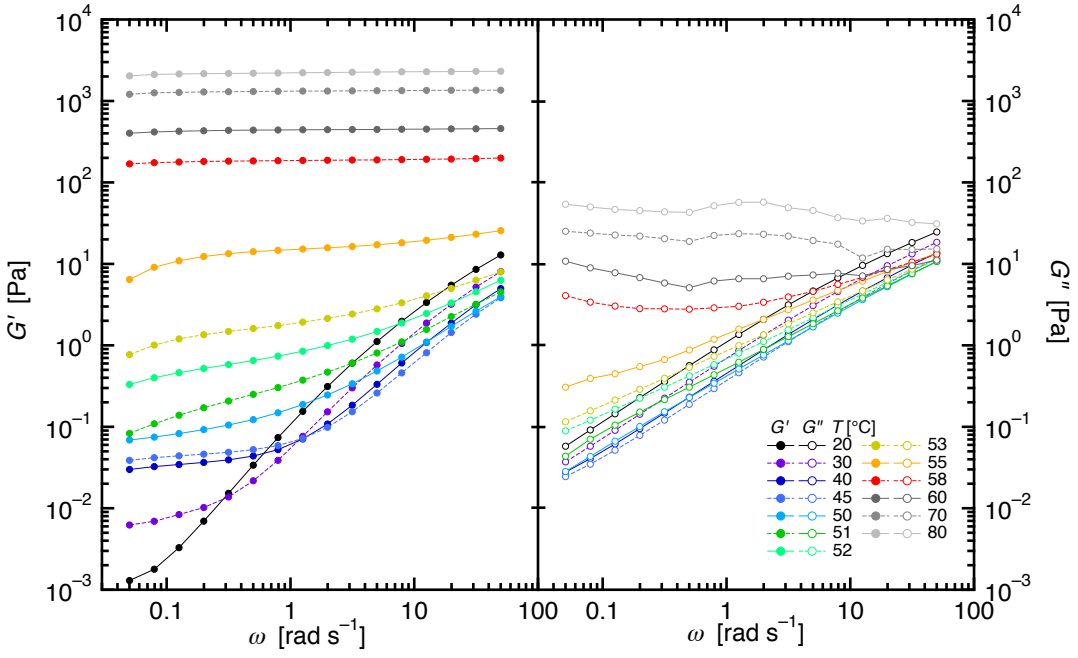

Figure 3.7: Isothermal frequency-dependent moduli of a 1.4 wt% solution of MC300, corresponding to $c/c^* = 10$. Measurements began at 20 °C, and temperature was incrementally increased to 80 °C, with 15 minutes of annealing time between measurements.

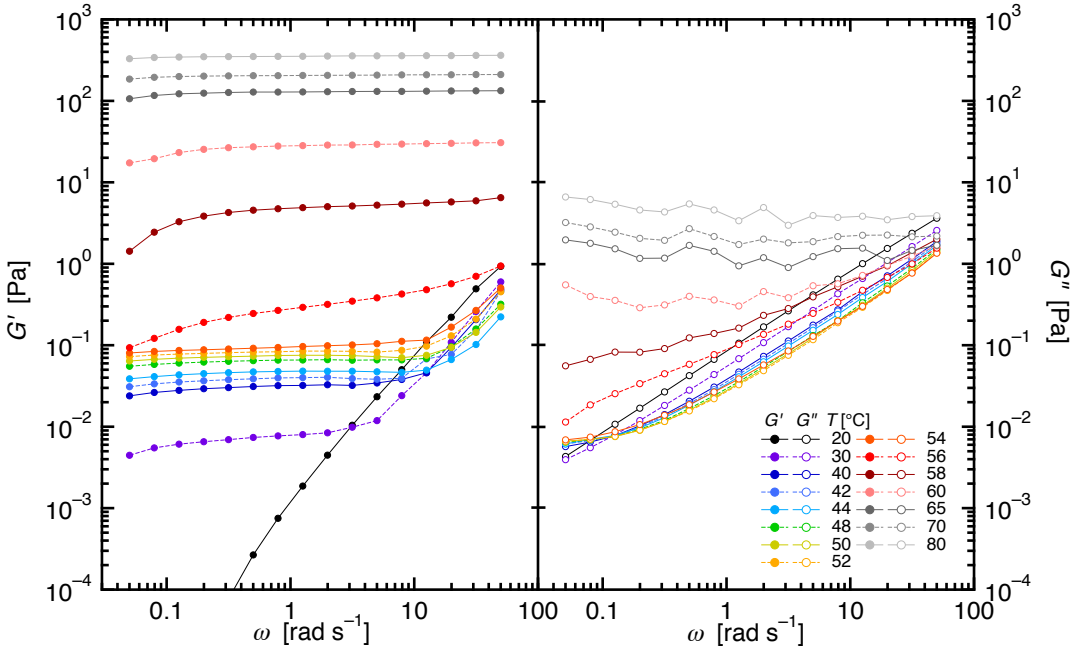

Figure 3.8: Isothermal frequency-dependent moduli of a 0.7 wt% solution of MC300, corresponding to $c/c^* = 5$. Measurements began at 20 °C, and temperature was incrementally increased to 80 °C, with 15 minutes of annealing time between measurements.

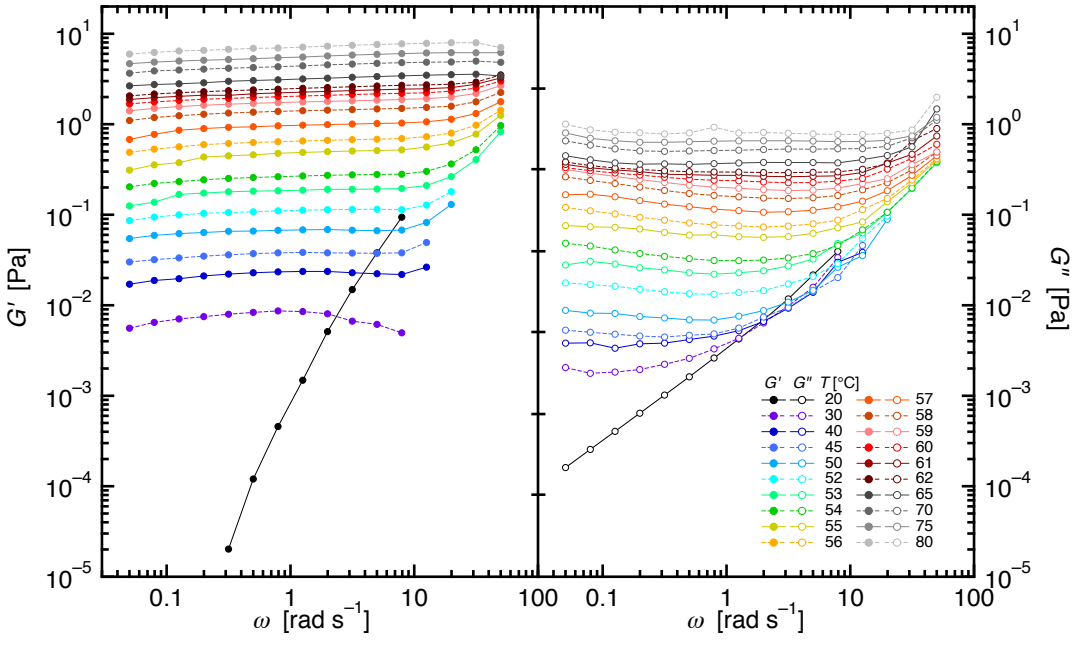

Figure 3.9: Isothermal frequency-dependent moduli of a 0.14 wt% solution of MC300, corresponding to $c/c^* = 1$. Measurements began at 20 °C, and temperature was incrementally increased to 80 °C, with 15 minutes of annealing time between measurements.

3.2.3 Isothermal Frequency Sweeps

Previous frequency sweeps of MC solutions have reported a low-frequency G' plateau that develops as temperature increases.[20–23] for a variety of temperatures, yet they only reported a single concentration of MC. Given the concentration dependence noted in Section 3.2.2, frequency sweeps as different concentrations will provide important insight to MC gelation. Figures 3.6, 3.7, 3.8, and 3.9 show frequency sweeps of MC300 solutions of 4 concentrations heated very slowly at 2 °C hr^{-1}: 2.8 wt%, 1.4 wt%, 0.7 wt%, and 0.14 wt% respectively. In each concentration of frequency sweep, MC at 20 °C shows terminal-like viscoelastic behavior ($G'(\omega) \sim 2$ and $G''(\omega) \sim 1$). The most concentrated MC300 sample in Figure 3.6 steadily transitions from a terminal viscoelastic fluid at 20 °C to a frequency-independent gel at 80 °C. As MC samples become less concentrated, the low frequency plateau begins to appear at temperatures 30 °C and above with the 1.4 wt% sample in Figure 3.7. For even less concentrated samples (Figures 3.8 and 3.9), $G'(\omega)$ is almost completely dominated by the low frequency plateau. MC samples that have the first rise in $G'(T)$ for low concentration samples also show a low frequency $G'(\omega)$ plateau. The plateau in G' for $T > 30$ °C in Figure 3.9 implies that low concentration ($c/c^* < 1$) MC solutions transition to a gel below 30 °C, which contributes to confusion in the MC literature about the location of the sol-gel transition. For this reason, the sol-gel transition will be more formally defined in the next section.

3.2.4 The Sol-Gel Transition by the Winter-Chambon Method

Chambon and Winter[101–103] defined the sol-gel transition for a crosslinking reaction of poly(dimethylsiloxane) with tetrasilane, and later extended the definition to polyurethane network polymerizations.[104] Aliquots of reaction mixture were prepared and allowed a designated time to react prior to quenching the crosslink reaction. A series of frequency sweeps provided $G'(\omega)$ and $G''(\omega)$ for a range of time points to span the extent of the reaction. The gel point was defined as the time that $G'(\omega)$ and

$G''(\omega)$ followed a simple power relation,

$$G'(\omega) \sim G''(\omega) \sim \omega^n \tag{3.1}$$

where n is defined as a relaxation exponent between zero and one, and related to the dynamic loss tangent, $\tan(\delta)$ by,

$$\tan(\delta) = \tan\left(\frac{n\pi}{2}\right). \tag{3.2}$$

At the gel point, the material is referred as a *critical gel*, and the ratio between $G''(\omega)$ and $G'(\omega)$ will be constant, and $\tan(\delta)$ is frequency independent. When $n = 1/2$, critical gels exhibit the property $G'(\omega) = G''(\omega)$. As $n \to 1$, then $G''(\omega) > G'(\omega)$, and the critical gel is relatively soft and fragile. As $n \to 0$, then the critical gel is stiff, $G''(\omega) < G'(\omega)$. The advantage to this method is that the gel point is determined explicitly, and for all ω, instead of $G' = G''$ for a single ω. The gel point for a system historically defined as the critical point of a percolating network,[105,106] and methods for determining the gel point experimentally prior to Winter and Chambon this was done by an extrapolation of steady-shear viscosity in the pre-gel regime to infinite viscosity[107] or in the post-gel regime to zero equilibrium modulus.[108] Furthermore, the relaxation exponent n gives insight into the degree of cross-linking per chain.

Since MC is a thermoreversible physical gel, the gelation reaction cannot be quenched as with poly(dimethylsiloxane) and polyurethane networks. However, since the gel develops slowly as temperature is raised, the gelation of MC were followed as a function of T, rather than with time as used by Winter and Chambon. Figures 3.10 through 3.13 show the gelation of MC upon heating, with frequency sweeps $G'(\omega)$ and $G''(\omega)$ replotted as $\tan(\delta)$ vs. T. Figure 3.10 is a MC300 solution of 4.2 wt% ($c/c^* = 30$). Each temperature in the top plot shows an isothermal frequency sweep, and the sample was incrementally heated to the next temperature to give a heating

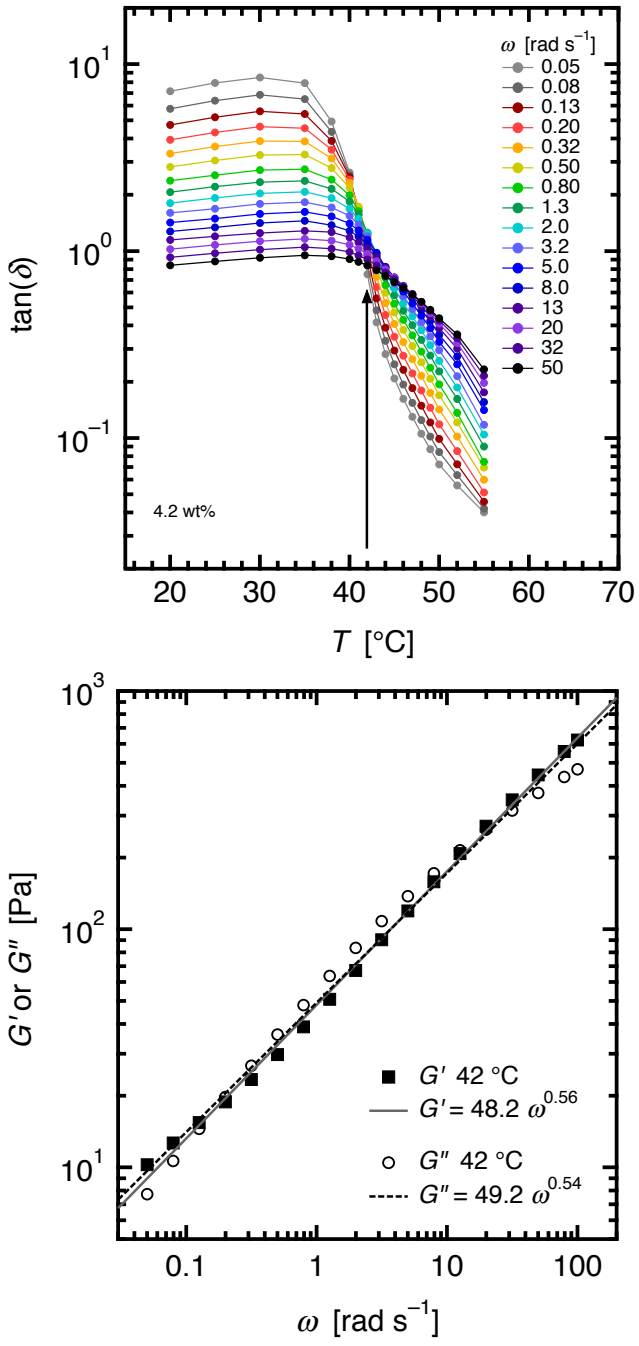

Figure 3.10: Dynamic loss tangent (top) of a 4.2 wt% solution of MC300 heated slowly from 20 to 55 °C from Arvidson et al.[52] $T_{gel} \approx 42$ °C occurs at the frequency convergence of tan(δ). Heating rate is approximately 2 °C h^{-1} in the vicinity of the sol-gel transition. Frequency dependent moduli (bottom) of the sample at the sol-gel transition denoted by the arrow. Reproduced with permission from the American Chemical Society copyright 2013.

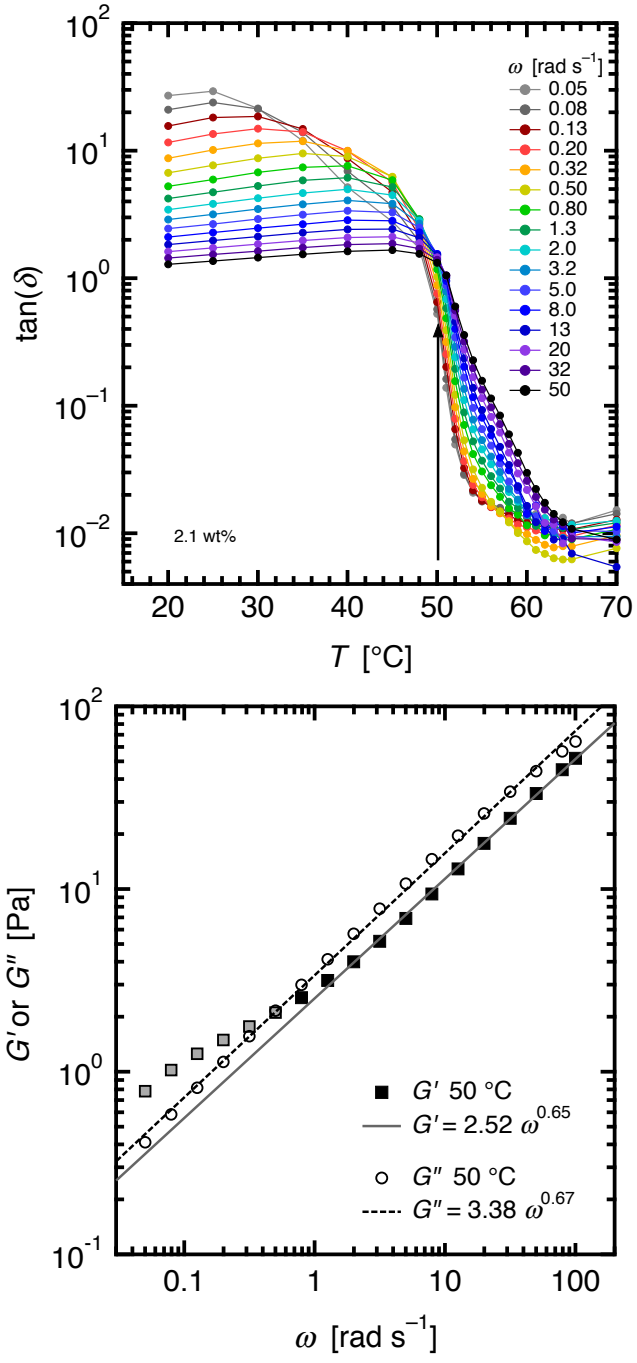

Figure 3.11: Dynamic loss tangent (top) of a 2.1 wt% solution of MC300 heated slowly from 20 to 70 °C from Arvidson et al.[52] $T_{\text{gel}} \approx 49$ °C occurs at the frequency convergence of tan(δ). Heating rate is approximately 2 °C h^{-1} in the vicinity of the sol-gel transition. Frequency dependent moduli (bottom) of the sample at the sol-gel transition denoted by the arrow. Gray colored storage moduli points have been omitted from the T_{gel} calculation. Reproduced with permission from the American Chemical Society copyright 2013.

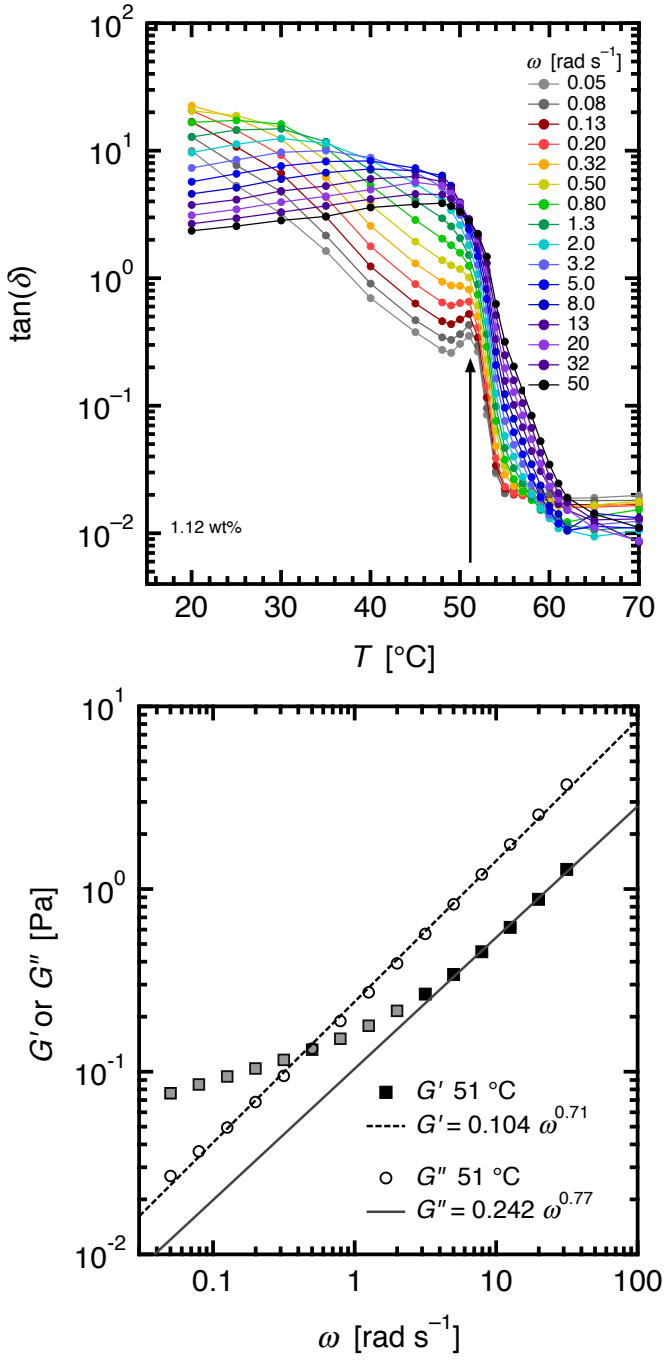

Figure 3.12: Dynamic loss tangent (top) of a 1.12 wt% solution of MC300 heated slowly from 20 to 70 °C from Arvidson et al.[52] $T_{\text{gel}} \approx 51$ °C occurs at the frequency convergence of tan(δ). Heating rate is approximately 2 °C h^{-1} in the vicinity of the sol-gel transition. Frequency dependent moduli (bottom) of the sample at the sol-gel transition denoted by the arrow. Gray colored storage moduli points have been omitted from the T_{gel} calculation. Reproduced with permission from the American Chemical Society copyright 2013.

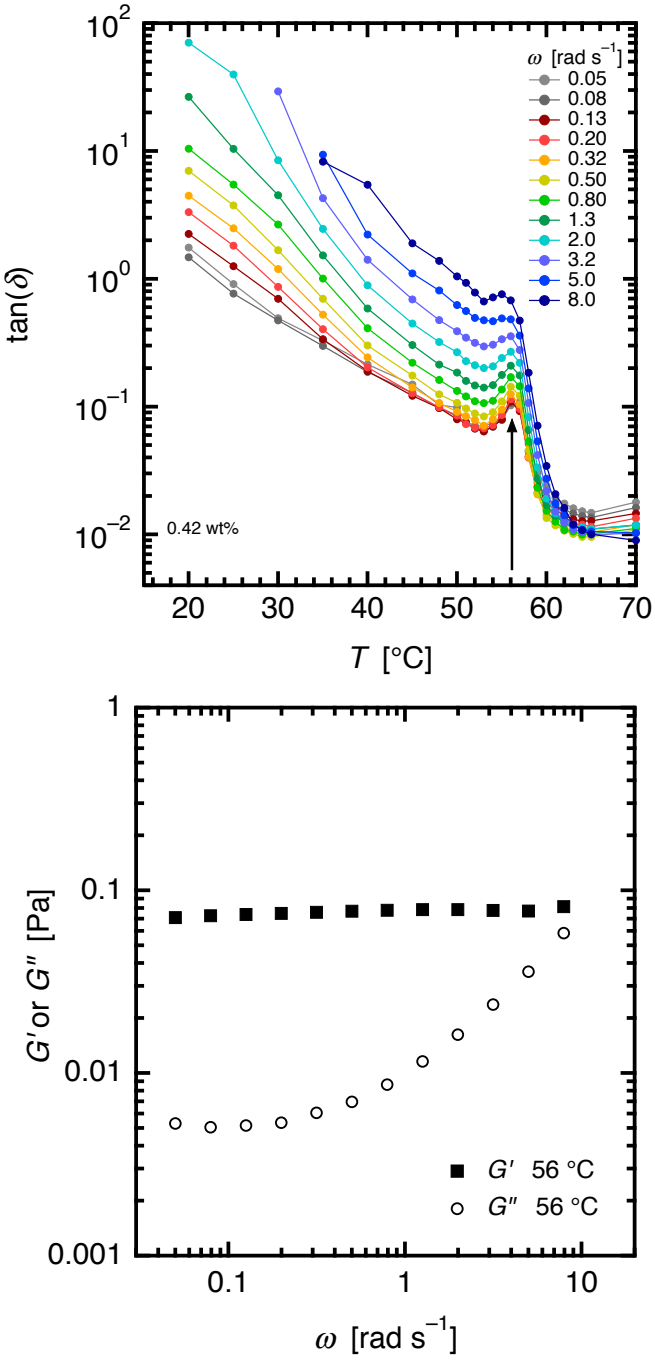

Figure 3.13: Dynamic loss tangent (top) of a 0.42 wt% solution of MC300 heated slowly from 20 to 70 °C from Arvidson et al.[52] $T_{gel} \approx 56$ °C occurs at the frequency convergence of tan(δ). Heating rate is approximately 2 °C h^{-1} in the vicinity of the sol-gel transition. Frequency dependent moduli (bottom) of the sample at the sol-gel transition denoted by the arrow. Gray colored storage moduli points have been omitted from the T_{gel} calculation. Reproduced with permission from the American Chemical Society copyright 2013.

rate of 2 °C hr^{-1}. T_{gel} occurs at the convergence of ω to a point, denoted by an arrow. The bottom plot shows $G'(\omega)$ and $G''(\omega)$ near T_{gel}, given by Equation 3.1. Figure 3.11 through 3.13 are the gel point analyses of MC300 solutions of decreasing concentrations from 2.1 wt% ($c/c^* = 15$), 1.12 wt% ($c/c^* = 8$), and 0.4 wt% ($c/c^* = 3$). With decreased concentration, the low-frequency plateau in $G'(\omega)$ was omitted from the T_{gel} calculation. As concentration decreases and the low-frequency G' plateau grows, the frequency-convergence in $\tan(\delta)$ diminishes, and a peak in $\tan(\delta)$ emerges. In Figure 3.13, the G' plateau extends to the measured frequency range, and only a peak in $\tan(\delta)$ can be used to determine T_{gel}.

The use of a peak in $\tan(\delta)$ is not an obvious choice for the gel point, but this is justified by the smooth trend noted in Figure 3.14. The values of T_{gel} determined by the

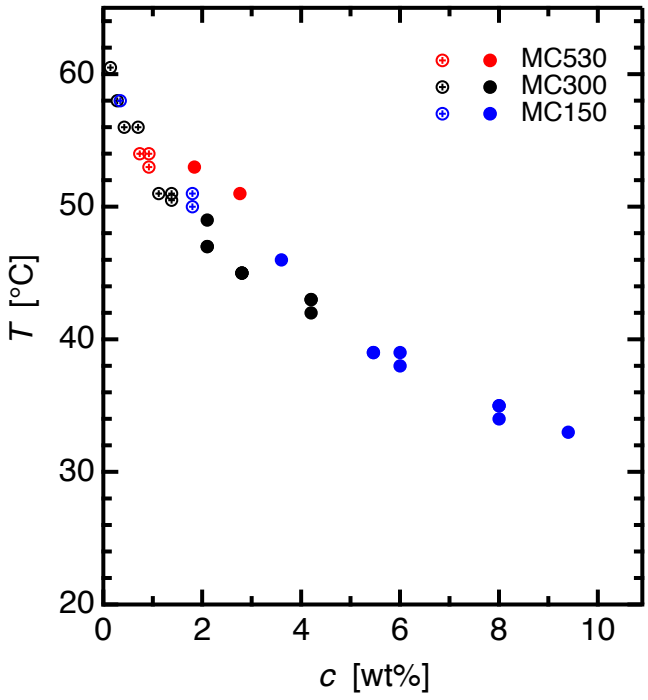

Figure 3.14: T_{gel} for three Ms determined by DMS on heating at 2 °C hr^{-1}, reported by Arvidson et al.[52] Filled circles are for full convergence in $\tan(\delta)$ whereas hollow circles with crosses indicate only a partial convergence or peak in $\tan(\delta)$ in the tested frequency range, indicative of an initial rise in G' prior to gelation. Reproduced with permission from the American Chemical Society copyright 2013.

Winter-Chambon method for three molecular weights of MC and many concentrations and also the peak in $\tan(\delta)$ show a smooth trend of decreasing T_{gel} with temperature. Included are concentrations which satisfy the Winter-Chambon criterion for gelation over the full range of measured frequencies, as well as those which exhibit frequency independent of $\tan(\delta)$ for a smaller range of frequencies. T_{gel} decreases with increasing concentration, although it is virtually independent of the molecular weight.

3.2.5 Cloud Point Measurements

As noted in Figure 1.3, MC solutions transition to optically turbid hydrogels on heating. This section investigates the cloud point using relative transmittance (T_{R}, the ratio between the transmittance at temperature T and the solution transmittance at 20 °C) measurements to compare to T_{gel} reported in the previous section. While it is widely recognized that the gelation and clouding of MC solutions are known to be related, the exact relation is controversial, in part because the cloud points (T_{cloud}) and T_{gel}s in previous studies are based upon varying definitions. One objective was to measure T_{R} of MC solutions under the same conditions used for T_{gel} (2 °C hr^{-1}), and compare the results to Figure 3.14. Based on the sensitivities and length scales associated with DMS versus turbidity, it was not expected that T_{gel} will correspond to a predetermined definition of cloud point (e.g., $T_{\text{R}} = 95\%$[21,43] or $T_R = 50\%$[17,55]). Rheology probes molecular interactions via macroscopic solution behavior while cloud point probes existence of structures with sizes that are on the order of the wavelength of light. T_{R} was measured over the clouding event as T_{R} decreases in MC solutions on heating, and was compared to Figure 3.14.

Figure 3.15 shows relative transmittance curves for MC over a range of concentrations. Upon heating, there is a plateau before a monotonic decrease in the transmittance. At low concentrations, the solutions are clear (that is, exhibit 100% transmittance compared to that of water) at 5 °C, while more concentrated solutions exhibit

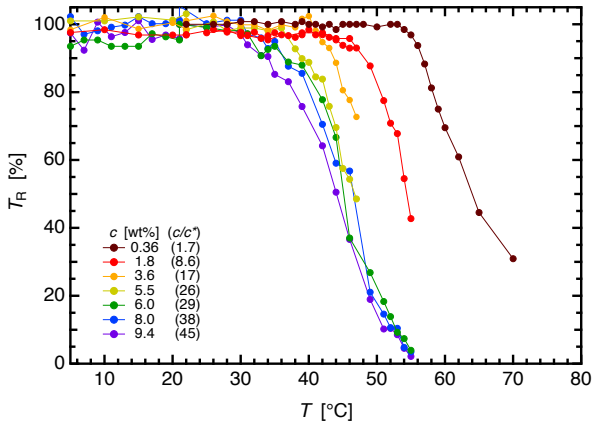

(a) MC150

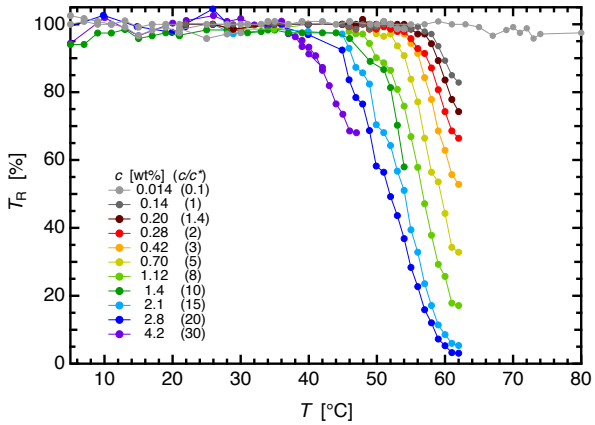

(b) MC300

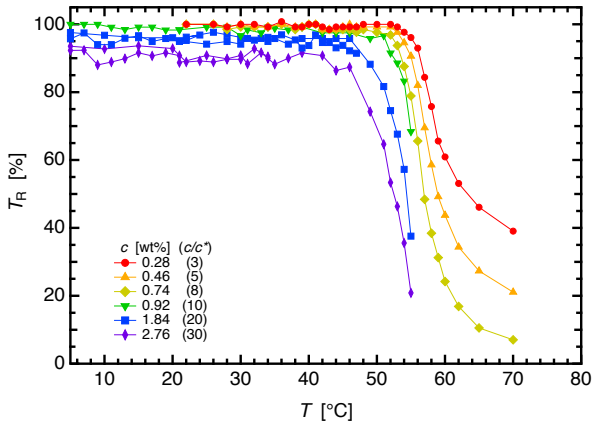

(c) MC530

Figure 3.15: Percent relative transmittance of MC solutions on heating. Each sample was heated at the same rate as Figures 3.10 through 3.13, with an effective heating rate of about 2 °C h^{-1} near the sol-gel transition. Figure (b)[52] reproduced with permission from the American Chemical Society copyright 2013.

reduced transmittance over the full measured range of temperatures compared to water. All solutions exhibit a plateau in transmittance at low temperatures and decrease sharply in a similar manner, regardless of concentration. Comparisons between T_{gel} and T_{R} will be made in Section 3.3.

3.3 Discussion

3.3.1 Sol-Gel Transition Plot

Figure 3.16 compares the rheological gel point of MC solutions with the cloud point defined as $T_{\mathrm{R}} = 86\%$ as well as two more commonly employed cutoffs, 50% and 95%. For the whole range of M, $T_{\mathrm{R}} = 86\%$ corresponds very closely to the rheological gelation temperature, while 95% and 50% tend to under- and overestimate, respectively, T_{gel}. Therefore, it is appropriate to name the temperature at which MC solutions

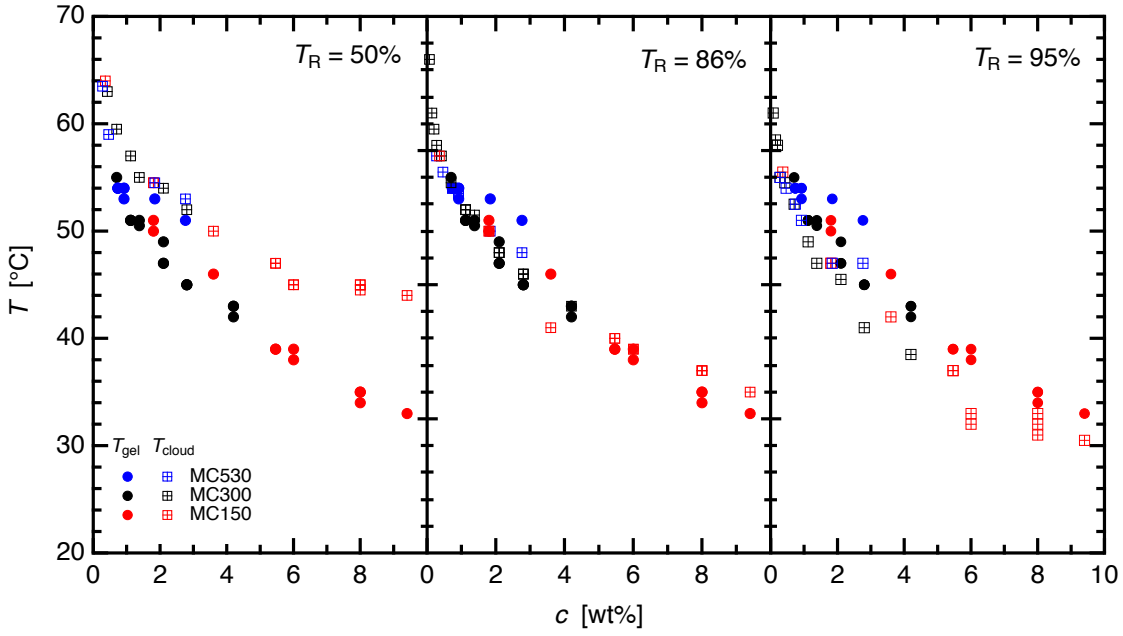

Figure 3.16: Comparision between the sol-gel transition (closed circles) and cloud points (open squares) defined by three definitions of the relative transmittance $T_{\mathrm{R}} = 50, 86, 95$, reported by Arvidson et al.[52] Heating rate was about 2 °C hr^{-1} for all the points displayed above.

reach $T_R = 86\%$ (on heating at 2 °C hr^{-1}) T_{cloud}. Included in Figure 3.16 are all the gel points from Figure 3.14. Clearly, the local maximum in tan(δ) is related to the cloud point in the same manner as the frequency convergence of tan(δ). From Figure 3.16, it is also apparent that the formation of nanoscale structure is accompanied by the presence of a volume-spanning network. These gel and cloud point data are consistent with a gelation scenario in which phase separation and gelation occur together; the association of different chains arrests macroscopic liquid-liquid phase separation. While it is not expected this same relationship (i.e., T_{gel} equals the temperature at which $T_R = 86\%$) to hold for all other polymers that form turbid gels the fact that such a close correspondence exists argues in favor of the view that phase separation and gelation are coupled events in MC solutions.

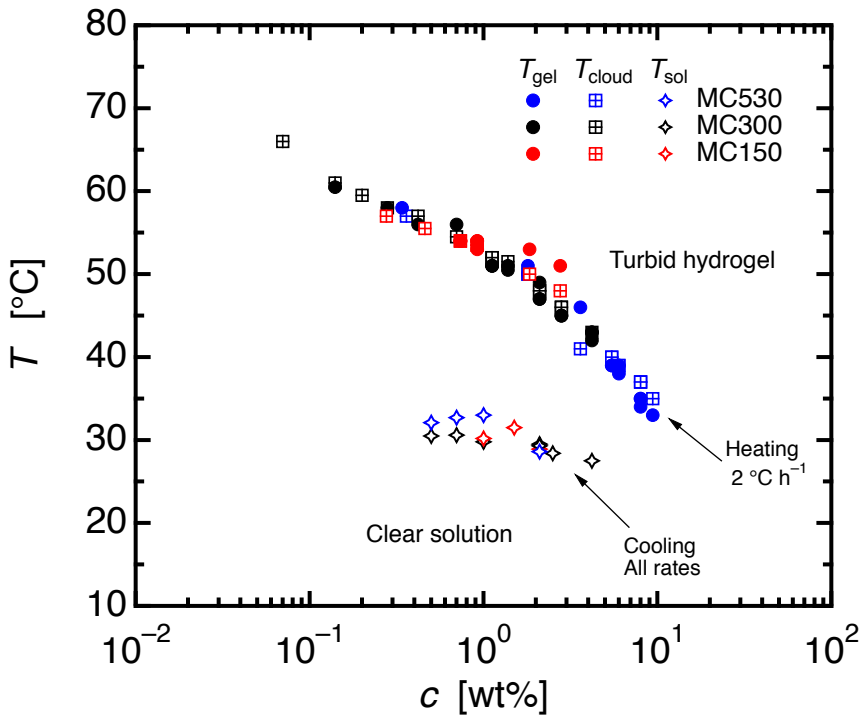

Figure 3.17: Phase diagram for three molecular weights of MC on heating including T_{gel} and $T_R = 86\%$, and T_{sol} on cooling, reported by Arvidson et al.[52] and McAllister et al.[109]

At this point an experimental sol-gel transition diagram can be assembled using T_{gel} and T_{cloud} obtained by DMS and cloud point measurements. Figure 3.17 includes T_{gel} and T_{cloud} from Arvidson et al.[52](on heating, 2 °C h^{-1}). Also included on the plot are the gel-sol transitions (T_{sol}, noted by stars on cooling in Figures 3.3 through 3.5), estimated by $T(G' = G'')$ on cooling, reported by McAllister et al.[109] The Winter-Chambon approach for determining T_{gel} will also work for T_{sol}, but is unnecessary due to the fact that that T_{sol} is relatively insensitive to cooling rate (Figure 3.5). So long as the relaxation exponent n is close to 0.5, $T(G' = G'')$ is a fair approximation for T_{gel} and T_{sol}. Hysteresis of MC gels between heating and cooling persists, even at the slow heating rates of 2 °C hr^{-1}, and the equilibrium behavior of MC solutions cannot be deduced using DMS or cloud point measurements. A feature of Figure 3.17 is that T_{gel} and T_{cloud} (determined by $T_R = 86\%$) can both be considered the sol-gel transition for a heating rate of 2 °C h^{-1}. Also notable is a systematic decrease in T_{gel} with concentration with no minimum in the sol-gel transition line, and that the sol-gel transition is independent of M. If the sol-gel transition for MC is related to a spinodal or binodal curve by Flory-Huggins theory for materials with an LCST, it would be expected to have a minimum. Figure 3.17 is also strikingly different from the diagrams prepared by Takahashi et al.[30] (Figure 1.12) or Chevillard et al.[43] (Figure 1.13). At this point, it was either correct to interpret that the sol-gel transition for MC is not a true phase separation, or the sol-gel transition line is not governed by Flory-Huggins theory (or both). Because it is not clear if the data in Figure 3.17 define equilibrium or stability limits, it is more appropriate to call it a "sol-gel transition diagram" rather than a true phase diagram. Chapter 6 will consider phase separation in MC solutions more completely.

3.3.2 Nature of MC gelation: nucleation and growth

Figure 3.5 indicates that the gelation of MC is heating rate dependent, whereas the transition from the gel back to the solution is independent of cooling rate. This suggests that MC gels develop by nucleation and growth, rather than by spontaneous phase separation. Viscoelastic phase separation (VPS) has been suggested by many for the gelation of MC by spinodal decomposition,[19,26,32,47–51] as an attempt to explain both the gelation mechanism and the LCST of MC. Spinodal decomposition is an instantaneous phase separation into polymer-rich and poly-lean phases, and will occur within a specific concentration range so long as the temperature quench (or for the case of LCST rapid temperature increase) occurs within the unstable region of a phase diagram. Therefore, the notion of VPS (Figure 1.11) as a mechanism for MC gelation is incorrect, and other structures must be considered.

Figure 3.18 compares the effect of heating rates and concentration on MC gelation. For a relatively concentrated solution, with $c = 2.1$ wt% ($c/c^* = 15$), heating rates of 0.03 and 0.2 °C min^{-1} shows that the sol-gel transition occurs at about the same T (black and red data). However, more dilute solutions, with $c = 0.014$ wt% ($c/c^* = 0.1$), heating rates of 0.03 and 0.2 °C min^{-1} show different sol-gel transitions (black and yellow data). The cause of the differences in gelation at slow heating rates is further evidence that MC gels develop by nucleation and growth: dilute samples associate to a gel much more slowly than concentrated ones. Due to the differences in gelation temperatures at rates of 0.03 and 0.2 rad s^{-1} between high and low concentrations, it is possible that T_{gel} is closer to equilibrium behavior between solution and gel at high concentrations than at lower concentrations.

3.4 Summary

The thermoreversible gelation of MC was investigated in detail for a range of Ms (approximately 1.5 to 5.3×10^5 g mol^{-1}) and concentrations ($c/c^* = 0.1$ to 30) by

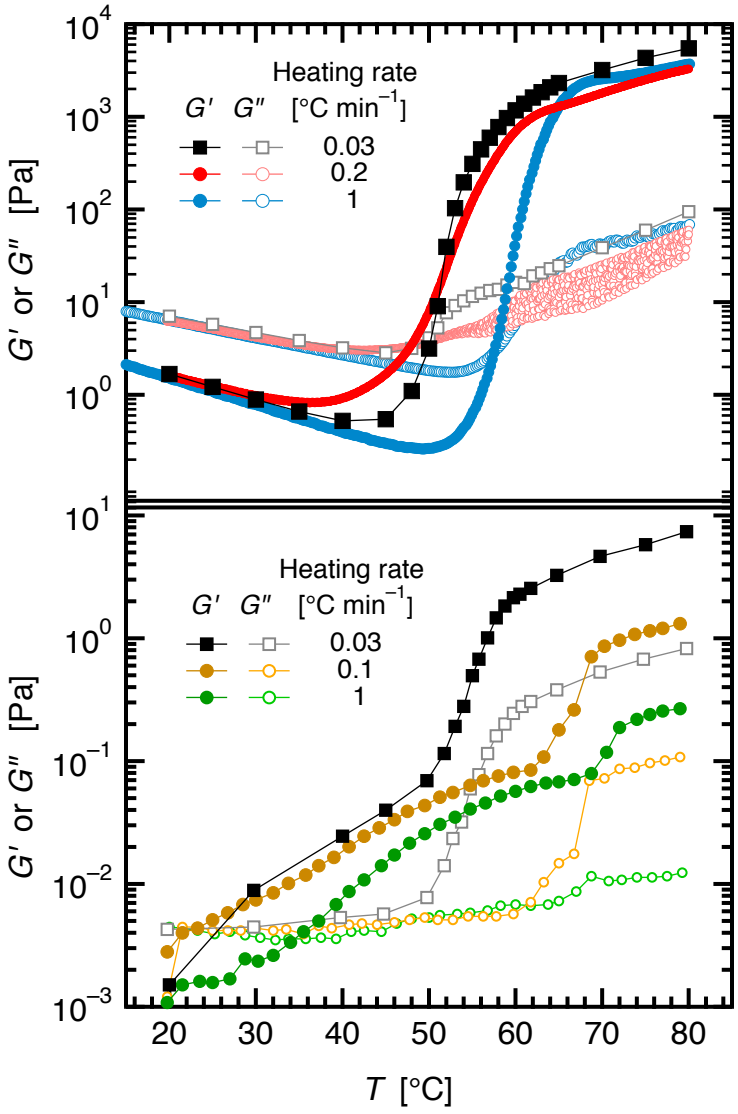

Figure 3.18: A comparision between the effect of heating rates on MC300 solutions of different concentrations. The top plot is for a 2.1 wt% solution (corresponding to $c/c^* = 15$ heated at 0.03, 0.2, and 1 °C min^{-1}. The bottom plot is for a 0.014 wt% solution (corresponding to $c/c^* = 0.1$ heated at 0.03, 0.1, and 1 °C min^{-1}. The black points are $\omega = 1.3$ rad s^{-1} extracted from incremental isothermal frequency sweeps to achieve the sloe heating rate (2 °C h^{-1}). Some of the data is from Arvidson et al.[52] $\gamma_0 = 5$ % and $\omega = 1.3$ rad s^{-1}.

DMS and optical cloud points. Solutions with concentrations above the entanglement threshold ($c/c^* > 12$) exhibit a well-defined gel point following the Winter-Chambon criterion. Solutions with concentrations between the entanglement concentration and the overlap concentration ($1 \leq c/c^* \leq 12$) gel upon heating but follow the Winter-Chambon criteria for gelation for only a few frequencies. Nevertheless, they exhibit a distinct rheological feature associated with gelling (local maximum in $\tan(\delta)$) and still provides the sol-gel transition temperature for a wide concentration of MC materials. Most importantly, DMS and turbidity measurements performed at comparable slow heating rates indicate that the T_{cloud} and T_{gel} points occur at consistent temperatures for a range of Ms, and are independent of M. Thus, the resulting sol-gel transition diagram (T vs. wt%) exhibits two regimes: clear solutions at lower T and cloudy gels at higher T, with a monotonic decrease in T_{gel} with increasing concentration.

Chapter 4

Gel Characterization using Neutron Scattering[i,ii]

4.1 Introduction

This chapter focuses on the physical structure within aqueous MC gels, to understand the basis for their high modulus. The combination of cryogenic transmission electron microscopy (cryo-TEM) and small-angle neutron scattering (SANS) provides a powerful means to capture a wide range of lengthscales to probe the structures within MC materials. It is demonstrated unambiguously that MC forms fibrillar gels, and the morphology and size scales measured in microscopy and scattering experiments are in excellent agreement. In addition, ultrasmall-angle neutron scattering (USANS) experiments allow for examination of the larger scale features, and are consistent with the turbidity of the gels. Detailed modeling of the SANS curves found the fibril diameter to be ca. 15 nm, which is in excellent agreement with cryo-TEM results. The

[i] Adapted with permission from Lott, J. R.; McAllister, J. W.; Arvidson, S. A.; Bates, F. S.; Lodge, T. P. *Biomacromolecules* **2013**, *14*, 2484-2488. Copyright 2013 American Chemical Society.

[ii] Adapted with permission from Lott, J. R.; McAllister, J. W.; Wasbrough, M.; Sammler, R. L.; Bates, F. S.; Lodge, T. P. *Macromolecules* **2013**, *46*, 9760-9771. Copyright 2013 American Chemical Society.

composition of individual fibrils in the gel state was determined, as well as the partitioning of chains between free and fibrillar states as the sample transverses the sol-gel transition. The increase in scattering correlates with the development of modulus of MC gels.

4.2 Results

This section consists of three parts: cyro-TEM images of MC hydrogels, SANS of MC solutions and gels, and USANS of MC gels. Experiments utilizing cryo-TEM were primarily done by Dr. Joseph Lott and Peter Schmidt, and those results are briefly described as they are significant for the choice of analysis used to interpret SANS and USANS data. For more information on cryo-TEM, please refer to one of the references listed in the footnote at the start of this chapter.

4.2.1 Cryo-TEM Images of MC Gels

Figure 4.1 displays transmission electron microscopy images of thin films of MC solutions vitrified from 65 °C, on a lacey carbon-supported TEM grid, with a film thickness of $100 - 300$ nm. The procedure used is described in Section 2.7. The darker colored bands between $100 - 200$ nm in width are the lacey carbon support grid, and the MC film is suspended in the interstitial spaces between the grid. The MC film consists of many small thread-like fibril structures, which have a diameter of 15 ± 2 nm and a large distribution in contour length (100 nm to 1 μm), measured by image analysis software (ImageJ, National Institutes of Health[110]). The structures observed in Figure 4.1 appear very similar to those reported by Bodvik et al., both in terms of the fibril morphology and dimension.[31,111] A consistent fibril diameter was noted for samples at 0.2 wt% and 0.4 wt% solutions, suggesting that the size scale of this fibril structure is independent of concentration over this range (viscosity limitations inhibit cryo-TEM imaging at higher concentrations). The morphology is

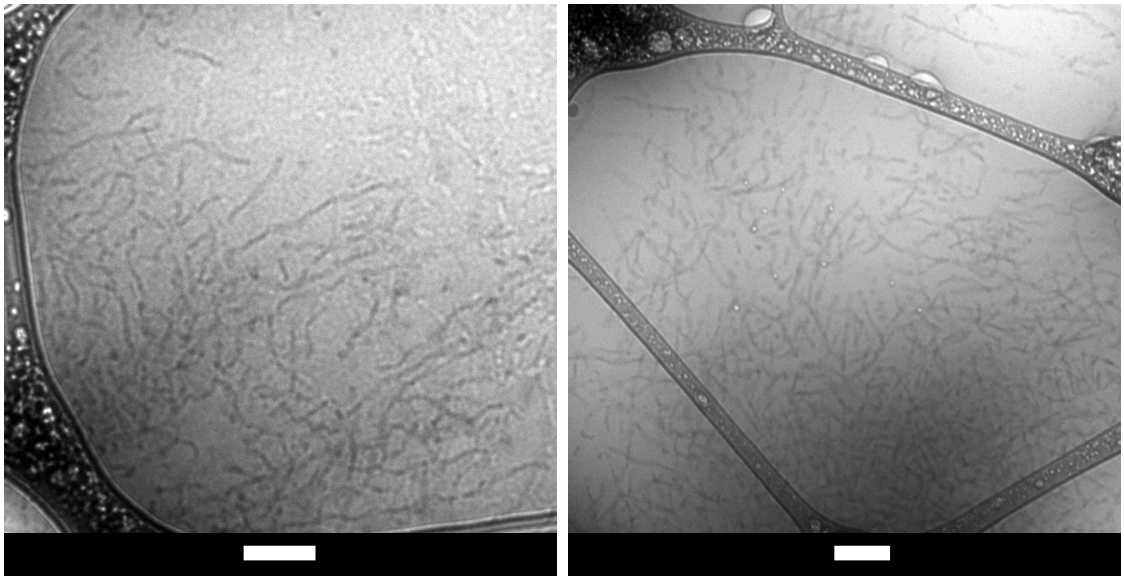

Figure 4.1: Cryogenic transmission electron micrograph image of 0.2 wt% (left) and 0.4 wt% (right) solution of MC300 heated to 65 °C for 30 minutes, then flash-vitrified onto a lacey carbon TEM grid reported by Lott et al.[16] Scale bar is 200 nm, and the average fibril diameter is 15 ± 2 nm. Reproduced with permission from the American Chemical Society.

striking, in that it indicates that MC gels have a different structure from any of the previous structures proposed for MC hydrogels (see Figures 1.10 and 1.11). However, it is important to use cryo-TEM primarily for qualitative analysis, since there are many opportunities for experimental artifacts (e.g. ice crystals, vitrified film irregularities, underfocus of the electron beam) which can lead to inaccuracies if the images are interpreted too literally. Additionally, when a 3-dimensional network is projected onto a 2-dimensional image, there may be some loss of structural information. For these reasons, scattering techniques are better suited for the quantitative analysis of MC hydrogels.

4.2.2 SANS of MC Solutions and Gels

SANS was chosen for quantitative determination of the dimensions associated with MC hydrogels, since the lengthscales probed vary from $5 - 500$ nm. Given the dimensions of the fibrils noted by cryo-TEM in Figure 4.1, SANS is a good choice for

scattering experiments to interpret the fibrillar structure more in depth. Previously, scattering of MC hydrogels showed no peaks or plateaus associated with a characteristic lengthscale, and scattering intensity decreased monotonically as q increases for MC samples between 40 and 70 °C as noted by Kobayashi et al,[20] (Figure 1.8). Furthermore, they found that the scattering intensities of MC hydrogels were equivalent when normalized by concentration. Previous reports[20,32] have only investigated a single M of MC, so one of the goals of this chapter was to compare SANS from different M of MC solutions and gels. Takahashi et al.[30] studied small-angle x-ray scattering of different M of MC hydrogels, but the actual data were not included in the publication. Additionally, the minimum q achieved by Takahashi et al. was 0.03 $Å^{-1}$, whereas with SANS the minimum q was 9×10^{-4} $Å^{-1}$ for the NG7 at NIST, and 5×10^{-3} $Å^{-1}$ for the CG2 at ORNL.

SANS for MC300, MC150, and MC530 samples can be seen in Figures 4.3, 4.2, and 4.4, respectively. These samples were incrementally heated for each measurement temperature, from 30 to 80 °C. Scattered intensity of MC solutions and gels arises from the difference scattering length density ($\Delta\rho$) between MC and the D_2O solvent.

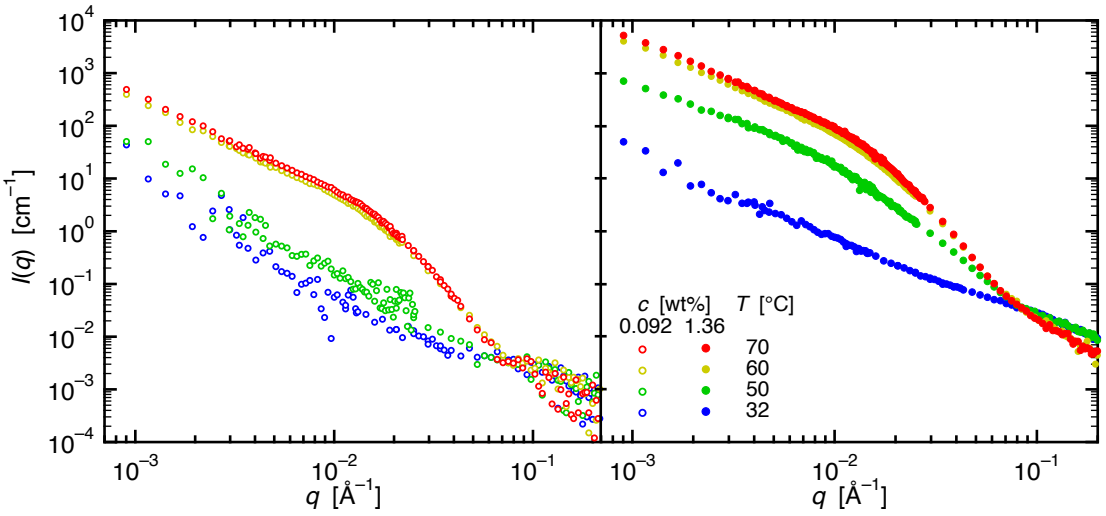

Figure 4.2: SANS of two concentrations (0.092 wt% on the left and 1.36 wt% on the right) in D_2O of MC300 gels at 32, 50, 60, and 70 °C . Reproduced with permission from Lott et al.[112], American Chemical Society copyright 2013.

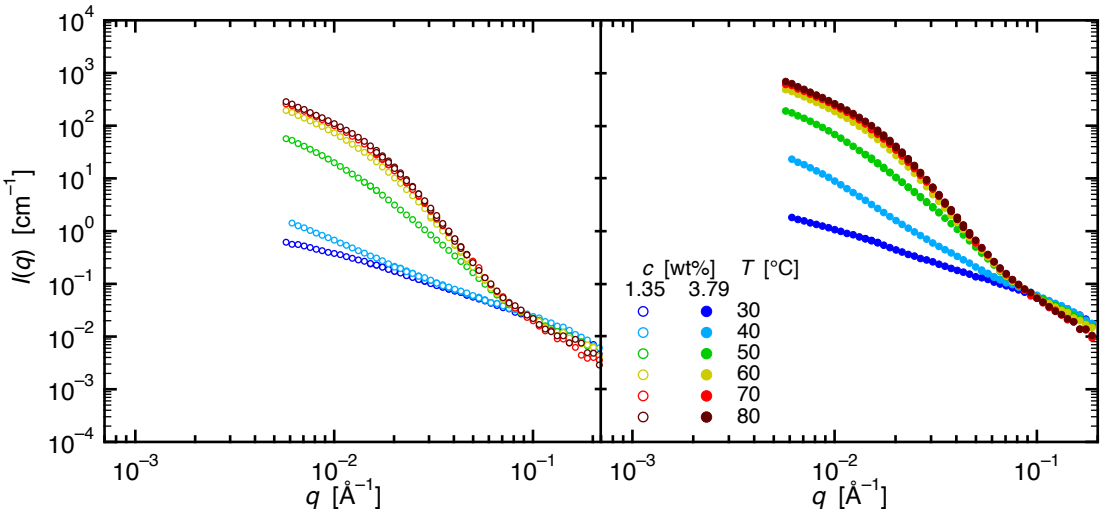

Figure 4.3: SANS of two concentrations (1.35 wt% on the left and 3.79 wt% on the right) in D_2O of MC150 gels at 32, 50, 60, and 70 °C . Reproduced with permission from Lott et al.[16], American Chemical Society copyright 2013.

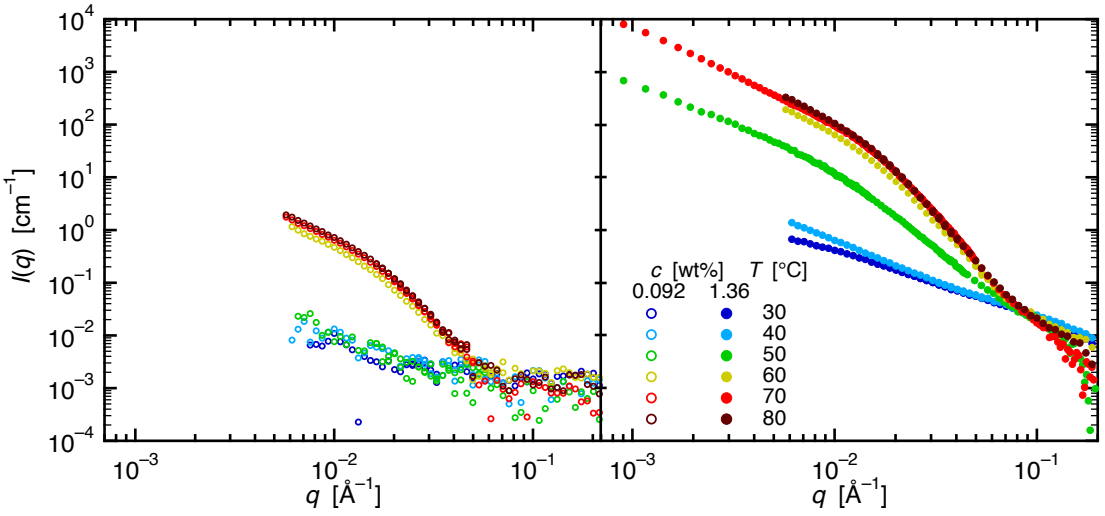

Figure 4.4: SANS of two concentrations (0.092 wt% on the left and 1.36 wt% on the right) in D_2O of MC530 gels at 32, 50, 60, and 70 °C . Reproduced with permission from Lott et al.[16], American Chemical Society copyright 2013.

At 30 °C scattering has a power slope of q^{-1} to $q^{-1.5}$ over the entire measured q range down to 9×10^{-4} Å^{-1}. With increased temperature, scattered intensity increases and a broad shoulder develops in the region $0.005 < q < 0.1$ Å^{-1}, which has two distinct regimes by 70 °C: Porod-like behavior of q^{-4} for $0.02 < q < 0.1$ Å^{-1}, and a power-law dependence of $q^{-1.7}$ for $q < 0.02$ Å^{-1}. Within the context of MC fibrils, the q^{-4} dependence of intensity for $0.02 < q < 0.1$ Å^{-1} is likely a result of the interface between the fibril and the solvent. Like the sol-gel transition, the development of the "fibril shoulder" is concentration dependent. In Figures 4.3 and 4.4, samples with a concentration of 0.092 wt% at 50 °C are below T_{gel} from Figure 3.17, all show very little change in $I(q)$ from 30 °C. Concentrations at 1.36 wt% or higher are near or above T_{gel} at 50 °C, and display the fibril shoulder. Intermediate temperatures between 30 and 70 °C were considered a transition from solution scattering (at low T), and as MC fibrils develop with increased T, the corresponding $I(q)$ shoulder grows. Temperatures at 70 °C and above show very little change in $I(q)$, which indicates at these lengthscales, MC hydrogels are not changing for heating past 70 °C. Scattering from five concentrations of MC300 at 70 °C is shown in Figure 4.5, and when $I(q)$ is normalized by solution

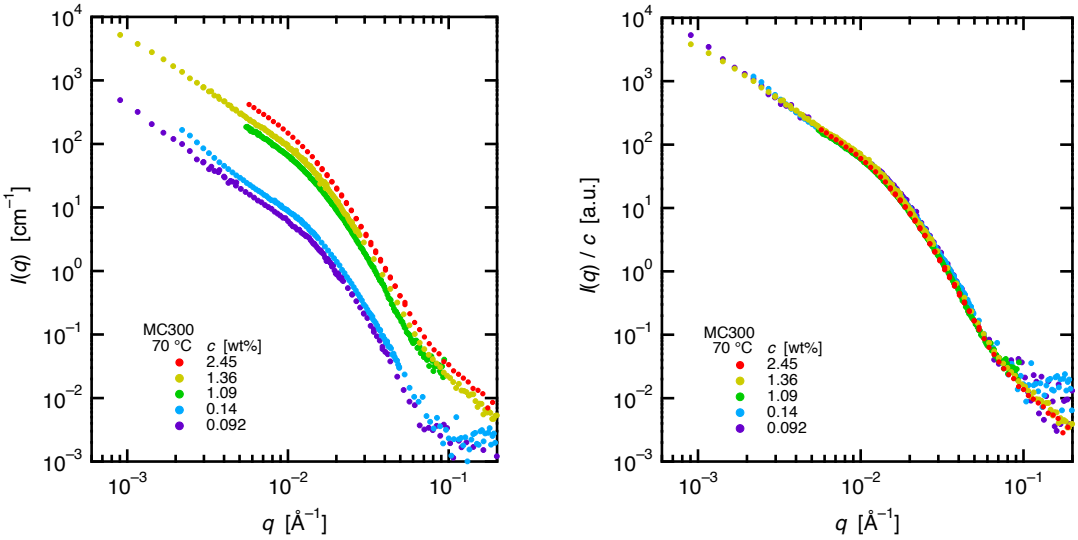

Figure 4.5: SANS of five concentrations of MC300 at 70 °C (left), and normalized by concentration (right). Some of the data reproduced with permission from Lott et al.,[16,112] American Chemical Society copyright 2013.

concentration, all scattering superposes onto a single curve. This was also noted by Kobayashi et al.[20] and indicates that the lengthscales contributing to the scattering, of MC hydrogels are independent of concentration, and that the increased $I(q)$ for more concentrated samples is only a result of more polymer present, which would be consistent with a fibrillar network with the mesh size larger than the minimum q.

The scattered intensity of three M of MC gels at 70 °C and a solution concentration of 1.36 wt% is shown in Figure 4.6. The data superpose, with no shifting of scattering intensity or wavevector. This property was also shown for much lower concentrations of MC with $c = 0.01$ wt%, which is a concentration that is too low for MC fibrils to percolate into a network.[112] Because the scattering of different molecular weights is the same for $0.0009 < q < 0.2$ Å^{-1} (corresponding to lengthscales between $5 - 500$ nm), this indicated that the structure of MC fibrils in the gel is independent of molecular weight as well as concentration. The self-similarity of MC hydrogels further distinguishes the fibrillar nature of MC hydrogels from a microphase separated "blob-like" structure (Figure 1.10) or viscoelastic phase separation (Figure

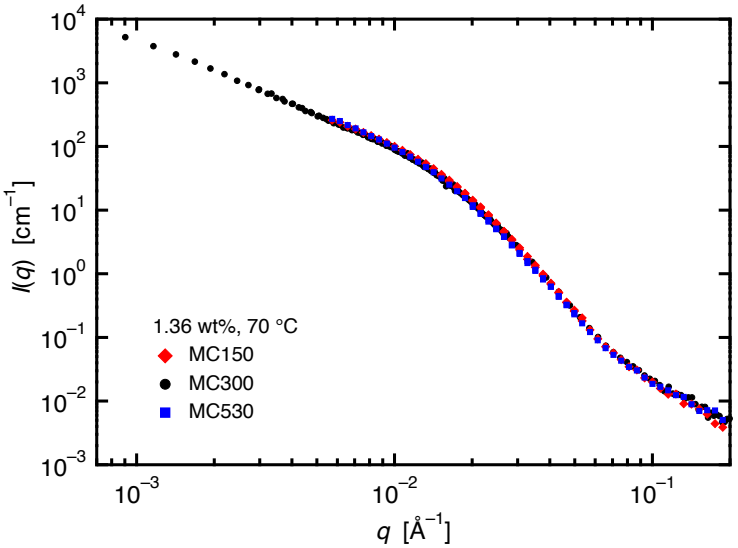

Figure 4.6: SANS of three molecular weights of MC with $c = 1.36$ wt% at 70 °C. Reproduced with permission from Lott et al.,[112] American Chemical Society copyright 2013.

1.11; both of which would have concentration and/or molecular weight dependence to their morphology.

4.2.3 USANS of MC Gels

The fibrillar structure noted in cryo-TEM images does notably itself explain the turbidity of MC hydrogels, which require scattering objects on the same lengthscale as the wavelength of visible light ($\lambda > 400$ nm). SANS begins to capture this lengthscale (near $q = 0.001$ Å^{-1}), and for all MC gels at 70 °C, there is no plateau at low q, with $I(q) \sim q^{-1.7}$. This could be expected, given the heterogeneity of the contour lengths of fibrils noted by cryo-TEM (100 nm to 1 μm). To expand the scope of scattering experiments, USANS measurements examined larger-scale features of the MC gels. Desmeared USANS data collected at 50 and then 70 °C for two MC samples are shown, along with the corresponding SANS curves in Figure 4.7. The overlap in the scattering curves from the two techniques is good, validating the USANS desmearing algorithm in addition to the absolute scaling of both sets of data. The combination of SANS and USANS provides a depiction of MC scattering over a broader q range. As q decreases, USANS data captures the same $q^{-1.7}$ behavior as observed in the SANS experiments for both MC300 and MC530 samples. At 50 and 70 °C, the MC300 samples display an upturn in slope (indicated by an arrow near $q = 3 \times 10^{-4}$ Å^{-1}), whereas no upturn is apparent in the MC530 sample. USANS indicates that MC hydrogels display heterogeneity in the fibril network which accounts for the turbidity of MC gels. The corresponding size scales of the upturn in $I(q)$ in MC300 are approximately 2 μm. Features of comparable size have been reported from FFT of optical micrographs[26] as well as light scattering[51] of aqueous MC. The fact that no plateau region is present at the lowest q range indicates that heterogeneities persist beyond the largest length scale accessed ($\approx$ 20 μm). The upturn in the USANS data adopt a $I(q) \sim q^{-3.5}$ dependence, which approaches Porod behavior. This may indicate that MC fibrils

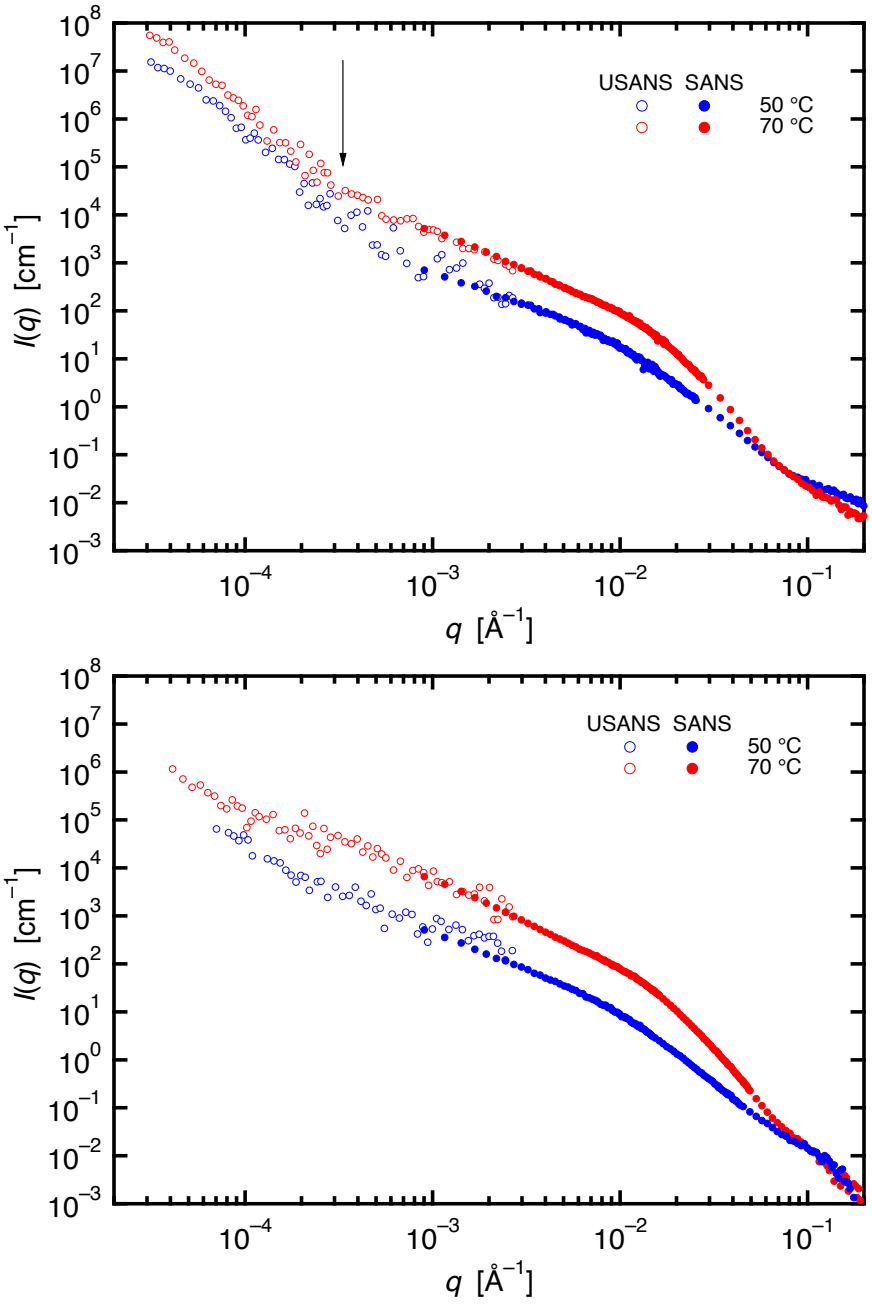

Figure 4.7: SANS (filled dots) and USANS (open dots) for 1.36 wt% solution of MC300 (top) and 1.24 wt% MC530 (bottom). Scattering was measured at 50 °C (blue) and 70 °C (red). The arrow on the MC300 plot indicates a change in power slope which is absent from the MC530 plot. USANS data have been desmeared to match intensities with SANS. Reproduced with permission from Lott et al.,[112] American Chemical Society copyright 2013.

aggregate into micron-sized "fibril-rich" and "fibril-poor" regions, and the Porod-like scattering reflects the interfaces between the two.

4.3 Analysis and Discussion

Based upon the fibrillar structure of MC hydrogels revealed by cryo-TEM in Figure 4.1, a model based upon the scattering of flexible cylinders in solution was chosen to fit to the SANS data presented in the previous section. The first part of this section includes a description of the model, and the fits to MC gels at 70 °C. The next part utilizes the absolute intensity of SANS in order to calculate amounts of MC and solvent contained within the fibrils. The section concludes with model fitting of MC solutions and gels using a linear combination of two models: one for semiflexible coils in solution, and the other the flexible cylinder model. The fraction of each model used in the fit gives an estimate to the fraction of MC fibrils in solution as the solution is heated, which correlates to the growth in modulus of MC hydrogels.

4.3.1 Modeling of SANS Data to a Flexible Cylinder Scattering Function

Pedersen and Schurtenberger[113] and also Chen et al.[114] developed a scattering function for flexible cylinders with excluded volume effects. The function is given by

$$I_{\mathrm{wc}}(q, L, b, R_{\mathrm{cs}}) = \phi_{\mathrm{cyl}}(\Delta\rho)^2 \Big\langle P_{\mathrm{cs}}(q, R_{\mathrm{cs}}) \Big\rangle Y_{\mathrm{wc}}(q, L, b) + BD \tag{4.1}$$

where q is the wavevector, L is the contour length of the fibril, b is the Kuhn length of the fibril, R_{cs} is the radius of the cross section of the fibril, ϕ_{cyl} is the volume fraction of fibrils, $\Delta\rho$ is the contrast in scattering length density between the fibrils and the solvent, and BD is a background correction term. The principle of the function rests on the assumption that $L \gg R_{\mathrm{cs}}$ and the respective scattering contributions can be

decoupled into the product of a cross-sectional form factor (P_{cs}) and a longitudinal form factor (Y_{wc}). Scattered intensity $I_{wc} \sim \phi_{cyl}(\Delta\rho)^2$, and requires the volume fraction and scattering length density of *fibrils*, not MC molecules, to interpret the absolute scattering intensity.

The function $P_{cs}(q, R_{cs})$ is the scattering function for the cross-section of a rigid rod[114] given by

$$P_{cs}(q, R_{cs}) = \left[\frac{2J_1(qR_{cs})}{qR_{cs}}\right]^2 \tag{4.2}$$

where $J_1(x)$ is the Bessel function of the first kind. The cross sectional term in Equation 4.1 also accounts for the dispersity in radii:

$$\Big\langle P_{cs}(q, R_{cs})\Big\rangle = \frac{\int N_{sz}(R_{cs})\, R_{cs}^2\, (P_{cs}(q, R_{cs}))\, dR_{cs}}{\int N_{sz}(R_{cs})\, R_{cs}^2\, dR_{cs}} \tag{4.3}$$

$$N_{sz}(R_{cs}) = \left(\frac{z+1}{\overline{R_{cs}}}\right)^{z+1} \exp\left[\frac{-R_{cs}(z+1)}{\overline{R_{cs}}}\right] \frac{R_{cs}^z}{\Gamma\,(z+1)} \tag{4.4}$$

where $N_{sz}(R_{cs})$ is a Schultz distribution of cylinder radii,[115] the mean cylinder radius given by $\overline{R_{cs}}$, Γ is the gamma function, and the width of the distribution described by z. Most lengthscale measurements using scattering have a distribution in characteristic lengths given in Equation 4.4, which is called the z-average.[27] The scattering function $Y_{wc}(q, L, b)$ was developed for worm-like chains defined by Kratky and Porod[116] with excluded volume effects included. As this function has no analytical solution a Monte Carlo simulation was utilized to provide a parameterized function for $Y_{wc}(q, L, b)$. The details for this calculation were developed by Chen et al.,[114] and were also reported in Lott et al.[112] From the cryo-TEM images, it was apparent that L was too large to be fully captured by the SANS data, so for the modeling of MC fibrillar gels, it was set arbitrarily large and effectively not used as a fitting parameter. This leaves five parameters to fit the SANS data to Equation 4.1: R_{cs}, z, b, ϕ_{cyl} and ρ_{cyl}.

In the fitting of SANS data to Equation 4.1, R_{cs} and z are determined by the function for cross-sectional area (Equations 4.2 through 4.4), and b is determined by the numerically solution to the function for a Kratky-Porod worm-like chain. ϕ_{cyl} and ρ_{cyl} arise from the magnitude of the absolute scattering, so the dimensions of MC fibrils can be fit with only three parameters: R_{cs}, z, and b, and can be given by

$$I_{wc}(q, L, b, R_{cs}) \sim \Big\langle P_{cs}(q, R_{cs}) \Big\rangle Y_{wc}(q, L, b) + BD \tag{4.5}$$

Initial guesses for R_{cs} were made using the dimensions of the fibrils in the cryo-TEM images, and Figure 4.8 shows the form factor for cross-section of rigid rods, $P_{cs}(q, R_{cs})$ (Equations 4.2 and 4.3) with $R_{cs} = 7.5$ nm fitted to scattering from a MC300 sample with $c = 1.36$ wt% at 70 °C. Figure 4.8 also displays the need for the radial dispersity term z to the fit, since SANS data for MC gels do not display

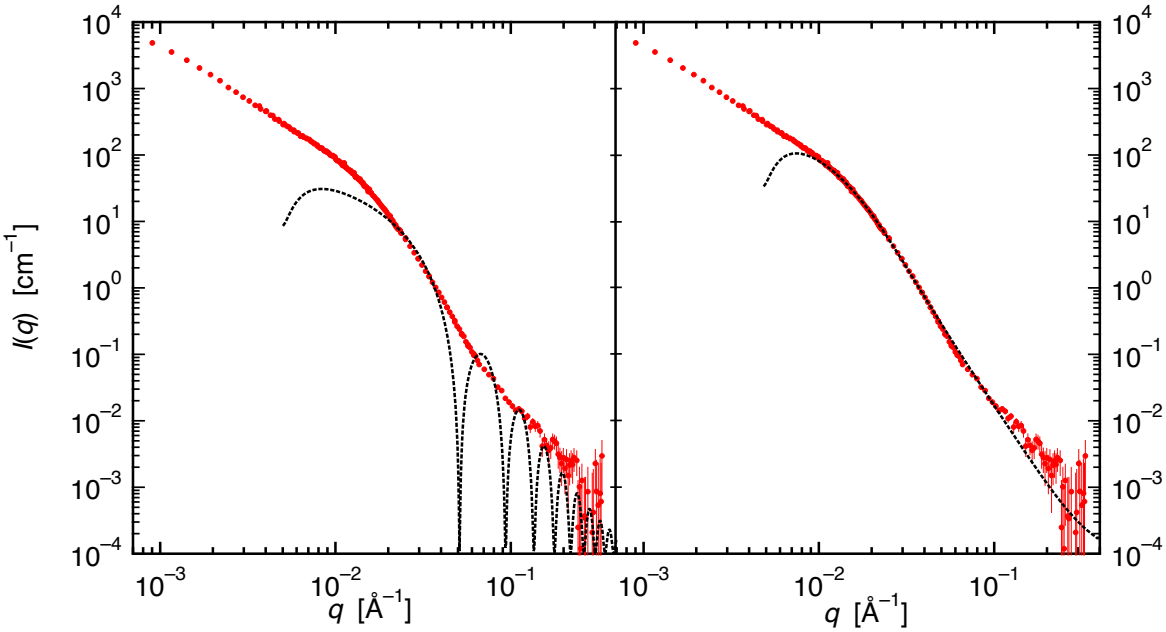

Figure 4.8: SANS for a 1.36 wt% solution of MC300 at 70 °C with the cross-sectional cylinder form factor $P_{cs}(q, R_{cs})$, (Equation 4.2) and the form factor including the dispersity in radii, $\langle P_{cs}(q, R_{cs}) \rangle$, (Equation 4.3). Cylinder diameter was guided by cryo-TEM images, $R_{cs} = 7.5$ Å^{-1} for both plots. The distribution in cylinder radii was given by $z = 0.5$ for the right plot.

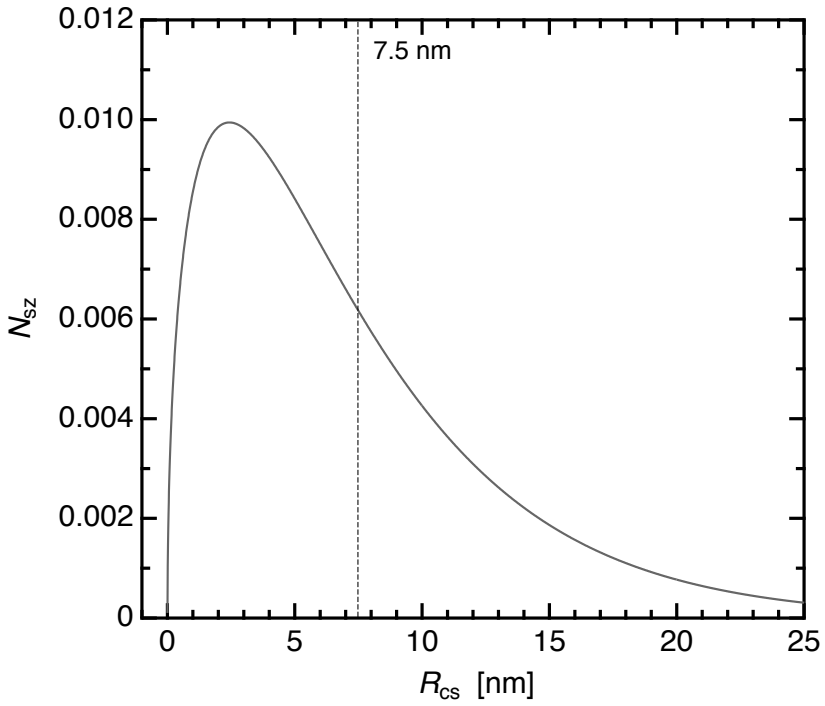

Figure 4.9: A Schultz distribution of R_{cs} given by Equation 4.4, with $R_{cs} = 7.5$ nm and $z = 0.5$.

any sign of oscillatory decay peaks from the Bessel function. The distribution of R_{cs} given by Equation 4.4 with $z = 0.5$ can be seen in Figure 4.9. The value $z = 0.5$ should be interpreted lightly, as there are a number of factors which can smear out the Bessel peaks in SANS data in addition to the simple distribution in R_{cs}. One is the distribution in neutron wavelengths ($\Delta\lambda/\lambda \approx 10\%$) which creates smearing in the neutron scattering. The fitting of SANS data to Equation 4.1 did not include smearing in order to simplify the model. Another cause for the smearing of Bessel peaks is the possible existence of fibril junctions. The cryo-TEM images in Figure 4.1 are unclear as to whether trifunctional fibril junctions are present in the gels, but their presence could significantly contribute varying lengthscales to the scattering to make individual peaks indistinguishable. Perhaps most significantly, Bessel peaks may not be visible due to scattering contributions from sub-fibril structures (with possibly a variety of lengthscales) which are not apparent from the SANS data presented here.

The flexible cylinder model makes the assumption that the fibrils are uniform, and for simplicity all deviations from ideal scattering suggested by Equation 4.1 are lumped together into the parameter z.

The wavevector associated with the "fibril shoulder" noted in Figures 4.5 and 4.6 arises from the term R_{cs}, and the break in slope near 0.015 Å^{-1} would be shifted to smaller q if the cylinder radius increases. The Kuhn length of the flexible cylinder, b, arises from the power slope at $q < 0.015$ Å^{-1}, and the power slope of $q^{-1.7}$ will decrease if the Kuhn length of the flexible cylinder increases. Though it was not a parameter that was utilized in the fitting of MC gels, the contour length term L, defines the wavevector at which the $I(q) \rightarrow I(0)$ with a plateau associated with the longest lengthscale in Equation 4.1 and 4.5. Model fits to Equation 4.5 for five concentrations of MC300 at 70 °C are shown in Figure 4.10, and Figure 4.11 shows the best fit for three M with a $c = 1.36$ wt% at 70 °C. The fit to SANS data over the measured q-range from $9 \times 10^{-4} < q < 0.1$ Å^{-1} is very good. $I(q) \sim q^{-4}$ in the range

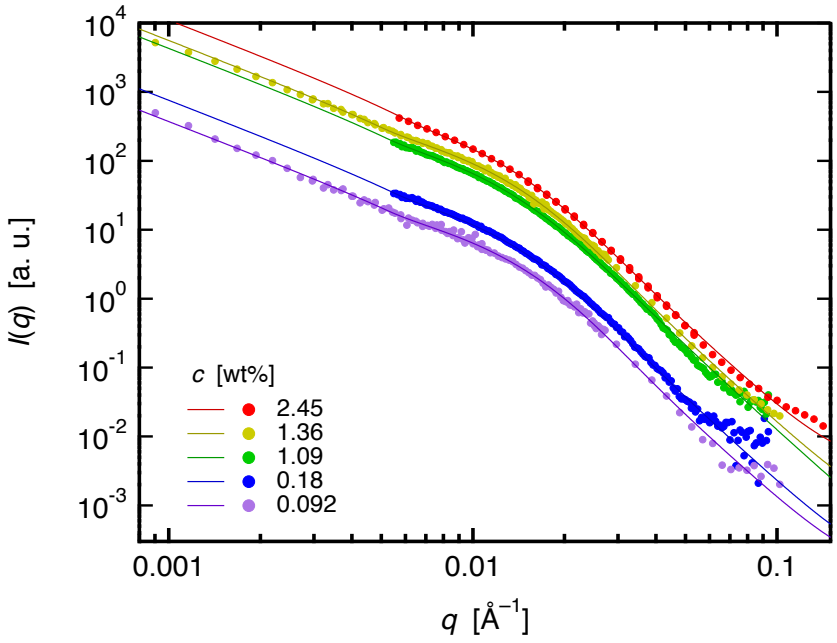

Figure 4.10: Flexible cylinder model fits to SANS of five concentrations of MC300 at 70 °C. Reproduced with permission from Lott et al.,[16,112] American Chemical Society copyright 2013.

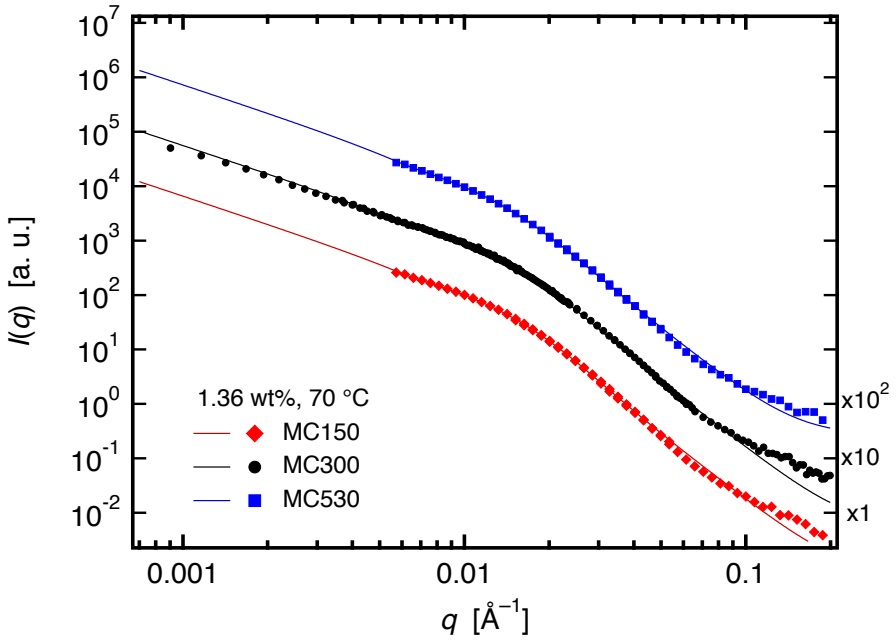

Figure 4.11: Flexible cylinder model fits to SANS of three molecular weights of MC with $c = 1.36$ wt% at 70 °C. Scattering data and model fits for MC300 and MC530 have been vertically shifted by a factor of 10 and 100, respectively to aid with visual clarity. Reproduced with permission from Lott et al.,[112] American Chemical Society copyright 2013.

$0.02 < q < 0.1$ Å^{-1}, which indicates scattering at the interface between the fibril and solvent.

Values for R_{cs}, z, and b for numerous concentrations and M can be found in Table 4.1. The average fibril dimensions for all three molecular weights and $0.01 < c < 3.79$ wt% were found to be $R_{cs} = 7.2 \pm 0.4$ nm, $z = 0.53$, and $b = 55 \pm 5$ nm. The fitting of MC gels to Equation 4.5 is consistent with the preliminary interpretations that the gel structure is independent of concentration and molecular weight: the parameters in Table 4.1 indicate uniform fibril dimensions in MC hydrogels. This confirms that the fibrillar structure is a property inherent to the polymer backbone and repeat units in MC, and not concentration or molecular weight.

Table 4.1: MC fibril dimensions obtained from fits to Equation 4.5 for Kuhn length (b), cylinder radius (R_{cs}), and Schultz dispersity of radii (z).

Sample	c [wt%]	ϕ	T [°C]	b [nm]	R_{cs} [nm]	z
MC150	1.36	0.0112	70	54	7.6	0.49
	1.36	0.0112	80	72	7.7	0.48
	1.36	0.0113	90	66	7.8	0.47
	3.79	0.0312	70	53	7.5	0.48
	3.79	0.0313	80	58	7.6	0.48
	3.79	0.0315	90	52	7.6	0.47
MC300	0.03	0.00025	70	50	6.9	0.57
	0.09	0.00074	70	58	6.8	0.52
	0.17	0.00139	70	51	6.8	0.53
	0.17	0.00139	70	55	6.5	0.56
	0.17	0.00139	70	57	6.9	0.54
	0.17	0.00141	90	55	6.6	0.51
	0.18	0.00147	70	57	7.4	0.50
	0.18	0.00148	75	58	7.3	0.50
	0.45	0.00368	65	58	6.9	0.57
	1.09	0.00894	70	59	6.7	0.58
	1.09	0.00895	75	61	6.7	0.58
	1.26	0.0103	70	50	7.4	0.51
	1.36	0.0112	70	61	7.0	0.54
	2.45	0.0201	70	52	6.9	0.58
	2.45	0.0202	80	51	7.9	0.48
	2.45	0.0203	90	51	7.6	0.51
MC530	0.01	0.00008	70	49	6.7	0.51
	0.01	0.00008	80	49	6.3	0.55
	0.01	0.00008	90	46	6.7	0.51
	1.26	0.0103	70	56	7.0	0.59
	1.36	0.0112	70	54	7.7	0.54
	1.36	0.0112	80	48	7.5	0.57
	1.36	0.0113	90	45	7.4	0.58
Average (± 1 Std. Dev.)				55 ± 5	7.2 ± 0.4	0.53

4.3.2 Calculation of the Water Content within MC Fibrils

An advantage to SANS is that the scattered intensity $I(q)$ is absolute, rather than relative (as is often the case with small-angle x-ray scattering), and this was used to investigate the internal composition of fibrils in MC gels. A preliminary assumption could be made of the terms for the volume fraction of cylinders, ϕ_{cyl}, and scattering length density of cylinders, ρ_{cyl} such that $\phi_{\text{cyl}} = \phi_{\text{MC}}$ and $\rho_{\text{cyl}} = \rho_{\text{MC}}$ (i. e. the fibrils consist of only MC and no solvent). When Equation 4.1 is plotted, using $\rho_{\text{cyl}} = \rho_{\text{MC}} = 1.293 \times 10^{-6}$ Å^{-2} and a fixed $\rho_{D_2O} = 6.335 \times 10^{-6}$ Å^{-2} for D_2O,[93] with the parameters b, R_{cs}, and z from the fitting to Equation 4.5, the predicted scattering consistently *overestimates* the actual scattering, as can be seen in Figure 4.12. This overestimation is the consequence that $\phi_{\text{cyl}} > \phi_{\text{MC}}$, and that the contrast between cylinders and solvent is less than it would be if the fibrils contained 100% MC.

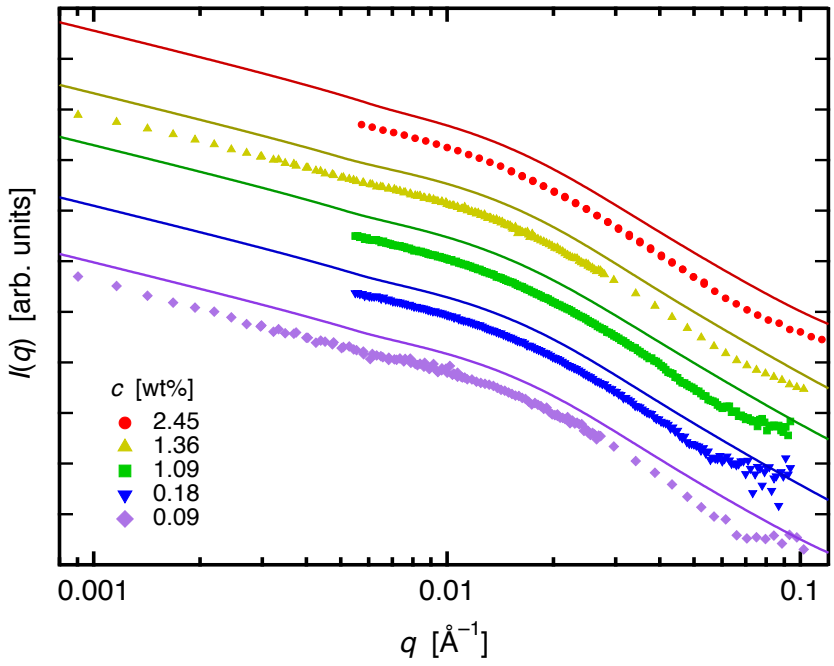

Figure 4.12: Flexible cylinder model fits (lines) to SANS of MC300 gels at 70 °C (points). Lines were predicted using Equation 4.1 assuming that $\rho_{\text{cyl}} = \rho_{\text{MC}}$ and $\phi_{\text{cyl}} = \phi_{\text{MC}}$, and the fibrils contain 100% MC. Each data set and model curve have been vertically shifted by the same amount to aid in clarity of viewing. Reproduced with permission from Lott et al.,[112] American Chemical Society copyright 2013.

In order to estimate the amount of solvent within MC fibrils, the assumption is made that all of the MC molecules in sample are present as fibrils. The temperature of 70 °C was chosen as the temperature at which all MC molecules have been incorporated into fibrils. The basis for this choice rested on a number of factors. First, previous studies of ^{1}H NMR on MC samples tracked methyl proton dynamics during the course of gelation, several groups have found the signal to disappear in the vicinity of 70 °C, indicating the immobilization of the protons.[18,32] Second, this is the lowest temperature for which SANS traces superpose after normalization for concentration (Figure 4.5). Finally, this is also the temperature at which the rheological properties and turbidity begin to plateau. Thus, 70 °C is an appropriate temperature for a "fully developed" gel state. Li also reached a similar deduction, based upon DMS frequency sweeps and differential scanning calorimetry (DSC) measurements.[23]

Absolute scattered intensity in Equation 4.1 scales with the product of the volume fraction of scatterers and the difference in scattering length density squared,

$$I_{\mathrm{wc}}(q) \sim \phi_{\mathrm{cyl}}(\Delta\rho)^2 \tag{4.6}$$

From Figure 4.12, it is apparent that the cylinders contain both MC and solvent, so the amount of polymer contained in the fibrils can be expressed as

$$\phi_{\mathrm{cyl}} = \frac{\phi_{\mathrm{MC}}}{x} \tag{4.7}$$

where x is the fraction of MC contained within the fibril. The scattering length density of the mixed-component cylinder (ρ_{cyl}) is equal to the volumetric average of ρ_{MC} and $\rho_{\mathrm{D_2O}}$:

$$\rho_{\mathrm{cyl}} = x\rho_{\mathrm{MC}} + (1-x)\rho_{\mathrm{D_2O}} \tag{4.8}$$

The square of the contrast between the cylinder and surrounding solvent is given by

$$(\Delta\rho)^2 = \left((x\rho_{\mathrm{MC}} + (1-x)\rho_{\mathrm{D_2O}}) - \rho_{\mathrm{D_2O}}\right)^2 = x^2(\rho_{\mathrm{MC}} - \rho_{\mathrm{D_2O}})^2 \tag{4.9}$$

Table 4.2: Fraction x of MC within fibrils, calculated from the ratio between SANS data for MC samples at 70 °C and Equation 4.1, assuming fibrils contain 100%. Reproduced with permission from Lott et al.[112], copyright 2013 the American Chemical Society.

Sample	c [wt%]	ϕ	x
MC150	1.36	0.0112	0.49 ± 0.02
	3.79	0.0312	0.46 ± 0.01
MC300	0.03	0.00025	0.24 ± 0.04
	0.09	0.00074	0.38 ± 0.05
	0.17	0.00139	0.40 ± 0.07
	0.18	0.00141	0.43 ± 0.05
	0.45	0.00368	0.36 ± 0.05
	1.09	0.00895	0.36 ± 0.03
	1.26	0.0103	0.38 ± 0.02
	2.45	0.0201	0.38 ± 0.02
MC530	0.01	0.00008	0.47 ± 0.09
	1.26	0.0103	0.398 ± 0.008
	1.36	0.0112	0.41 ± 0.01
Average			0.40 ± 0.05

Combining Equations 4.7 and 4.9 into Equation 4.6 gives

$$I_{\mathrm{wc}}(q) \sim x\, \phi_{\mathrm{MC}}\, (\rho_{\mathrm{MC}} - \rho_{\mathrm{D_2O}})^2 \tag{4.10}$$

Therefore, the ratio between the measured SANS (points) and the predicted scattering (lines) in Figure 4.12 for the range $0.0009 < q < 0.1$ Å^{-1} gives x. Values of x can be found in Table 4.2, with an average of $x = 40 \pm 5\%$. The MC content within fibrils was found to be consistent across multiple concentrations and M, further corroborating that the structure of MC fibrils is independent of concentration and molecular weight.

The finding that water occupies more than half of the volume of the fibrils indicates there may be different modes of binding between the water within the interior of the fibril and the water that makes up the vast (>95%) majority of the gel outside

the fibril. Since MC is hygroscopic in nature, several groups have studied hydration and swelling properties as well the binding of water to MC powders, films, and gels.[19,117–122] Because of the heterogeneous substitution of the MC chains, many types of water-polymer interactions are possible. Fourier transform infrared (FT-IR) spectroscopy measurements have revealed a number of water-water and water-polymer interactions, among them water-polymer hydrogen bonds. In a simple approximation, the binding state of a particular water molecule to the MC chain can be described by one of two states: free and tightly bound. DSC measurements can determine the amount of free water by measuring the portion of the water in the sample that is able to freeze at low temperatures. Water that is tightly bound to the polymer chain lacks the mobility required to freeze, so the population that is tightly bound will not contribute to the thermal event recorded in DSC thermograms. Using this approach, several groups have calculated the stoichiometry of the fully hydrated solution state and found that there are 5-6 mol of water bound per mole MC repeat unit.[117,122] If free water in the solution is disregarded and a system is considered only to contain the tightly bound water molecules and the polymer chains, the resulting volume fraction of MC would be approximately 60%. While the SANS data presented here give no indication as to whether solvent within the fibrils is "bound" to MC or not, given the large excess of water in the gels (>95% solvent), it is interesting to note that the ratio of tightly bound water to polymer at low temperatures is similar to the ratio of solvent to polymer within each fibril, at high temperatures in the gel state.

Notably absent from this analysis of fibril composition is the specific morphology of how MC chains are packed into fibrils. The fact that the fibrils consist of approximately 40% MC and 60% water is an important clue to the internal structure of fibrillar MC gels. Bodvik et al. also captured cryo-TEM images of MC gels, and postulated that the chain backbones are ordered parallel to one another within the fibril.[31] However, this geometry offers no clear explanation as to why the fibril diameter is consistent across a large concentration range. The well-defined diameter

could be the result of chain folding such that the backbones are on average perpendicular to the fibril axis, yet this could result in sheets rather than fibrils. A third possibility is that the chains adopt a helical conformation so that the helical radius dictates the fibril diameter. This hypothesis is supported by the fact that the fibril diameter of 15 nm is very similar to the Kuhn length for dilute MC chains in water (16 ± 3 nm),[123,124] and Haque and Morris measured the depolarization of visual light on heating and cooling.[18] That the optical rotation of MC solution changes on heating indicates that the cellulose backbone undergoes conformational rearrangement on heating resulting in a change in overall chirality of the chains. Possibilities for the internal structure of MC fibrils will be discussed further in Chapter 6.

4.3.3 MC Fibril Development and Gelation

Up to this point, SANS of MC gels only has been examined. This section considers the solution scattering of MC, and the transition to a gel upon heating. Both cryo-TEM and SANS taken at low temperatures (solution state) show no trace of fibrillar structures.[16,112] The shoulder at $q \approx 0.015$ Å^{-1} seen for MC gels is not present in the scattering profile for the solutions. The nature of these curves at low-q obeys a power-law behavior previously noted by Chatterjee et al.[32] To model solution behavior of MC, they employed an empirical model to fit the SANS data:

$$I(q) = aq^{-m} + \frac{I(0)}{1 + q^2\xi^2} + BD \tag{4.11}$$

where the aq^{-m} captures the power-slope behavior at low-q, an Ornstein-Zernike term to provide a correlation length (ξ) between molecules in a solution, and BD is a background term. While there are likely better choices to model SANS of semiflexible coils in solution,[113] this simple model was used only to provide a baseline solution response to compare SANS of intermediate temperatures. As the temperature is increases, SANS curves increase in intensity and the fibril shoulder at $q \approx 0.015$ Å^{-1}

develops.

Previous cryo-TEM results showed that at pregel temperatures (55 °C) a very small amount of fibrils form that have the same diameter of 15 nm.[112] With this in mind, it was hypothesized that the scattering at intermediate temperatures was result of a combination of two components: fibrils with the same composition and dimension as found at 70 °C, and free chains with the same characteristics as found at low temperatures (25 °C). A linear combination of the solution (Equation 4.11 and gel-state scattering (Equation 4.1) functions to fit the data at intermediate temperatures estimated the relative fractions of the polymer in each state. Thus the progression of fibril growth with temperature for aqueous MC materials can be quantitatively modeled.

Figures 4.13 and 4.14 show a progression of SANS on heating (left) and cooling (right) for 1.09 wt% and 0.18 wt% solutions of MC300, respectively. The solid lines

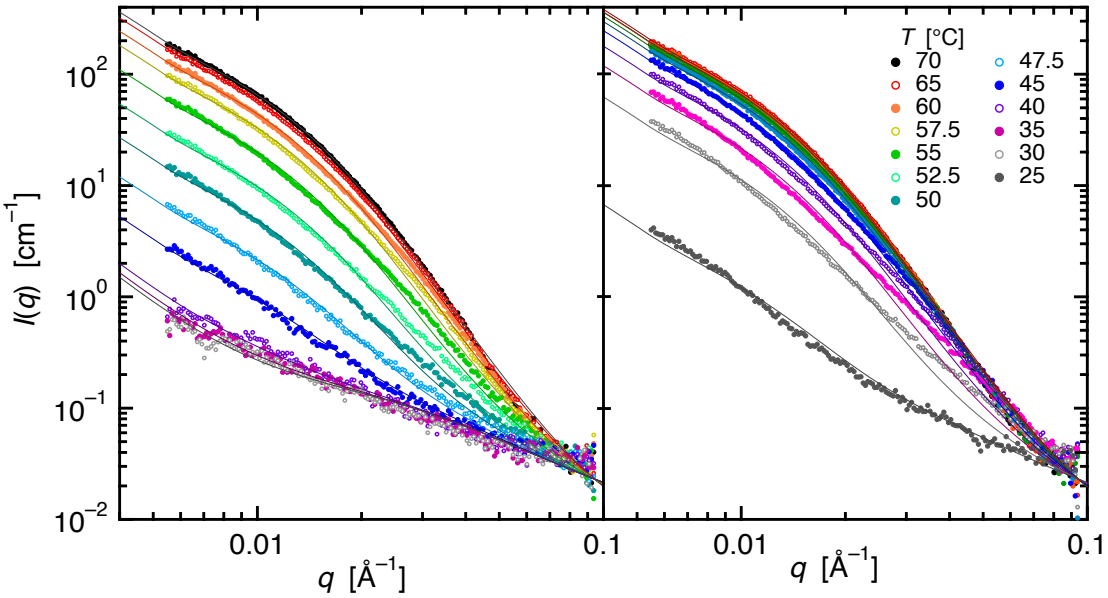

Figure 4.13: Fits to a linear combination of flexible cylinder and coil models on heating (left) and cooling (right) of a 1.09 wt% sample of MC300. Reproduced with permission from Lott et al.,[112] American Chemical Society copyright 2013.

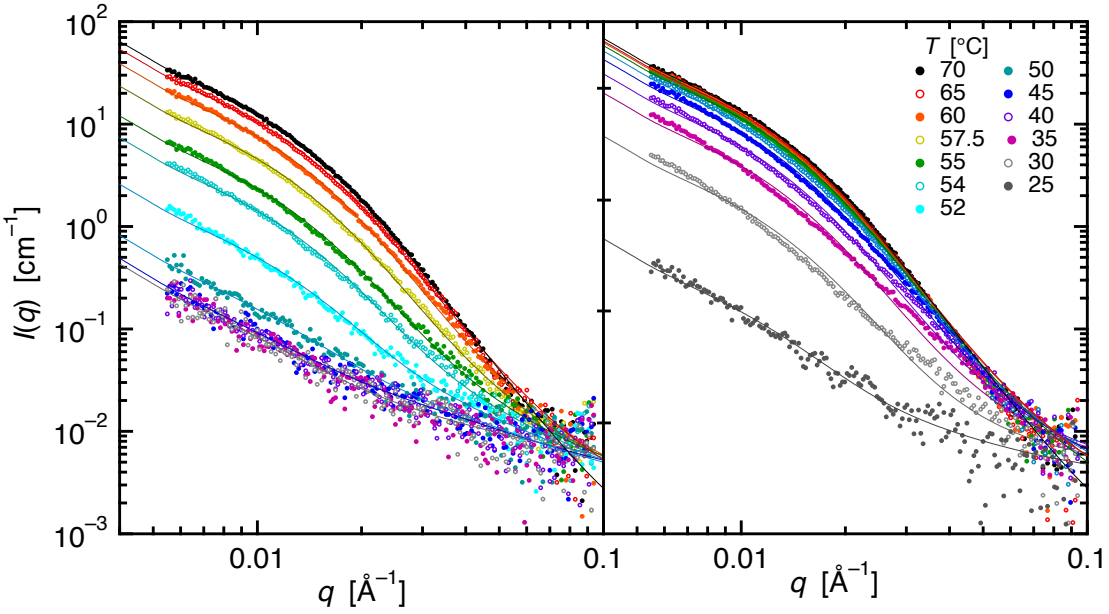

Figure 4.14: Fits to a linear combination of flexible cylinder and coil models on heating (left) and cooling (right) of a 0.18 wt% sample of MC300.

represent the best fits to the data; the highest temperature trace was fit using Equation 4.1, the lowest temperature trace was fit using eq 4.11, and the intermediate temperatures were fit using linear combinations of the two. The linear combination of the solution and gel-state scattering functions provides a good fit to all temperatures between 25-70 °C on heating and cooling. The balance between solution and gel scattering required to approximate the scattering data at intermediate temperatures gives the fraction of polymer of the sample that has been incorporated into the fibril state at a given temperature.

Like the sol-gel transition of MC on heating and cooling, SANS on heating and cooling display hysteresis and there is a strong resemblance between the storage modulus G' and the fraction of Equation 4.1 used to fit intermediate temperatures between 25-70 °C, which can be seen in Figure 4.15. The axis labeled "fraction of MC in fibrils" reports a number between 0 and 1 which indicates the fraction of the flexible

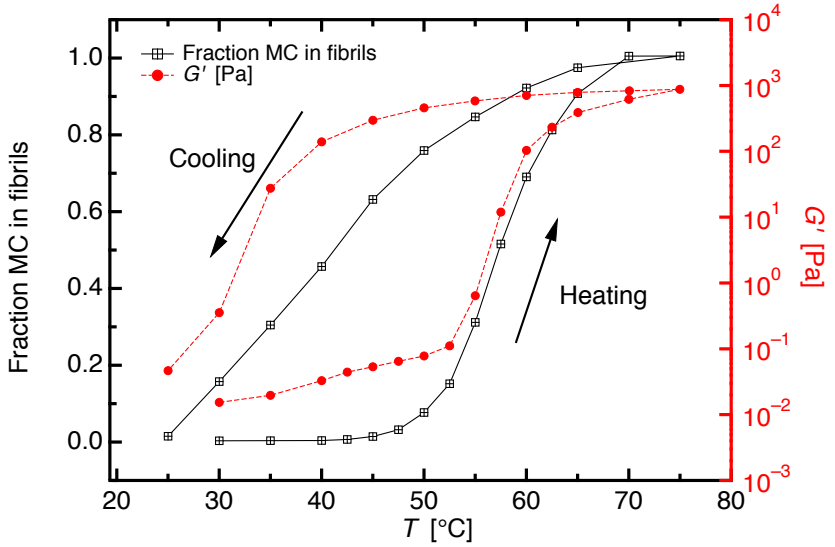

Figure 4.15: Fraction of the total polymer chains that are incorporated into fibrils (black squares) as calculated by taking linear combinations of the solution (25 °C) and gel (70 °C) SANS curves for a MC300 solution with a mass fraction of 1.09%. Storage modulus (red circles) for a MC300 sample with a mass fraction of 1.09% measured using a thermal history to match the SANS experiment with $\omega = 1$ rad s^{-1} and $\gamma_0 = 5\%$. In both traces, connecting lines are provided to guide the eye.

cylinder model used to fit the SANS data in Figure 4.13, which is compared to values of storage modulus G' (with $\omega = 1$ rad s^{-1} and $\gamma_0 = 5\%$) on heating and cooling at approximately the same rate as data collection on the SANS instrument by performing a series of frequency sweeps. Figure 4.15 shows hysteresis on heating an cooling for both experiments, and the agreement confirms that the gelation MC is a direct result of the fibrillar network structure. The scaling of the G' axis in Figure 4.15 is somewhat arbitrary, yet the connection between gel modulus and the fraction of MC in the solution containing fibrils is evident.

4.4 Summary

A fibrillar gel structure was found to dominate MC solutions at elevated temperatures using cryo-TEM and SANS. At low temperatures ($T \leq 30$ °C) no fibrils were detected, and at high temperatures ($T \geq 70$ °C), fibrils dominated the sample. SANS data was

modeled using a flexible cylinders model, to give dimension of the fibrils which are independent of M_w or c. The fibrils have diameters and Kuhn lengths of roughly 15 and 50 nm, respectively. It was found that the fibrils contain a significant portion of water and that MC occupies about 40% of the total volume of the fibril, and that the growth of modulus of MC upon heating directly correlates to the presence of fibrils in the system.

Chapter 5

Mechanical Response of MC Hydrogels[i,ii]

5.1 Introduction

Armed with the characterization of fibrils by small-angle neutron scattering from the previous chapter, this chapter returns to the mechanical properties of MC hydrogels. The discovery that MC hydrogels consist of a network of aggregated filament represents a departure from previous interpretations of rheological experiments, where a network of entangled chains has been used to describe the MC hydrogel structure.[18,21–23,30,33,43] In Chapter 4 it was shown that MC solutions associate into remarkably uniform fibrils on heating, with a diameter of 15 ± 2 nm that is independent of MC molar mass or concentration. This chapter investigates dynamic mechanical spectroscopy of MC hydrogels in the linear viscoelastic regime (LVE) and also the nonlinear viscoelastic regime (NVLE), which can be described in terms of an established model for a network of filamentous elastic gels originally developed

[i]Adapted with permission from Arvidson, S. A.; Lott, J. R.; McAllister, J. W.; Zhang, J.; Bates, F. S.; Lodge, T. P.; Sammler, R. L.; Li, Y.; Brackhagen, M. *Macromolecules* **2013**, *46*, 300-309. Copyright 2013 American Chemical Society.

[ii]Adapted with permission from McAllister, J. W.; Lott, J. R.; Schmidt, P. W.; Bates, F. S.; and Lodge, T. P. *ACS Macro Letters* **2015**, *4*, 538-542. Copyright 2015 American Chemical Society.

for protein hydrogels like fibrin and actin. Additionally, large-amplitude oscillatory shear (LAOS) of MC hydrogels was investigated, and the shape of the oscillatory strain response provides insight into the interactions and connectivity of MC fibrils.

5.2 Results

This section is arranged from low applied stress amplitude (σ_0) using small-amplitude oscillatory shear (SAOS) to probe the LVE regime, and steadily increasing σ_0 into the NVLE regime using LAOS. All experiments were performed using stress-controlled rheometers (see Section 2.3.1), in which a sinusoidal stress $\sigma(t)$ with amplitude σ_0 is applied to a sample, and the oscillatory strain response $\gamma(t)$ is recorded. Experiments included measurements of the hot-gel modulus of MC hydrogels, stress sweeps to illustrate the onset of shear hardening as the gels develop, measurements of normal stresses, and LAOS measurements.

5.2.1 MC Hot Gel Modulus

Figure 5.1 shows the storage modulus G' for MC of numerous c and M at 80 °C, taken at a frequency of $\omega = 1\ \mathrm{rad\,s^{-1}}$ and $\gamma_0 = 5\%$ (SAOS, in strain-control mode). The modulus of MC hydrogels scale as $G \sim \phi^{2.27}$, independent of M. Figure 5.1 also contains the entanglement modulus of poly(vinyl acetate) (PVAc) in toluene,[125] in which $G' \sim \phi^{2.35}$, and also poly(ethylene oxide) (PEO) in 1,4-dioxane,[126] in which $G' \sim \phi^{2.35}$. It may be tempting to infer from Figure 5.1 that because all three materials, PVAc, PEO, and MC have a similar scaling of modulus, they have similar network structures which determine the gel modulus, as many previous researchers have concluded.[18,21–23,30,33,43]

In order to determine if the fibrillar structure noted in Chapter 4 is a dominant contributor to the gel modulus it is useful to consider the simplest scenario of gelation:

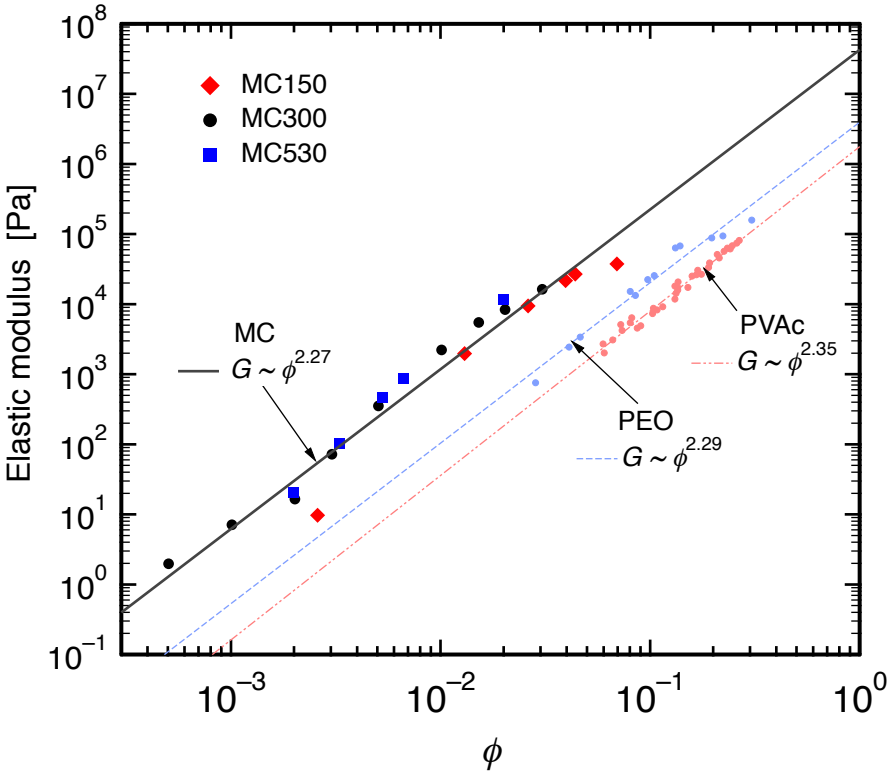

Figure 5.1: Elastic modulus (G') of MC hydrogels at 80 °C plotted versus volume fraction. Solid line corresponds to combined best fit of three Ms. Also shown is the elastic modulus of swollen networks of poly(vinyl acetate) (PVAc) in toluene[125] and poly(ethylene oxide) (PEO) in 1,4 dioxane.[126] MC data reproduced with permission from Arvidson et al.[52] Copyright 2013 the American Chemical Society.

that the gel is a solvent-swollen network of entangled chains. As developed by de Gennes,[127] for a swollen entangled network of individual polymer chains. The shear modulus G is given by,

$$G \approx k_{\mathrm{b}}T(v^{3/4}a^{3/2})\phi^{9/4} \tag{5.1}$$

where v is the volume of the network without polymer chains, and a is the distance between repeat units in space (not end-to-end distance). Equation 5.1 is primarily used as a scaling relationship, $G \sim \phi^{9/4}$, and agrees nicely with each of the polymers in Figure 5.1. Experimentally, scaling exponents between 2.0 and 2.5 have

been reported.[128–130] In order to differentiate MC hydrogels from other swollen polymer networks, an extrapolation to $\phi = 1$ approximates the elastic modulus for the entangled melt of each material, with $G_e \approx 2$ and ≈ 4 MPa for PVAc and PEO, respectively. The molecular weight between entanglements (M_e) can be calculated using the equation,[88]

$$G_e = \frac{\rho RT}{M_e} \tag{5.2}$$

which gives $M_e \approx 1700$ and 800 $\mathrm{g\,mol^{-1}}$ for PVAc and PEO respectively, corresponding to about 24 repeat units for PVAc, and 18 repeat units for PEO. This is reasonable, given that PEO is more flexible than PVAc.[87] The modulus of MC is roughly an order of magnitude greater than PEO networks, and at $\phi = 1$ gives an entangled melt modulus of ≈ 40 MPa, and using the same calculation, gives $M_e \approx 90$ $\mathrm{g\,mol^{-1}}$, corresponding to about a half of an MC repeat unit ($M_0 = 187$ $\mathrm{g\,mol^{-1}}$). MC gelation cannot be a consequence of immobilized entanglements, since $N_e < 1$ anhydroglucose unit is a difficult scenario to picture, and the fibrillar structure is an active contributor to the gel modulus of MC. It is for this reason that alternate gel network structures will be considered for the remainder of the chapter.

5.2.2 Strain Hardening of MC Hydrogels

A critical definition when considering SAOS and LAOS is the difference between "small" and "large" applied σ_0. As explained in Chapter 2, when σ_0 increases above a critical value, it will appear as if G' or G'' increases or decreases. When G' or G'' is dependent on the applied σ_0, this is traditionally referred to as LAOS. An example of a stress sweep that is typically performed to determine the LVE regime is shown in Figure 5.2. In order to perform SAOS measurements, a value of σ_0 is chosen where G' and G'' are independent of σ_0 on the left region of the plots. In the right region of the plots in Figure 5.2 denoted as the NVLE regime, MC solutions (left plot, in blue) display *shear-thinning*, in which the apparent dynamic moduli decrease with increased σ_0. In contrast, MC gels (right plot, in red) display *shear-hardening*, in

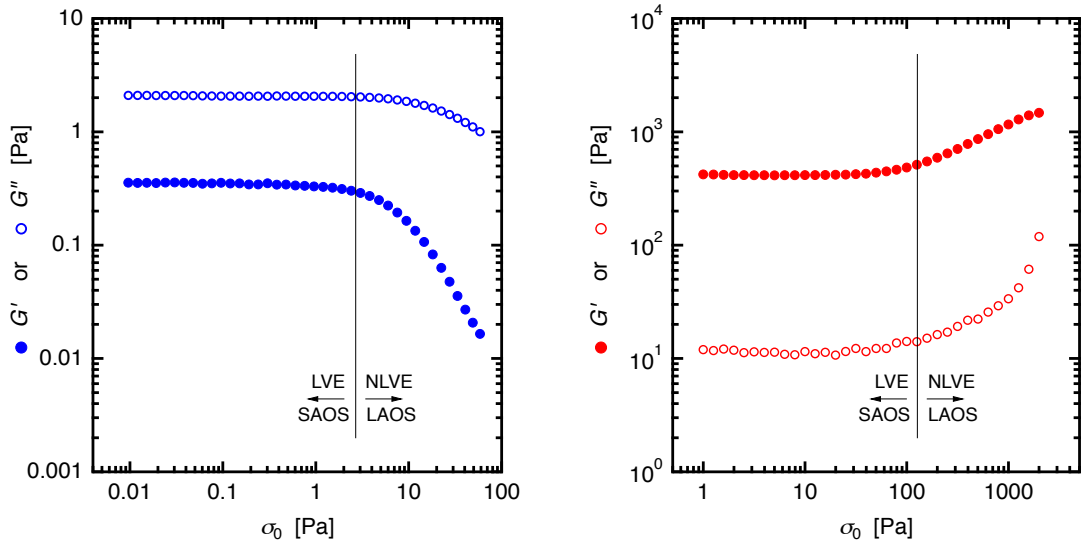

Figure 5.2: Stress sweep for a 1.4 wt% solution of MC300 at 10 °C (left) and 70 °C (right). Measurement was made with parallel plates, with an oscillation frequency of $\omega = 1$ rad s^{-1}.

which the apparent dynamic moduli increase with increased σ_0. Shear hardening is a common property for protein networks,[99,131–133] yet reports of shear hardening in polysaccharide gels are scarce. A filament stretching model developed for actin gels was applied to MC hydrogels in the discussion section, with very good agreement to define the onset of the NVLE regime.

Stress sweep experiments were used to probe the transition from shear thinning to shear hardening behavior as the gelation temperature is traversed. Figure 5.3 illustrates the change in mechanical response as a 1.4 wt% solution of MC300 is heated from 30 to 70 °C. Below the gelation temperature (T_{gel} = 51 °C for this sample, see Section 3.2.4), the sample exhibits shear thinning at high stresses, typical of polymer solutions and which is usually ascribed to partial alignment of chains with the flow field. When the temperature is raised in the vicinity of T_{gel}, MC displays shear hardening at moderate σ_0, followed by shear thinning at higher σ_0 Once T_{gel} is exceeded, the plateau modulus rapidly increases as temperature is further raised, consistent with gelation. At high σ_0 the samples display shear hardening, with the stress corresponding to the onset of nonlinearity increasing with temperature. Figure

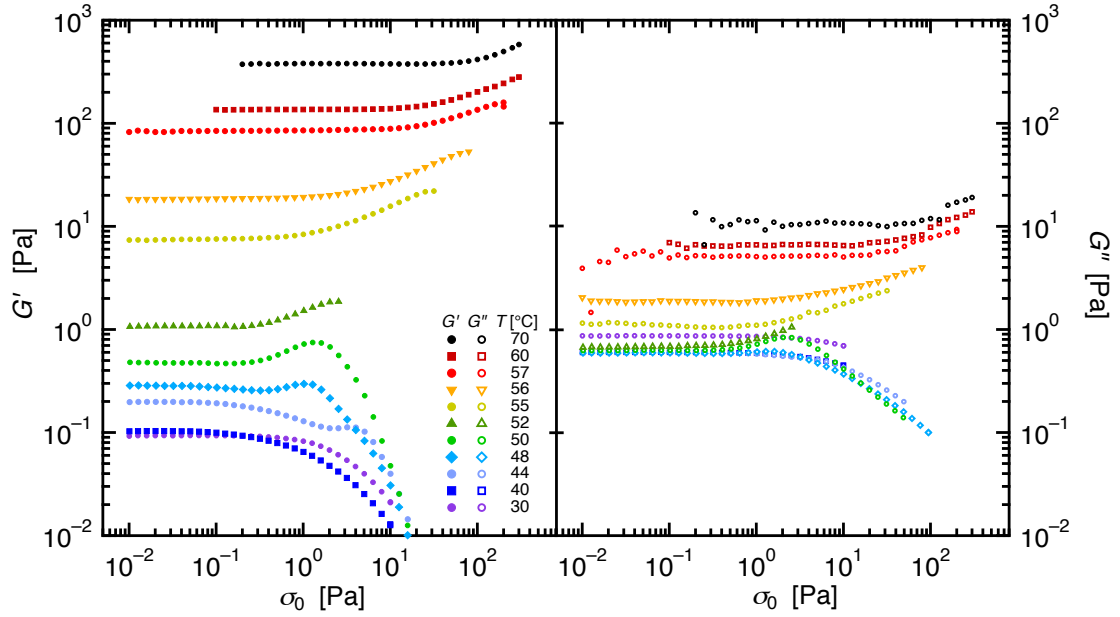

Figure 5.3: Stress sweep for a 1.4 wt% solution of MC300, heated from 30 to 70 °C, at an oscillation frequency of $\omega = 1$ rad s^{-1}. Reproduced with permission from McAllister et al.[134] Copyright 2015, the American Chemical Society.

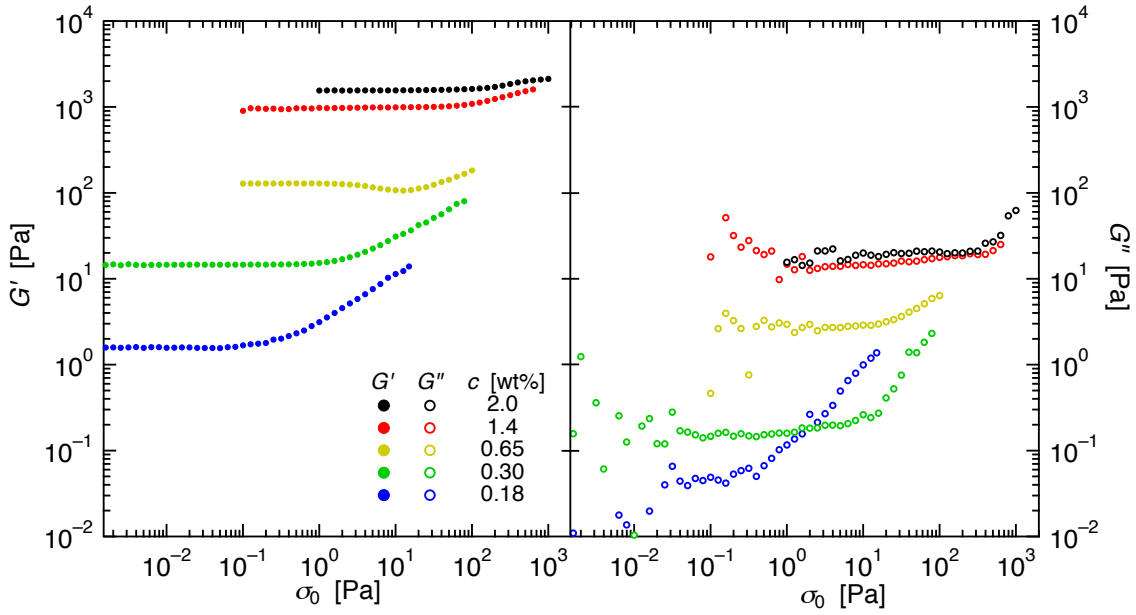

Figure 5.4: Stress sweep for five concentrations of MC300 at 70 °C and an oscillation frequency of $\omega = 1$ rad s^{-1}.

5.4 shows stress sweeps for five concentrations of MC300 at 70 °C. The onset of shear hardening increases to higher σ_0 as concentration increases, although the onset of shear hardening occurs at approximately the same strain amplitude (γ_0) for different concentrations (see Figure 3.2). Mechanistically, one explanation for shear thickening arises when the network strands are fully extended under moderate shear, and the force required to stretch the strand further increases drastically. If the filaments in a network are nearly fully extended (opposed to Gaussian coils for networks of individual chains), then under shear response to extension outpaces the resistive forces to compression, for equal strains, resulting in a higher modulus of the material.

5.2.3 Normal Stresses in MC Hydrogels

When most materials are subjected to a shear stress, there are translated stresses in directions perpendicular to the shear direction.[135] Nearly all modern rheometers are equipped with an axial force transducer, and an example of the signal response can be seen in Figure 5.5. Under high stress, MC solutions show a positive axial stress, as shown in the top plot, similar to most polymeric solutions, melts, and networks exhibit a positive axial force under hugh shear.[136] Interestingly MC hydrogels exhibit *negative* axial stresses under shear, as shown in Figure 5.5 in the bottom plot. However, the measurement of the axial stress is different from a normal stress, and it is important to make the distinction clear. The normal stress is determined from the axial stress measurement, and must be defined first.

To formally define normal stresses[136] that act upon a material under uniaxial shear deformation, consider a simple model material with a rectangular box-like shape with thickness g which undergoes shear deformation by a strain vector $\mathbf{s}$, shown in Figure 5.6. When a shear stress on the the 2 plane in the 1 direction ($\boldsymbol{\sigma}_{21}$ in blue) the material deforms by a strain vector $\boldsymbol{\gamma}_{12} = \mathbf{s}/g$. The orthogonal stress vectors $\boldsymbol{\sigma}_{11}$, $\boldsymbol{\sigma}_{22}$, and $\boldsymbol{\sigma}_{33}$ in each cartesian direction (in red) define the resultant stresses on the

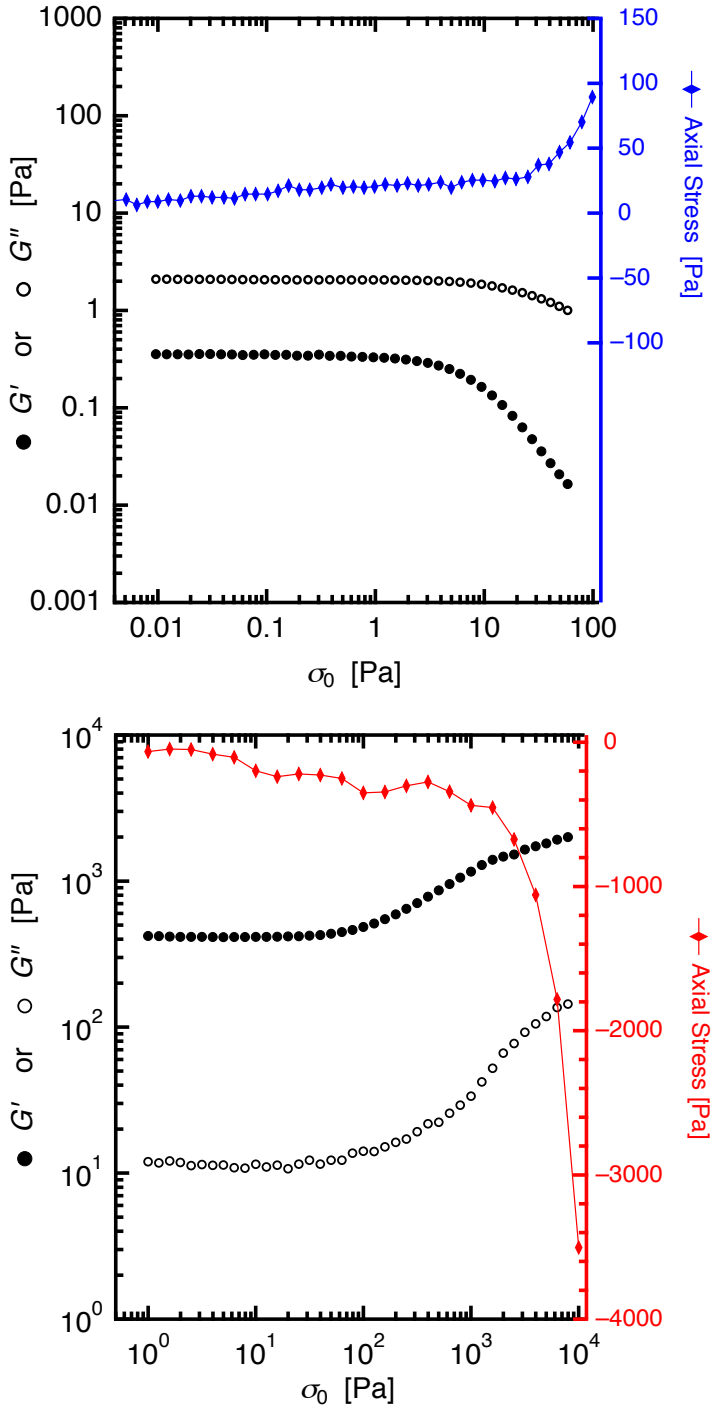

Figure 5.5: G', G'', and the axial stress (not normal stresses) of a 1.4 wt% solution of MC300 measured at 10 °C (top) and 70 °C (bottom) with $\omega = 1\ \mathrm{rad\,s^{-1}}$ and cone and plate geometry with a specified gap of 50 μm. At high σ_0 MC solutions display a positive axial stress, which is a force pressing the rheometer plates apart. For MC gels at high temperatures, the axial stress is negative, which contracts the rheometer plates together.

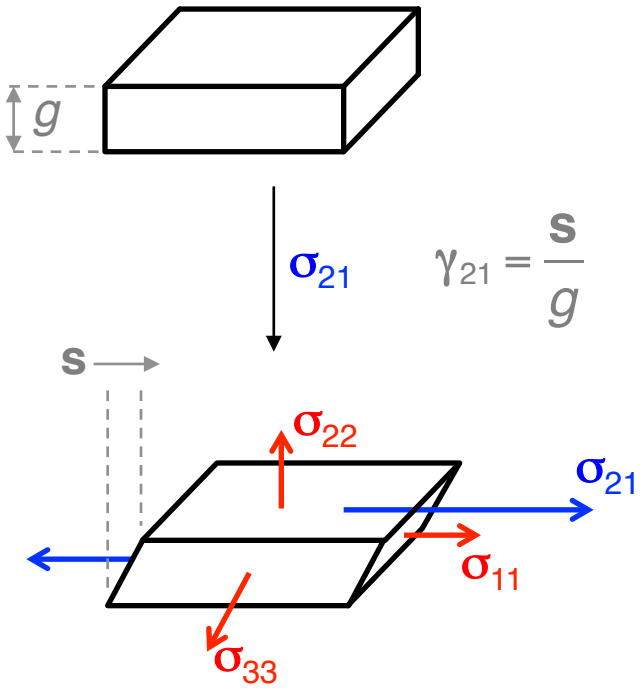

Figure 5.6: Diagram illustrating the stress vectors on an elastic material. A shear stress on the 2 plane in the 1 direction ($\boldsymbol{\sigma}_{21}$) deforms the sample with a strain vector $\boldsymbol{\gamma}_{21} = \mathbf{s}/g$. The orthogonal stress vectors on the sample $\boldsymbol{\sigma}_{11}$, $\boldsymbol{\sigma}_{22}$, and $\boldsymbol{\sigma}_{33}$ define the stress vectors that the material exhibits. Figure adapted with permission from Macosko.[136] Copyright 1994 Wiley.

deformed box. Three functions which define the deformation of a material are given by,

$$G \equiv \frac{\boldsymbol{\sigma}_{21}}{\boldsymbol{\gamma}_{21}} \tag{5.3}$$

$$\mathbf{N}_1 \equiv \boldsymbol{\sigma}_{22} - \boldsymbol{\sigma}_{11} \tag{5.4}$$

$$\mathbf{N}_2 \equiv \boldsymbol{\sigma}_{33} - \boldsymbol{\sigma}_{22} \tag{5.5}$$

where G is the shear modulus, and $\mathbf{N}_1$ and $\mathbf{N}_2$ are the first and second normal stress differences, respectively. $\mathbf{N}_1$ is the stress difference on the material perpendicular to the shear plane, which a force in the direction of the sample thickness g in Figure 5.6. Positive $\mathbf{N}_1$ is a stress difference acting to stretch the material in the 2 direction,

where as a negative $\mathbf{N}_1$ $\mathbf{N}_2$ is the stress difference on the material perpendicular to the shear direction, akin to a centrifugal force when the sample is disk shaped and the deformation is rotational. Two other sets of stresses can be similarly defined for the other two cartesian directions, bringing the total number of stresses to define the deformation of a material to nine, which is relevant for anisotropic materials. For MC fibril networks which are isotropic, Equations 5.3 to 5.5 are sufficient to completely define the deformation. In practice, it is common to refer to the deformation stress and strain vectors just by their magnitudes, $|\boldsymbol{\sigma}_{21}| = \sigma$, $|\mathbf{N}_1| = N_1$, $|\mathbf{N}_2| = N_2$, and $|\boldsymbol{\gamma}_{21}| = \gamma$, which simplifies the analysis due to the angular rotation of the rheometer plates.

The axial stress from Figure 5.5 is the overall force orthogonal to the rheometer plates, and it requires some modification in order to obtain $\mathbf{N}_1$ and $\mathbf{N}_2$ for the sample. Both normal stresses can be obtained when stress sweeps are performed using both parallel plate and cone and plate geometries. Figure 5.7 shows the axial force for the same 1.4 wt% sample of MC300 at 70 °C. For a cone and plate geometry, N_1 can be obtained directly[136] using,

$$N_1 = \frac{2F_z}{\pi r^2} \tag{5.6}$$

where F_z is the axial force, and r is the radius of the cone. The variable gap across the radius of the cone gives a constant strain across the sample, which allows for direct comparison between F_z and N_1. For parallel plate geometry, the strain during deformation for a parallel plate geometry is non constant (it varies from zero strain at the center to the reported strain at the edge of the plate), and the measured axial force is a combination of N_1 and N_2,

$$N_1 - N_2 = \frac{4F_z}{\pi r^2}. \tag{5.7}$$

If a sample is tested with both parallel plates and cone and plate, then both normal stress differences can be determined. Usually, the magnitude of N_2 is between a third

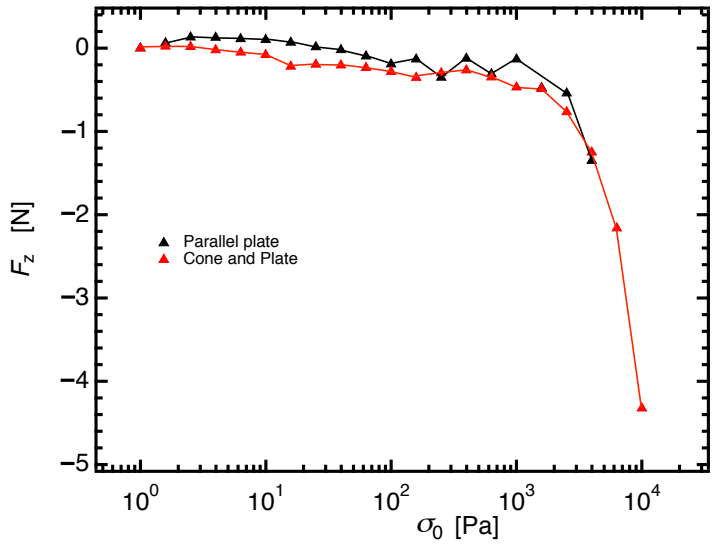

Figure 5.7: Axial force for a sample of 1.4 wt% MC300 at 70 °C using cone and plate (gap = 50 μm, specified) and parallel plate (gap $\approx$ 500 μm) geometries, with $\omega = 1$ rad s^{-1}

and a quarter of N_1, and they have opposite signs in order to conserve density in incompressible materials.[135,136]

Figure 5.8 displays N_1 and N_2 for MC gels at 70 °C. At high shear stress, MC samples have negative N_1 and positive N_2, which means that MC gels pull the rheometer plates together under high shear, and the sample presses out from the gap between the plates. This behavior is the opposite of most polymer networks and melts, which have a positive N_1 and a negative N_2.[137,138] The absolute magnitude of the negative normal stress for a MC gel is more than an order of magnitude larger than the positive normal stress for the MC solution of the same concentration. Materials with negative N_1 and positive N_2 are an unusual property, but not completely unique; other materials with this behavior emulsions of particles which are near their glass transition temperature,[139] suspensions of multi-walled carbon nanotubes,[140] and filamentous protein networks such as fibrinogen, actin, and collagen.[138,141,142]

There is a similar overarching structure between protein gels, MC gels, and carbon nanotubes, as they all can be approximated by semi-flexible cylinders. This strongly

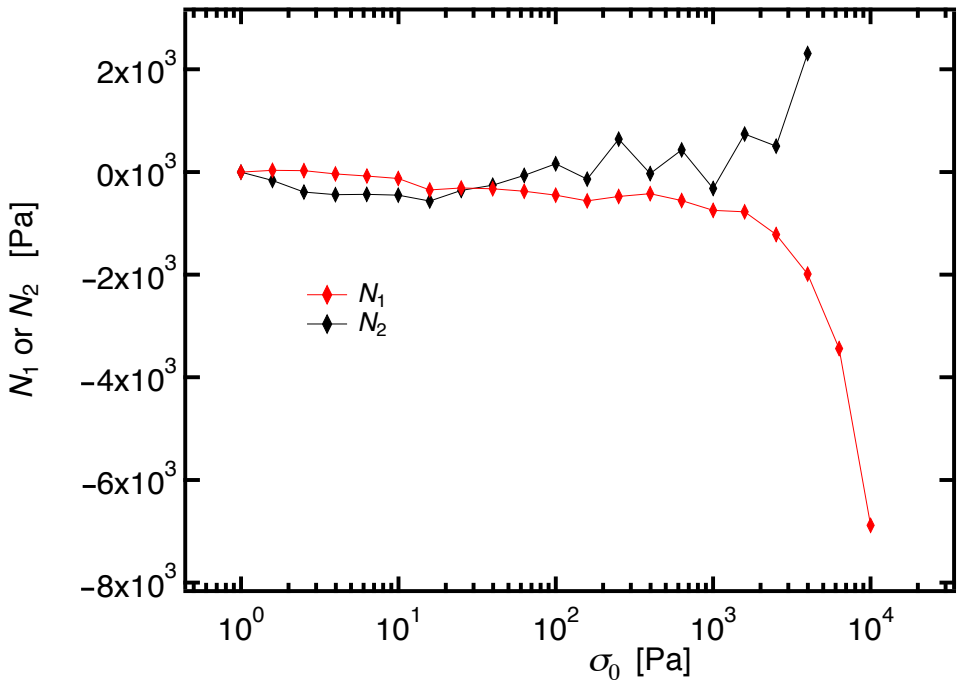

Figure 5.8: Normal stress differences N_1 and N_2 for a 1.4 wt% solution of MC300 at 70 °C, with $\omega = 1$ rad s^{-1}. Negative N_1 and positive N_2 at high shear is consistent with fibrillar networks,[142] and the opposite of most other polymeric networks.[137,138]

suggests that a similar mechanism at play. For these materials, it is thought that for isotropically oriented filaments, shearing will stretch and compress approximately the same number of filaments, but because the stretching of a filament exerts a greater force on the sample than compressing a filament, there is a net negative tension on the sample directions orthogonal to the shear direction.[138] In the direction of shear, response to extension outpaces the resistive forces to compression extension, leading to shear hardening discussed in the previous section. Negative N_1 and positive N_2 are commonly seen with materials that undergo shear hardening. Negative N_1 and positive N_2 are also the opposite of the behavior of gels composed of flexible polymer chains[135,138] and further supports the notion that the bulk mechanical properties of MC are a result of the fibril structure. The discovery of materials exhibiting negative normal stresses is relatively recent, and this property could potentially be exploited

for new applications. For example, compression in directions normal to shear will increase friction between two surfaces.

5.2.4 Large Amplitude Oscillatory Shear of MC

As described in Section 2.3.2, when it appears as if the dynamic moduli change with higher σ_0, G' and G'' are no longer formally defined, because the strain response cannot be described as a linear combination of in-phase and out-of phase sinusoidal functions. While the parallel plate geometry is suitable for SAOS experiments, because the strain experienced by the sample varies with radius, it is not a good choice for LAOS experiments as it is important that the strain experienced by the sample is uniform. Therefore, the cone and plate geometry is a better choice when performing LAOS experiments since the strain on the sample is constant throughout the sample. Another important requirement is to collect the raw oscillatory torque-displacement data, which can be converted into sinusoidal $\sigma(t)$ and $\gamma(t)$. To utilize this, many researchers use dataloggers retrofitted onto rheometers when these data are not available in the stock software.[80,143] However, the TRIOS$^{\text{TM}}$software interface from TA instruments is one of the only commercially available software packages with the ability to record raw waveform data, so any TA rheometers that use TRIOS can successfully be used for LAOS (DHR or ARES-G2 rheometers). For these experiments the stress-controlled DHR rheometer with a cone geometry ($r = 20$ mm, cone angle $= 2°$, and a specified gap of 50 μm) was used with a Peltier heating platform for the lower plate. Samples were covered to minimize condensation, and the edge of the sample was coated in low-viscosity silicone oil (see Section 2.3.2).

Figure 5.9 displays the strain response for a MC solution at 10 °C at $\sigma_0 = 0.12$ Pa, which is in the LVE regime (see Figure 5.5) and at $\sigma_0 = 48$ Pa, which is in the NVLE regime. MC solutions at 10 °C have a phase angle δ of close to $\pi/2$ radians, indicating that $G'' \gg G'$, and the response is mostly that of a viscous liquid. It is difficult to see an apparent difference between the two $\gamma(t)$ curves (in red), and more sophisticated

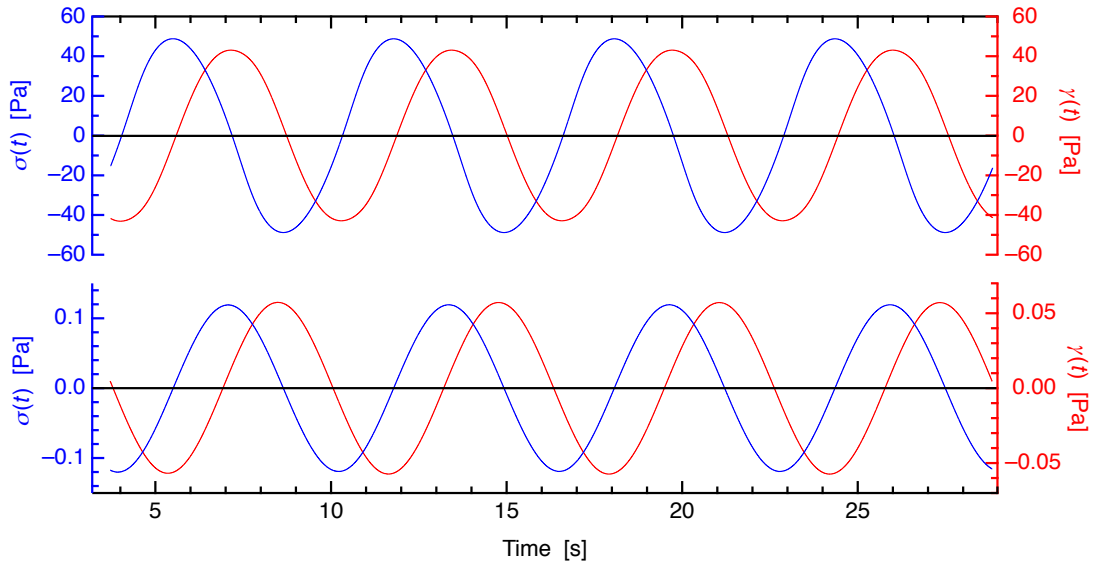

Figure 5.9: LAOS responses for a 1.4 wt% solution of MC300 at 10 °C and $\omega = 1$ rad s^{-1} with $\sigma_0 = 0.12$ Pa (bottom), and 48 Pa (top). Data was taken on a cone and plate fixture, with a specified gap of 50 μm. The is little visible differences between the two plots, even though the top plot is deep into the shear-thinning part of the stress sweep (see Figure 5.5). The data are plotted as lines since the number of data points are too many to individually distinguish (ca. 2400 per oscillation).

analysis is required to detect nonlinearities as will be discussed further in Section 5.3.2. Figure 5.10 displays LAOS responses of MC gels at 70 °C. They have small values of δ, indicating that $G'' \ll G'$, and the response is mostly that of an elastic solid. Interestingly, Figure 5.10 displays an obvious progression from the LVE regime at $\sigma_0 = 50$ Pa, and into the NVLE regime at $\sigma_0 = 500$ and 2500 Pa. As σ_0 increases, $\gamma(t)$ begins gains a more rectangular shape. Mechanistically, the rectangular shape can be attributed to shear hardening in MC gels: beginning from a minimum in $\sigma(t)$, the initial stress rate is zero ($\dot{\sigma}(t)$=0), and as stress is applied to the sample, the sample initially resists deformation until $\dot{\sigma}(t)$ approaches a maximum. The sample then rapidly deforms until on the sample causes a very rapid change in $\gamma(t)$, until $\dot{\sigma}(t)$ approaches zero again and $\sigma(t)$ reaches a maximum. For the top plot in Figure 5.10, the noise in the highest σ_0 is a instrumental artifact known as "stress ringing,"

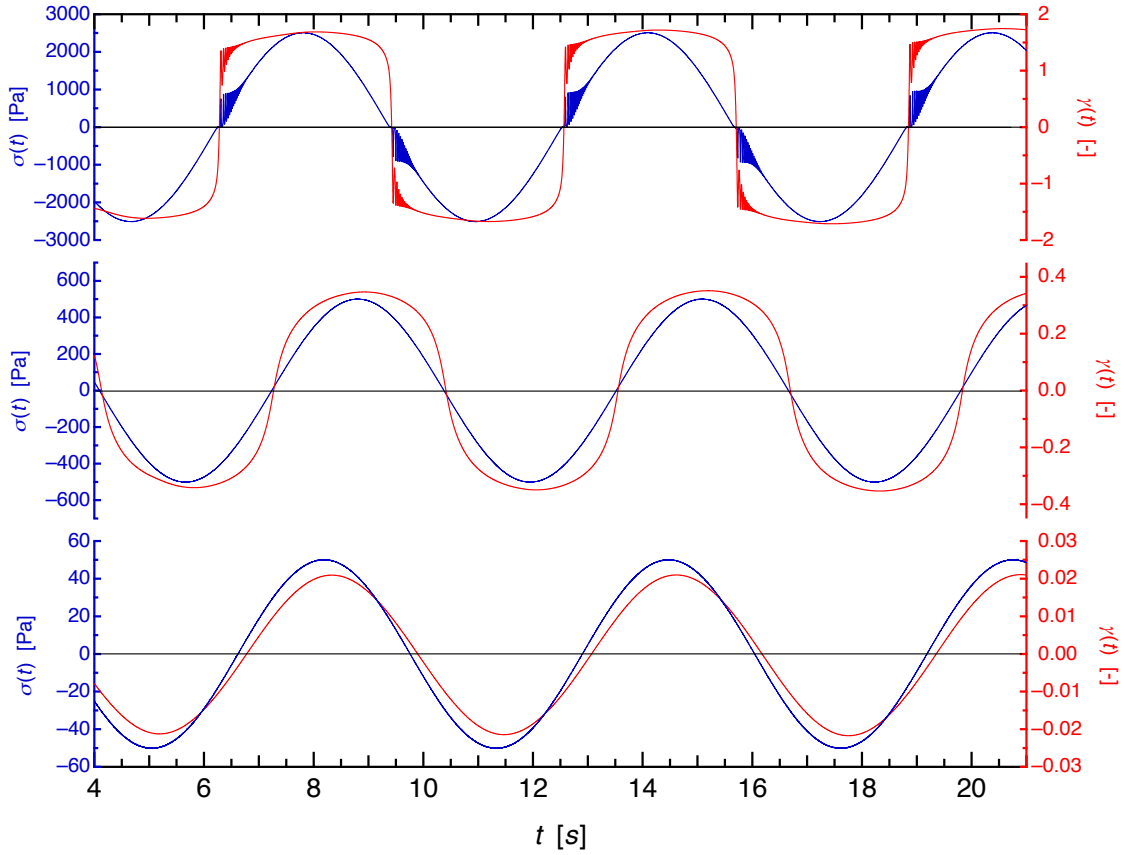

Figure 5.10: LAOS responses for a 1.4 wt% solution of MC300 at 70 °C and $\omega = 1\ \mathrm{rad\,s^{-1}}$, with $\sigma_0 = 50$ Pa (bottom), 500 Pa (middle), and 2500 Pa (top). The bottom plot is within the LVE regime, and the middle and top plots are in the shear-hardening NVLE regime. Data was taken on a cone and plate fixture, with a specified gap of 50 μm. The data are plotted as lines since the number of data points are too many to individually distinguish (ca. 2400 per oscillation).

which is an inertial effect that arises from the rapid start-stop motion on the motor-transducer assembly for stress-controlled rheometers. This has been well-reported in creep experiments.[144]

Most LAOS experiments which have been reported utilize a strain-controlled rheometer (termed LAOStrain) like the ARES or ARES-G2,[81,143,145] and reports of LAOS using stress-controlled rheometers (LAOStress) as presented here are scarce. Interestingly Klein et al.[143] and Hyun et al.[145] reported rectangular wave behavior in

shear-thinning colloidal suspensions in experiments using strain control. They reported that shear-hardening materials show a triangular-shaped wave, as also noted by Kang et al.[146] This result is seemingly the opposite of the results presented in Figure 5.10. There are two possible reasons for this. First, the shape of the LAOS response is likely intimately related to the microstructure of the material, so it may be inappropriate to make the claim that a particular wave shape in LAOS is associated with shear thinning or hardening behavior. Second, it is entirely possible that LAOStrain and LAOStress provide different and complementary LAOS responses, and can provide critical insight to the microstructure of a wide variety of materials.[86] One method of analysis of LAOS responses has utilized Fourier transform (FT) analysis[143,147,148] on the nonlinear response, which results in a FT spectrum of frequency harmonics to characterize the LAOS response. FT analysis of Figures 5.9 and 5.10 is discussed in Section 5.3.2.

5.3 Discussion

This section consists of two parts. First, a filament stretching model developed by MacKintosh et al.[132,133] is applied to the stress sweeps of MC gels at 70 °C. Using results from the fitting of SANS data from Chapter 4, a critical stress (σ_c) at which MC gels of varying concentrations is successfully calculated. The second part consists of FT analysis of LAOS responses from Figures 5.9 and 5.10. The magnitude of frequency harmonics in MC solutions and gels will be discussed, as well as the merits and disadvantages of the FT analysis of LAOS data.

5.3.1 Filament Stretching of MC Gels

A mechanical model developed by MacKintosh et al.[132,133] was used to describe the elasticity of actin solutions and gels. It has more recently been applied to interpret a variety of other biopolymer systems such as neurofilaments,[133] gels from self-assembled β-hairpins,[149] and fibrin protofibrils.[99] This section begins with an overview of the filament network model. The elasticity of the filament network derives from the average force response of a single filament,

$$f \sim 3k_{\mathrm{B}}T\frac{l_{\mathrm{p}}^2}{\left\langle L^2\right\rangle^2}\gamma L_{\mathrm{e}} \tag{5.8}$$

where f is the average force to deform a semiflexible filament in the network by a strain γ, l_{p} is the persistence length of the filament, $\langle L^2\rangle$ is the mean square end-to-end length of the filament, and L_{e} is average distance between filament entanglements. Equation 5.8 differs from the force to extent a Gaussian chain in a network ($f \sim 3k_{\mathrm{B}}T/\langle h^2\rangle$)[87] as it includes an l_{p} term, and filaments in the network are assumed to be nearly fully extended, $\left\langle L^2\right\rangle^{1/2}/L \approx 1$, which is unlike $\langle h^2\rangle$ for a Gaussian coil. It is assumed that the length of filaments is greater than the distance between entanglements, $L \gg L_{\mathrm{e}}$, and because the filaments are are nearly fully extended, L_{e} is close to $\left\langle L^2\right\rangle^{1/2}$, so $L_{\mathrm{e}}/\left\langle L^2\right\rangle^2 \approx 1/L_{\mathrm{e}}^3$. The elastic modulus, G, of the filament network is given by,

$$G = 6k_{\mathrm{B}}T\, d_{\mathrm{f}}\,\frac{l_{\mathrm{p}}^2}{L_{\mathrm{e}}^3} \sim k_{\mathrm{B}}T\frac{l_{\mathrm{p}}^2}{\xi^2\, L_{\mathrm{e}}^3} \tag{5.9}$$

where ξ is the mesh size of the network, and is related to d_{f}, the filament-length density and to the volume fraction of filaments ϕ_{f} by $d_{\mathrm{f}} = \phi_{\mathrm{f}}/(\pi r^2) \sim 1/\xi^2$. Contrasted with the modulus for flexible chain networks, $G = 3k_{\mathrm{B}}T/\xi^3$, Equation 5.9 depends additionally on l_{p} and L_{e}. De Gennes et al.[150] reported that for a network of semirigid rods, ξ scales with concentration by the relation,

$$\xi \sim a\phi^{-1/2} \tag{5.10}$$

where a is the diameter of the rod (or monomer size) and ϕ is the volume fraction. Equation 5.10 is relevant for networks such that $\xi < l_p$. This is contrasted with a network flexible chains, $\xi \sim 2a\phi^{-3/4}$, (see Equation 5.1).[127] Substituting Equation 5.10 into Equation 5.9 along with the assumption that L_e is of similar size to ξ since the filaments are nearly fully extended, gives the scaling relationship,

$$G \sim \ k_B T \, \frac{l_p^2}{a^5} \, \phi^{5/2}. \tag{5.11}$$

MacKintosh et al. further argued that the when the filament density is high, $\xi \ll l_p$, the probability that a filament in the network is entangled increases, which decreases the scaling in Equation 5.11 to,

$$G \sim k_B T \, \frac{l_p^{1.4}}{a^{4.4}} \, \phi^{11/5}. \tag{5.12}$$

Both Equations 5.11 and 5.12 suggest that networks will have similar scaling to G as networks of flexible polymers (9/4) from Equation 5.1 and in Figure 5.1. This has been confirmed by modulus measurements of other filamentous gels, including actin[132] and fibrinogen.[142]

Yao et al.[133] extended the model developed by MacKintosh et al. to describe a characteristic tension of a single filament proportional to $k_B T \, l_p / L_e^2$. When extended to the entire network, the corresponding critical stress, σ_c is given by,

$$\sigma_c = k_B T \, d_f \, \frac{l_p}{L_e^2}. \tag{5.13}$$

This equation predicts the stress at which the filaments within the network on average are fully extended, and begin to exhibit shear-hardening for reasons described in Section 5.2.2.[99,142] In order to predict σ_c for MC gels using Equation 5.13, the following parameters are needed: l_p, d_f, and L_e. Fortunately, one of these values have already been calculated from Chapter 4 using fitting of SANS data to a flexible cylinder

model, and the other two can be calculated from those parameters. The persistence length l_p for MC fibrils were already satisfactorily calculated in Section 4.3.1. As was previously mentioned, the filament density is related to volume fraction by $d_f = \phi_f/(\pi r^2)$. However, ϕ_f is the volume fraction of fibrils (not polymer) and using the same logic from Section 4.3.2 that MC fibrils contain a fraction of polymer, $\phi_{MC} = x\phi_f$, the filament length-density d_f is related to MC solution concentration by,

$$d_f = \frac{\phi_{MC}}{x\pi R_{cs}^2} \tag{5.14}$$

where R_{cs} is the fibril radius calculated in Section 4.3.1. It is worth noting that Equation 5.14 makes the assumption that essentially all MC molecules are contained within the fibrils, which for reasons noted in Section 4.3.2 is appropriate for MC hydrogels at 70 °C.

Figure 5.11 show the results of MC fibril dimensions obtained from fitting of SANS data[16,112] from Chapter 4 to Equation 4.5. Data are from Tables 4.1 and 4.2, and fit to linear regressions with respect to ϕ. While one of the conclusions of Chapter 4 was that the fibril dimensions are independent of concentration, linear regressions as a composite for all SANS results were used in order to obtain a statistical average for numerous concentrations and molecular weights. The slopes for each of the parameters in Figure 5.11 have a slight concentration dependence, but it is zero within the uncertainty of the parameters. Using calculated values of x and R_{cs} from Figure 5.11 for a series of values of ϕ, the fibril length-density d_f was calculated in Figure 5.12 using Equation 5.14.

With d_f estimated for MC gels, the length between fibril entanglements, L_e was calculated by using the hot-gel moduli in the LVE regime in Figure 5.1 and Equation 5.9. The data in Figure 5.1 are for MC gels at 80 °C, whereas d_f, l_p are for MC gels at 70 °C, but the difference in gel modulus and also SANS between these two temperatures was negligible, and it was assumed that the structures of the gel at 70 and 80 °C were equivalent. The average distance between fibril entanglements L_e

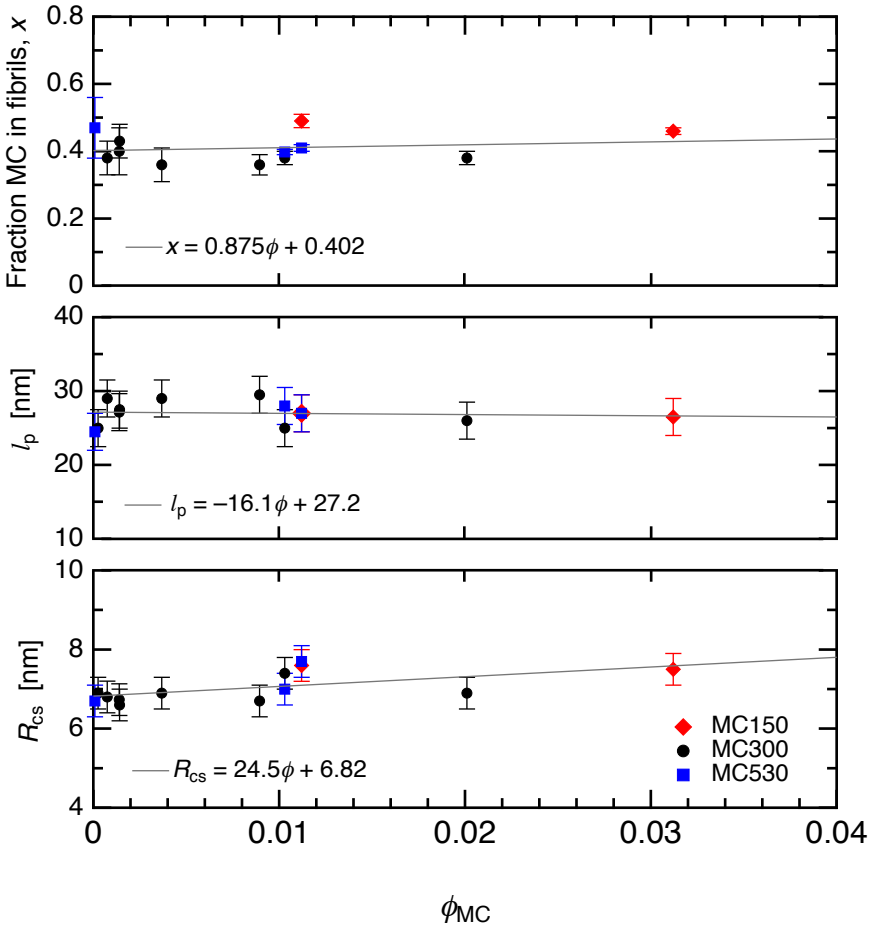

Figure 5.11: MC fibril dimensions obtained from fitting of SANS data from Chapter 4 to Equation 4.5 for fibril radii (R_{cs}, bottom), persistence lengths (l_p, middle), and the fraction of MC within fibrils (x,top, calculated from Equation 4.10). Also included are linear regressions of the data with respect to concentration. These data are used to estimate d_f and L_e.

in the gels as a function of MC solution concentration are displayed in Figure 5.13. For gel concentrations of practical interest, the values for L_e are on the order of ca. $10-100$ nm, broadly consistent with what is observed the cryo-TEM images in Figure 4.1. Quantification of the distance between fibril cross-links based solely on cryo-TEM images should be avoided since these represent 2D projections of a 3D gel network. In fact, precise values for L_e cannot be readily determined experimentally, so the values in Figure 5.13 provide a level of insight previously lacking in MC gels. However, since

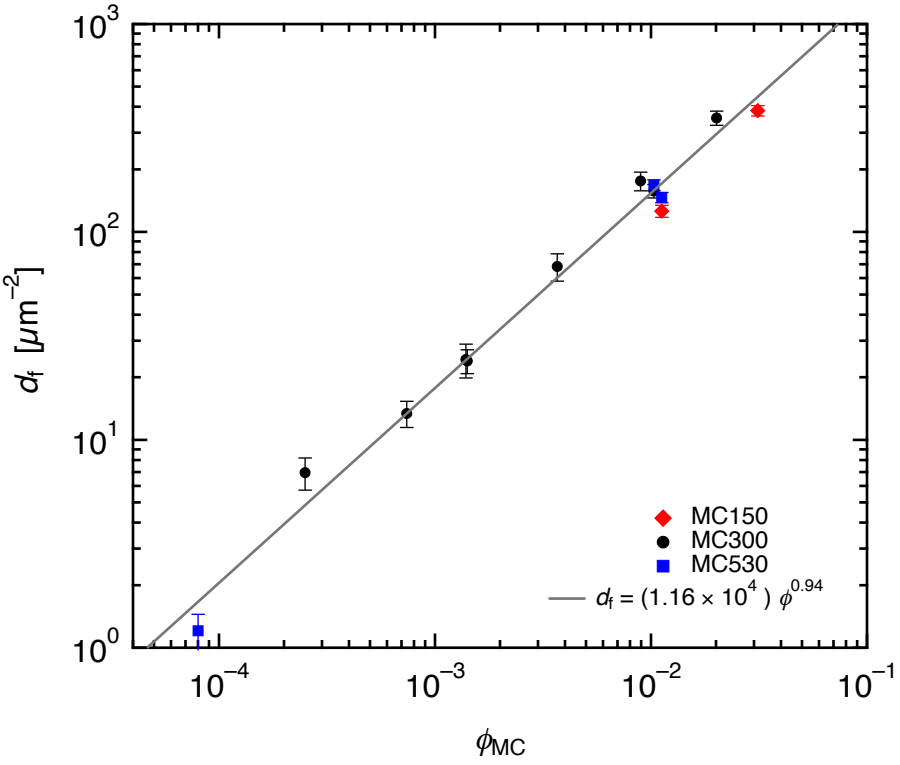

Figure 5.12: The fibril-length density for numerous concentrations calculated from Equation 5.14

the network dimensions of the scale shown in Figure 5.13 do not satisfactorily account for the optical turbidity observed in the gel state and that larger-scale (> 500 nm) heterogeneities must also exist in the gel network[16,112] not made in the calculations of d_f or L_e. The implications when considering d_f or L_e assumes the fibrils form an entangled defect-free network. The deviations are apparent when considering the power slope for the calculation of d_f in Figure 5.12. Equation 5.14 predicts that $d_f \sim \phi$, and is equivalent within error to the fit of the data given by $d_f \sim \phi^{0.94}$. Likewise it is expected that $L_e \sim \phi^{-2/3}$, which is equivalent within error to the experimental data in Figure 5.13 with $L_e \sim \phi^{-0.62}$. The values of d_f and L_e account for the average of the entire gel structure, and the micron-sized "bundles" of fibrils noted in cryo-TEM images[16] and interpreted from USANS measurements (Figure 4.7)[112] mean that the presence of relatively fibril-free voids in the network will cause the dimensions of

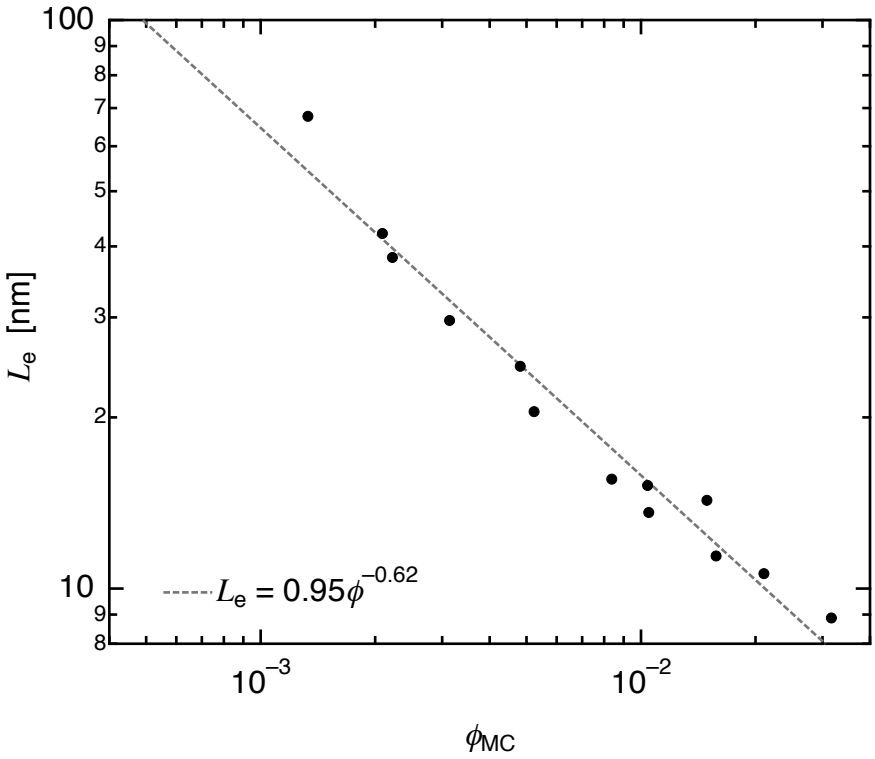

Figure 5.13: Calculated distance between cross-links as a function of concentration for MC gels using Equation 5.9.

the local mesh in fibril-rich aggregates to have larger d_f and smaller L_e for a given concentration of MC.

Using Equation 5.13 along with the calculated values of d_f and L_e, and l_p from Table 4.1, the critical stress (σ_c) that the network is predicted to deviate from linearity can be estimated. Table 5.1 summarizes values for d_f, L_e, and σ_c for five concentrations of MC gels from Figure 5.4. The values of σ_c agree nicely with the onset of shear-hardening of MC hydrogels, as shown in Figure 5.14. For the concentration range spanning 0.18 to 2.0 wt%, σ_c accurately predicts the oscillatory stress in which MC gels begin to exhibit shear-hardening behavior. As the concentration of the gels increases, nonlinearity sets in at higher stresses. It is apparent that Equation 5.13 affords very satisfying predictions for stresses that range over almost 2 orders of magnitude. This is remarkable in light of several considerations in addition to

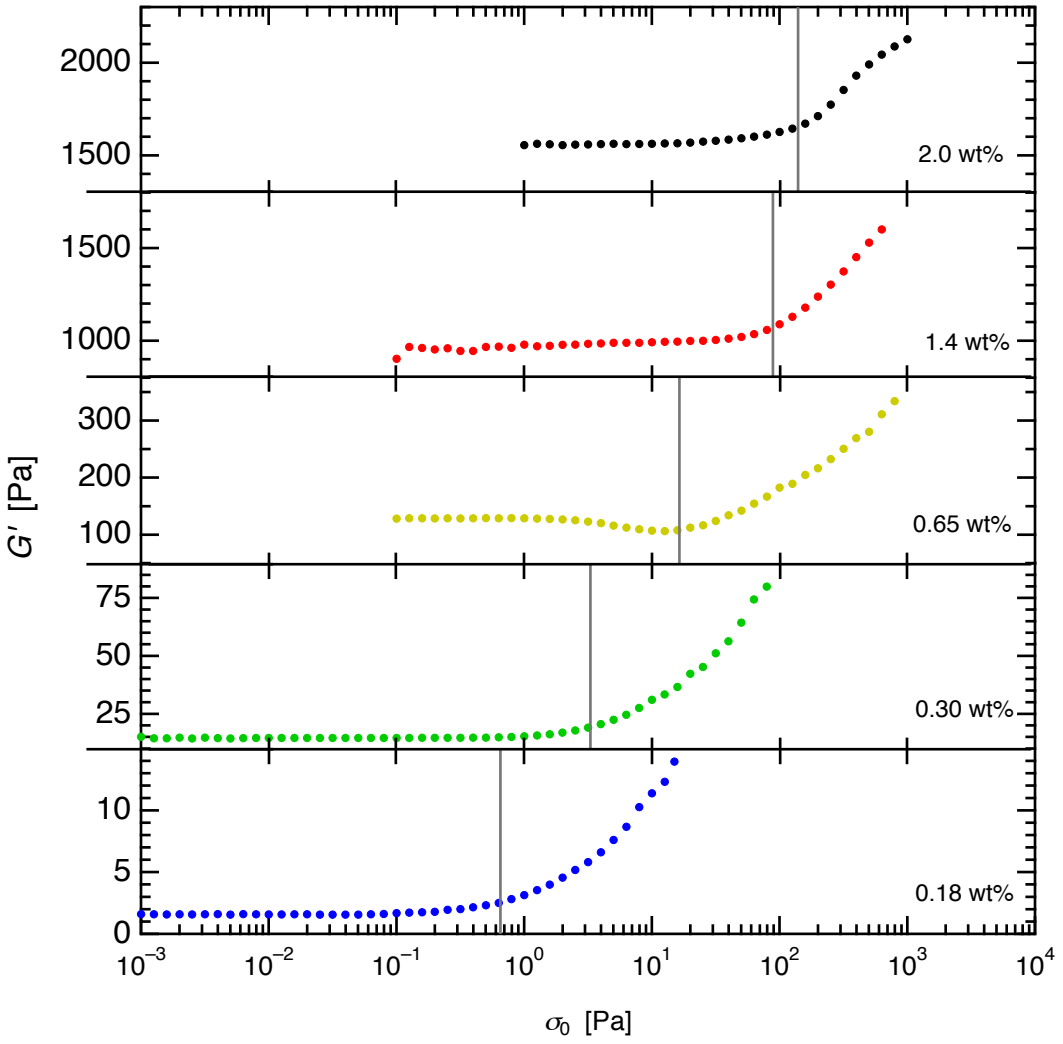

Figure 5.14: Predictions of the critical stress σ_c (vertical lines) calculated from Equation 5.13 compared to G' versus oscillatory stress for aqueous MC300 gels at 70 °C of varying concentrations, with $\omega = 1$ rad s^{-1}.

Table 5.1: Characteristic dimensions of MC hydrogels determined from the parameters of the fits to SANS data

c [wt%]	ϕ	d_f [μm^{-2}]	L_e [nm]	σ_c [Pa]
0.18	0.00133	23	68	0.65
0.30	0.00222	38	38	3.3
0.65	0.00481	78	25	16.4
1.4	0.0104	160	15	89
2.0	0.0149	224	14	140

the micron-sized heterogeneity of MC hydrogels discussed previously. At 70 °C, each concentration is a different distance in temperature from the associated T_{gel} (see Figure 3.17). Mechanistically, the model developed by MacKintosh and Yao explain the shear hardening in filament networks. Since the filaments in a network are nearly fully extended (opposed to Gaussian coils for networks of individual chains), then under shear response to extension outpaces the resistive forces to compression, for equal strains, resulting in a higher modulus of the material. To explain negative N_1, shearing will stretch and compress approximately the same number of filaments, but because the stretching of a filament exerts a greater force on the sample than compressing a filament, there is a net negative tension on the sample directions orthogonal to the shear direction. This model has assumed that the network nodes in MC hydrogels are entanglements of fibrils, though the exact nature of the network nodes MC is not yet known. It is possible that MC fibrils could also contain multifunctional junctions (crosslinks) in addition to the entanglements considered here.

Another model has been developed by Dobrynin and Carrillo[151,152] predicts the shear stress (σ_{xy}) of a shear thickening material in terms of an applied strain (γ). It uses only two adjustable parameters, a network shear modulus G, and a chain

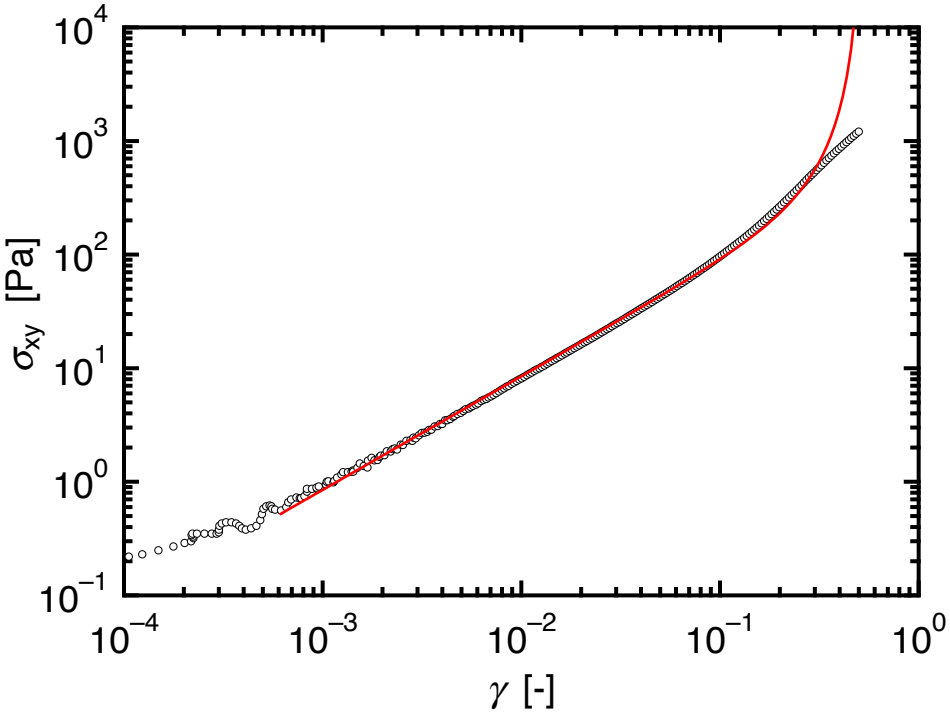

Figure 5.15: Steady shear of a 1.4 wt% sample of MC300 at 70 °C. This measurement was made using an ARES-G2 rheometer with a 50 mm cone and plate and 0.05 mm specified gap. The red line is a fit to the shear deformation model proposed by Dobrynin and coworkers,[151,152] gives the ratio of mean-square end-to-end distance of the unperturbed strand to the mean-square ent-to-end distance of the fully stretched strand, $\beta = \langle R_{in}^2 \rangle / R_{max}^2 = 0.92$ and a shear network modulus of $G = 9.0$ Pa.

elongation ratio β,

$$\sigma_{xy}(\gamma) = \frac{G\gamma}{3}\left[1 + 2\left(1 - \frac{\beta(\gamma^2+3)}{3}\right)^{-2}\right], \tag{5.15}$$

where $\beta = \langle R_{in}^2 \rangle / R_{max}^2$ is the ratio between the mean-square end-to-end distance of an unperturbed filament and the mean-square end-to-end distance of a fully stretched filament. Figure 5.15 shows steady shear of a 1.4 wt% MC300 sample at 70 °C measured on an ARES-G2 rheometer fitted with a 50 mm-diameter cone and plate and a specified gap of 50 μm. The fit of the data to Equation 5.15 is shown by the red line. The fit gives a chain elongation ratio of $\beta = 0.92$ and a shear network modulus $G = 9.0$ Pa. While Equation 5.15 is appealing in its simplicity, the nature

of the "shear network modulus" term (G) is unclear. For an MC300 sample at this concentration, SAOS gives an elastic modulus of $G' = 950$ Pa (Figure 5.14), and the slope of the low-strain linear section of Figure 5.15 gives $\sigma_{xy}/\gamma = 807$ Pa, which are very different from the shear network modulus of 9 Pa predicted by Equation 5.15. Similarly for fibrinogen and actin protein gels reported by Carrillo et al.,[152] the shear network modulus is much less than the bulk elastic modulus or the storage modulus. The relationship between the shear network modulus from Equation 5.15 and measured moduli of the sample has not been established by the authors.

5.3.2 Fourier Transform Analysis of LAOS Responses

The Fourier transformation (FT) converts a time-dependent signal $s(t)$ into a spectrum of frequencies, $S(\omega)$. It is utilized for signal processing in a wide variety of chemical analyses, including FT-infrared spectroscopy, nuclear magnetic resonance spectroscopy, and electron microscopy. Formally, the FT is defined as,

$$s(t) = \frac{1}{2\pi}\int_{-\infty}^{\infty} S(\omega)e^{+i\omega t}d\omega, \quad S(\omega) = \int_{-\infty}^{\infty} s(t)e^{-i\omega t}dt. \tag{5.16}$$

Converting from $s(t)$ to $S(\omega)$ is a Fourier transform, and converting $S(\omega)$ to $s(t)$ is an inverse Fourier transform. FT is a complex transformation, and it is nearly always performed using fast Fourier transform (FFT) algorithms. Most FFTs require 2^n data points equally spaced in time to perform the transformation.[153] However for a set consisting of m data points, it is likely that $m \neq 2^n$, so there are two methods to rectify this problem. The first is to fill z zeros onto the end of the dataset until the next highest 2^n points is reached, so that $m + z = 2^n$. This method is useful when the number of data points is small (ca. < 200), but will introduce temporal errors into the transformed data.[80] Another method is to rebucket the dataset from $m \rightarrow m_{rb}$ points into the next lowest factor of 2^n points. To do this, the time space between each point is increased so that there are now $m_{rb} = 2^n$ points, where $m_{rb} < m$. Each data

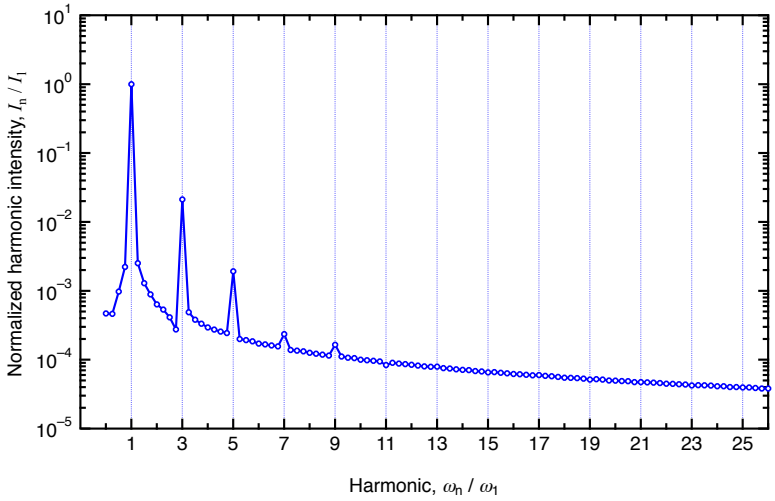

Figure 5.16: FT spectrum of a LAOS strain response for a 1.4 wt% solution of MC300 at 10 °C with a primary oscillation frequency of $\omega_1 = 1$ rad s^{-1}, and a stress amplitude of $\sigma_0 = 33$ Pa, which was in the shear-thinning regime of the stress sweep.

point from m is extrapolated to new data points in m_{rb} based upon the original data. This method results in a loss of resolution of the transformed data, but no temporal errors as with the first method. Rebucketing is a preferred method when the number of data points is large (ca. > 1000). Since modern computer electronics can record and process large amounts of data very quickly, the second method is most often used when applying FFTs to data. For this analysis, the LAOS responses in Figures 5.9 and 5.10 contained 10 oscillatory cycles and 24528 data points. These data were rebucketed to $2^{14} = 16384$ data points, and analyzed using the prime-factor FFT algorithm.[153] All calculations were made with the software package IgorPro (version 6.36, WaveMetrics Inc.). Even with the loss of resolution by rebucketing the data, there were ca. 1600 data points per oscillation for the analysis, which was sufficient to obtain a reliable FT spectrum.

Use of the FT to interpret LAOS data was first reported by Dodge and Krieger in 1971,[154] and has been widely utilized since.[80,143,147,148] The rationale is since the LAOS response is a complicated oscillatory function, it can be expressed as a sum of sinusoidal functions of differing frequencies. The large-amplitude periodic strain $\gamma(t)$

from responses similar to Figure 5.9 was processed to obtain a spectrum of frequency harmonics. Figure 5.16 shows the FT spectrum of a 1.4 wt% solution of MC300 at 10 °C and an applied $\sigma_0 = 33$ Pa, which was well into the shear-thinning part of the stress sweep. For reference, the stress sweep is plotted again in Figure 5.18. The peak intensities were normalized so that ω_1 (the primary oscillation, corresponding to $\omega = 1$ rad s^{-1}) is unity. Higher order harmonics are a result of higher frequencies, and ω_n corresponds to $\omega = n$ rad s^{-1}, where n is an integer. The FT spectrum for this sample displays low intensity odd-numbered harmonics up to about ω_9. Given the first higher-order harmonic at ω_3 has an intensity which is about 1/100 that of the primary oscillation, this explains why it was difficult to detect nonlinearities by eye in Figure 5.9.

In contrast with MC solutions at low temperatures, the onset of shear hardening was visibly apparent in the LAOS responses from Figure 5.10. Figure 5.17 shows FT spectra for $\sigma_0 = 10$, 100, and 1000 Pa of a 1.4 wt% solution of MC300 at 70 °C. $\sigma_0 = 10$ Pa was within the LVE regime where G' and G'' were independent of σ_0, For the LVE in the top plot, there is a very small contribution of ω_3, which is less than 1/1000 that of the primary oscillation. For $\sigma_0 = 100$ and 1000 Pa, which were in the shear-hardening part of the stress sweep (see Figure 5.18), odd-numbered harmonics appear similar to the MC solution in Figure 5.16, and peaks are visible out to about ω_{15} for $\sigma_0 = 100$ Pa. The oscillation $\sigma_0 = 1000$ Pa was chosen rather than $\sigma_0 = 2500$ Pa from Figure 5.10 to avoid the noise created from stress-ringing. Odd-numbered harmonics appear out past ω_{250}. In order to visualize the harmonic contributions to the signal, Figure 5.18 plots the first three harmonics after the primary (I_3, I_5, and I_7) as a function of σ_0 an MC solution at 10 °C (5.18a) and gel at 70 °C (5.18b). For solutions in Figure 5.18a, the onset of shear-thinning occurs at about the same σ_0 as the rise in ω_3 from the FT spectrum. However, for MC gels in Figure 5.18b, ω_3 begins to have a measurable influence on $\gamma(t)$ around $\sigma_0 = 40$ Pa, which is a slightly lower stress than was predicted for the sample using the model by MacKintosh et al. and

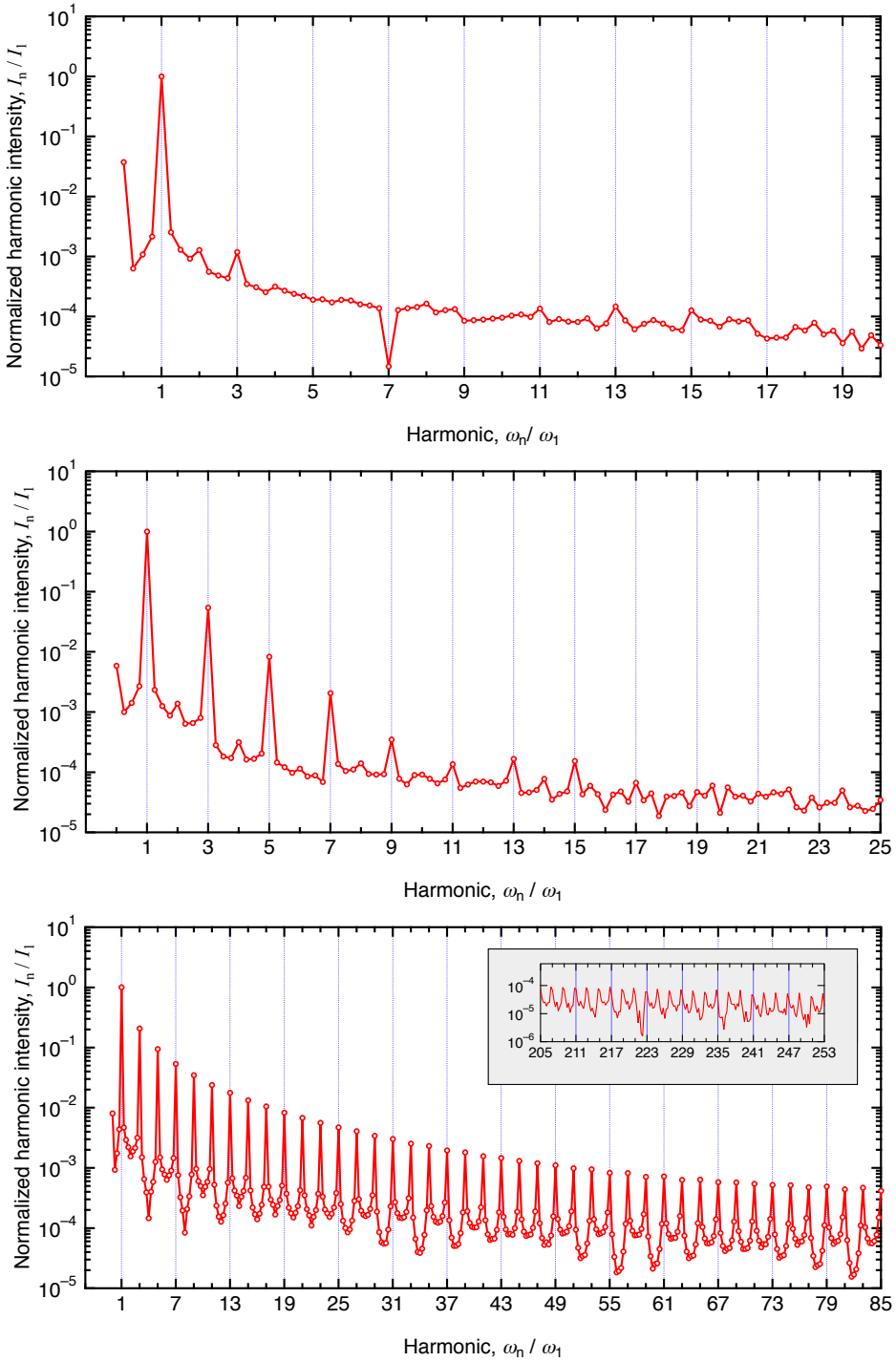

Figure 5.17: FT spectra of a LAOS strain responses for a 1.4 wt% gel of MC300 at 70 °C with a primary oscillation frequency of $\omega_1 = 1$ rad s^{-1}, and a stress amplitude of $\sigma_0 = 10$ Pa (top), 100 Pa (middle) and 1000 Pa (bottom). The top plot was within the LVE regime, while the middle and bottom plots were in the shear-hardening regime of the stress sweep.

Yao et al.,[132,133] 89 Pa, from Section 5.3.1. Nonetheless, both methods successfully detect the onset of nonlinearities to the oscillatory strain.

Klein et al. have proposed[143] that there are four fundamental types of mechanisms that exist in LAOS: linear, shear-softening, shear-hardening, and wall slip. These correspond to four basic wave shape responses: sine, rectangular, triangular, and sawtooth, respectively. This is an interesting idea, but since this paper considered only LAOStrain, and described shear-hardening as a triangular-shaped wave. This is contrasted with the rectangular wave from as LAOStress presented in this chapter. This may simply be one of the differences between LAOStress and LAOStrain, which is currently an active area of research.[86] Before the idea of four fundamental nonlinear oscillatory responses proposed by Klein et al. can be adequately used to describe any material, the difference between LAOStress and LAOStrain should be examined.

While FT analysis of LAOS is a relatively straightforward and robust technique, one of the difficulties with the procedure is attempting to assign meaning to the higher order harmonic peaks in the FT spectra. Some researchers have attempted by defining nonlinear coefficients associated with I_3/I_1, but it has only been a mathematical definition[145,147] and not one associated with a physical process associated with the sample. Ewoldt et al. fitted LAOStrain data using a series of Chebyshev polynomials,[81,82] and this approach has been widely utilized (the 2008 paper by Ewoldt et al. has been cited nearly 200 times at the time of this writing). However like FT spectra, the meaning of higher order peaks remain unexplained. For a FT or Chebyshev spectrum like Figure 5.17 at high σ_0, assigning a specific meaning to the higher-order harmonic peaks mean that there would be hundreds (or more) of material functions. Since oscillatory rheometry measures primarily elasticity and viscosity, assigning meanings with each higher harmonic peak is a flawed approach in my opinion.

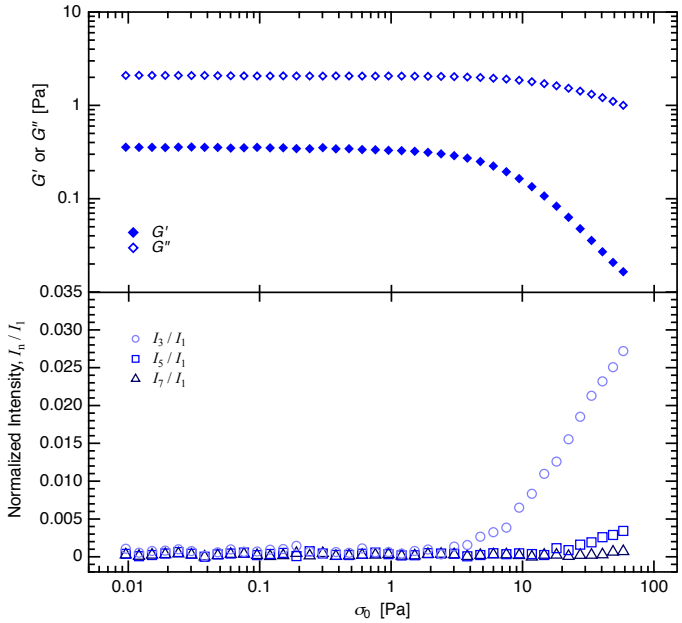

(a) 1.4 wt% solution of MC300, 10 °C: plot of the first three harmonic peaks after the primary, I_3, I_5, I_7, a function of σ_0 (bottom), compared to the stress sweep of G' and G''(top).

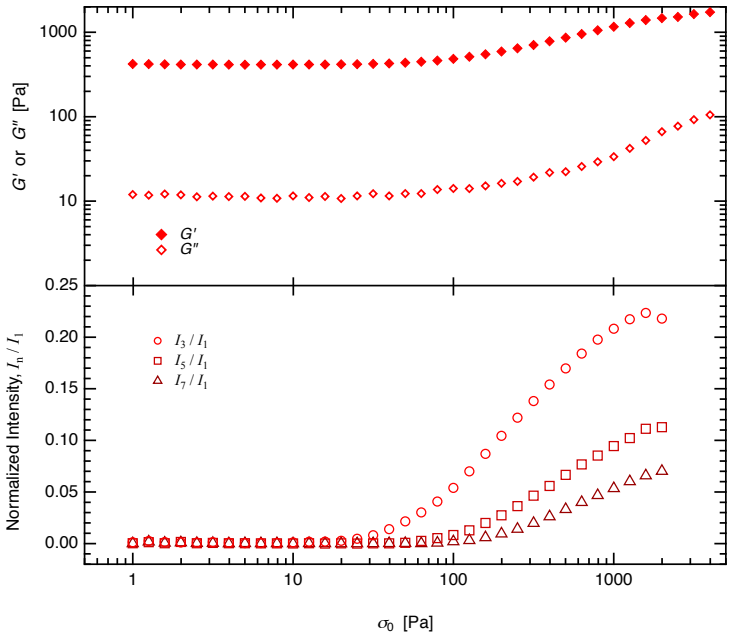

(b) 1.4 wt% gel of MC300, 70 °C: plot of the first three harmonic peaks after the primary, I_3, I_5, I_7, a function of σ_0 (bottom), compared to the stress sweep of G' and G'' (top).

Figure 5.18: A comparision between the appearance of higher order harmonic peaks in the FT spectra to $G' - G''$ stress sweeps.

5.4 Summary

The moduli of MC hydrogels was compared to other flexible and semiflexible networks, and a mechanical model for probing the mechanical properties of filamentous gels was be applied to fibrillar MC gels. It was found that MC hydrogels shear-harden, like many protein networks, and a negative first normal stress difference (N_1) occurs at high stresses. MC transitions from a shear-thinning material as a solution to a shear-hardening material as a gel. Shear hardening in MC gels ultimately arises because the fibrils in the MC network are nearly fully extended, so the shear response to extension outpaces the resistive forces to compression. Likewise, negative N_1 arises from shear stress compressing and stretching approximately the same number of filaments, but because the stretching of a filament exerts a greater force on the sample than compressing a filament, there is a net negative tension on the sample directions orthogonal to the shear direction. The onset of shear hardening was successfully predicted using a filament-based mechanical model originally developed by MacKintosh et al.[132]

Large-amplitude oscillatory shear responses were measured for MC solutions at low temperature and gels at high temperature, and the LAOS response was analyzed using the FT to give a spectrum of frequency harmonics. The onset of shear hardening in MC gels was detected by the intensity (I_3/I_1) of the first frequency harmonic, ω_3, after the primary oscillation harmonic (ω_1). The appearance of I_3/I_1 occurred at about the same applied stress amplitude as was determined by the filament stretching model.

In comparision to other biological systems that are highly sensitive to pH, ionic strength, and other factors, MC offers a facile and robust platform to experimentally probe the application of filament-based mechanical models. Interestingly, despite the enormous extent of heterogeneity in MC (amount and regiospecificity of methoxyl substitutions, broad M distributions, dispersity of fibrillar radii and contour lengths, and heterogeneity in cross-link functionality and density) MC gels can still serve as

powerful model polymer systems.

Chapter 6

Light Scattering of Dilute MC Solutions[i]

6.1 Introduction

This chapter addresses the phase behavior of dilute solutions of MC, to provide insight into the thermodynamic properties that govern the formation of the fibrillar structure at elevated temperature. Static light scattering (SLS) on dilute MC solutions was measured to determine the z-average radius of gyration (R_g), weight-average molecular weight (M_w), and second virial coefficient (A_2) at temperatures between 15 and 55 °C using a Zimm analysis. The R_g for a given M_w is consistent with semiflexible coils, and it was found that the theta temperature (T_θ) for MC in water with 48 ± 2 °C, and $A_2 < 0$ for $T > T_\theta$, consistent with a lower critical solution temperature (LCST). In addition, time-dependent scattering of solutions of MC below the theta temperature (T_θ) showed signs of slow aggregation, which is inconsistent with the concept of phase separation into two isotropic phases based upon Flory-Huggins theory. It was speculated that the underlying phase behavior for MC in water must account for the

[i]Adapted with permission from, McAllister, J. W. and Schmidt, P. W. and Dorfman, K. D. and Lodge, T. P. and Bates, F. S. *Macromolecules* **2015**, *Accepted for Publication.*

semiflexible nature of the chains, and therefore separate into an isotropic phase and a liquid crystalline nematic phase.

As described in the Section 1.3.2, the wavevector q is defined by the scattering angle θ, incident light wavelength (λ_0), and solvent index of refraction n,

$$q = |\mathbf{q}| = \frac{4\pi n}{\lambda_0} \sin\left(\frac{\theta}{2}\right). \tag{6.1}$$

The characteristic size scale for any particular wavevector can be approximated using the definition of Bragg diffraction, $D = 2\pi/q$. Scattered radiation probes reciprocal space, due to the inverse relationship between q and D. When scattering from molecules is essentially point scattering ($qR_g \ll 1$), it is referred to as the *Raleigh regime* and scattered light is defined as the Rayleigh ratio, R_θ, which is the ratio between the scattered intensity, I_{ex}, scaled by the sample-to-detector distance r,

$$R_\theta \equiv \frac{I_{ex} r^2}{I_0}. \tag{6.2}$$

I_{ex} has units of intensity per volume, whereas I_0 is just intensity, so R_θ has units of inverse length. The Rayleigh ratio has been accurately measured for many solvents at numerous incident wavelengths, so a photodiode signal can be calibrated to absolute R_θ.[90] R_θ is the magnitude of scattering as $q \to 0$. Using a virial expansion, R_θ can be related to dilute polymer concentration c and weight-average molecular weight M_w by,

$$\lim_{q\to 0} \frac{Kc}{R_\theta} = \frac{1}{M_w} + 2A_2 c + 3A_3 c^2 + \cdots \tag{6.3}$$

where A_2 and A_3 are the second and third virial coefficients, and K is a collection of optical constants given by,

$$K = \frac{4\pi(\partial n/\partial c)^2 n^2}{\lambda_0^4 N_A} \tag{6.4}$$

where n is index of refraction of the solvent, $\partial n/\partial c$ is the differential refractive index increment and N_A is the Avogadro constant. $\partial n/\partial c$ for MC in water was measured at

25 and 50 °C using a differential refractometer, and was determined to be 0.136±0.001 and $0.137 \pm 0.001 \mathrm{cm}^3\mathrm{g}^{-1}$, respectively (2.6) in agreement with previous reports.[20,65] A_2 and A_3 can be determined by the concentration dependence of the zero-q absolute scattering intensity R_θ. Positive values of A_2 indicate a good solvent, in which solvent-polymer interactions are preferred over polymer-polymer interactions. The opposite scenario occurs when A_2 is negative: a poor solvent, in which polymer-polymer interactions are favored. $A_2 = 0$ defines the special case where polymer-water and polymer-polymer interactions are nearly equivalent.

When the lengthscale associated with q increases so that it is slightly smaller than a polymer chain on average ($qR_\mathrm{g} \leq 1$), destructive interference between adjacent scattered photons causes a decrease in scattered intensity from R_θ. The form factor, $P(q)$,[95] is the ratio of scattered intensity I_s at a wavevector q to the scattered intensity as $q \to 0$ (R_θ),[88]

$$P(q) = \frac{I_\mathrm{s}(q)}{R_\theta} = \frac{1}{N^2} \sum_{j=1}^{N} \sum_{k=1}^{N} \frac{\sin(q\overrightarrow{r_{jk}})}{q\overrightarrow{r_{jk}}} \tag{6.5}$$

which is the double sum over all adjacent jth and kth segments for a polymer consisting of N segments and $\overrightarrow{r_{jk}}$ is the vector connecting the ith and jth segments. $P(q)$ can be estimated by a Taylor series, and then related to the radius of gyration of the polymer by,

$$P(q) = 1 - \frac{q^2 R_\mathrm{g}^2}{3} + \frac{q^4 R_\mathrm{g}^4}{40} + \cdots \tag{6.6}$$

The third term in Equation 6.6 can almost always be considered negligible, and is often expressed as Guinier's law,[95]

$$\lim_{c \to 0} P(q) \approx \exp\left(\frac{-q^2 R_\mathrm{g}^2}{3}\right). \tag{6.7}$$

If the scattering gives a linear plot of $\ln R_\theta$ vs. q^2, then R_g can be measured independent of the shape of the particle, which has a slope of $-R_\mathrm{g}^2/3$. This scattering region ($qR_\mathrm{g} \leq 1$) is called the *Guinier regime*. When a plot of $\ln R_\theta$ vs. q^2 is made at

finite concentration, an *apparent* radius of gyration is measured ($R_{g,app}$), and should be reported as such.

Equations 6.3 and 6.6 can be combined to give the Zimm equation,[27]

$$\frac{Kc}{R_\theta} = \frac{1}{M_w}\left(1 + \frac{q^2 R_g^2}{3} + \cdots\right) + 2A_2 c + \cdots \tag{6.8}$$

Scattering intensities from numerous wavevectors and concentrations combine to give a Zimm plot, illustrated in Figure 1.7, from which M_w, R_g, and A_2 can be determined. Equation 6.8 assumes the third virial coefficient, A_3, to be negligible, and is usually appropriate for polymers with $M < 10^4$.

For many polymer solutions it is accurate to apply corrections to the Zimm analysis proposed by Berry[155] which empirically minimizes contributions of A_3 by relating it to A_2 using the parameter,

$$\alpha_3 = \frac{3A_3 M_w/(A_2 M_w)^2 - 1}{2}) \tag{6.9}$$

and assuming $\alpha \approx -1/2$, since $A_3 < A_2$. The Berry-modified Zimm equations (often called Berry equations)[155,156] are given by

$$\lim_{q\to 0}\left(\frac{Kc}{R_\theta}\right)^{1/2} = \frac{1}{M_w^{1/2}}\Big(1 + A_2 M_w c + \alpha_3 (A_2 M_w c)^2 + \cdots\Big) \tag{6.10}$$

and,

$$\lim_{c\to 0}\left(\frac{Kc}{R_\theta}\right)^{1/2} = \frac{1}{M_w^{1/2}}\left(1 + \frac{q^2 R_g^2}{6} + \cdots\right). \tag{6.11}$$

Most polymers of modest M have measurable A_3 and modern light scattering software usually has the option to perform the approximation automatically. Equations 6.10 and 6.11 were developed for flexible polymers in a good solvent, and this correction is often appropriate to use, since A_3 will have an increasing effect with larger polymers.[155]

6.2 Results

6.2.1 Zimm plots of aqueous methylcellulose solutions

SLS measurements were taken on aqueous solutions of MC150, MC300, and MC530 at temperatures between 15 and 55 °C, with concentration ranges listed in Table 6.1. Using the approximation that $c^* \approx 1/[\eta]$, the chain overlap concentration (c^*), was estimated[88] from intrinsic viscosities ($[\eta]$), reported by Arvidsion et al.[52] For each polymer, care was taken so that each of the concentrations was well below the chain overlap concentration c^* to ensure the measured scattering would be of independent coils in solution. Dust can be problem for aqueous light scattering measurements, so the vials to contain the samples were meticulously cleaned, and MC samples prepared with 0.2-μm filtered ultrapure water with a conductivity of at least 18 MΩcm. MC solutions were filtered through a 0.45-μm filter prior to the SLS measurement. For each temperature, fresh aliquots of MC solutions were removed from the refrigerator at 5 °C and annealed at the desired test temperature for 1 hour prior to the measurement. Figure 6.1 shows Berry-modified Zimm plots for four temperatures of an MC300 solution. Each color represents a concentration, and the listed concentrations in the legends were adjusted slightly for density changes at different temperatures. R_g was obtained by extrapolation to $c = 0$ using Equation 6.11 (black squares). The concentration-dependent scattering in Figure 6.1 shows linear dependence, and this

Table 6.1: MC solutions for static light scattering

Sample	$[\eta]$[52] ($\mathrm{ml\,g^{-1}}$)	c^* ($\mathrm{mg\,mL^{-1}}$)	Conc. range ($\mathrm{mg\,mL^{-1}}$)
MC150	473 ± 3	2.1	$0.3 - 0.9$
MC300	736 ± 36	1.4	$0.2 - 0.6$
MC530	1093 ± 18	0.93	$0.1 - 0.5$

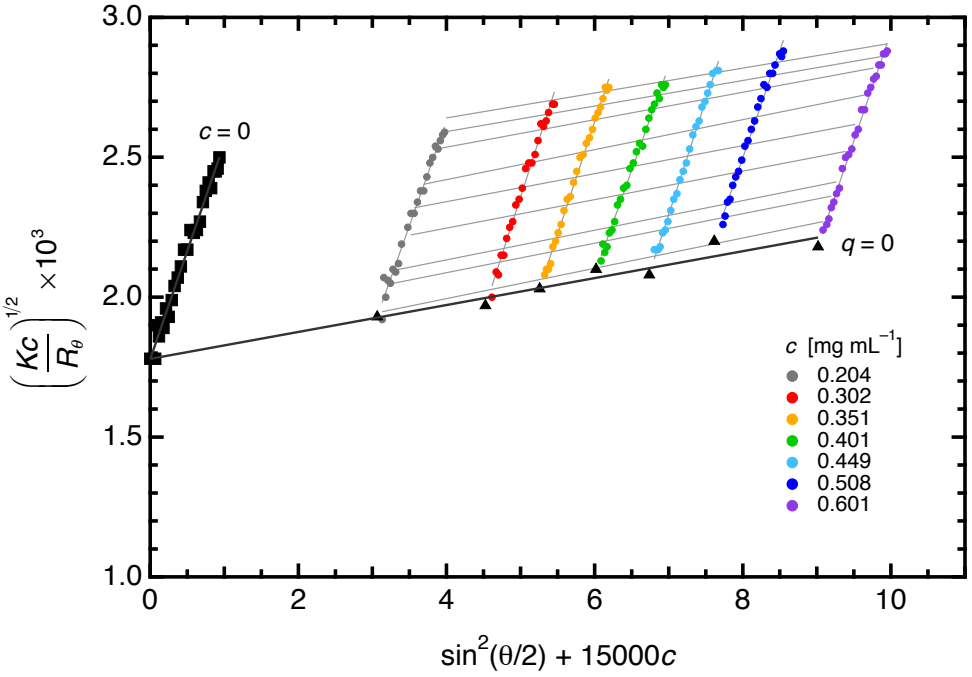

(a) 15 °C

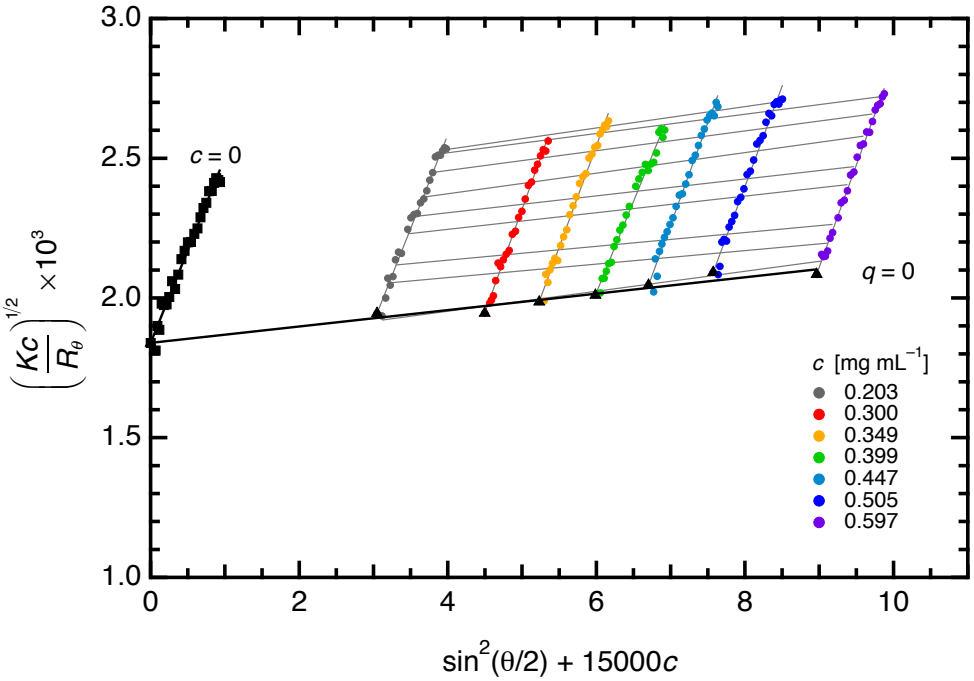

(b) 40 °C

Figure 6.1: Berry-modified Zimm plots of MC300 solutions at 15 and 40 °C.

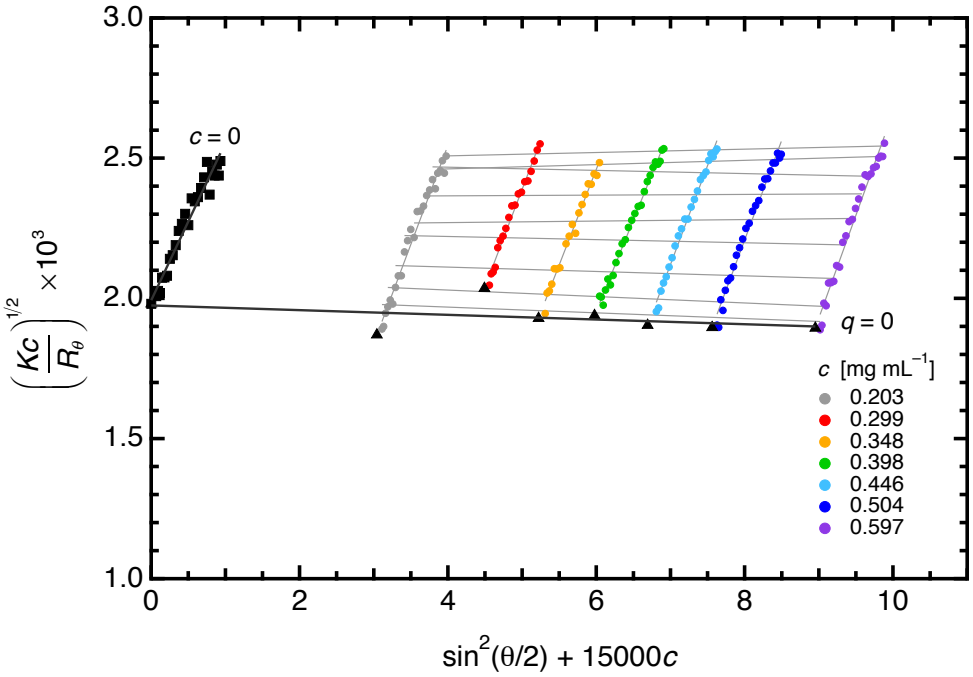

(c) 47 °C

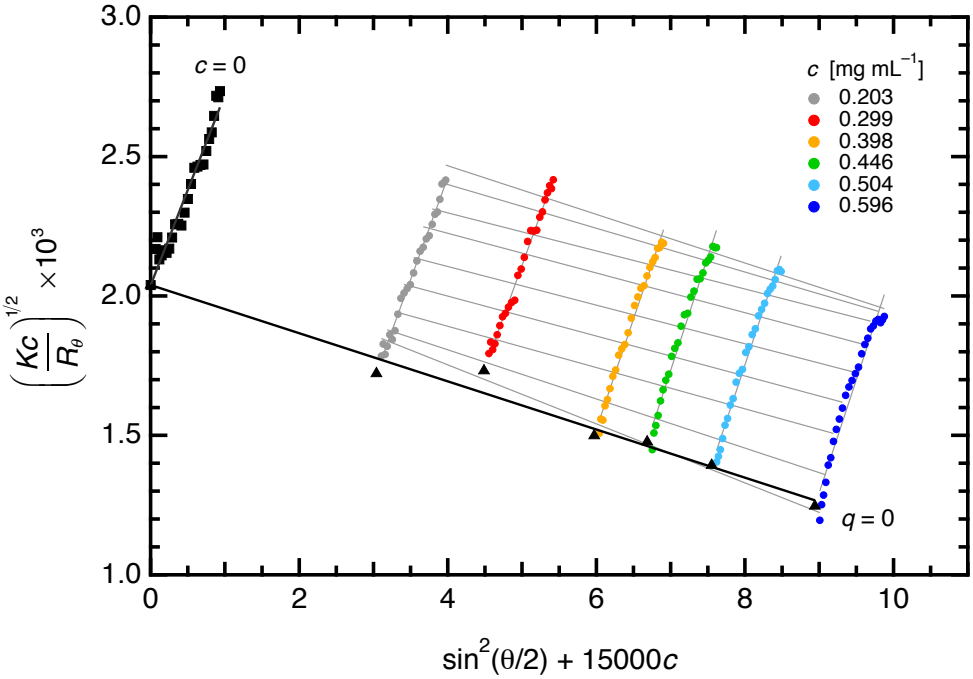

(d) 53 °C

Figure 6.1: (Continued) Berry-modified Zimm plots of MC300 solutions at 47 and 53 °C.

Table 6.2: Berry-modified Zimm plot results of MC300 from Figure 6.1

T (°C)	$M_w \times 10^{-5}$ ($\mathrm{g\,mol^{-1}}$)	R_g (nm)	$A_2 \times 10^3$ ($\mathrm{cm^3\,mol\,g^{-2}}$)
15	3.2 ± 0.2	61.5 ± 0.9	1.3 ± 0.2
40	3.0 ± 0.1	56.0 ± 0.9	0.8 ± 0.2
47	2.6 ± 0.2	49 ± 1	-0.2 ± 0.4
53	2.9 ± 0.2	56 ± 4	-2.2 ± 0.6

indicates that MC chains are in the Guinier regime (Equation 6.7), and are semi-flexible coils in solution for the period of the measurement. A_2 was obtained using Equation 6.10, and the slope of the lines fit to extrapolations to zero angle (black triangles). M_w was obtained by the common intercept between the $q = 0$ and $c = 0$ linear regressions, and is consistent from 15 to 53 °C. The data from the plots in Figure 6.1 are summarized in Table 6.2.

M_w for many temperatures of MC150, MC300 and MC530 can be noted in Figure 6.2. Molecular weights in this temperature range were determined to be equivalent within experimental uncertainty: $M_\mathrm{w} = (1.7 \pm 0.2) \times 10^5$ $\mathrm{g\,mol^{-1}}$, $(2.9 \pm 0.4) \times 10^5$ $\mathrm{g\,mol^{-1}}$, and $(5.3 \pm 0.8) \times 10^5$ $\mathrm{g\,mol^{-1}}$ for MC150, MC300, and MC530 respectively. These values are consistent with prior analysis by Arvidson et al. using size exclusion chromatography and intrinsic viscosity[52] Because M_w is independent of temperature within error, it infers that MC exists as independent coils in solution for the period of at least one hour after heating from 5 °C. A summary of R_g for the three polymers are displayed in Figure 6.3, which changes little between 15 and 55 °C, with $R_\mathrm{g} = 44.1 \pm 0.7$ nm, 57.5 ± 1.4 nm, and 70 ± 2 nm for MC150, MC300, and MC530, respectively.

A_2 is plotted as a function of inverse temperature for the three MC samples in Figure 6.4. The magnitude of A_2 comes from the slope of the lines fit to extrapolations

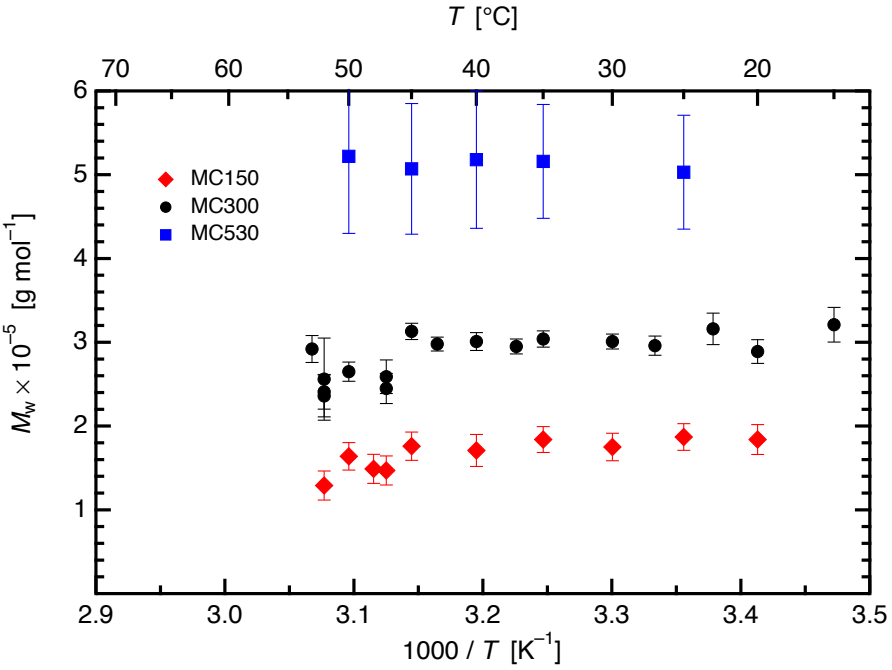

Figure 6.2: Weight-average molecular weights for three molecular weights of MC at temperatures between 15 and 55 °C.

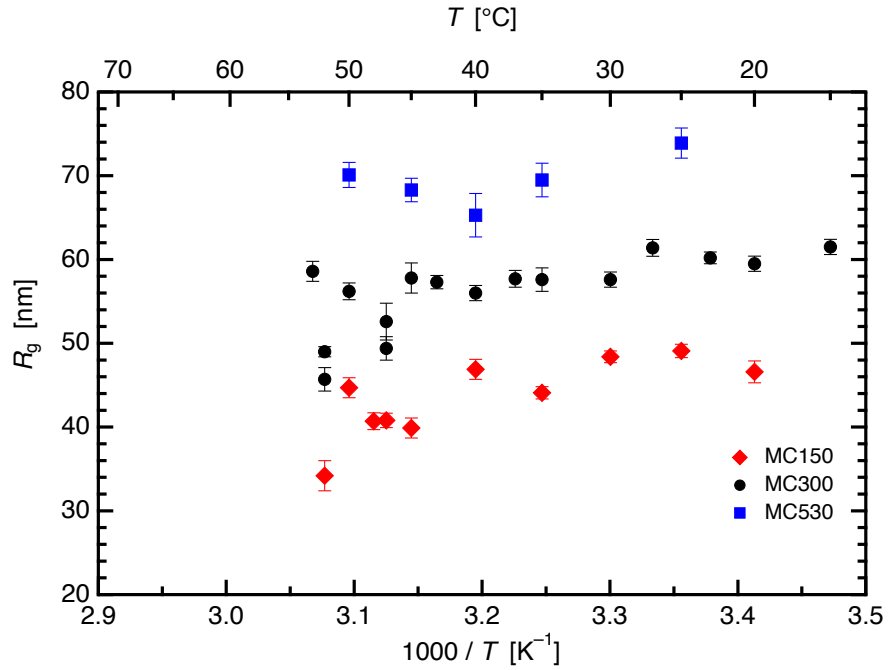

Figure 6.3: z-average radii of gyration for three molecular weights of MC at temperatures between 15 and 55 °C.

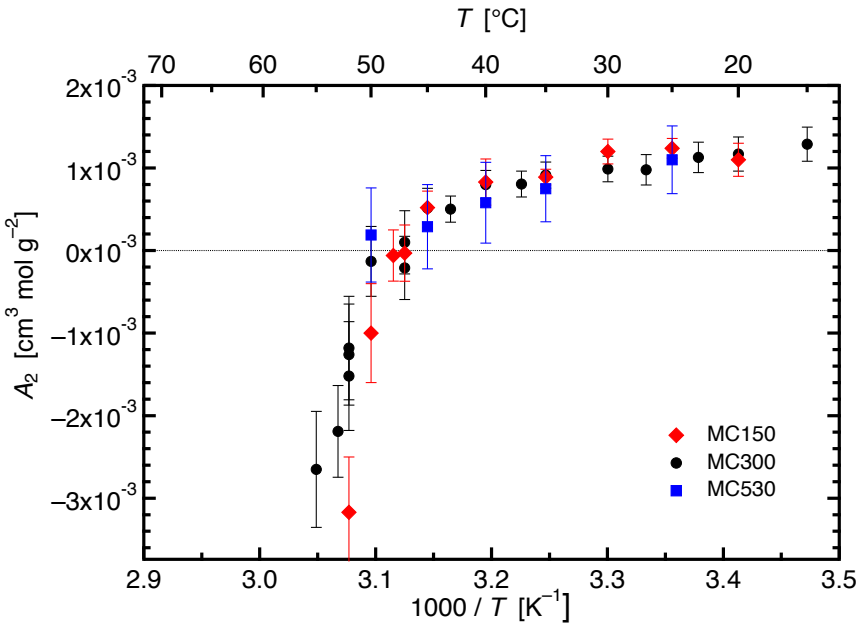

Figure 6.4: Second virial coefficients for three molecular weights of MC at temperatures between 15 and 55 °C.

to $q = 0$, and gives $A_2 > 0$ at 15 and 40 °C, $A_2 \approx 0$ at 48 °C, and $A_2 < 0$ at 53 °C. This indicates that water is good solvent for MC at temperatures less than about 48 °C, and a poor solvent for MC300 at temperatures above 48 °C. $T_\theta = 48 \pm 2$ °C, which is in good agreement with osmotic pressure measurements by Kato et al.[24] for a MC with $M = 5.1 \times 10^4$ g mol^{-1} and a $DS = 1.2$. As the temperature increases above 48 °C, the magnitude of $A_2 < 0$, suggests that water rapidly becomes an increasingly poorer solvent. It should be noted that at these concentrations (0.1 to 0.8 mg mL^{-1}) MC solutions do not turn visibly turbid on the timescale of the measurement, in agreement with turbidity measurements reported in Section 3.2.5.[52] An unusual feature of these results is the very strong temperature dependence of A_2 above 48 °C, which could indicate an intramolecular conformational change in MC prior to the growth of fibril aggregates, which has been suggested by optical rotation measurements of MC solutions.[18,157] However, a largely temperature-independent R_g (Figure 6.3) argues against this interpretation.

The assumptions made by Equations 6.10 and 6.11, that the third virial coefficient

A_3 can be empirically related to A_2, was developed for poly(styrene) solutions (a flexible polymer chain) in organic solvents[155] and has been widely accepted as a correction to most polymer solutions. A detailed study on the applicability of Equation 6.9 to semiflexible polymers like MC has not been performed to date, so it is possible that the empirical relationship between A_2 and A_3 is different for semiflexible polymers in solution, in which case the values obtained for A_2 should be interpreted cautiously. If the empirical relationship between A_2 and A_3 is different for semiflexible polymers, Equation 6.9 would have a different form, and A_2 will change slightly. However, semiflexible polymers like MC tend to have a smaller A_3 than flexible polymers of the same M,[158] so Equation 6.9 may suitable for semiflexible polymers. Comparative

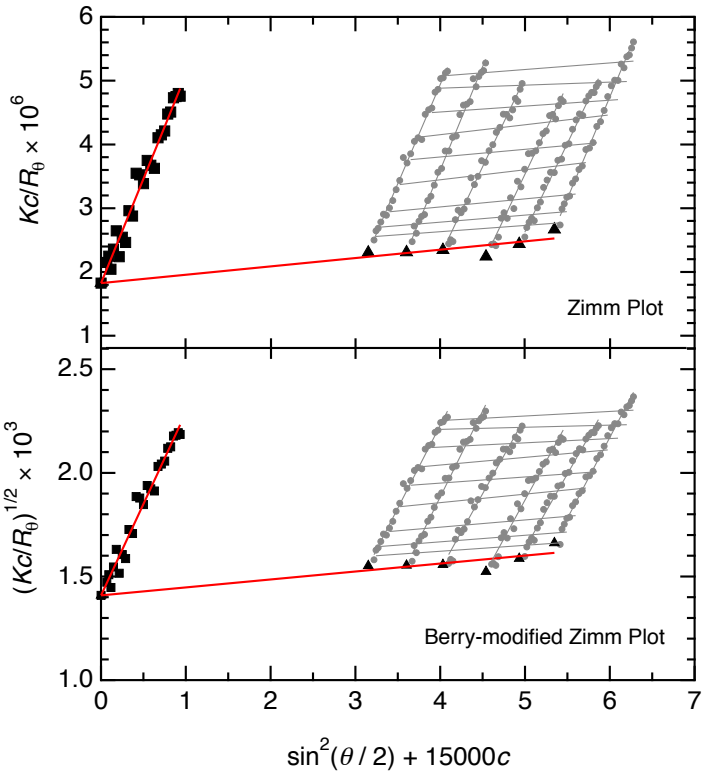

Figure 6.5: Comparative Zimm plots with and without the Berry approximation of an MC530 sample taken at 25 °C. The unmodified Zimm plot (top) gives $M_w = (5.5 \pm 0.8) \times 10^5$ g mol^{-1}, $R_g = 88 \pm 3$ nm, and $A_2 = (9.9 \pm 0.4) \times 10^{-4}$ cm^3 mol g^{-2}. The Berry-modified Zimm plot (bottom) gives $M_w = (5.0 \pm 0.7) \times 10^5$ g mol^{-1}, $R_g = 74 \pm 2$ nm,and $A_2 = (9.1 \pm 0.4) \times 10^{-4}$ cm^3 mol g^{-2}.

Zimm plots with and without the Berry approximation are provided in Figure 6.5. M_w for both plots are within the uncertainty of the measurement, as are A_2 (for the unmodified Zimm plot and Berry-modified Zimm plots, $A_2 = (9.9 \pm 0.4) \times 10^{-4}$ and $(9.1 \pm 0.4) \times 10^{-4}$ cm^3 mol g^{-2}, respectively). Interestingly, there is a sizable difference in R_g with and without the Berry approximation. Use of the Berry approximation gives $R_g = 74 \pm 2$ nm which is about 12% smaller than without $R_g = 88 \pm 3$. This is a larger difference than the uncertainty in the measurement (ca. 3%), and may give a clue regarding use of the Berry approximation for semiflexible polymers. A possible experiment to rigorously check the validity of Equation 6.9 for semiflexible polymers, a system with an organic solvent would be preferable so that dust contamination of the samples could be minimized. A solution of poly(n-hexyl isocyanate) in n-hexane studied by Jinbo et al.[158] would be a good model system.

6.2.2 Time-dependent SLS of dilute MC solutions

For the SLS measurements reported in Section 6.2.1 it was assumed that dilute solutions of MC were unchanging during the course of the measurement. In Chapter 3, it was found that the development of MC gels is time-dependent (Figure 3.5). To assess the stability of the homogeneous solutions for $A_2 < 0$ in Figure 6.4, a freshly prepared 0.3 mg mL^{-1} sample of MC300 was heated to 48 °C for one hour, and SLS data were collected. Then the sample was rapidly quenched (ca. 10 s) to 15 °C and scattering data collected again. Figure 6.6 shows Guinier plots of the associated data at 48 and 15 °C, which yield apparent radii of gyration, $R_{g,app} = 52 \pm 1$ nm and 55 ± 1 nm, respectively, consistent within experimental uncertainty with Figure 6.3. This confirms that the Zimm plots in Figure 6.1 and the parameters M_w, R_g, and A_2 in Figures 6.2 through 6.4 were collected prior to MC aggregation.

During the collection of data for the Zimm plots, some of the samples were left for a few days at 44 °C. After this time, there were found to be very small, (< 0.5 mm) precipitated aggregates visible in the MC solutions. This was puzzling, since

$T_\theta = 48 \pm 2$ °C, and it was previously assumed that MC chains would remain dissolved in solution if $A_2 > 0$. In order to study the precipitation of MC more closely, a 0.3 mg mL^{-1} solution of freshly prepared MC300 was heated from 5 to 40 °C, held at that temperature for 1 h, and then probed by SLS. Figure 6.7 displays the resulting R_θ versus q data (red points) modeled with Guinier's law, Equation 6.7, which gives $R_{g,app} = 51 \pm 2$ nm, which, within the range of the previous R_g obtained in Figure 6.3. The sample was annealed at 40 °C for 12 days (with gentle stirring, ca. 60 rpm) while periodically obtaining SLS data. Results shown in Figure 6.7 reveal that the scattering intensity increases dramatically during this time (violet, green, and blue data points). After 2 days at 40 °C, MC has aggregated to the point that the light scattering data lie outside the Guinier regime, which corresponds to features greater than about 1 μm in size. For these samples a Zimm analysis is not possible since $qR_g > 1$. Scattering intensity increases further with longer times, which is attributed to growth of larger aggregates of MC. The power slopes were added to the annealed

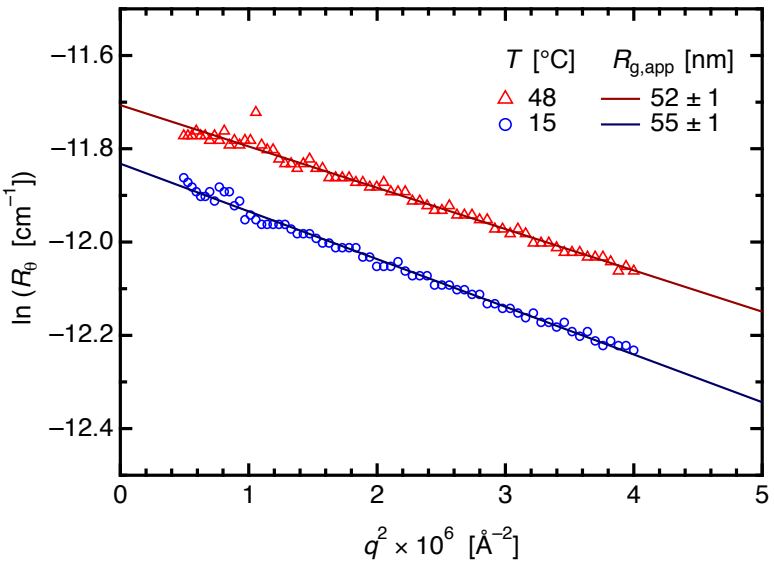

Figure 6.6: Guinier plots of a 0.30 mg mL^{-1} MC300 solution heated to 48 °C (red points) and held long enough to collect the data ($\sim$ 30 min) and the same sample cooled back to 15 °C (blue points). For the timescale of the measurement, MC solutions heated to T_θ for a short time remain as semiflexible coils in solution and do not aggregate.

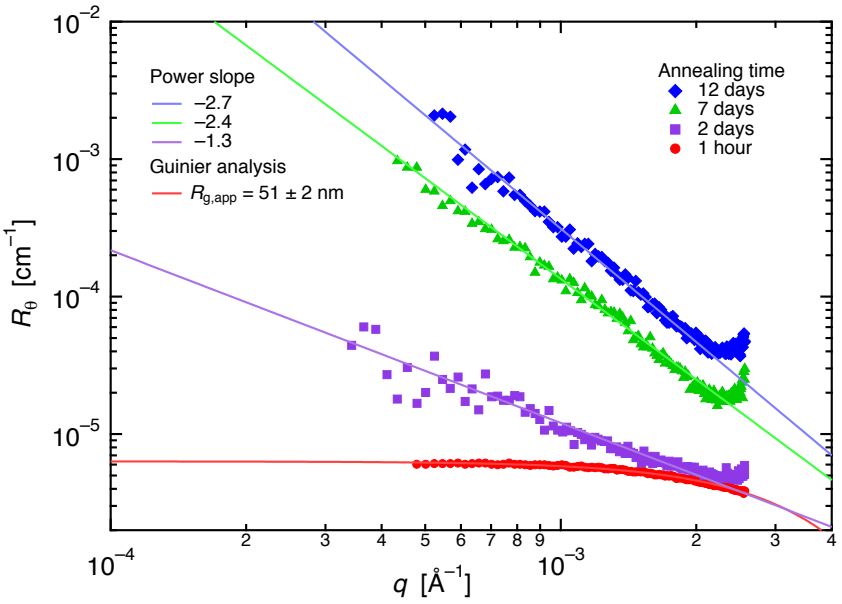

Figure 6.7: Light scattering from a 0.30 mg mL^{-1} solution of MC300 at 40 °C. At short times (up to a few hours) a Guinier function gives an apparent radius of gyration, and a Zimm plot analysis is appropriate. The increase in scattering indicates that MC slowly aggregates over time. The increase in scattering at $q \approx 0.002$Å^{-1} results from large-angle (>120°) backscattering.

data in Figure 6.7 as an indication of the change of the scattering intensity over time, which increases from a $R_\theta \sim q^{-1.3}$ dependence after 2 days to a $R_\theta \sim q^{-2.7}$ after 12 days. For times longer than 12 days, it was not possible to collect SLS data, as the particle sizes were too large to give a reliable signal. The upturn in

Figure 6.8: A photograph of the solution of MC300 from Figure 6.7 which has annealed for 15 days at 40 °C. Polymer aggregates are clearly visible (the white spot at the bottom of the vial is a stir bar).

scattering at about $2 \times 10^{-3}\text{Å}^{-1}$ is the result of high-angle ($> 120°$) backscatter from the micron-sized aggregates. After 12 days, dilute MC solutions from $0.2 < c < 0.6$ mg mL^{-1} have visibly precipitated aggregates of polymer similar to Figure 6.8. When the precipitated aggregates were centrifuged, filtered, and dried, less than 1% of MC by mass remains dissolved in the solution. This result is surprising, since $A_2 > 0$ at 40 °C, hence MC coils would be expected to remain in solution. This is very different behavior from MC solutions held in the refrigerator at 5 °C, which remain stable in solution for many weeks.

In order to elucidate the morphology of the MC aggregates from Figure 6.8, cryo-TEM experiments were conducted by Peter Schmidt on a 2.0 mg mL^{-1} solution of MC300 annealed at 40 °C for 21 days without stirring. Figure 6.9 confirmed the presence of fibrils in the sample. 2.0 mg mL^{-1} was the lowest concentration at which could reliably image multiple fibrils within the field of view in the cryo-TEM instrument, and was a higher concentration ($c \approx c^*$), than was used in the SLS measurements. Fibril diameters were determined to be 16 ± 4 nm using image analysis software (ImageJ, National Institutes of Health[110]), in agreement with the previous reports that dealt with more concentrated MC hydrogels in Figure 4.1.[16,112] It should be noted that the fibrils in the cyroTEM images in Figure 6.9 would not be visible to the naked

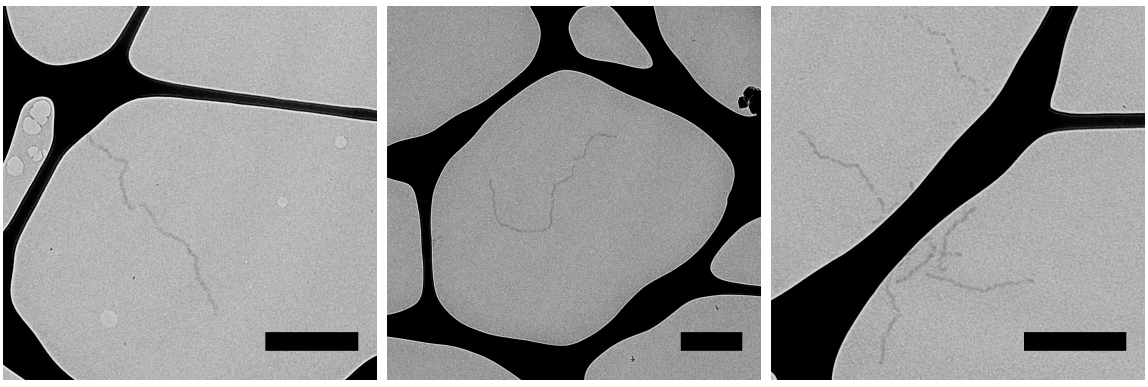

Figure 6.9: Cryo-TEM micrographs of a thin film of 2.0 mg mL^{-1} solution of MC300 after annealing for 21 days at 40 °C. The black web is the lacey carbon support grid, and the thread-like structures are MC fibrils. Image analysis of the fibrils gives an average diameter of 16 ± 4 nm. Scale bar denotes 500 nm. Images were taken by Peter Schmidt.

eye, so it cannot be definitively concluded that the micron sized aggregates have a fibrillar structure. Due to the cryo-TEM sample preparation technique (see Section 2.7), it was not possible to position one of the micron-sized aggregates onto a TEM grid; they were assumed to have been blotted away by the VitroBot device. However given the heterogeneity in the fibril network seen in Figure 4.1, and other images in Lott et al.,[112] taken along with the USANS of a MC hydrogel in figure 4.7, it was presumed that the micron-sized features visible in Figure 6.8 are aggregates of fibrils.

6.3 Discussion

This section considers possible explanations phase separation when $A_2 > 0$ in MC solutions. The evidence to suggest that MC solutions phase separate at high temperatures include visually turbid gels (as in Figure 1.3), dilute solutions of MC show suspended precipitate (Figure 6.8), and SLS measurements of dilute solutions indicate signs of aggregation (Figure 6.7). In order to calculate phase diagrams for MC, an effective interaction parameter χ_{eff} was extracted from the experimentally measured A_2. Spinodal curves were calculated using Flory-Huggins theory with a critical volume fraction (ϕ_{c}), critical effective interaction parameter ($\chi_{\text{c,app}}$), and temperature (T_{c}) expected of LCST-type behavior. A phase diagram is proposed consisting of semiflexible coils in solution that form a nematic liquid crystalline phase developed by Flory.[159–161] By fitting of the gel dissolution temperature (T_{sol}) from Chapter 3 to an equilibrium phase transition consisting of isotropic semiflexible coils and nematic liquid crystals, coexistence curves for MC are proposed. This section concludes with a speculative explanation of MC fibrils in terms of the phase diagram for semiflexible coils.

6.3.1 Estimation of χ_{eff} in MC Solutions

The Flory-Huggins model describes the free energy of mixing (ΔG_{m}) for polymer solutions is widely used, and is given by,

$$\frac{\Delta G_{\text{m}}}{k_{\text{B}}T} = (1-\phi)\ln(1-\phi) + \frac{\phi}{N}\ln\phi + \chi\phi(1-\phi). \tag{6.12}$$

The equation in this form (per $k_{\text{B}}T$) refers to the free energy of mixing per lattice site. The first two logarithmic terms estimate the combinatorial entropy of mixing, and the last term estimates the enthalpy of mixing. Formally, the Flory interaction parameter (χ) is the energy required exchange a lattice of solvent molecules with a single polymer chain. In order to account for some of the discrepancies of Equation 6.12, χ is often replaced with a new function, called the effective chi parameter, which includes all the excess free energy of mixing and expresses it as a sum of excess entropic (χ_{s}) and enthalpic ((χ_{h}) inconsistencies,

$$\chi_{\text{eff}} = \chi_{\text{h}} + \chi_{\text{s}} = \frac{A}{T} + B \tag{6.13}$$

where A and B are constants related to a specific polymer-solvent pair. For a polymer exhibiting LCST-type behavior as MC is presumed to be, $A < 0$ and $B > 0$. Hydrogen bonding plays an important role in the intermolecular interactions of MC in water, and must be considered for any interpretations of χ_{eff}. For solutions of poly(ethylene oxide) (PEO) in water, Matsuyama and Tanaka[162] and Dormidontova[163] accounted for hydrogen bonding effects by incorporating them into the χ_{h} term of Equation 6.13. Since PEO has a simple structure and predictable hydrogen bonding, this approach worked well. MC has a much more complex structure (Figure 2.2) with many possible hydrogen bonding donor and acceptor sites dependent on the methoxyl substitution at the C2, C3, and C6 carbons of the anhydroglucose units, which will make predicting ΔG_{m} in water more difficult. By the highly nonlinear form of A_2 versus inverse

temperature in Figure 6.4, it was expected that χ_{eff} would need additional terms to account for the aqueous solution behavior of MC.

χ_{eff} is related to the second virial coefficient A_2 determined in the previous section by,

$$\chi_{\text{eff}} = \frac{1}{2} - \frac{\overline{V_{\text{s}}} M_0^2 A_2}{\overline{V_{\text{p}}}^2} \tag{6.14}$$

where $\overline{V_{\text{s}}}$ and $\overline{V_{\text{p}}}$ are the molar volumes of solvent and polymer respectively. Equation 6.14 also gives the classic understanding of χ: at the theta temperature $A_2 = 0$ and $\chi = 1/2$; for poor solvents, $A_2 < 0$ and $\chi > 1/2$; and for good solvents, $A_2 > 0$ and $\chi < 1/2$. The estimation of χ_{eff} made from Equation 6.14 is for the solution average of for all MC molecules in the solution, and care should be taken if χ_{eff} is interpreted in terms of interaction energies of individual lattice sites. The values of A_2 from Figure 6.4 were plotted as χ_{eff} versus inverse temperature in Figure 6.10,

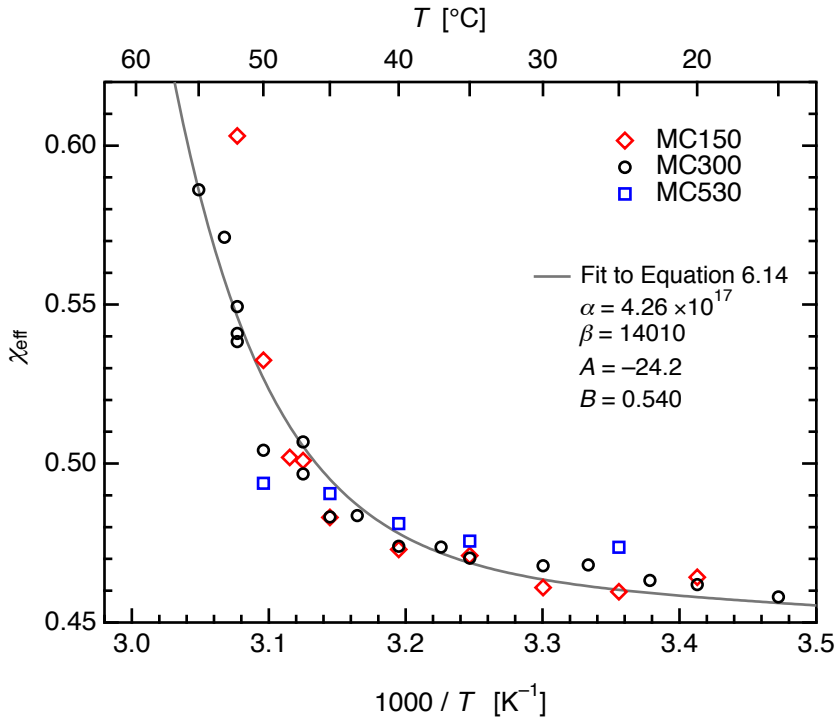

Figure 6.10: Values of χ_{eff} calculated from A_2 in Figure 6.4 using Equation 6.14. The curve is a fit of χ_{eff} to Equation 6.15. Phenomenologically, χ_{eff} has the form $AT^{-1} + B$ for $T < 30$ °C, and $\alpha \exp[\beta T^{-1}]$ for $T > 40$ °C.

using $\overline{V_s} = 18$ cm^3 mol^{-1}, $\overline{V_p} = 139.5$ cm^3 mol^{-1}, and $M_0 = 187.4$ g mol^{-1}. The resultant χ_{eff} retains the steep change for $T > 48$ °C, so it is clear that Equation 6.13 is not suitable to fit the data. Instead, the approach taken was to use a four-term expression for χ_{eff} to account for the nonlinearities in Figure 6.10 given by,

$$\chi_{eff} = \alpha \exp\left[\beta T^{-1}\right] + \frac{A}{T} + B \tag{6.15}$$

where α and β are phenomenological fitting parameters to account for other intermolecular interactions and hydrogen bonding not included in χ_h and χ_s at high temperatures (the values for these coefficients are shown on the plot in Figure 6.10). As with other polymers characterized by an LCST, the fit of χ_h to Equation 6.15 yields $A < 0$ and $B > 0$. This method is a phenomenological approach to estimate the complex intermolecular interactions aqueous MC solution. The fit to Equation 6.15 is good, and can serve as a crude estimation for modeling the thermodynamics of MC in water.

6.3.2 Flory-Huggins Theory Applied to Aqueous MC Solutions

With an estimation for χ_{eff} as a function of temperature in hand, calculations of possible phase diagrams of MC were made. The simplest choice is to use the Flory-Huggins model.[87] Spinodals were calculated using the stability criteria for polymer solutions given by the second derivative of free energy in Equation 6.12 with respect to concentration. The calculated spinodals for MC are shown in Figure 6.11, using values of χ_{eff} according to the curve in Figure 6.10 and Equation 6.15. The spinodals for three uniform molecular weights of MC with $M = 1.49 \times 10^5$, 2.98×10^5, and 5.30×10^5 g mol^{-1} (associated with samples MC150, MC300, and MC530 respectively) are shown in Figure 6.11. The green line indicates $T_\theta = 48$ °C determined from SLS measurements, and the green box indicates the temperature and concentrations at

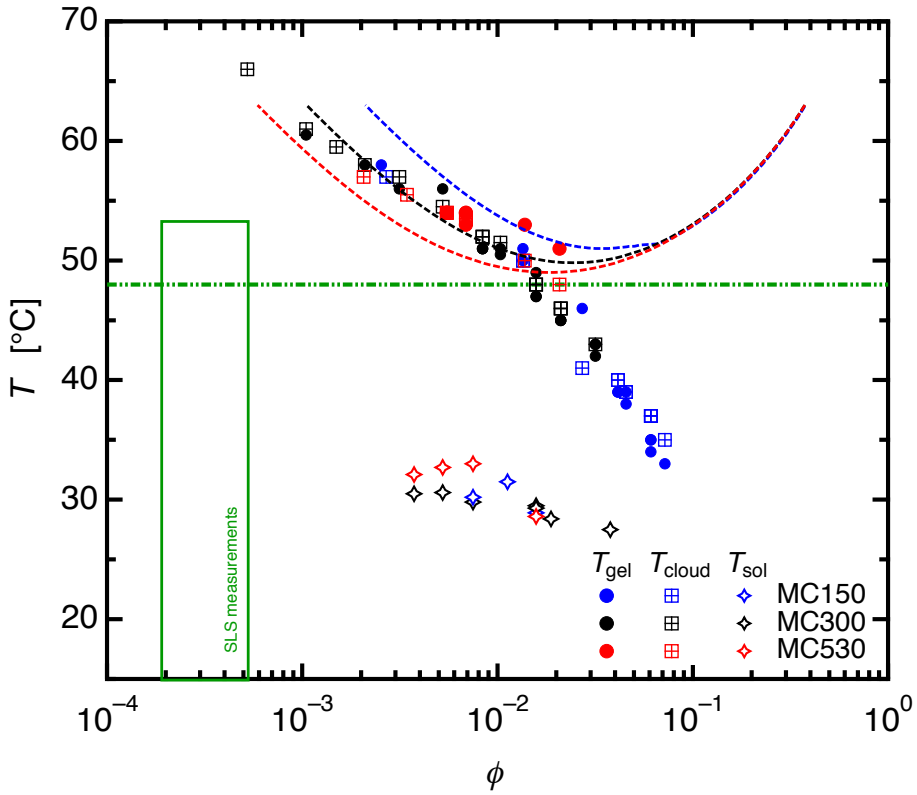

Figure 6.11: Calculated spinodals for MC in water using values for χ_{eff} determined by Figure 6.10 and Equation 6.15. The dashed lines are the spinodal curves for uniform M of MC with $M = 1.49 \times 10^5$, 2.98×10^5, and 5.30×10^5 g mol^{-1}, estimating the samples MC150, MC300, and MC530 respectively. $T_\theta = 48$ °C is denoted by the green line, and the box indicates the temperature and concentrations at which SLS measurements were taken. For reference the data for the sol-gel transition of MC is from Figure 3.17 from Arvidson et al.[52]is included.

which SLS measurements were taken. For reference, the data points for the sol-gel transition from Figure 3.17 are included as well. For low concentrations of MC (ca. $\phi < 0.02$), the spinodals calculated by Flory-Huggins theory agree reasonably well with the values of T_{gel} and T_{cloud}. The sol-gel transition of MC shows no indication of a critical composition ϕ_{c} predicted by Flory-Huggins, and for higher concentrations (ca. $\phi < 0.02$), there is very little agreement between values of T_{gel} and T_{cloud} and the calculated spinodals. The binodals predicted by Flory-Huggins (not calculated) would have the same basic shape as the spinodals, with a wider dish-like shape with the same ϕ_{c}. As a clarification, the spinodal curves calculated here have the appearance

of parabolas rather than the asymmetric concave-up shape because Figure 6.11 is a semilog plot.

Flory-Huggins model does not fully account for the phase separation in MC solutions, especially for $\phi > 0.02$. Equation 6.12 assumes isotropic phase separation into globules, and MC forms microstructured fibrils of uniform diameter. It is possible that for low concentrations an expression for the phase separation of MC may have a form similar to the Flory-Huggins model, but as noted in Figures 6.7 and 6.8, phase separation can occur even when $\chi_{\text{eff}} < 1/2$ (below 48 °C). Interestingly, as a consequence of the highly nonlinear χ_{eff} from Figure 6.10, the molecular weight dependence is much smaller than if χ_{eff} had a linear dependence with inverse temperature. In order to further understand the phase separation of MC in water, alternative theories based upon the semiflexible nature of MC in water were considered.

6.3.3 Liquid Crystallinity in Semiflexible Polymer Solutions

Flory has described the phase behavior of stiff rod-like chains and semiflexible coils that form nematic liquid crystals in solution.[159–161] based on a one-dimensional orientational (nematic) order parameter. To differentiate nomenclatures, this will be referred to as Flory's 1956 theory. For semiflexible chains, the free energy of mixing is given by,

$$\frac{\Delta G_{\text{m}}}{RT} = n_1 \ln \phi_1 + n_2 \ln \phi_2 - (n_1 + y n_2) \ln \left[1 - \phi_2 \left(1 - \frac{y}{x_{\text{k}}} \right) \right] - n_2 \left[\ln(x_{\text{k}} y^2) - y + 1 \right] + \chi x_{\text{k}} n_2 \phi_1 \quad (6.16)$$

where volume fractions of solvent and polymer are given by ϕ_1 and ϕ_2, respectively (and $\phi_2 = 1 - \phi_1$), and n_1, n_2 are the moles of solvent and polymer, respectively. x_{k} is the *axial ratio*, which describes the stiffness of the polymer chains and is estimated by the Kuhn length of a polymer chain and its effective diameter, $x_{\text{k}} = l_{\text{k}}/d$. y is a

parameter that describes the orientational order of the solution, and is defined by,

$$\phi_2 = \left(\frac{x_\mathrm{k}}{x_\mathrm{k} - y}\right)\left(1 - e^{-2/y}\right) \tag{6.17}$$

which ranges from $1 \leq y \leq x_\mathrm{k}$. When $y = 1$, the solution has perfect nematic order, and when $y = x_\mathrm{k}$, the solution is completely isotropic. The chemical potentials for the isotropic solution ($y = x_\mathrm{k}$) are given by

$$\left(\frac{\Delta\mu_1}{RT}\right)_{y=x_\mathrm{k}} = \ln(1-\phi_2) + \left(1 - \frac{1}{x_\mathrm{k}}\right)\phi_2 + \chi x_\mathrm{k}\phi_2^2 \tag{6.18}$$

and

$$\left(\frac{\Delta\mu_2}{RT}\right)_{y=x_\mathrm{k}} = \ln\frac{\phi_2}{x_\mathrm{k}} + (x_\mathrm{k}-1)\phi_2 - 2\ln x_\mathrm{k} + \chi x_\mathrm{k}(1-\phi)^2. \tag{6.19}$$

Note these Equations contain no n_2 terms, so the equilibrium phase diagram is dependent on x_k and not M. The chemical potentials for the nematic phase ($y = 1$) are different, and outside the context of this work. As a consequence of the parameter y, a solution of semirigid polymers (when $x_\mathrm{k} > 6.7$) can phase separate even at the athermal limit, $\chi = 0$ (unlike Flory-Huggins, Equation 6.12). This means that there will be some concentrations ϕ_2 in which a homogeneous solution will phase separate at any value of χ (or T).

Figure 6.12 displays the mean-field binodal curves for $x_\mathrm{k} = 20$, 35, and 50, which were calculated numerically from a MatLab script developed by Prof. Kevin Dorfman. This phase diagram explains why semiflexible polymers can phase separate even when the solvent is "good" (e.g. $\chi_\mathrm{eff} < 1/2$ and $A_2 = 0$). As chain stiffness (x_k) increases, the phase boundary between an isotropic solution (**I**) and two phases (**I** + **N**) is shifted to smaller ϕ and lower χ. For chains with $x_\mathrm{k} = 35$ and stiffer, $\chi = 1/2$ results in almost no thermodynamically stable solutions in the concentration range $0.001 < \phi < 1$.

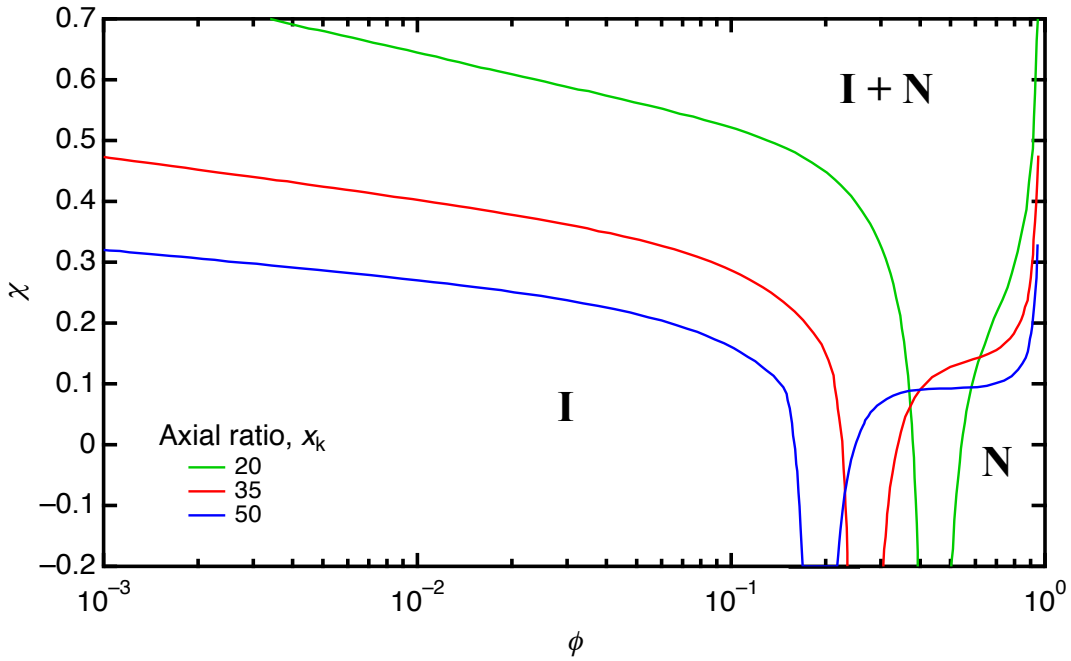

Figure 6.12: Mean-field coexistence curves for semiflexible coils with liquid crystalline elements for different axial ratios as predicted by Flory,[159–161] predicting isotropic (**I**) and nematic (**N**) phases. Calculated numerically using a MatLab script developed by Prof. Kevin Dorfman.

6.3.4 Phase Diagram for Aqueous Methylcellulose Solutions

Values of χ_{eff} for MC solutions were applied to the phase diagram for Flory's 1956 theory. The Kuhn length of MC has been measured to be 16 ± 3 nm,[123,124] with a chain diameter on the order of 0.5 nm, giving $x_k \approx 35$. Figure 6.13 shows sol-gel transition (T_{gel}) and gel-sol transition (T_{sol}) from Figure 3.17, plotted with respect to T and also χ_{eff}. Also included are binodal curves for $x_k = 23$, 26, and 28, which lie within the range of T_{gel} and T_{sol}. The Flory theory for semiflexible coils does have an appealing aspect with relation to the gelation of MC: there is no minimum in the phase boundary, which is consistent with T_{gel} and T_{sol}. Lateral intrachain hydrogen bonding along the cellulose backbone (especially between C2 and C6 groups on adjacent anhydroglucose units) likely contributes to chain stiffness, and at elevated

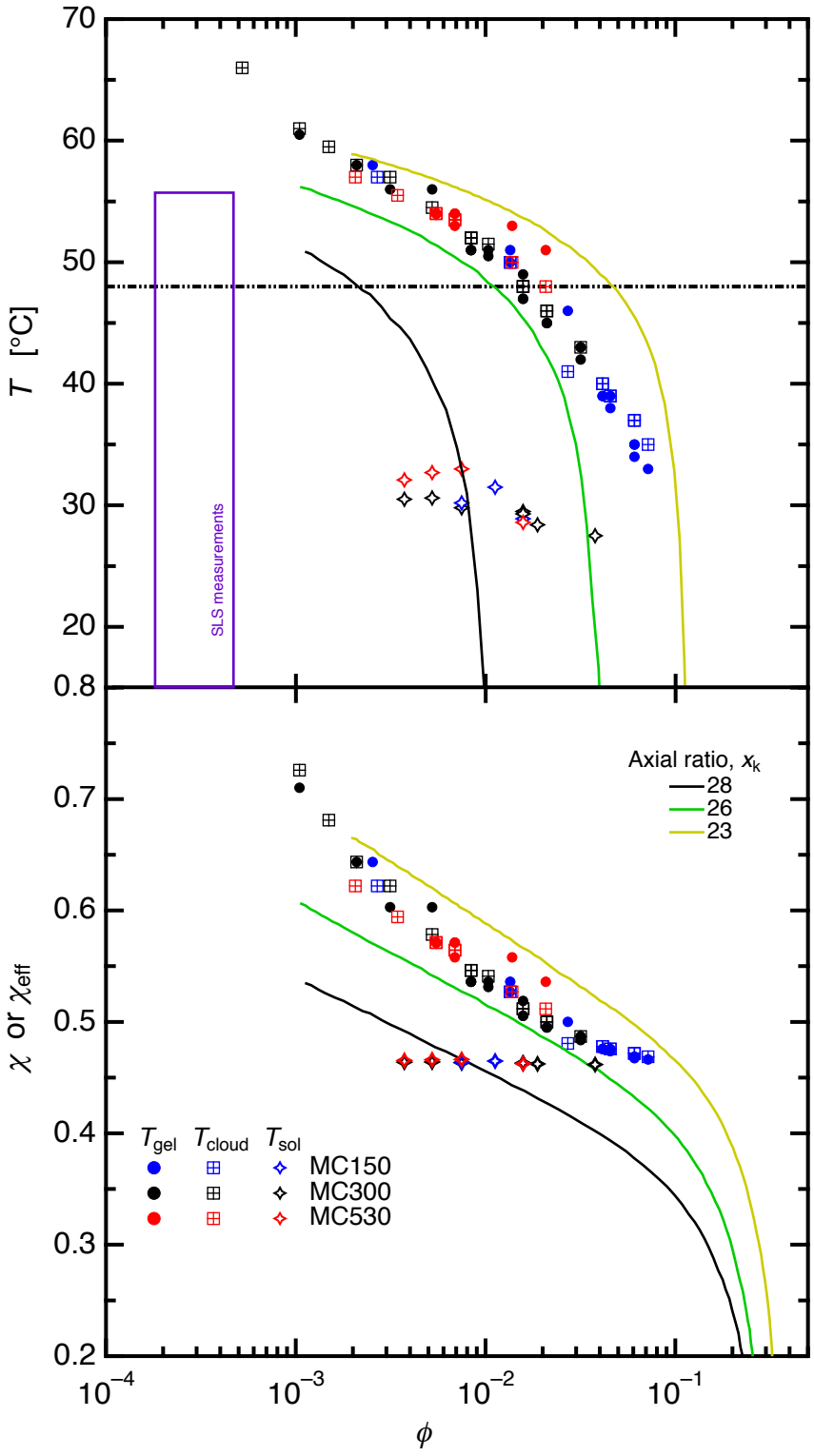

Figure 6.13: Binodal curves for $x_k = 23$, 26, and 28 plotted in terms of χ and T from Equation 6.15 compared to experimentally measured T_{sol} (on cooling, stars) and T_{gel} (on heating, circles) from Arvidson et al.[52]

temperature the breaking of hydrogen bonds may cause a decrease in l_k and x_k,[163] so $x_k = 35$ may not be required. T_{sol} obtained on cooling was associated to the binodal curve, while T_{gel} obtained on heating is within the metastable region between the binodal and spinodal curves. The stability limit for semiflexible chains from the isotropic solution has not been reported at the time of this writing, though the spinodal curve of the nematic phase was considered by Dorgan.[164,165] In principle, the spinodal would arise from Flory-Huggins theory, possibly with an added term to describe the orientational order (y). In this case, the spinodal curves plotted in Figure 6.11 are largely correct for low concentrations. It is unclear if there would be a "stability channel" or if $\chi_{c,eff}$ exists at a critical composition ϕ_c.

Given the assumptions that were made in the estimation of χ_{eff}, it is to be expected that the semiflexible binodal curves do not fit quantitatively to the experimental data. One assumption was that $A_2 = 0$ is the same temperature, 48 ± 2 °C for all concentrations of MC. Concentration dependence of χ_{eff} (and also A_2) is likely, since R_θ depends on $(\partial^2 G_m/\partial\phi^2)^{-1}$.[87] Incorporation of a $\chi_{eff}(\phi)$ term may improve upon the poor agreement between the coexistence curves to experimental data.[87] It is well known that hydrogen bonding of water changes significantly as temperature increases.[166–169] It is likely that changes in hydrogen bonding between water to water, water to MC, and also MC to MC changes at elevated and concentration and temperature in ways not predicted by these measurements. If A_2 for MC in water has a concentration dependence it is possible that it decreases with concentration, in which case the dashed line in Figure 6.13 would have a negative slope with concentration. As a consequence, the coexistence curves would also be shifted to lower χ_{eff} and T, and closer to the T_{sol} and T_{gel} data.

6.3.5 Methylcellulose Fibril Structure

Neither the Flory's 1956 theory nor the proposed phase diagram for MC considers the microstructured fibrils present in MC gel which were extensively characterized in Chapters 4 and 5. The internal structure of MC fibrils has not been determined, but there are a number of features of MC fibrils which are known from which a fibril structure can be proposed. First, they have uniform diameters independent of concentration and molecular weight, $d = 14 \pm 1$ nm. Second, the fibrils on average contain 40% polymer and 60% solvent. Third, the Kuhn length of MC chains is very close to the fibril diameter, at 16 ± 3 nm.[123,124] Fourth, MC solutions display a strong change in optical rotation of polarized light on heating and cooling[18,157] which correlates to the development of the gel modulus, with similar hysteresis. Recently, Kong et al.[170] studied the chain collapse of self-attractive semiflexible polymers using coarse-grained simulations. They reported that certain combinations of Kuhn length and intrachain attractive interactions result in toroidial and hollow cylinder shapes, rather than the familiar coil-to-globular transition of flexible polymers. It is hypothesized that phase separated MC consists of interconnected, collapsed toroids, which wind together axially to produce a fibril.

The aggregation of MC into fibrils is driven by the overarching isotropic-nematic phase separation, but because MC coils in solution are long (the degree of polymerization of MC150 is about 800) true nematic ordering on relevant timescales is unlikely. The fibrillar structure of MC is a kinetic compromise to achieve nematic ordering; MC chains collapse into somewhat disorganized cylinders or toroids, which entangle with one another axially driven by the nematic order parameter of the system. The proposed structure of MC fibrils as a disorganized, entangled helix is illustrated schematically in Figure 6.14. This structure of aggregated MC also can explain visual differences in the contour lengths of fibrils seen in cryo-TEM images. When the solution is heated to 70 °C, and the MC gel develops very quickly the structure is

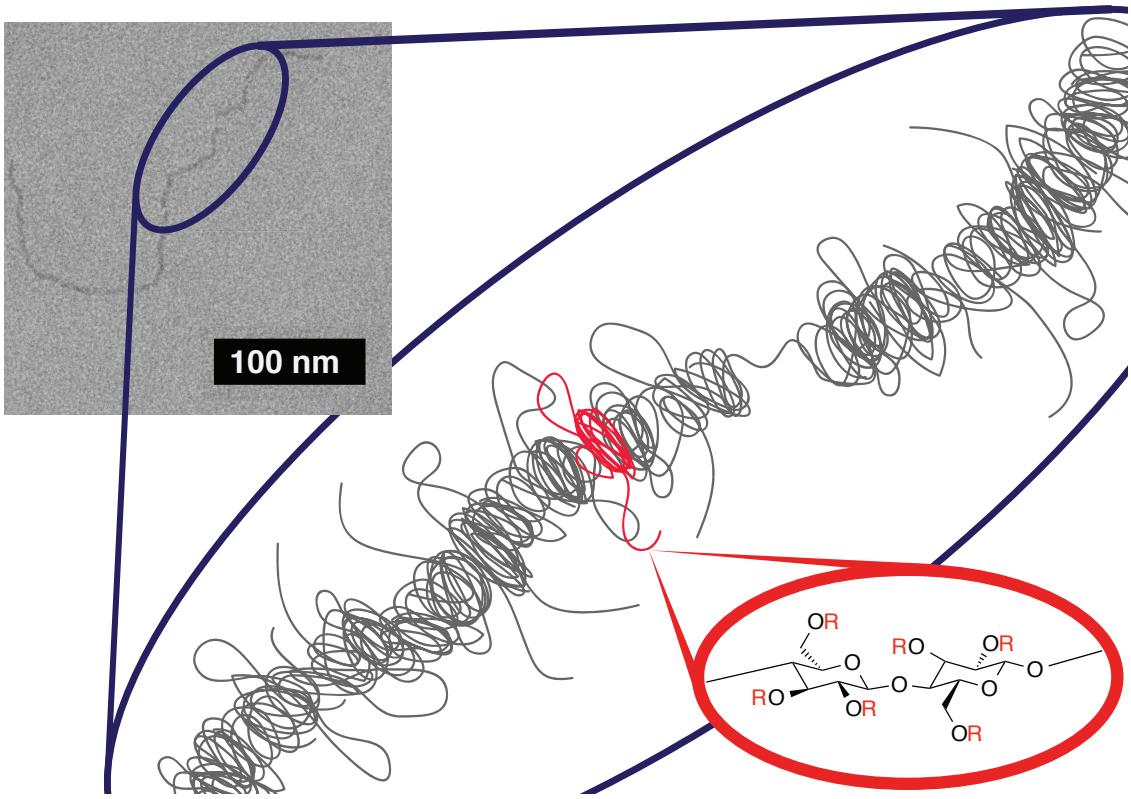

Figure 6.14: Schematic representation of the structure of MC fibrils. The fibrils consist of collapsed cylindrical and/or toroidal chains (predicted by Kong et al.[170]) assembled axially into fibrils so as to achieve a degree of nematic ordering. The portion of the fibril in red approximates a single MC chain with $N \approx 800$, corresponding to the MC150 sample.

very heterogeneous, with a wide distribution in contour lengths and significant fibril branches, (see Figure 4.1) yet when the solution is heated to a lower temperature like 40 °C (Figure 6.9) or 45 °C[31] fibrils are longer with fewer apparent branch points. When the solution is heated to just above T_{sol} fibrils develop under conditions of slow nucleation and slow growth, and when the solution is rapidly heated to 70 °C, fibrils nucleate and grow rapidly with many defects.

Cellulose, both as a crystalline material[171] and also in solution[172] has a helical pitch to the polymer backbone. It is hypothesized that the "handedness," of the cellulose backbone is carried over into MC solutions, in which the collapsed toroids assemble to retain the helical nature present in unsubstituted cellulose. If this is the case, the driving force to form fibrils would be a *cholesteric* order parameter rather

than a nematic one. Evidence for cholesteric liquid crystalline phases have been reported in cellulose in 1-allyl-3-methylimidazolium chloride,[172] ethylcellulose ($DS \approx 2.5$) in glacial acetic acid,[173] cellulose tricarbanilate in methyl ethyl ketone,[173] and hydroxypropylcellulose ($DS \approx 2.8$) in water.[174] In addition, aqueous MC solutions show a strong change in optical rotation on heating and cooling, which correlates to the as shown in Figure 6.15. Changes in the orientation of polarized light indicate a change in chiriality of a material, and if the collapsed coils within the MC fibrils consisted of a racemic mixture of left- and right-wound toroids, then the overall fibrillar gel would show very little difference in optical rotation from an isotropic solution. The consideration that many other cellulose derivatives (often with a degree of substitution higher than MC presented here) have shown evidence of a helical

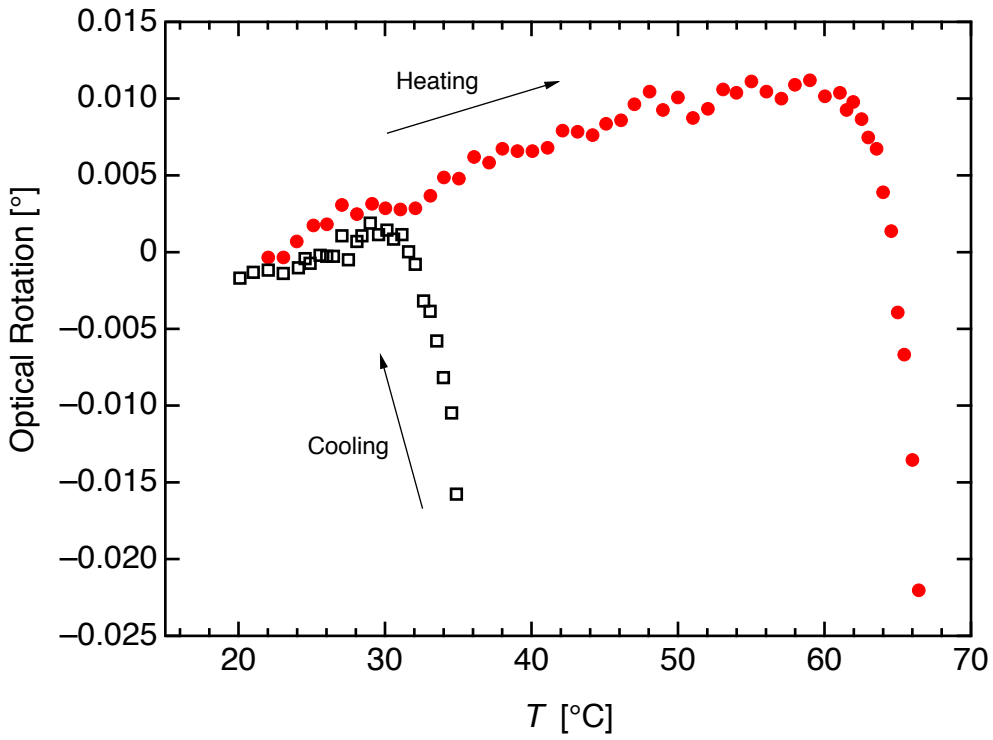

Figure 6.15: Optical rotation of a 2.5 wt% MC solution in water with a $M \approx 3.8 \times 10^5$ g mol^{-1} and $DS \approx 1.8$. Measurement was made on heating (red circles) and cooling (black squares) at 1 °C min^{-1}. There is a strong change in optical rotation angle at about 60 °C on heating which is close to T_{gel}, and 30 °C on cooling which is close to T_{sol}. Data from Yin et al.[157] Reproduced with permission from Wiley-Verlag, copyright 2006.

nematic liquid crystalline phase taken together with the optical rotation data from Figure 6.15 is the basis for the hypothesis presented that MC fibrils are cholesteric. The nature of the liquid crystalline element in MC hydrogels (nematic or cholesteric) is a possibility for future research efforts.

6.4 Summary

Static light scattering measurements were conducted on dilute solutions of three molecular weights of MC. M_w, R_g, and A_2 were determined over a range of temperatures between 15 and 55 °C. The theta temperature of MC in water was found to be $T_\theta = 48 \pm 2$ °C, in agreement with previous osmotic pressure measurements.[24] MC solutions begin to aggregate into micron-sized precipitates at temperatures at least as low as 40 °C (and $A_2 > 0$), determined by SLS and visible to the naked eye (Figures 6.7 and 6.8). MC aggregation occurs while water is still a "good" solvent ($T < T_\theta \approx 48$ °C), which is in conflict with Flory-Huggins theory, in which flexible coils phase separate into an isotropic 2-phase mixture when $A_2 < 0$ and $\chi > \chi_c$.

The phase behavior of semiflexible coils using the the 1956 theory developed by Flory[159–161] based upon the coexistence of isotropic and nematic phases, was compared to experimentally determined sol-gel transition (T_{gel}) and gel-sol transition (T_{sol}). It was proposed that MC fibrils are a kinetically-trapped compromise of the system in an effort to achieve nematic ordering, and the structure of MC fibrils are an aggregation of axially oriented toroidal and cylindrical shapes. Finally, it was speculated that the nature of the fibrils is cholesteric rather than nematic, and fibrils are comprised of collapsed toroidal shapes with the same chirality.

Chapter 7

Conclusion

7.1 Project Summary

Methylcellulose is a material with a long history, first reported synthesized in 1913,[15] with the reversible thermogelation first reported in 1935.[5] Despite the long history, there have been many conflicting publications throughout the years to describe the nature of the gel that forms on heating, ranging from a network of physically crosslinked chains to spinodal decomposition. Even 100 years after the reported synthesis of MC, the gel was poorly understood, and the goals of this project were to characterize the gelation of aqueous methylcellulose solutions on heating, describe the microstructure associated with MC hydrogels, and to propose a thermodynamic explanation for the development of the gel structure.

In chapter 3, a robust metric to define the sol-gel transition (T_{gel}) using dynamic mechanical spectroscopy (DMS) was utilized, based upon criteria developed by Winter and Chambon.[101,102] It was found that gelation of MC is independent of molecular weight, and dependent on concentration; higher concentrations undergo T_{gel} at lower temperatures than lower concentrations.[52] It was found that T_{gel} ranges from about 60 °C for solution concentrations at about 0.1 wt% to 40 °C for 5 wt% (see Figure 3.17). The rate at which the solution was heated also affected the T_{gel}, which suggested that

MC hydrogels develop by nucleation and growth. Hysteresis exists between heating and cooling, in which the gel phase persists on cooling and the gel-sol transition (T_{sol}) is approximately 30 °C, relatively independent of heating rate, concentration, and molecular weight. Measurements of solution turbidity were comparable to T_{gel} when the solutions were heated at similar rates for a wide range of concentrations and three molecular weights. A sol-gel transition diagram was prepared, which exhibits two regimes: clear solutions at low T, and cloudy gels at higher T, with a monotonic decrease in T_{gel} with increasing concentration.

Chapter 4 utilized small-angle neutron scattering (SANS) to characterize the fibrillar structure in MC hydrogels discovered using cryogenic transmission electron microscopy (cryo-TEM).[16,112] SANS data for MC hydrogels were modeled using a flexible cylinder model which resulted in a remarkably uniform diameter of 14 ± 1 nm, consistent with sizes determined from cryo-TEM images. The fibril diameter is uniform for concentrations from 0.01 to 5 wt% and numerous molecular weights, though the contour lengths of the fibrils vary from 100 nm or less up to microns in length. It was found that MC fibrils contain a significant portion of water: ca. 60% water and 40% polymer. The development of the fibrillar structure correlates to the to the growth on elastic modulus on heating, suggesting that the modulus of MC hydrogels is a consequence of a fibrillar network.

The elastic properties of MC hydrogels were investigated in Chapter 5.[134] MC gels undergo shear-hardening, in which the elastic modulus increases at high stresses. Accompanying shear hardening, the gels also exhibit negative first normal stress difference, in which the material contracts in directions normal to shear. The properties of shear-hardening and negative normal stresses are characteristic of filamentous gels, and is found in many in many protein gels. A model to describe the elasticity of actin gels[132] was successfully utilized to predict the onset of shear-hardening of MC hydrogels, using the fibril dimensions determined from Chapter 4. Large-amplitude

oscillatory shear responses were analyzed using a Fourier transform technique to detect the onset of higher-order frequency harmonics; the appearance of which agrees with the onset of shear-hardening predicted by the actin model. MC provides a robust platform to probe the nonlinear rheological responses of fibril based materials, as it is relative insensitive to changes in pH and ionic strength, unlike protein networks.

Chapter 6 investigated dilute MC solutions using static light scattering.[109] Weight-average molecular weights (M_w), z-average radii of gyration (R_g), and second virial coefficients (A_2) for three molecular weights of MC at many temperatures between 15 and 55 °C were determined from Berry-modified Zimm plots, and it was found that the theta temperature for MC was $T_\theta = 48 \pm 2$ °C, which was in agreement with earlier osmotic pressure measurements.[24] For $T > 48$ °C water is a poor solvent for MC indicated by $A_2 < 0$. For $T < 48$ °C water is a seemingly good solvent for MC indicated by $A_2 > 0$, although it was found that dilute solutions of MC will aggregate into micron-sized particles at 40 °C, over a period of days. This result is in conflict with Flory-Huggins theory, which predicts that a polymer solution phase separates into an isotropic 2-phase mixture when $A_2 < 0$. An effective interaction parameter χ_{eff} was estimated from measured values of A_2, from which binodal curves for MC were estimated using a theory developed by Flory in 1956 based upon coexistence of isotropic and nematic phases.[159,160] Finally, it was proposed that MC fibrils are a kinetically-trapped compromise driven by an underlying nematic ordering, and they are comprised of collapsed toroidal structures entangled together axially (see Figure 6.14).

7.2 Future Research Directions

There are a number of unanswered questions remaining with the conclusion of this work. A fibrillar structure was proposed in Chapter 6 and research is currently underway to elucidate how MC molecules are arranged into the uniform-diameter fibrils.

Small-angle x-ray scattering (SAXS) and wide-angle x-ray scattering (WAXS) of concentrated (ca 5 wt%) MC hydrogels may give some indication of the morphology of MC molecules within the fibrils. Another method which could be used to elucidate the sub-fibril structure is to collect anisotropic scattering from flow-aligned fibrils. The constructive interference produced by aligned fibrils would increase the scattering signal in directions parallel and/or perpendicular to the flow direction resulting anisotropic scattering, which may provide evidence of domain spacing or characteristic lengthscales within the fibrils. These experiments could be performed by measuring scattering data of a MC sample pumped through a quartz capillary and heated stage. The equipment is available for use at the 5ID-D beamline at the Advanced Photon Source of Argonne National Laboratory. Another possibility is to measure SANS under steady shear using a rheometer with specially designed quartz concentric cylinders. This equipment is available to use at the NIST Center for Neutron Research. In either case, collection of anisotropic scattering data from a solution of MC fibrils under shear would provide some insight into the nature of MC fibrils.

Another unknown question is the chiral nematic nature of MC fibrils, discussed briefly in Section 6.3.5. Cholesteric liquid crystals are usually detected by changes to polarized light, either by optical rotation[18,157] or by polarized light microscopy.[172,175] Figure 6.15 shows the optical rotation for one concentration of MC on heating and cooling at 1 °C min^{-1}, and if changes in optical rotation correlates to the sol-gel and gel-sol transitions, as well as the appearance of fibrils, then the case for cholesteric MC fibrils would be strengthened. If MC fibrils are chirial, a cholesteric order parameter could be used to construct a phase diagram for MC, it may agree better with experimental data than the nematic order parameter in Figure 6.13.

Additionally, kinetic experiments are underway to characterize aggregation rates for MC fibrils, based upon an Avrami analysis. Time-resolved experiments on MC solutions (using rheometry, small-angle x-ray scattering, SANS, or possibly optical rotation) can provide insight to the kinetic development of the fibrillar network. The

kinetics of nucleation and growth of MC fibrils can provide a complementary understanding of the phase separation of semiflexible coils compared to the phase separation of flexible ones.

With a measure of understanding of methylcellulose in hand, other cellulose ethers can be studied to determine the influence that the substituted groups and also the degree of substitution (DS) has on their solution behavior. Currently, the experiments on hydroxypropylmethylcellulose (HPMC) solutions are underway, using many of the same techniques that were presented in this dissertation. Interestingly, HPMC samples turn turbid at high temperatures similar to MC, yet in general do not develop a gel structure.[26,176] Other possible cellulose ethers that could be insightful to study are hyroxypropylcellulose (HPC), and also carboxymethylcellulose (CMC). CMC also forms hydrogels, and is a polyelectrolyte, which provides an interesting set of properties by itself.[177]

There are also a few open fundamental issues on a variety of topics which were noted during the course of this research project. One was the interpretation of large-amplitude oscillatory shear (LAOS) of microstructured materials (section 5.3.2). It is well agreed[80] that LAOS provides a wealth of structural information regarding microstructured fluids. However, there have been limitations to date in the interpretation of LAOS data. Many LAOS analysis techniques are based upon fitting the response to a Fourier series[147] or a Chebyshev series[81], and interpreting the resulting higher frequency harmonics. This is a robust technique mathematically, yet the proposal to assign a material function definition to higher order frequency harmonics is a slippery slope—how many definitions are required to describe the material? If a LAOS response has hundreds of frequency harmonics (as in Figure 5.17), interpretations of individual harmonics provides a flawed approach in my opinion. Interpretations of LAOS data is a field of active research, with Randy Ewoldt[86] and Simon Rogers[84] (both at the University of Illinois–Champaign-Urbana) utilizing the technique to better understand microstructured materials.

The applicability of the Berry approximation to the light scattering of dilute semiflexible coils is another topic that remains unanswered. The Berry approximation (Equation 6.9) was developed for flexible polymers (poly(styrene)) in organic solvents, and it is unclear if it is rigorously applicable to semiflexible coils. While the research presented in this dissertation found the difference in an unmodified Zimm plot and a Berry-modified Zimm plot to be within the uncertainty of the measurement (Figure 6.5), it was also found that R_g between the two plots was statistically different. SLS measurements in water inherently gives results with more noise than organic solvents, so experiments on the light scattering of semiflexible polymers in an organic solvents could quantitatively confirm whether the use of the Berry-approximation for semiflexible coils is appropriate. Jinbo et al.[158] previously evaluated the second (A_2) and third (A_3) virial coefficients for a solution of poly(n-hexyl isocyanate) in n-hexane, and concluded that semiflexible polymers tend to have a smaller A_3 than flexible polymers of the same M. This polymer-solvent system would be a good model system to evaluate the applicability of the Berry approximation to semiflexible coils.

MC is a fascinating material with a long history. As is often the case in research the discoveries made during this project have been significant, leading to many new questions. It is likely that given the rich morphology present, its interesting rheological behavior, and continued commercial significance, MC will continue to be relevant for many years to come.

Appendix A

Low-molecular weight MC

This section includes some discussion on a lower M sample of MC, denoted MC49, with $M_w = 4.6 \times 10^4$ g mol^{-1}. This material is different from the other MC samples by its synthesis method. Wood pulps are not available for lower M cellulose, so the material is prepared by subjecting longer-chain MC materials to acid hydrolysis to cleave $\beta(1 \rightarrow 4)$ glucose linkages and reduce the molecular weight. When T_{gel} and T_{cloud} for MC49 are considered, this lower-M sample undergoes gelation prior to $T_R < 86\%$, so by the this definition of T_{cloud}, this material will also include a clear gel phase. The definition $T_{gel} = T_{R,86\%}$ is not accurate for smaller M materials, and the importance of this deviation is still poorly understood. It could also be that the difference in T_{gel} and T_{cloud} for MC49 is a result of an unforeseen side reaction during its preparation by acid hydrolysis, which affects the gelling properties. Because a sample of this M is not available prepared from native cellulose, the discrepancies of MC49 cannot be rectified using the methods presented in Chapter 3.

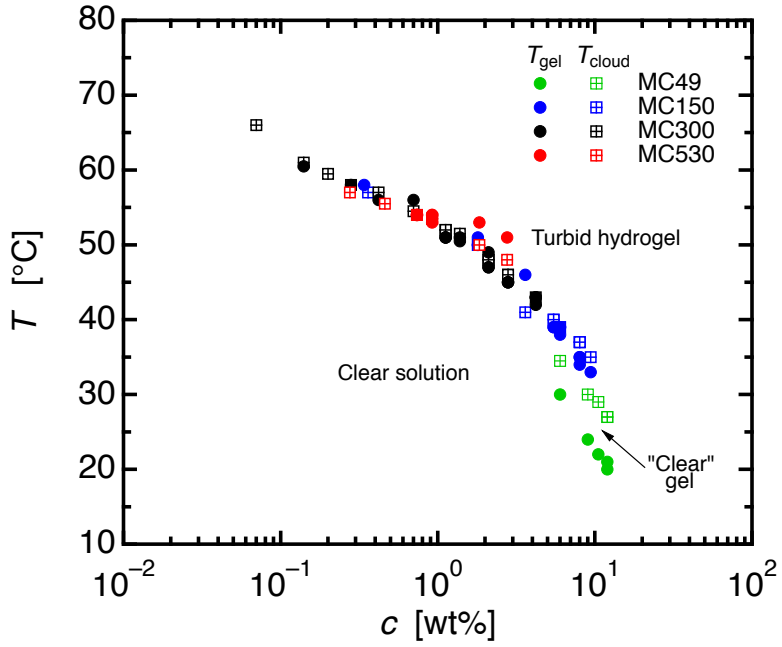

Figure A.1: Sol-gel transition diagram with T_{gel} and $T_R = 86\%$ on heating, including the lowest M sample: MC49, denoted in green. MC49 has different gelation properties than other M, and will gel about 5 °C prior to $T_R = 86\%$.

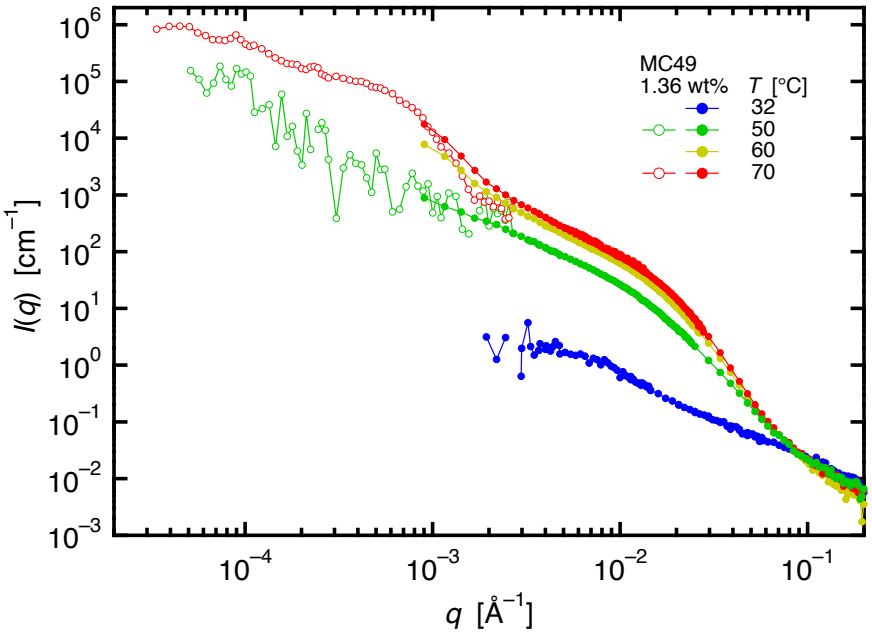

Figure A.2: SANS (filled circles) and USANS (open circles) for 1.36 wt% MC49 on heating. USANS data have been desmeared. 70 °C USANS seems to approach a plateau at lowest q, suggesting the longest lengthscale. This may explain the "clear gel" phase noted in Figure A.1.

Appendix B

S-type MC materials

The samples designated MC160S and MC400S are termed S-type MC samples, and have been prepared using an altered preparation technique from regular MC.[70] The

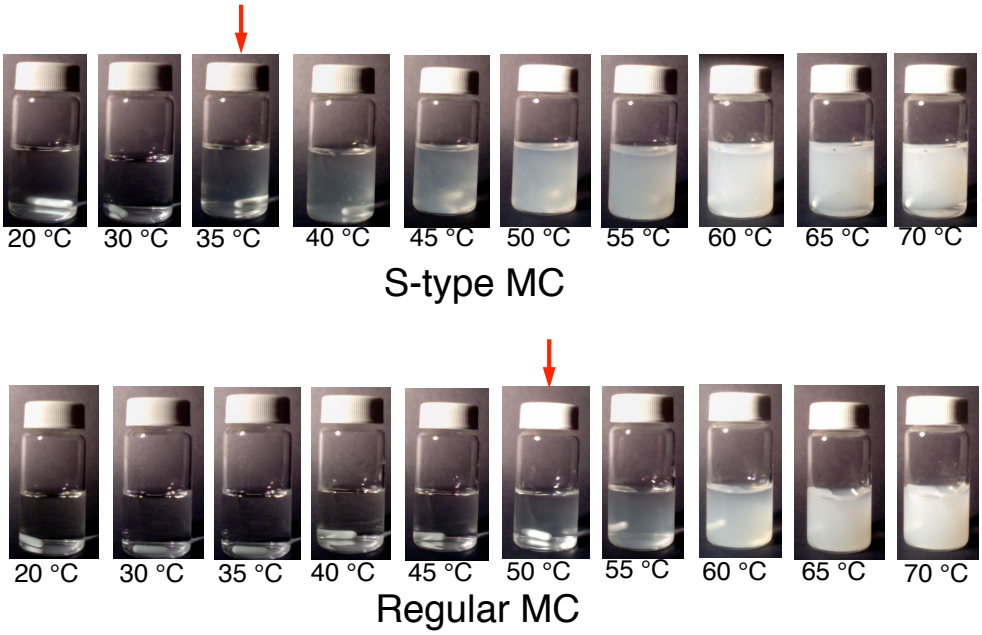

Figure B.1: Photographs of the thermogelation of S-type (MC400S) and regular (MC300) MC solutions on heating, with a concentration of 1.5 wt% MC, with 20 °C on the left slowly heated to 70 °C on the right. The red arrows indicate the appearance of the solution at $T_R \approx 86\%$.

practical difference is that S-type MC materials will undergo the transition to a turbid hydrogel at lower temperatures, with the hysteresis between heating and cooling also shifting. The degree of substitution (DS) of S-type MC materials is the same as regular MC, and additional factors influence the gelation of the S-type MC materials. Figure B.1 displays the visual difference in the onset of a turbid hydrogel on heating, and Figure B.2 shows the sol-gel and gel-sol transitions on heating and cooling, respectively using the Winter-Chambon technique.

Figure B.3 shows the sol-gel transition diagram on heating at 2 $^{\circ}\mathrm{C\,h^{-1}}$ for two molecular weights of S-type MC solution as compared to regular MC. S-type MC solutions of MC160S and MC400S undergo the sol-gel transition approximately 20 $^{\circ}$C lower then regular MC solutions of similar concentrations. While only one cloud point measurement was made on a solution of 1.5 wt% MC400S, $T_R = 86\%$ occurs at about the same temperature as T_{gel}. Like regular MC materials, gelation of S-type MC undergo a monotonic decrease in T_{gel} with increasing concentration. As with the lower sol-gel transition temperature, the "fibril shoulder" appears at lower temperature in SANS, seen in Figure B.4.

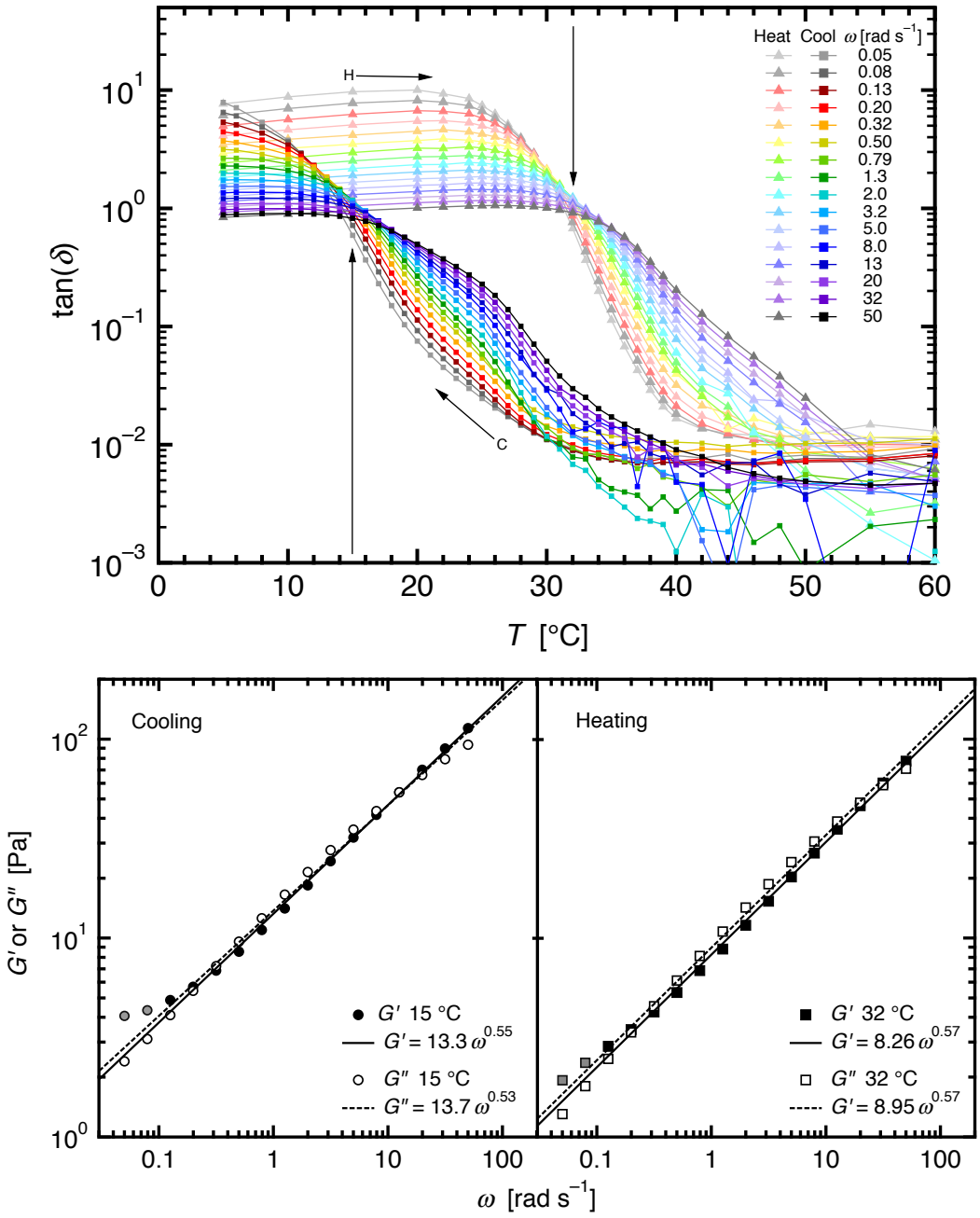

Figure B.2: Dynamic loss tangent (top) of a 1.8 wt% solution of MC400S heated slowly from 5 to 60 °C then cooled back to 5 °C. $T_{gel} \approx 32$ °C occurs at the frequency convergence of tan(δ), while $T_{sol} \approx 15$ °C. Heating and cooling rates are approximately 2 °C h^{-1} in the vicinity of the sol-gel transition. Frequency dependent moduli (bottom) of the sample at T_{gel} and T_{sol} denoted by arrows. Gray colored storage moduli points have been omitted from the fit.

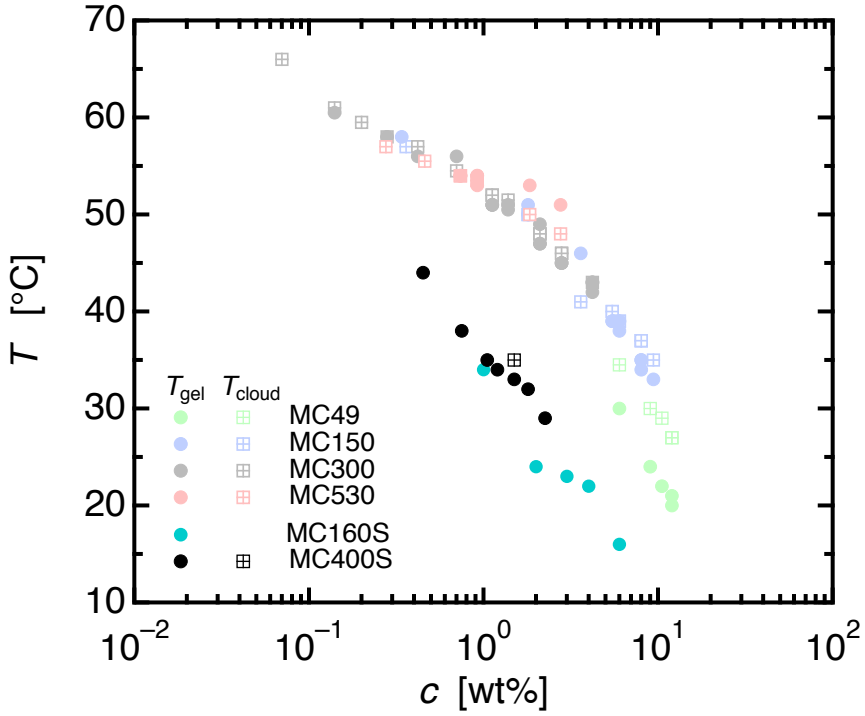

Figure B.3: Phase diagram for two molecular weights of S-type MC, compared to traditional MC. Heating rate was about 2 °C hr^{-1} for all the points displayed.

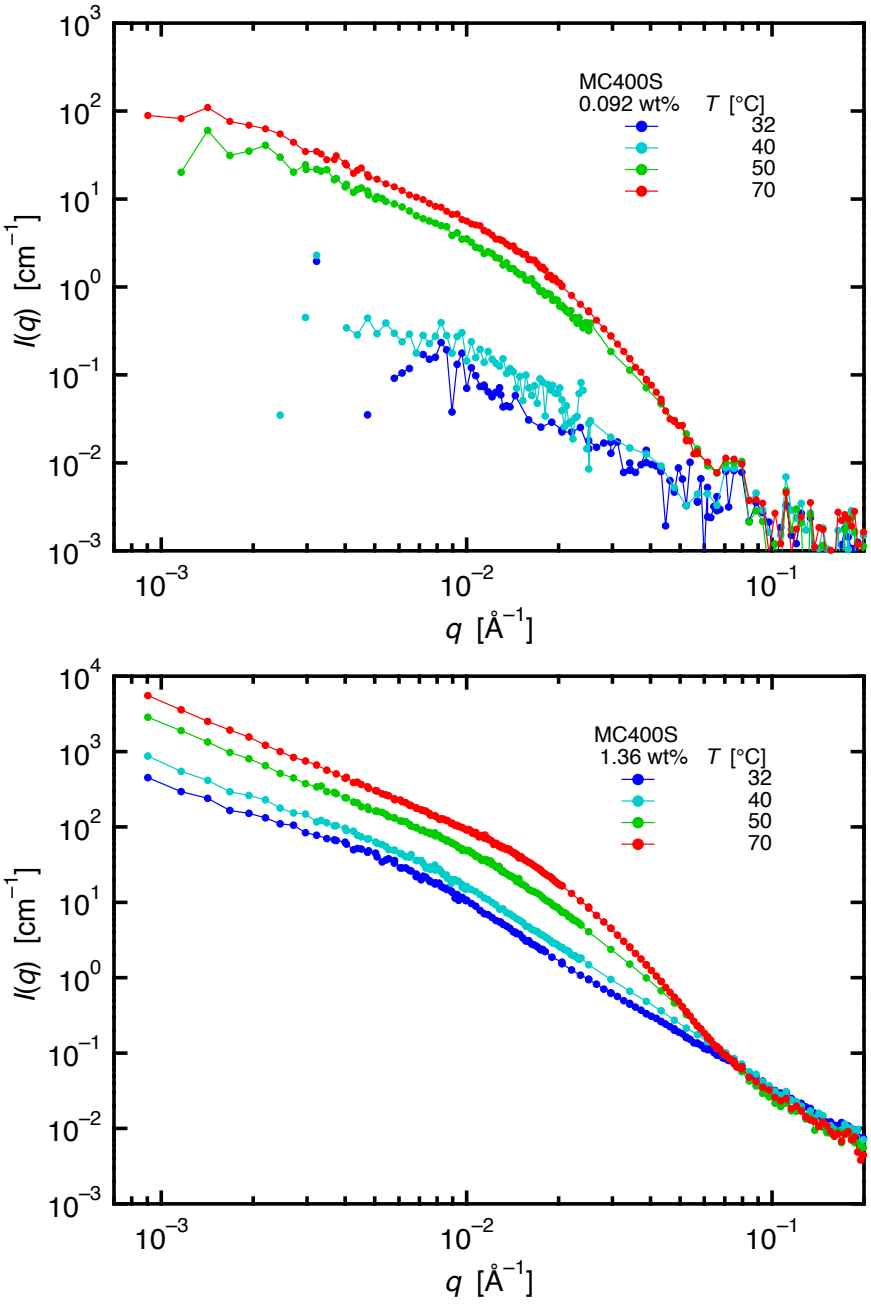

Figure B.4: SANS for two concentrations of MC400S: 0.092 wt% (top) and 1.36 wt% (bottom). The "fibril shoulder" develops at lower temperatures, consistent with the lower sol-gel transition temperature of S-type MC materials.

References

[1] Klemm, D.; Heublein, B.; Fink, H.-P.; Bohn, A. *Angewandte Chemie, International Edition* **2005**, *44*, 3358–93.

[2] Global Cellulose Acetate Market to Reach 980.5 Thousand Metric Tons by 2015, According to a New Report by Global Industry Analysts, Inc. 2011; http://www.prweb.com/releases/cellulose_acetate/flake_plastics_filter_tow/prweb8067438.htm.

[3] Cellulose Ethers Market by Derivative (Methyl, Ethyl, Hydroxyethyl, Hydroxypropyl & Carboxymethyl Cellulose), by Application & by Geography - Global Trends & Forecast to 2019. 2014; http://www.marketsandmarkets.com/Market-Reports/cellulose-ethers-market-782.html.

[4] Koch, W. *Industrial & Engineering Chemistry* **1937**, *29*, 687–690.

[5] Heymann, E. *Transactions of the Faraday Society* **1935**, *31*, 846.

[6] U.S. Code of Federal Regulations, 21 CFR Part 182.1480: Indirect Food Substances Affirmed as Generally Recognized as Safe. http://www.gpo.gov/fdsys/granule/CFR-2011-title21-vol3/CFR-2011-title21-vol3-sec182-1480.

[7] Majewicz, T. G.; Podlas, T. J. *Kirk-Othmer Encyclopedia of Chemical Technology*, 5th ed.; John Wiley & Sons, Inc.: Hoboken, NJ, USA, 2000; Vol. 5; pp 445–466.

[8] METHOCEL^{TM}The Right Food Ingredient for Making Healthier, Better Tasting and Better Looking Food. 2015; `http://pharmaandfood.dow.com/en/food-solutions/products/methocel`.

[9] Playing with Fire and Water. (2008, March 16). Methylcellulose Primer [Blog Post]. `http://www.playingwithfireandwater.com/foodplay/2008/03/methylcellulose.html`.

[10] Wirick, M. G. *Journal of Polymer Science Part A-1: Polymer Chemistry* **1968**, *6*, 1965–1974.

[11] METHOCEL^{TM}Efficient and Versatile - the Twin Faces of a Market Leader. 2015; `http://pharmaandfood.dow.com/en/pharma-solutions/products/methocel`.

[12] Ishikawa, T.; Watanabe, Y.; Takayama, K.; Endo, H.; Matsumoto, M. *International Journal of Pharmaceutics* **2000**, *202*, 173–178.

[13] Yin, L.; Hillmyer, M. A. *Molecular Pharmaceutics* **2014**, *11*, 175–185.

[14] Ricarte, R. G.; Lodge, T. P.; Hillmyer, M. A. *Molecular Pharmaceutics* **2015**, *12*, 983–990.

[15] Denham, W. S.; Woodhouse, H. *Journal of the Chemical Society, Transactions* **1913**, *103*, 1735.

[16] Lott, J. R.; McAllister, J. W.; Arvidson, S. A.; Bates, F. S.; Lodge, T. P. *Biomacromolecules* **2013**, *14*, 2484–8.

[17] Sarkar, N. *Journal of Applied Polymer Science* **1979**, *24*, 1073–1087.

[18] Haque, A.; Morris, E. R. *Carbohydrate Polymers* **1993**, *22*, 161–173.

[19] Sarkar, N. *Carbohydrate Polymers* **1995**, *26*, 195–203.

[20] Kobayashi, K.; Huang, C.-I.; Lodge, T. P. *Macromolecules* **1999**, *32*, 7070–7077.

[21] Desbrières, J.; Hirrien, M.; Ross-Murphy, S. B. *Polymer* **2000**, *41*, 2451–2461.

[22] Li, L.; Thangamathesvaran, P. M.; Yue, C. Y.; Tam, K. C.; Hu, X.; Lam, Y. C. *Langmuir* **2001**, *17*, 8062–8068.

[23] Li, L. *Macromolecules* **2002**, *35*, 5990–5998.

[24] Kato, T.; Yokoyama, M.; Takahashi, A. *Colloid and Polymer Science* **1978**, *256*, 15–21.

[25] Hirrien, M.; Desbrieres, J.; Rinaudo, M. *Carbohydrate Polymers* **1996**, *31*, 243–252.

[26] Fairclough, J. P.; Yu, H.; Kelly, O.; Ryan, A. J.; Sammler, R. L.; Radler, M. *Langmuir* **2012**, *28*, 10551–7.

[27] Zimm, B. H. *The Journal of Chemical Physics* **1948**, *16*, 1099.

[28] Heimenz, P.; Lodge, T. P. *Polymer Chemistry*, 2nd ed.; CRC Press: New York, 2007.

[29] Guillot, S.; Lairez, D.; Axelos, M. A. V. *Journal of Applied Crystallography* **2000**, *33*, 669–672.

[30] Takahashi, M.; Shimazaki, M. *Journal of Polymer Science Part B* **2001**, *39*, 943–946.

[31] Bodvik, R.; Dedinaite, A.; Karlson, L.; Bergström, M.; Bäverbäck, P.; Pedersen, J. S.; Edwards, K.; Karlsson, G.; Varga, I.; Claesson, P. M. *Colloids and Surfaces A: Physicochemical and Engineering Aspects* **2010**, *354*, 162–171.

[32] Chatterjee, T.; Nakatani, A. I.; Adden, R.; Brackhagen, M.; Redwine, D.; Shen, H.; Li, Y.; Wilson, T.; Sammler, R. L. *Biomacromolecules* **2012**, *13*, 3355–69.

[33] Hirrien, M.; Chevillard, C.; Desbrières, J.; Axelos, M.; Rinaudo, M. *Polymer* **1998**, *39*, 6251–6259.

[34] Nishinari, K. *Colloid & Polymer Science* **1997**, *275*, 1093–1107.

[35] Nishinari, K.; Hofmann, K. E.; Moritaka, H.; Kohyama, K.; Nishinari, N. *Macromolecular Chemistry and Physics* **1997**, *198*, 1217–1226.

[36] Takahashi, M.; Shimazaki, M.; Yamamoto, J. *Journal of Polymer Science Part B* **2001**, *39*, 91–100.

[37] Heymann, E.; Bleakey, H. G.; Docking, A. R. *The Journal of Physical Chemistry* **1937**, *42*, 353–368.

[38] Neely, W. B. *Journal of Polymer Science Part A: General Papers* **1963**, *1*, 311–320.

[39] Kelly, O. Investigations into the Phase Behaviour of Aqueous Cellulose Ethers. Ph.D. thesis, University of Sheffield, 2010.

[40] Yu, H. The Physics of Cellulose Ethers: Phase Separation and Gelation. Ph.D. thesis, University of Sheffield, 2011.

[41] Hofmeister, F. *Journal of the Chemical Society, Abstracts* **1889**, *56*, 425.

[42] Wilson, E. K. *Chemical & Engineering News Archive* **2007**, *85*, 47–49.

[43] Chevillard, C.; Axelos, M. A. V. *Colloid & Polymer Science* **1997**, *275*, 537–545.

[44] Taribagil, R. R.; Hillmyer, M. a.; Lodge, T. P. *Macromolecules* **2009**, *42*, 1796–1800.

[45] Taribagil, R. R.; Hillmyer, M. a.; Lodge, T. P. *Macromolecules* **2010**, *43*, 5396–5404.

[46] Zhou, C.; Hillmyer, M. A.; Lodge, T. P. *Macromolecules* **2011**, *44*, 1635–1641.

[47] Rees, D. *Chemistry and Industry* **1972**, 630–636.

[48] Tanaka, F.; Edwards, S. F. *Macromolecules* **1992**, *25*, 1516–1523.

[49] Tanaka, F. *Advances in Colloid and Interface Science* **1996**, *63*, 23–40.

[50] Tanaka, F. *Polymer Physics*; Cambridge University Press: Cambridge, 2011.

[51] Villetti, M. A.; Soldi, V.; Rochas, C.; Borsali, R. *Macromolecular Chemistry and Physics* **2011**, *212*, 1063–1071.

[52] Arvidson, S. A.; Lott, J. R.; McAllister, J. W.; Zhang, J.; Bates, F. S.; Lodge, T. P.; Sammler, R. L.; Li, Y.; Brackhagen, M. *Macromolecules* **2013**, *46*, 300–309.

[53] Tanaka, H. *Journal of Physics: Condensed Matter* **2000**, *12*, R207–R264.

[54] Tanaka, F.; Ishida, M. *Journal of the Chemical Society, Faraday Transactions* **1995**, *91*, 2663.

[55] Zheng, P.; Li, L.; Hu, X.; Zhao, X. *Journal of Polymer Science, Part B* **2004**, *42*, 1849–1860.

[56] Huang, W.; Dalal, I. S.; Larson, R. G. *The Journal of Physical Chemistry B* **2014**, *118*, 13992–14008.

[57] Ruta, B.; Czakkel, O.; Chushkin, Y.; Pignon, F.; Nervo, R.; Zontone, F.; Rinaudo, M. *Soft Matter* **2014**, 4547–4554.

[58] Jee, A.-y.; Curtis-Fisk, J. L.; Granick, S. *Macromolecules* **2014**, *47*, 5793.

[59] McKee, J. R.; Hietala, S.; Seitsonen, J.; Laine, J.; Kontturi, E.; Ikkala, O. *ACS Macro Letters* **2014**, *3*, 266–270.

[60] Hu, Z.; Patten, T.; Pelton, R.; Cranston, E. D. *ACS Sustainable Chemistry & Engineering* **2015**, *3*, 1023–1031.

[61] Staudinger, H. *Berichte der deutschen chemischen Gesellschaft (A and B Series)* **1920**, *53*, 1073–1085.

[62] Mischnick, P. *Cellulose* **2002**, *8*, 245–257.

[63] Zeisel, S. *Monatshefte für Chemie und verwandte Teile anderer Wissenschaften* **1886**, *7*, 406–409.

[64] Kern, H.; Choi, S.; Wenz, G.; Heinrich, J.; Ehrhardt, L.; Mischnick, P.; Garidel, P.; Blume, A. *Carbohydrate Research* **2000**, *326*, 67–79.

[65] Spurlin, H. M. *Journal of the American Chemical Society* **1939**, *61*, 2222–2227.

[66] Dow Answer Center: METHOCEL^{TM}Bulk Density. 2011; `http://dowac.custhelp.com/app/answers/detail/a_id/774`.

[67] Usmanov, K. U.; Sushkevitch, T. I. *Journal of Polymer Science* **1962**, *58*, 1325–1331.

[68] Levi, M.; Sellen, D. *Carbohydrate Research* **1967**, *5*, 351–355.

[69] Sun, R. C.; Tomkinson, J. *Separation Science and Technology* **2005**, *39*, 391–411.

[70] Reibert, K. C.; Conklin, J. R. Cellulose Ether Having Enhanced Gel Strength and Composition Containing It. US Patent US6228416 B1. 2001.

[71] Takahashi, S.-I.; Fujimoto, T.; Miyamoto, T.; Inagaki, H. *Journal of Polymer Science Part A* **1987**, *25*, 987–994.

[72] Arisz, P. W.; Kauw, H. J.; Boon, J. J. *Carbohydrate Research* **1995**, *271*, 1–14.

[73] Desbrières, J. *Carbohydrate Polymers* **1998**, *37*, 145–152.

[74] Itagaki, H.; Tokai, M.; Kondo, T. *Polymer* **1997**, *38*, 4201–4205.

[75] Liu, H.; Zhang, L.; Takaragi, A.; Miyamoto, T. *Polymer Bulletin* **1998**, *40*, 741–747.

[76] Sekiguchi, Y.; Sawatari, C.; Kondo, T. *Carbohydrate Polymers* **2003**, *53*, 145–153.

[77] METHOCEL™Cellulose Ethers Technical Handbook. 2002; `http://www.dow.com/dowwolff/en/pdf/192-01062.pdf`.

[78] Costello, B. The AR-G2 Magnetic Bearing Rheometer. 2005; `http://www.tainstruments.com/main.aspx?n=2&id=181&main_id=232&siteid=11`.

[79] Franck, A. Understanding Instrument Inertia Corrections in Oscillation. 2005; `http://www.tainstruments.com/main.aspx?n=2&id=181&main_id=499&siteid=19`.

[80] Hyun, K.; Wilhelm, M.; Klein, C. O.; Soo, K.; Gun, J.; Hyun, K.; Jong, S.; Ewoldt, R. H.; Mckinley, G. H. *Progress in Polymer Science* **2011**, *36*, 1697–1753.

[81] Ewoldt, R. H.; Hosoi, A. E.; McKinley, G. H. *Journal of Rheology* **2008**, *52*, 1427.

[82] Ewoldt, R. H. Nonlinear viscoelastic materials : bioinspired applications and new characterization measures. Ph.D. thesis, Massachusetts Institute of Technology, 2009.

[83] Rogers, S. A.; Erwin, B. M.; Vlassopoulos, D.; Cloitre, M. *Journal of Rheology* **2011**, *55*, 435.

[84] Rogers, S. A.; Lettinga, M. P. *Journal of Rheology* **2012**, *56*, 1.

[85] Rogers, S. A. *Journal of Rheology* **2012**, *56*, 1129.

[86] Ewoldt, R. H. *Journal of Rheology* **2013**, *57*, 177.

[87] Hiemenz, P. C.; Lodge, T. P. *Polymer Chemistry*, 2nd ed.; CRC Press: Boca Raton, 2007.

[88] Rubinstein, M.; Colby, R. H. *Polymer Physics*; Oxford University Press: New York, 2003.

[89] Anderson, R. J. *Applied Optics* **1969**, *8*, 1508–9.

[90] Moreels, E.; De Ceuninck, W.; Finsy, R. *The Journal of Chemical Physics* **1987**, *86*, 618–623.

[91] Glinka, C. J.; Barker, J. G.; Hammouda, B.; Krueger, S.; Moyer, J. J.; Orts, W. J. *Journal of Applied Crystallography* **1998**, *31*, 430–445.

[92] Barker, J. G.; Glinka, C. J.; Moyer, J. J.; Kim, M. H.; Drews, A. R.; Agamalian, M. *Journal of Applied Crystallography* **2005**, *38*, 1004–1011.

[93] Kienzle, P. Neutron Activation and Scattering Calculator. 2013; `https://www.ncnr.nist.gov/resources/activation/`.

[94] Kline, S. R. *Journal of Applied Crystallography* **2006**, *39*, 895–900.

[95] Roe, R.-J. *Methods of X-Ray and Neutron Scattering in Polymer Science*; Oxford University Press: New York, 2000.

[96] Schnablegger, H.; Singh, Y. *The SAXS Guide*; 2011.

[97] Lake, J. A. *Acta Crystallographica* **1967**, *23*, 191–194.

[98] Takeshita, H.; Saito, K.; Miya, M.; Takenaka, K.; Shiomi, T. *Journal of Polymer Science, Part B: Polymer Physics* **2010**, *48*, 168–174.

[99] Storm, C.; Pastore, J. J.; MacKintosh, F. C.; Lubensky, T.; Janmey, P. A. *Nature* **2005**, *435*, 191–194.

[100] *CRC Handbook of Chemistry and Physics*, 74th ed.; CRC Press: Boca Raton, FL, 1993-1994; p 6:10.

[101] Winter, H. H.; Chambon, F. *Journal of Rheology* **1986**, *30*, 367.

[102] Chambon, F.; Petrovic, Z. S.; MacKnight, W. J.; Winter, H. H. *Macromolecules* **1986**, *19*, 2146–2149.

[103] Winter, H. H. *Polymer Engineering and Science* **1987**, *27*, 1698–1702.

[104] Chambon, F.; Winter, H. H. *Journal of Rheology* **1987**, *31*, 683.

[105] Stockmayer, W. H. *The Journal of Chemical Physics* **1944**, *12*, 125.

[106] Stauffer, D.; Coniglio, A.; Adam, M. *Polymer Networks*; Springer Berlin Heidelberg: Berlin, Heidelberg, 1982; Chapter 44, pp 103–158.

[107] Macosko, C. W.; Miller, D. R. *Macromolecules* **1976**, *9*, 199–206.

[108] Miller, D. R.; Macosko, C. W. *Macromolecules* **1976**, *9*, 206.

[109] McAllister, J. W.; Schmidt, P. W.; Dorfman, K. D.; Lodge, T. P.; Bates, F. S. *Macromolecules* **2015**, *Accepted for Publication*.

[110] Rasband, W. S. ImageJ. `http://rsbweb.nih.gov/ij/index.html`.

[111] Bodvik, R.; Karlson, L.; Edwards, K.; Eriksson, J.; Thormann, E.; Claesson, P. M. *Langmuir* **2012**,

[112] Lott, J. R.; McAllister, J. W.; Wasbrough, M.; Sammler, R. L.; Bates, F. S.; Lodge, T. P. *Macromolecules* **2013**, *46*, 9760–9771.

[113] Pedersen, J. S.; Schurtenberger, P. *Macromolecules* **1996**, *29*, 7602–7612.

[114] Chen, W.-R.; Butler, P. D.; Magid, L. J. *Langmuir* **2006**, *22*, 6539–48.

[115] Kotlarchyk, M.; Stephens, R. B.; Huang, J. S. *The Journal of Physical Chemistry* **1988**, *92*, 1533–1538.

[116] Kratky, O.; Porod, G. *Journal of Colloid Science* **1949**, *4*, 35–70.

[117] McCrystal, C. B.; Ford, J. L.; Rajabi-Siahboomi, a. R. *Journal of Pharmaceutical Sciences* **1999**, *88*, 792–796.

[118] Velazquez, G.; Herrera-Gómez, A.; Martín-Polo, M. O. *Journal of Food Engineering* **2003**, *59*, 79–84.

[119] Fechner, P. M.; Wartewig, S.; Kiesow, A.; Heilmann, A.; Kleinebudde, P.; Neubert, R. H. H. *The Journal of Pharmacy and Pharmacology* **2005**, *57*, 689–698.

[120] Lin, S. Y.; Wang, S. L.; Wei, Y. S.; Li, M. J. *Surface Science* **2007**, *601*, 781–785.

[121] Buslov, D. K.; Sushko, N. I.; Tretinnikov, O. N. *Journal of Applied Spectroscopy* **2008**, *75*, 514–518.

[122] Higuera, A.; Bellantone, R. A. *Carbohydrate Polymers* **2010**, *81*, 578–583.

[123] Pavlov, G. M. *The European physical journal. E, Soft matter* **2007**, *22*, 171–80.

[124] Patel, T. R.; Morris, G. A.; Garcia de la Torre, J.; Ortega, A.; Mischnick, P.; Harding, S. E. *Macromolecular Bioscience* **2008**, *8*, 1108–1115.

[125] Zrinyi, M.; Horkay, F. *Polymer Bulletin* **1980**, *3*, 665–670.

[126] Hild, G.; Okasha, R.; Macret, M.; Gnanou, Y. *Die Makromolekulare Chemie* **1986**, *187*, 2271–2288.

[127] de Gennes, P.-G. *Scaling Concepts in Polymer Physics*; Cornell University Press: Ithaca, 1979; pp 156–160.

[128] Candau, S.; Bastide, J.; Delsanti, M. *Polymer Networks*; Springer Berlin Heidelberg: Berlin, Heidelberg, 1982; pp 27–71.

[129] Scanlan, J. C.; Winter, H. W. *Macromolelcules* **1991**, *24*, 47–54.

[130] Kundu, S. K.; Yoshida, M.; Shibayama, M. *Journal of Physical Chemistry B* **2010**, *114*, 1541–1547.

[131] Erk, K. a.; Henderson, K. J.; Shull, K. R. *Biomacromolecules* **2010**, *11*, 1358–1363.

[132] MacKintosh, F. C.; Käs, J.; Janmey, P. *Physical Review Letters* **1995**, *75*, 4425–4428.

[133] Yao, N. Y.; Broedersz, C. P.; Lin, Y.-C.; Kasza, K. E.; MacKintosh, F. C.; Weitz, D. A. *Biophysical Journal* **2010**, *98*, 2147–53.

[134] McAllister, J. W.; Lott, J. R.; Schmidt, P. W.; Sammler, R. L.; Bates, F. S.; Lodge, T. P. *ACS Macro Letters* **2015**, *4*, 538–542.

[135] Ferry, J. D. *Viscoelastic Properties of Polymers*, 3rd ed.; Wiley: New York, 1980.

[136] Macosko, C. W. *Rheology: Principles, Measurements, and Applications*; Wiley: New York, 1994.

[137] Jerke, G.; Pedersen, J.; Egelhaaf, S.; Schurtenberger, P. *Physical Review E* **1997**, *56*, 5772–5788.

[138] Janmey, P. A.; McCormick, M. E.; Rammensee, S.; Leight, J. L.; Georges, P. C.; MacKintosh, F. C. *Nature materials* **2007**, *6*, 48–51.

[139] Montesi, A.; Peña, A. a.; Pasquali, M. *Physical Review Letters* **2004**, *92*, 058303.

[140] Lin-Gibson, S.; Pathak, J. a.; Grulke, E. a.; Wang, H.; Hobbie, E. K. *Physical Review Letters* **2004**, *92*, 048302.

[141] Cioroianu, A. R.; Storm, C. *Physical Review E* **2013**, *88*, 1–9.

[142] Broedersz, C. P.; Kasza, K. E.; Jawerth, L. M.; Münster, S.; Weitz, D. A.; MacKintosh, F. C. *Soft Matter* **2010**, *6*, 4120.

[143] Klein, C. O.; Spiess, H. W.; Calin, A.; Balan, C.; Wilhelm, M. *Macromolecules* **2007**, *40*, 4250–4259.

[144] Ewoldt, R. H.; Mckinley, G. H. *Rheology Bulletin* **2007**, *76*, 4–6,22–24.

[145] Hyun, K.; Nam, J. G.; Wilhelm, M.; Ahn, K. H.; Lee, S. J. *Korea-Australia Rheology Journal* **2003**, *15*, 97–105.

[146] Kang, H.; Wen, Q.; Janmey, P. A.; Tang, J. X.; Conti, E.; MacKintosh, F. C. *The Journal of Physical Chemistry. B* **2009**, *113*, 3799–805.

[147] Wilhelm, M.; Reinheimer, P.; Ortseifer, M. *Rheologica Acta* **1999**, *38*, 349–356.

[148] NeidhŽfer, T.; Wilhelm, M.; Debbaut, B. *Journal of Rheology* **2003**, *47*, 1351.

[149] Ozbas, B.; Rajagopal, K.; Schneider, J. P.; Pochan, D. J. *Physical Review Letters* **2004**, *93*, 1–4.

[150] De Gennes, P.; Pincus, P.; Velasco, R.; Brochard, F. *Journal de Physique* **1976**, *37*, 1461–1473.

[151] Dobrynin, A. V.; Carrillo, J.-M. Y. **2011**, 140–146.

[152] Carrillo, J.-M. Y.; MacKintosh, F. C.; Dobrynin, A. V. *Macromolecules* **2013**, *46*, 3679–3692.

[153] Chan, S.; Ho, K. *IEEE Transactions on Circuits and Systems* **1991**, *38*, 951–953.

[154] Dodge, J. S.; Krieger, I. M. *Transactions of the Society of Rheology* **1971**, *15*, 589.

[155] Berry, G. C. *The Journal of Chemical Physics* **1966**, *44*, 4550.

[156] Berry, G. C.; Cotts, P. M. In *Modern Techniques for Polymer Characterisation*, 1st ed.; Pethrick, R. A., Dawkins, J. V., Eds.; Wiley-Interscience, 1999; Chapter 4.

[157] Yin, Y.; Nishinari, K.; Zhang, H.; Funami, T. *Macromolecular Rapid Communications* **2006**, *27*, 971–975.

[158] Jinbo, Y.; Sato, T.; Teramoto, A. *Macromolecules* **1994**, *27*, 6080–6087.

[159] Flory, P. J. *Proceedings of the Royal Society A: Mathematical, Physical and Engineering Sciences* **1956**, *234*, 73–89.

[160] Flory, P. J. *Proceedings of the Royal Society A: Mathematical, Physical and Engineering Sciences* **1956**, *234*, 60–73.

[161] Flory, P. J.; Matheson, R. R. *The Journal of Physical Chemistry* **1984**, *88*, 6606–6612.

[162] Matsuyama, A.; Tanaka, F. *Physical Review Letters* **1990**, *65*, 341–344.

[163] Dormidontova, E. E. *Macromolecules* **2002**, *35*, 987–1001.

[164] Dorgan, J. R. *Liquid Crystals* **1991**, *10*, 347–355.

[165] Dorgan, J. R. *Journal of Chemical Physics* **1993**, *98*, 9094.

[166] Starr, F. W.; Nielsen, J. K.; Stanley, H. E. *Physical Review Letters* **1998**, *82*, 2294–2297.

[167] Steinel, T.; Asbury, J. B.; Zheng, J.; Fayer, M. D. *The Journal of Physical Chemistry. A* **2004**, *108*, 10957–10964.

[168] Smith, J. D.; Cappa, C. D.; Wilson, K. R.; Cohen, R. C.; Geissler, P. L.; Saykally, R. J. *Proceedings of the National Academy of Sciences* **2005**, *102*, 14171–14174.

[169] Huang, C. et al. *Proceedings of the National Academy of Sciences* **2009**, *106*, 15214–15218.

[170] Kong, M.; Saha Dalal, I.; Li, G.; Larson, R. G. *Macromolecules* **2014**, *47*, 1494–1502.

[171] Nishiyama, Y.; Sugiyama, J.; Chanzy, H.; Langan, P. *Journal of the American Chemical Society* **2003**, *125*, 14300–6.

[172] Song, H.; Zhang, J.; Niu, Y.; Wang, Z. *The Journal of Physical Chemistry B* **2010**, *114*, 6006–6013.

[173] Vogt, U.; Zugenmaier, P. *Berichte der Bunsengesellschaft für physikalische Chemie* **1985**, *89*, 1217–1224.

[174] Fortin, S.; Charlet, G. *Macromolecules* **1989**, *22*, 2286–2292.

[175] Nishida, R.; Takahashi, M. *Polymer Journal* **2008**, *40*, 148–153.

[176] Haque, A.; Richardson, R. K.; Morris, E. R.; Gidley, M. J.; Caswell, D. C. *Carbohydrate Polymers* **1993**, *22*, 175–186.

[177] Laaser, J. E.; Jiang, Y.; Sprouse, D.; Reineke, T. M.; Lodge, T. P. *Macromolecules* **2015**, *48*, 2677–2685.